université
PARIS-SACLAY

Precision spectroscopy and control of individual nuclear spins in the solid state

Spectroscopie de précision et contrôle des spins nucléaires individuels à l'état solide

Thèse de doctorat de l'université Paris-Saclay

École doctorale n° 564, Physique en Ile-de-France (PIF)
Spécialité de doctorat : Physique
Graduate School : Physique. Référent : Faculte de Sciences d'Orsay

Thèse préparée dans l'unité(s) de recherche **Service de Physique de l'État Condensé** (Université Paris-Saclay, CEA, CNRS), sous la direction de **Patrice BERTET**, directeur de recherche, CEA Saclay, et **Emmanuel FLURIN**, directeur de recherche, CEA Saclay.

Thèse soutenue à Paris-Saclay, le 30 mars 2026, par

Jaime TRAVESEDO

Composition du Jury

Membres du jury avec voix délibérative

Christopher EICHLER Professeur, Friedrich-Alexander University	Président
Daniella GOLDFARB Professeure, Weizmann Institute of Science	Rapporteur & Examinatrice
Tim TAMINIAU Directeur de recherche, Technische Universiteit Delft	Rapporteur & Examinateur
Ilya KUPROV Professeur, Weizmann Institute of Science	Examinateur

THESE DE DOCTORAT

NNT : 2026UPASP020

université PARIS-SACLAY | ÉCOLE DOCTORALE Physique en Île-de-France (PIF)

Titre : Spectroscopie de précision et contrôle des spins nucléaires individuels à l'état solide

Mots clés : Resonance Paramagnetique Electronique (RPE), Resonance Magnetic Nucleaire (RMN), Computation quantique.

Résumé : Repousser la sensibilité de la spectroscopie par résonance magnétique nucléaire jusqu'à la limite du spin nucléaire unique est un objectif poursuivi de longue date. Une telle avancée trouverait des applications aussi bien en informatique quantique qu'en spectroscopie de haute précision. Jusqu'à présent, les seuls mécanismes permettant de détecter des spins nucléaires individuels reposent sur l'utilisation d'un spin électronique situé à proximité, qui se couple via l'interaction hyperfine et agit comme une antenne locale. Ainsi, la détection d'un spin nucléaire individuel nécessite la lecture d'un spin électronique unique.

Jusqu'à récemment, la détection de spins électroniques uniques était limitée à des méthodes de lecture électrique ou optique, qui ne permettent la détection que pour certains systèmes spécifiques, restreignant ainsi le champ d'étude. Notre groupe a récemment développé une nouvelle méthode permettant de détecter des spins électroniques à 10 mK. En couplant le spin électronique à un résonateur de faible volume modal et à facteur de qualité élevé, le taux de relaxation radiative du spin est augmenté par l'effet Purcell. L'émission spontanée est détectée par un détecteur novateur reposant sur un qubit transmon supraconducteur, le SMPD. Comme cette méthode repose uniquement sur le couplage dipolaire magnétique entre le moment magnétique du spin et un résonateur, cette approche entièrement micro-ondes devrait en principe être largement applicable à une grande variété de systèmes à spins électroniques non appariés.

Dans cette thèse, nous développons un ensemble de nouvelles méthodes pour lire et mesurer le spectre de spins nucléaires individuels couplés à un spin électronique, lui-même mesuré par comptage de photons micro-ondes. Nous appliquons ces méthodes à l'exploitation d'un registre à deux qubits de spins nucléaires, ainsi qu'à la spectroscopie haute résolution d'une impureté individuelle de spin nucléaire 9/2. Dans l'ensemble, les méthodes présentées dans cette thèse démontrent le potentiel du comptage de photons micro-ondes pour l'informatique quantique et la spectroscopie de précision.

Title : Precision spectroscopy and control of individual nuclear spins in the solid state

Keywords : Electron Paramagnetic Resonance (EPR), Nuclear Magnetic Resonance (NMR) Quantum computing.

Abstract : Pushing the sensitivity of nuclear magnetic resonance spectroscopy down to the single nuclear spin limit is a long-standing goal, and would find applications both in quantum computing and in high-precision spectroscopy. So far, the only mechanisms to detect individual nuclear spins use an electron spin in close proximity, which couples via hyperfine interaction and acts as a local antenna. Therefore, individual nuclear spin detection requires single electron spin readout.

Until recently, detection of single electron spins has been limited to electrical or optical readout, which achieves single electron spin detection only for certain specific systems, thus limiting the range of study. Our group has recently developed a new method to detect electron spins at 10 mK. By coupling the electron spin to a low-mode-volume, high-quality-factor resonator, the radiative relaxation rate of the spin is enhanced by the Purcell effect. The spontaneous emission is detected by a novel detector relying on superconducting transmon qubit, the SMPD. As it relies solely on the magnetic dipole coupling of the spin magnetic moment to a resonator, this all-microwave method should be in principle broadly applicable to a large range of unpaired electron spin systems.

In this thesis, we develop a range of new methods to readout and measure the spectrum of individual nuclear spins coupled to an electron spin, itself measured by microwave photon counting. We apply these methods to the operation of a two-nuclear-spin-qubit register, and to the high-resolution spectroscopy of an individual nuclear-spin-9/2 impurity. Overall, the methods presented in this thesis demonstrate the potential of microwave photon counting for quantum computing and precision spectroscopy.

À Carla

Acknowledgements

I would like to spend a few pages acknowledging everyone who has helped me throughout my PhD.

First, I want to thank my two fantastic supervisors, Patrice and Emmanuel.

Patrice, you have been a kind and wise mentor, teaching me lessons I will carry through life. You have helped me develop a scientific and critical mindset, you have fostered my curiosity and helped me develop rigor. Thank you deeply for your patience and availability in the lab, always ready for a discussion or a question. Thank you for thoroughly reviewing this manuscript, your advice and comments have made it much better. Also, after four years, you have managed to teach me the difference between a microsecond and a millisecond, which is nice.

Emmanuel, thank you for your passion and sharing your deep, intuitive knowledge. You motivated me when I was feeling down, which was invaluable to me. I have learned so much working with you, while also having a lot of fun together, betting beers on the T_2^* of the nuclear spins or fighting for control over the keyboard.

James, the amount of things you have taught me is on a par with Patrice and Emmanuel. You have shown me how to manage the day-to-day needs of an experiment, with your passionate and positive mindset. You have also been a fantastic friend and colleague, the time working together on the spin experiment holds some of the best memories of my PhD.

The group is home to a lot of fantastic people whom I want to thank sincerely, both for their help in the lab and for the fun times that we had together.

When I joined the group, both Leo and Eric were close to finishing their thesis. Both of them took time to show me the ropes and help me get acquainted with the many complex parts of the experiment. Thank you, Eric, I really enjoyed working together in room 102, my first interaction with some real spins. It was very inspiring to see your calm and meticulous work, as well as your passion for a greener Earth. Thank you, Leo, I remember fondly the time we spent together measuring your SMPD and the spins in room 4, which would later become my main battle station. I was really happy when I heard you were coming back with us, and it's been great having you back in the lab these last few months.

I also want to thank the postdocs from the beginning of the PhD. Thank you, Boris, for your patience, kind words, and in-depth explanations whenever I had a question. I loved climbing with you many times in Massy and the climbing expedition in Normandy. Thanks, Yutian, for keeping in contact after you left the lab, and thank you for inviting us over to Notre Dame University when we were in Chicago. The museum card you left us in compensation for the five-hour drive was more than worth it: I went three times to the Art Institute! I'm very happy every time we have crossed paths during the March Meeting.

I would like to thank my fellow PhD students, who made the days in the lab brighter and the late nights closing fridges or debugging code far more bearable.

Zhiren, you are the giant on whose shoulders we stand, as the work in my thesis builds directly upon yours. Thank you so much for your advice in the lab and for the cooking nights together at the South-East Asia house in Cité. Also, thank you for the amazing cakes you have brought to the lab over the years, you are a fantastic chef. Alexandre, thank you for your calm and collected advice, both on life and in the lab. I regret not having worked together on the same project, it would have been really fun.

Louis, thank you so much for being such a kind and helpful friend. We have been desk buddies almost from the very beginning (after stealing the office from Eric and Leo ;)), and I have really enjoyed writing our papers, thesis, and, in general, working together there. I will always remember our rock-star trip around Chicago, going on lab visits in that ridiculous Dodge Charger, it was fantastic. It was really fun listening to the crazy American radio and spotting the insane billboards (CHEESE?).

Brian, thank you for showing me how rewarding teaching can be. The passion you show for your students, who deeply appreciate you, demonstrates your amazing qualities as a teacher. We should call the Assurance Maladie again at some point, I'm sure they miss us. Alexander, thank you for being such a reliable friend, always there to talk about life's problems and to laugh them off together. I have a great memory of the times

the three of us spent playing Diablo 2 together and eating bad pizza, it was the highlight of many bleak weeks.

A la mafia hispana del laboratorio, Joan, Diego y Jon, os aprecio un montón; me encanta pasarme de vez en cuando por vuestro laboratorio y estar un rato con vosotros. Joan, eres un gran amigo, disfruto muchísimo de nuestras charlas sobre física y la vida en general. Me hace muy feliz que nuestros siguientes pasos nos lleven a Delft al mismo tiempo. Amigo, te vas a comer el mundo. Diego, me ha encantado conocerte y salir de fiesta juntos. La fête de la Cité en la casa belga, falsificando los papelitos con colonia, fue un momento muy top que me hace reír muchísimo. Jon, muchas gracias por los consejos sobre cómo sobrevivir un postdoc y tu enorme serenidad.

Will (my hommieee), I have really enjoyed working with you in the lab. It has been a great pleasure to see you take over the experiment and make it your own. I have learned a lot from your patience and positivity. Also, thank you *so* much for the amazing Chinese food you have cooked for me. Nicolas, I really enjoy our friendship, it's always great to talk to you and spend time together. I have great memories from the conference in Nice, going swimming in the morning and having fantastic pizzas in the evening. Paddy, I loved working together. Thanks for your optimism and joy, it was great having you in Paris for a while. Dominik, I learned a lot from working with you, thanks for your strong convictions and engaging discussions. It was great living in the Swiss house together! Leo, thanks for always having a kind word and caring for people around you. I hope Singapore is treating you well. Lou, thanks for always being there to vent and rant about life and capitalism, you always make me feel better after we talk. Steffano, thanks for your humor and great attitude, the small coffee breaks at the back of the lab *à la française* are always very fun.

André, you have been a great mentor and friend. You are extremely patient and meticulous, and you have taught me a lot about how to be rigorous in the lab. You have also been a great friend, and I really enjoyed all our evenings in Massy climbing together. Xianjing, thanks for your advice during the postdoc hunt, it was great to chat about the options and hear your strong opinions!

To the new students of the lab, Jannis, Malo, Leon, and Johan, I hope you enjoy your years in Quantronics as much as I have enjoyed mine. It's a fantastic adventure, full of broken amplifiers and pulse sequences you don't completely understand.

I also want to thank all the permanent members of the group for their advice, mentorship, and kindness. Thank you, Patrick, for our time fabricating the sample together. Despite my shaky hands and general carelessness, we managed to make a superhero device in the end. Thank you, Dennis, Carles, Olivier, Philippe, Hélène, Marcelo, and Hugues for being so passionate about research, for always having a moment to discuss, and for your constant encouragement. A gigantic thanks to the lab engineers Paul, Pascal, Pief, and Sebastian, without whom no research would have been possible. Thanks to the SPEC secretaries, Nathalie and Julie, who have helped countless times. Many thanks to François and Gwen for their role in managing all PhD students in SPEC.

I want to thank our external collaborators. Many thanks to Philippe Goldner and Diana Serrano for providing the $CaWO_4$ sample and Sylvain Bertrana for the EPR characterization. Thanks to Sen Lin and Ren-bao Liu for the CCE simulations, and thanks to Thibault Charpentier for the DFT analysis of the quadrupole interaction.

Outside the lab, a lot of people have supported and helped me in my personal life.

A mis más viejos amigos, Jorge, Diego e Íñigo, os llevo siempre conmigo. Hemos crecido juntos, desde que éramos unos mocosos en la máquina de Coca-Cola en el pasillo del colegio, hasta donde estamos hoy, repartidos por doquier. Me alegra muchísimo reencontrarnos cada año en Navidad y ver cómo hemos cambiado. Diego, te echo de menos.

A mis amigos de la universidad (aunque más bien es Antares), Sara, Ricardo, Miguel, Delfa, Alex y Patri, os quiero muchísimo y os echo de menos en la misma cantidad. Habéis sido mi sol y mi luna durante mis años en Física UAM. No creo que hubiera aguantado si no hubiera sido por vosotres. Las distancias no son amables con las amistades, pero la nuestra ha perdurado y espero que así continúe de por vida.

Guillaume mon pote, merci d'être un si bon ami, les cours ensemble à Durham ainsi que les heures passées dans la bibliothèque et les fêtes bizarres avec des Anglais font partie de mes meilleurs souvenirs de l'Erasmus.

I want to thank all the great people of the Quantum Devices master. It was one of the most fun years of my studies, and it made living in a new foreign city much easier. Thanks, Julien, for being such a fun friend. The two visits to Bonn were great, and I'm already looking forward to the next one.

Finally, I want to give thanks to the people closest to my heart, who I love unconditionally.

A Fernando y Rosa, aunque no lo parezca, las cosas no han cambiado tanto desde pijama y botas. Muchas gracias, Totó, por ser mi inspiración desde pequeñito, por venir cada semana a vernos a Irene y a mí, por hacer que me enamore de los números y las ciencias. Muchas gracias, Tatá, por enseñarme el valor de la lectura, si Totó me dio las ciencias, tú me has dado las letras.

Irene, hermanita, cómo te quiero y cómo te echo de menos. Muchas gracias por ser pesada, chillona, listilla y la mejor hermana del mundo. Qué orgulloso estoy de ti.

Papá y Mamá, os quiero muchísimo y os doy las gracias por vuestro amor infinito. Soy la persona que soy por vuestro amor, vuestra educación, vuestro cariño... vuestro todo. Me habéis apoyado en cada paso del camino, decir que no estaría aquí si no fuera por vosotros se quedaría corto.

Carla, mi amor: thank you for everything. These last six years together have made me the happiest person in the world. From Taco Tuesday to living together, it has been a fantastic journey together. You have supported and helped me, especially while writing this manuscript, and I can never thank you enough. I love you so much, and I can't wait to see what the future holds for us.

Thank you all. This has all been worth it because of you.

Contents

Contents vii

1. Résumé détaillé 1

2. Introduction 10
2.1. Measuring the fluorescence of individual electron spins . . . 11
2.2. Detection of individual nuclear spins and dynamical nuclear polarization . . . 13
2.3. A register of two nuclear spin qubits . . . 15
2.4. Precision spectroscopy on a 9/2 nuclear spin . . . 16

Background 18

3. Electron spins, nuclear spins and their interaction 19
3.1. An electron in free space . . . 19
3.2. Er^{3+} ions in $CaWO_4$ . . . 20
Free-ion Hamiltonian . . . 20
$CaWO_4$ crystal . . . 21
Crystal-field Hamiltonian . . . 22
Spin-1/2 approximation . . . 24
Linear electric field effect . . . 25
Summary . . . 26
3.3. Nuclear spins in $CaWO_4$ . . . 27
Nuclear Zeeman interaction . . . 27
Electric Quadrupole interaction . . . 27
3.4. Hyperfine interaction . . . 29
3.5. The spin Hamiltonian . . . 30
3.6. Nuclear spin $\frac{1}{2}$ . . . 32
3.7. Quadrupolar spins . . . 34

4. Er^{3+} spin coupled to a cavity 37
4.1. Quantum circuits . . . 37
4.2. Spin-resonator coupling . . . 38
Driving the Er^{3+} spin . . . 40
4.3. The effect of the environment . . . 41
Resonator losses . . . 41
Spin losses . . . 42
4.4. Microwave photon counting . . . 44
4.5. Single-spin detection by microwave photon counting . . . 45

5. Nuclear spin control via microwaves 47
5.1. Driving a ^{183}W nuclear spin through the Er^{3+} spin . . . 47
Zero- and double-quantum transitions . . . 47
AC-Zeeman shifts . . . 48
Cross-relaxation probability . . . 49
Stimulated Raman driving . . . 50
5.2. High-spin generalization . . . 52
Zero- and double-quantum transitions . . . 52
Cross-relaxation rates . . . 54
Stimulated Raman driving . . . 55
5.3. Summary . . . 55

6. Sample and setup **57**
6.1. Sample . . . 57
Resonator design and fabrication . . . 57
6.2. Measurement setup . . . 60
6.3. Superconducting resonator characterization . . . 61
Magnetic field alignment . . . 61
6.4. SMPD frequency tuning . . . 63
6.5. Erbium ensemble spectroscopy . . . 64
6.6. Individual Er^{3+} spins . . . 66

^{183}W NUCLEAR SPINS **69**

7. All-microwave detection and control of individual ^{183}W nuclear spins **70**
7.1. State-of-the-art . . . 70
7.2. Single Er^{3+} spins characterization . . . 73
7.3. Nuclear spin quantum jumps . . . 74
Time trace analysis . . . 74
Tracking procedure . . . 77
7.4. Single-shot readout . . . 79
7.5. Sideband driving and nuclear spin identification . . . 83
7.6. Solid effect DNP . . . 85
7.7. Conclusion and outlook . . . 87

8. Individual nuclear spins in the solid state for quantum computing **88**
8.1. State of the art . . . 88
8.2. Spin system . . . 92
8.3. Preparation and readout . . . 93
8.4. Stimulated Raman driving . . . 94
Single-qubit gates . . . 96
8.5. Nuclear spin coherence time . . . 98
8.6. Entangling the nuclear spins . . . 99
8.7. Bell state tomography . . . 100
8.8. Decoherence-free subspace . . . 102
8.9. Conclusion and outlook . . . 103

^{93}Nb NUCLEAR SPIN **105**

9. Precision spectroscopy of a ^{93}Nb nuclear spin **106**
9.1. State-of-the-art . . . 106
9.2. Spin system . . . 110
9.3. Readout, preparation and control . . . 113
9.4. Identification and site assignment . . . 117
9.5. Precision NMR spectroscopy . . . 118
9.6. Hamiltonian parameters fit . . . 121
Fitting $\mathscr{H}^{(\Downarrow)}$ and $\mathscr{H}^{(\Uparrow)}$ . . . 121
Fitting $\mathscr{H}$ . . . 125
9.7. Origin of the SDQ interaction . . . 128
Pseudo-quadrupole interaction . . . 128
Electrostatic coupling . . . 130
9.8. Octupole and hexadecapolar bounds . . . 131
9.9. Conclusion and outlook . . . 132

10. Conclusion and future directions **134**

Appendix **136**

A. Rotation of the quadrupole tensor around the z-axis **137**

B. Single Microwave Photon Detector **139**
B.1. Working principle 139
B.2. SMPD Circuit 140
B.3. Performance metrics 142

C. Time-dependent Hamiltonian simulations **145**

D. Monte Carlo Markov Chain fitting procedure **146**
D.1. Ground and excited fits 147
D.2. Full Hamiltonian fit 148

Bibliography **150**

List of Figures

1.1. Principe de mesure . . . 2
1.2. Cristal $CaWO_4$ . . . 3
1.3. Détection de spins individuels de ^{183}W et DNP . . . 5
1.4. Registre de qubits à deux spins nucléaires . . . 6
1.5. Spectroscopie NMR de précision d'un spin nucléaire ^{93}Nb . . . 8
1.6. Reconstruction du tenseur quadrupolaire . . . 9

2.1. Measurement principle . . . 11
2.2. $CaWO_4$ crystal . . . 12
2.3. Detection of individual ^{183}W and DNP . . . 13
2.4. A two nuclear spin qubit register . . . 14
2.5. Precision NMR spectroscopy of a ^{93}Nb nuclear spin . . . 16
2.6. Quadrupole tensor reconstruction . . . 17

3.1. Energy splitting diagram from free-ion to effective spin-1/2 . . . 21
3.2. $CaWO_4$ crystal . . . 21
3.3. Crystal field levels . . . 24
3.4. Zeeman splitting of the Z_1 doublet . . . 26
3.5. Quadrupole charge diagram . . . 28
3.6. ^{183}W -Er^{3+} coupled system . . . 32
3.7. Energy level diagram of an Er^{3+} coupled to a nuclear spin-9/2 . . . 35
4.1. Lumped element resonator . . . 37

4.2. Energy of a harmonic oscillator . . . 38
4.3. Spin dynamics . . . 41
4.4. Resonator coupled to a spin . . . 43
4.5. Operational efficiency of an SMPD . . . 44
4.6. Detection Scheme . . . 45
5.1. Energy level diagram of an Er^{3+} coupled to a nuclear spin-1/2 . . . 47

5.2. AC Zeeman shift diagram . . . 49
5.3. Stimulated Raman Scheme . . . 50
5.4. Raman Rabi frequency as a function of Δ . . . 51
5.5. Energy level diagram of an Er^{3+} coupled to a nuclear spin-9/2 . . . 52
5.6. Spin ladder operators for $I = 9/2$ . . . 53

6.1. Sample micrograph and coupling map . . . 58
6.2. Resonator assembly . . . 59
6.3. Wiring diagram . . . 60
6.4. Resonator fit . . . 61
6.5. Magnetic field alignment . . . 62
6.6. Resonator response to in-plane field . . . 63
6.7. Buffer frequency tuning . . . 63
6.8. High power spectroscopy . . . 64
6.9. Sample Field Alignment . . . 65
6.10. Low power spectroscopy and electron spin characterization . . . 67
6.11. 2D single spin spectroscopy . . . 68
7.1. NV center in diamond . . . 70

7.2. State-of-the-art: Single-shot readout of a ^{14}N nuclear spin . . . 71

7.3. State-of-the-art: Single-shot readout of a ^{31}P nuclear spin . . . 72
7.4. Er^{3+} time traces . . . 75
7.5. Er^{3+} time trace analysis . . . 76
7.6. Hyperfine coupling between Er^{3+} and ^{183}W . . . 77
7.7. $CaWO_4$ crystal with magnetically similar sites . . . 77
7.8. Rudimentary tracking scheme . . . 78
7.9. Ramsey tracking scheme . . . 78
7.10. Nuclear single-shot readout trace . . . 79
7.11. Nuclear single-shot readout pulse sequence . . . 80
7.12. Nuclear single-shot readout fidelity . . . 80
7.13. ^{183}W sideband spectroscopy . . . 84
7.14. ^{183}W sideband Rabi oscillations . . . 85
7.15. Solid-effect DNP . . . 86
7.16. Time traces under DNP . . . 86

8.1. State-of-the-art: Two-qubit gates in NV centers in diamond. . . . 89
8.2. State-of-the-art: Decoherence-free subspace . . . 89
8.3. State-of-the-art: Two-qubit gates in phosphorus in silicon . . . 90
8.4. $CaWO_4$ with two ^{183}W nuclear spins . . . 92
8.5. Energy level system of one Er^{3+} spin with two ^{183}W nuclear spins . . . 92
8.6. Electron spin spectra for each nuclear spin state . . . 93
8.7. Two ^{183}W nuclear spin readout . . . 94
8.8. Stimulated Raman Scheme . . . 95
8.9. Two-qubit Raman driving . . . 96
8.10. NMR spectra and Rabi driving of Qb1 and Qb2 . . . 97
8.11. Unconditional spectroscopy . . . 97
8.12. Extended duration Raman Rabi on Qb1. . . . 98
8.13. Ramsey measurement for Qb1 and Qb2 . . . 98
8.14. Echo measurement for Qb1 and Qb2 . . . 99
8.15. SEDOR measurement . . . 99
8.16. Conditional spectroscopy and CNOT gate . . . 100
8.17. Bell state tomography . . . 101
8.18. Decoherence-free subspace . . . 102

9.1. State-of-the-art: Nuclear spectrum of a ^{14}N spin . . . 107
9.2. State-of-the-art: Correlations between ^{14}N parameters . . . 107
9.3. State-of-the-art: Nuclear spectrum of a ^{123}Sb spin . . . 108
9.4. State-of-the-art: Strain map on silicon . . . 109
9.5. Rotation pattern and time trace of ^{93}Nb – Er^{3+} system . . . 111
9.6. Energy level diagram of an Er^{3+} coupled to a nuclear spin-9/2 . . . 112
9.7. Mixing terms and cross-relaxation probabilities . . . 113
9.8. Single-shot readout of the ^{93}Nb spin state . . . 113
9.9. ZQ transition spectroscopy . . . 114
9.10. Nine ZQ transitions and Rabi oscillations . . . 115
9.11. Estimated value of $A_\perp$ . . . 115
9.12. Polarization sequence . . . 116
9.13. NMR spectroscopy of a ^{93}Nb nuclear spin. . . . 116
9.14. Rabi oscillations for all ^{93}Nb transitions . . . 117
9.15. $A_\perp$ measured through stimulated Raman driving . . . 117
9.16. $CaWO_4$ crystal structure with ^{93}Nb . . . 117
9.17. Measured and calculated hyperfine coupling as a function of θ_S . . . 118
9.18. ^{93}Nb Ramsey measurements . . . 119
9.19. ^{93}Nb transition frequency drift . . . 120
9.20. Effect of ^{183}W polarization . . . 120
9.21. Hahn echo coherence . . . 121

9.22. Residuals for the $\mathscr{H}^{(\Downarrow)}$ and $\mathscr{H}^{(\Uparrow)}$ fit . . . 124
9.23. Quadrupole principal values . . . 125
9.24. Quadrupole tensor in 3D . . . 128
9.25. SDQ coupling strength vs in-plane angle . . . 128
9.26. Pseudo-quadrupole shift simulation . . . 130
9.27. Octupole and hexadecapole posterior distributions . . . 132

B.1. SMPD working principle . . . 139

B.2. SMPD cycle . . . 140
B.3. SMPD circuit . . . 141

D.1. MCMC chain . . . 146
D.2. Corner plots of the separate Hamiltonian fits . . . 147
D.3. Corner plot of the full Hamiltonian fit . . . 148

List of Tables

3.1. Crystal field parameters . . . 23
3.2. Magneto-optic parameters . . . 26

7.1. Electron spin characterization . . . 73
7.2. Cross-relaxation probability . . . 76
7.3. Hyperfine coupling measurement . . . 76

8.1. Er_4 characterization. . . . 92
8.2. Truth table for a CNOT gate. . . . 100

9.1. Er^{3+} characterization . . . 111
9.2. Gyromagnetic ratios of stable nuclei with spin $I = 9/2$. . . . 117

B.1. SMPD frequencies . . . 142

1. Résumé détaillé

La résonance magnétique est une technique spectroscopique qui exploite le couplage entre des spins et un rayonnement électromagnétique afin de sonder les propriétés microscopiques de la matière. Ce domaine se divise généralement en résonance paramagnétique électronique (Electron Paramagnetic Resonance, EPR) [1] et en résonance magnétique nucléaire (Nuclear Magnetic Resonance, NMR) [2], selon la nature des spins étudiés : respectivement des spins électroniques célibataires (électrons non appariés) ou des spins nucléaires. En raison de l'omniprésence des spins dans la matière, les techniques de résonance magnétique trouvent de nombreuses applications, allant de l'imagerie médicale [3] à la science des matériaux [4], en passant par la biologie [5] et le contrôle qualité pharmaceutique [6].

[1]: Abragam (1986), *The Principles of Nuclear Magnetism*

[2]: Slichter (1996), *Principles of Magnetic Resonance*

[3]: Lauterbur (1973), 'Image Formation by Induced Local Interactions'

[4]: Haworth et al. (2022), 'Solid-State NMR Studies of Coatings and Interfaces in Batteries'

[5]: Wüthrich (1989), 'Protein Structure Determination in Solution by Nuclear Magnetic Resonance Spectroscopy'

[6]: Holzgrabe (2010), 'Quantitative NMR Spectroscopy in Pharmaceutical Applications'

Une limitation importante des techniques conventionnelles de résonance magnétique est leur faible sensibilité. Comme l'interaction entre les spins et les champs électromagnétiques est faible, de grands ensembles de spins sont nécessaires pour produire un signal détectable. Par conséquent, la plupart des mesures donnent accès à des grandeurs moyennées sur l'ensemble, tandis que les variations microscopiques et locales restent difficiles à atteindre.

En utilisant des amplificateurs limités par le bruit quantique et des résonateurs supraconducteurs, la sensibilité a été poussée à l'extrême, au point de permettre la détection de dix spins électroniques [7]. La détection d'un spin unique a été réalisée dans un petit nombre de systèmes à l'état solide, tels que les centres NV dans le diamant [8] et les impuretés donneuses dans le silicium [9]. Cela a été rendu possible grâce à des mécanismes spécifiques à chaque système, notamment des transitions optiques sélectives en spin et la conversion spin-charge. Les résultats obtenus dans ces systèmes montrent comment des spins électroniques et nucléaires individuels dans l'état solide peuvent être utilisés pour le calcul quantique [10, 11] et la spectroscopie de haute précision [12, 13].

[7]: Ranjan et al. (2020), 'Electron Spin Resonance Spectroscopy with Femtoliter Detection Volume'

[8]: Jelezko et al. (2002), 'Single Spin States in a Defect Center Resolved by Optical Spectroscopy'

[9]: Morello et al. (2010), 'Single-Shot Readout of an Electron Spin in Silicon'

[10]: Bradley et al. (2019), 'A Ten-Qubit Solid-State Spin Register with Quantum Memory up to One Minute'

[11]: Edlbauer et al. (2025), 'An 11-Qubit Atom Processor in Silicon'

[12]: Abobeih et al. (2019), 'Atomic-Scale Imaging of a 27-Nuclear-Spin Cluster Using a Quantum Sensor'

[13]: Breitweiser et al. (2024), 'Quadrupolar Resonance Spectroscopy of Individual Nuclei Using a Room-Temperature Quantum Sensor'

Récemment, notre groupe a montré que des impuretés paramagnétiques individuelles dans un diélectrique pouvaient être détectées via la fluorescence micro-onde de leur transition de spin électronique à 10 mK [14]. Cette méthode est, en principe, applicable à un grand nombre d'espèces paramagnétiques et de substrats, puisqu'elle requiert uniquement d'augmenter le taux d'émission spontanée du spin électronique au-delà du taux de relaxation non radiative à des températures cryogéniques. **Cette thèse montre comment le comptage de photons micro-ondes peut être utilisé pour détecter et contrôler de manière cohérente des spins nucléaires individuels couplés à un seul spin électronique.** De plus, nous démontrons une spectroscopie de précision des transitions NMR et montrons comment les spins nucléaires peuvent trouver des applications en calcul quantique.

[14]: Wang et al. (2023), 'Single-Electron Spin Resonance Detection by Microwave Photon Counting'

La thèse est divisée en trois parties. La première partie du manuscrit décrit le système physique et le dispositif expérimental. Nous introduisons l'Hamiltonien de spin des spins électroniques de Er^{3+} dans $CaWO_4$, les spins nucléaires présents dans le cristal et leur interaction. Nous décrivons comment le couplage du spin de Er^{3+} à un résonateur accroît le taux de relaxation spontanée via l'effet Purcell, ainsi que le dispositif de détection : le détecteur de photons micro-ondes uniques. En outre, nous présentons

les techniques micro-ondes utilisées pour contrôler l'état de spin nucléaire. La deuxième partie de ce travail est consacrée à la détection et au contrôle des spins nucléaires de ^{183}W. Nous mesurons des sauts quantiques de l'état de spin nucléaire et démontrons la spectroscopie hyperfine ainsi qu'une préparation déterministe à l'aide de seules impulsions micro-ondes. Par ailleurs, nous utilisons une excitation Raman stimulée par micro-ondes afin de démontrer des portes à un et deux qubits dans un registre à deux qubits de spins nucléaires de ^{183}W. Nous mesurons également des temps de cohérence de l'ordre d'une seconde, parmi les plus longs mesurés dans l'état solide. Dans la troisième partie de la thèse, nous étudions une impureté ^{93}Nb de spin nucléaire 9/2. Nous généralisons les techniques présentées ci-dessus et réalisons une spectroscopie de précision des transitions de spin nucléaire.

Mesurer la fluorescence de spins électroniques individuels

Les spectromètres EPR impulsionnels conventionnels mesurent la magnétisation transverse d'ensembles de spins électroniques, qui rayonnent collectivement un champ cohérent détecté par une antenne proche. Les efforts visant à accroître la sensibilité de la spectroscopie EPR pour la détection de petits échantillons ont conduit à concevoir des résonateurs de détection à faible volume de mode, ce qui est avantageusement obtenu à l'aide de résonateurs métalliques plans. Des électrodes en métal normal conduisent à des facteurs de qualité dans la gamme 10–100 [15, 16], tandis que des facteurs de qualité plus élevés et des volumes de mode plus faibles peuvent être atteints avec des résonateurs supraconducteurs [17]. Notre groupe a poussé ces efforts à la limite en refroidissant l'échantillon à des températures millikelvin et en utilisant des amplificateurs micro-ondes supraconducteurs atteignant la limite quantique de sensibilité [18],

[15]: Narkowicz et al. (2008), 'Scaling of Sensitivity and Efficiency in Planar Microresonators for Electron Spin Resonance'

[16]: Dayan et al. (2018), 'Advanced Surface Resonators for Electron Spin Resonance of Single Microcrystals'

[17]: Wallace et al. (1991), 'Microstrip Resonators for Electron-spin Resonance'

[18]: Bienfait et al. (2016), 'Reaching the Quantum Limit of Sensitivity in Electron Spin Resonance'

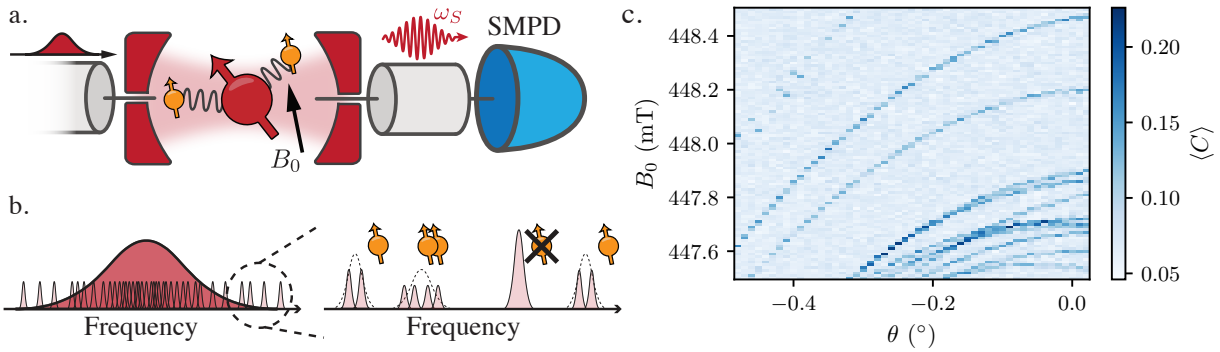

Figure 1.1.: Dispositif expérimental et principe de mesure. **a.** Le système physique est constitué de spins électroniques individuels (rouge) couplés magnétiquement à leur environnement de spins nucléaires (orange) ainsi qu'à une cavité supraconductrice. Le spin électronique (de fréquence ω_S) est porté dans son état excité par une impulsion micro-onde (gaussienne, rouge). Le taux de relaxation spontanée est augmenté par l'effet Purcell, et la fluorescence micro-onde (ligne rouge) est collectée par un détecteur de photons micro-ondes uniques (SMPD). **b.** Élargissement inhomogène et élargissement dipolaire nucléaire. *(gauche)* Le rapport gyromagnétique de chaque spin Er^{3+} est modifié par l'environnement local, et le signal d'ensemble est donc élargi. Cet effet, appelé élargissement inhomogène, est présent à l'état solide en raison des contraintes locales et des mécanismes de compensation de charge à la position de chaque ion. *(droite)* Sur les ailes du signal élargi inhomogènement, des spins individuels peuvent être résolus. À l'échelle du spin unique, la fréquence de résonance dépend du bain de spins nucléaires, auquel le spin électronique est couplé par interaction dipolaire magnétique. Si le couplage entre spins électroniques et nucléaires est plus fort que le taux de décohérence du spin électronique, plusieurs pics peuvent être résolus. **c.** Spectroscopie par comptage de photons en fonction de l'amplitude et de l'angle du champ magnétique. L'augmentation du nombre moyen de comptages détectés $\langle C \rangle$ correspond au signal de fluorescence d'un ou plusieurs spins. Des spins individuels peuvent être résolus, et les différences de rapport gyromagnétique dues à l'élargissement inhomogène apparaissent clairement.

obtenant une sensibilité suffisante pour détecter 10 spins avec un temps d'intégration d'une seconde [7]. In fine, le bruit résiduel est entièrement dû aux fluctuations du vide du champ micro-onde. Bien que ces dernières puissent être légèrement réduites au moyen d'états micro-ondes comprimés (squeezed) [19], cela n'a pas suffi pour atteindre la sensibilité au spin unique.

[7]: Ranjan et al. (2020), 'Electron Spin Resonance Spectroscopy with Femtoliter Detection Volume'

[19]: Bienfait et al. (2017), 'Magnetic Resonance with Squeezed Microwaves'

Une nouvelle méthode de détection pour la spectroscopie EPR, permettant de dépasser ces limitations, a été récemment démontrée dans notre groupe, comme illustré sur la Figure 2.1a. Cette méthode repose sur la détection de la fluorescence micro-onde émise par les spins électroniques lorsqu'ils relaxent vers leur état fondamental, de façon analogue aux techniques de comptage de photons dans le domaine optique [20]. Pour mesurer cette fluorescence, nous utilisons un détecteur de photons micro-ondes uniques (Single Microwave Photon Detector, SMPD), un dispositif supraconducteur qui associe l'arrivée d'un photon à l'état d'un qubit transmon [21]. En détectant l'énergie du photon plutôt que sa quadrature, la technique est insensible aux fluctuations du vide. Toutefois, la détection de spins électroniques via leur fluorescence micro-onde doit surmonter un obstacle majeur : le taux d'émission spontanée d'un spin dans l'espace libre est extrêmement faible (10^{-12} s^{-1}) et, à l'état solide, la décroissance non radiative via l'interaction avec les phonons constitue le mécanisme dominant.

[20]: Albertinale et al. (2021), 'Detecting Spins by Their Fluorescence with a Microwave Photon Counter'

[21]: Lescanne et al. (2020), 'Irreversible Qubit-Photon Coupling for the Detection of Itinerant Microwave Photons'

En couplant inductivement les spins électroniques à un résonateur de faible volume de mode et de fort facteur de qualité, le taux de relaxation radiative peut être amplifié via l'effet Purcell [22]. Des résonateurs supraconducteurs ont permis de démontrer des facteurs de Purcell de l'ordre de 10^{14}, conduisant à des taux de relaxation radiative de l'ordre de 10^3 s^{-1}. Cette augmentation extrême est rendue possible par la nature supraconductrice des dispositifs, qui réduit fortement les pertes internes, et par la concentration du champ magnétique dans une petite région au moyen d'éléments inductifs localisés tels que des nanofils [14].

[22]: Purcell (1946), 'Spontaneous Emission Probabilities at Radio Frequencies'

[14]: Wang et al. (2023), 'Single-Electron Spin Resonance Detection by Microwave Photon Counting'

Par ailleurs, deux difficultés peuvent être atténuées lorsqu'on opère à des températures cryogéniques. Premièrement, le rayonnement micro-onde du corps noir est exponentiellement supprimé, ce qui réduit le nombre de photons thermiques à l'entrée du SMPD et améliore ainsi le rapport signal-sur-bruit de détection. Deuxièmement, le bain de phonons est « gelé » et le taux de relaxation non radiative est réduit. Dans ces conditions, il a été possible de démontrer la détection d'un spin unique par comptage de photons micro-ondes [23–25].

[23]: Wang (2023), 'Addressing Individual Electronic Spins with a Microwave Superconducting Resonator'
[24]: Balembois (2023), 'Magnetic Resonance of a Single Electron Spin and Its Magnetic Environment by Photon Counting'
[25]: Pallegoix (2025), 'High Performance Microwave Photon Counter and Application to Single Spin Magnetic Resonance'

Le schéma de mesure est représenté sur la Figure 2.1a. Un spin électronique est couplé à une cavité résonante (tous deux en rouge). La cavité est couplée à deux ports, entrée et sortie. Une excitation micro-onde (gaussienne, rouge) porte le spin électronique dans l'état excité. Le spin relaxe rapidement via l'effet Purcell et émet un photon incohérent dans le port de sortie, lequel est acheminé vers le SMPD où il est détecté. Le spin électronique est également couplé aux spins nucléaires de l'environnement (orange) via l'interaction hyperfine. L'état du spin nucléaire influence donc la fréquence du spin électronique, et la résolution de ces décalages permettrait la détection d'un spin nucléaire unique.

Les spins électroniques dans les solides possèdent des fréquences de Larmor différentes en raison de variations de leur environnement local électrostatique ou magnétique. Il en résulte que la largeur spectrale du signal d'ensemble est beaucoup plus grande que la largeur des composantes associées à chaque spin individuel (voir Figure 2.1b). Cet « élargissement inhomogène » limite la résolution spectrale en spectroscopie EPR et

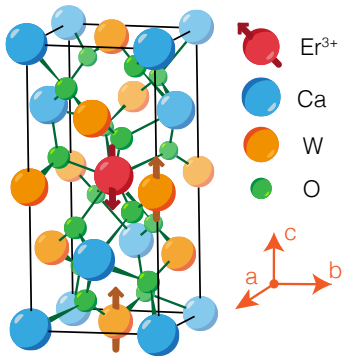

Figure 1.2.: Première maille élémentaire d'un cristal de $CaWO_4$, centrée autour d'un ion Er^{3+} substitutionnel.

constitue l'une des motivations de l'EPR à spin unique. Dans les expériences présentées dans cette thèse, l'élargissement inhomogène nous aide au contraire à adresser des spins individuels situés sur les bords de la distribution inhomogène, comme illustré sur la Figure 2.1b.

Pour réaliser nos expériences, nous utilisons le degré de liberté de spin d'un ion Er^{3+} dans $CaWO_4$. La première maille élémentaire du cristal est représentée sur la Figure 2.2, l'ion Er^{3+} étant au centre. Ces ions sont des impuretés paramagnétiques dans le réseau cristallin, possédant un spin électronique non apparié. Ils peuvent être décrits efficacement comme un spin électronique $S = 1/2$ de fréquence ω_S avec un facteur gyromagnétique anisotrope. Le matériau hôte est choisi en raison de sa faible densité de moments magnétiques nucléaires, ce qui permet d'obtenir de longs temps de cohérence pour le spin électronique [26]. Un motif de rotation résolu au niveau du spin unique est présenté sur la Figure 2.1c. La figure montre le nombre moyen de comptages mesuré $\langle C \rangle$ après excitation micro-onde en fonction de l'amplitude et de l'angle du champ magnétique. Une augmentation de $\langle C \rangle$ indique la présence d'un ou plusieurs spins Er^{3+} . Chaque parabole correspond à un spin Er^{3+} unique avec un facteur gyromagnétique différent et peut être suivie indépendamment en fonction de θ. Dans ce manuscrit, nous étudions l'environnement de spins nucléaires de ces spins et sondons leurs interactions avec les spins nucléaires voisins.

[26]: Le Dantec et al. (2021), 'Twenty-Three–Millisecond Electron Spin Coherence of Erbium Ions in a Natural-Abundance Crystal'

Détection de spins nucléaires individuels et polarisation nucléaire dynamique

Dans la deuxième partie du manuscrit, nous présentons les principaux résultats expérimentaux obtenus dans cette thèse. Dans le Chapitre 7, nous démontrons des méthodes permettant de lire l'état, de mesurer le spectre et de polariser des spins nucléaires à proximité immédiate des spins électroniques. Nous tirons parti de la sensibilité au spin électronique unique et de la longue cohérence des spins Er^{3+} pour détecter des spins nucléaires proches. Le bain nucléaire dans $CaWO_4$ est dominé par les spins nucléaires ^{183}W , avec une abondance d'environ $\sim 14\%$. Par conséquent, chaque spin Er^{3+} peut avoir un environnement différent : certains n'auront aucun ^{183}W voisin[1], tandis que d'autres pourront en avoir plusieurs. Comme illustré sur la Figure 2.3a, lorsqu'un spin Er^{3+} est couplé à un spin nucléaire ^{183}W , le couplage hyperfin scinde les fréquences de transition du spin électronique selon l'état du spin nucléaire ^{183}W , $\omega_S^{\uparrow}$ et $\omega_S^{\downarrow}$.

1: Nous utilisons « voisin » pour désigner des sites du réseau situés dans la première maille élémentaire du cristal, centrée autour de l'impureté.

Dans le Chapitre 7, nous sondons l'environnement de spins nucléaires par spectroscopie EPR à haute résolution, à champ magnétique fixé, dans une configuration où un Er^{3+} unique est en résonance avec la cavité. Nous mesurons le nombre de comptages après une impulsion micro-onde en fonction de la fréquence de l'impulsion et du temps (voir Figure 2.3b). Pour certains spins Er^{3+} , la fréquence présente un comportement télégraphique, que nous associons à des sauts quantiques, en temps réel, de l'état d'un spin nucléaire ^{183}W voisin.

En exploitant la séparation spectrale des transitions du spin électronique, nous obtenons une lecture en un seul coup, sans démolition quantique (QND), de l'état du spin nucléaire. Le protocole de lecture applique deux impulsions micro-ondes entrelacées, chacune à l'une des transitions EPR permises, et collecte les comptages de fluorescence après chaque

impulsion. L'histogramme de la différence de comptages montre deux pics symétriques et nettement résolus (voir Figure 2.3c), ce qui permet une lecture single-shot de l'état du spin nucléaire.

Les transitions zéro-quantum et double-quantum (représentées sur la Figure 2.3a par des flèches pointillées) sont faiblement permises en raison du terme anisotrope de l'interaction hyperfine et changent simultanément l'état du spin électronique et du spin nucléaire. En EPR d'ensemble, ces transitions faiblement permises sont exploitées dans des mesures d'ELDOR-detected NMR (EDNMR) pour sonder les spectres hyperfins [27]. Ici, nous démontrons une EDNMR sur spin unique en excitant les transitions ZQ/DQ sur un spin Er^{3+} unique. Nous utilisons les spectres obtenus (montrés sur la Figure 2.3d) pour identifier le spin nucléaire couplé comme étant un ^{183}W.

[27]: Schosseler et al. (1994), 'Pulsed ELDOR Detected NMR'

Une exigence clé pour la spectroscopie à spin unique et le calcul quantique est la préparation déterministe de spins nucléaires individuels dans un état arbitraire. Nous obtenons une polarisation déterministe vers $|\downarrow\rangle$ ($|\uparrow\rangle$) en excitant les transitions ZQ (DQ) puis en attendant la relaxation du spin électronique. Après plusieurs itérations, le spin nucléaire aboutit systématiquement dans l'état désiré, comme l'illustre le diagramme de niveaux de la Figure 2.3a. Comme montré sur la Figure 2.3e, après

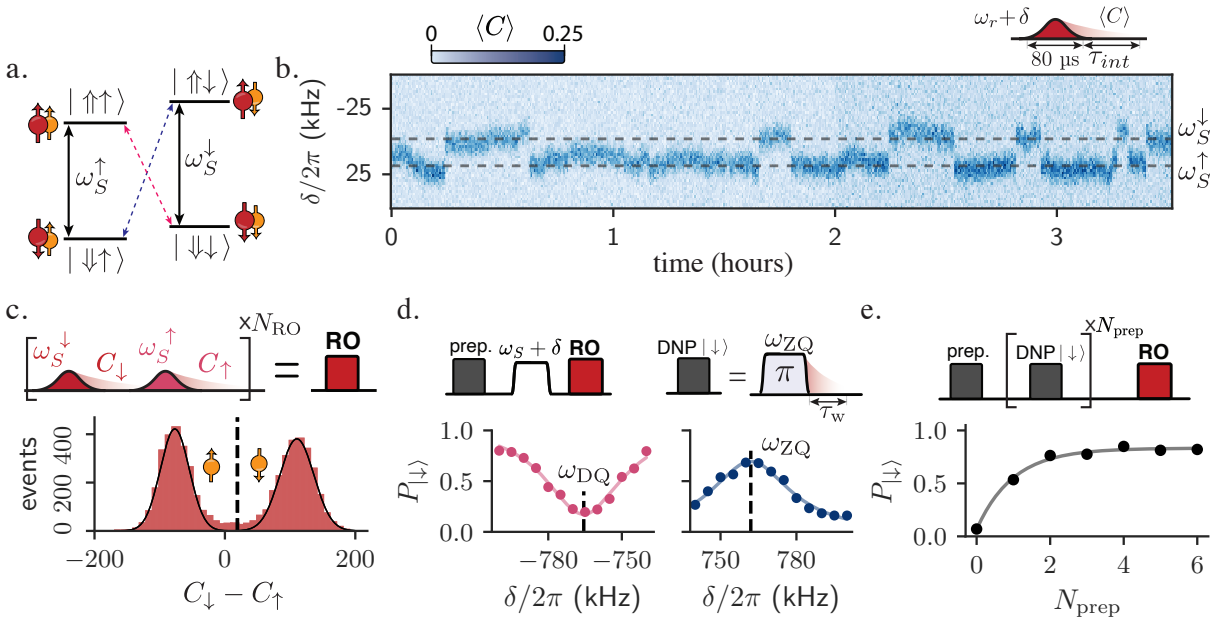

Figure 1.3.: Détection de spins nucléaires individuels et polarisation nucléaire dynamique. **a.** Système de niveaux d'énergie d'un spin électronique Er^{3+} couplé à un spin nucléaire ^{183}W. Les états associés aux niveaux d'énergie sont représentés schématiquement. Les deux transitions EPR permises sont indiquées par des flèches noires, et les transitions ZQ et DQ par des flèches pointillées bleues et rouges. **b.** Spectroscopie par comptage de photons d'un spin Er^{3+} unique en fonction du temps. Le spin Er^{3+} est accordé sur la fréquence du résonateur et une impulsion micro-onde à la fréquence $\omega_r + \delta$ est appliquée à l'échantillon, suivie d'une intégration des comptages avec le SMPD. Les comptages moyennés sur l'ensemble $\langle C \rangle$ sont tracés en fonction de la fréquence de l'impulsion et du temps de mesure. Les deux fréquences EPR permises sont mises en évidence par une ligne grise pointillée. La séquence d'impulsions est indiquée en bas à droite. **c.** Lecture en un seul coup (single-shot) de l'état du spin nucléaire. *(haut)* Séquence d'impulsions de lecture. Le nombre de comptages après excitation de chacune des transitions EPR permises est mesuré pendant N_{RO} itérations afin d'obtenir $C_\downarrow$ et $C_\uparrow$. *(bas)* Distribution de $C_\downarrow - C_\uparrow$ pour $N_{\mathrm{RO}} = 10^3$ avec événements. La ligne verticale pointillée fixe le seuil de lecture de l'état nucléaire. **d.** Spectroscopie EDNMR sur spin unique. *(haut gauche)* Séquence d'impulsions EDNMR. Après préparation du spin nucléaire dans $|\downarrow\rangle$ ou $|\uparrow\rangle$, une impulsion de fréquence $\omega_S + \delta$ est appliquée à l'échantillon, suivie d'une lecture nucléaire. *(haut droite)* Définition de l'impulsion de DNP. Une impulsion π est appliquée à la fréquence de la bande latérale ZQ, suivie d'un temps d'attente $\tau_w = 5$ ms. *(bas)* Population du spin nucléaire en fonction de la fréquence δ de l'impulsion EDNMR. Le spin nucléaire a été préparé dans $|\downarrow\rangle$ ($|\uparrow\rangle$) pour le graphe de gauche (droite). **e.** DNP sur spin unique. *(haut)* Séquence d'impulsions. Le spin est préparé dans l'état $|\uparrow\rangle$, puis N_{prep} impulsions de DNP sont appliquées, avant la lecture nucléaire. *(bas)* Population du spin nucléaire en fonction du nombre d'impulsions de DNP N_{prep}. Les données (marqueurs) sont ajustées par une courbe exponentielle (ligne).

l'application de quelques impulsions π ZQ résonantes avec la transition ZQ, nous observons que le spin nucléaire ^{183}W est préparé de manière déterministe dans $|\downarrow\rangle$. Ce schéma de polarisation est la version « spin unique » d'une méthode inventée par Abragam et Proctor pour des ensembles de spins, appelée polarisation nucléaire dynamique par effet solide (solid-effect dynamical nuclear polarization, DNP) [28].

[28]: Abragam, A., Procto, W. (1958), 'Une Nouvelle Méthode de Polarisation Des Noyaux Atomiques Dans Les Solides'

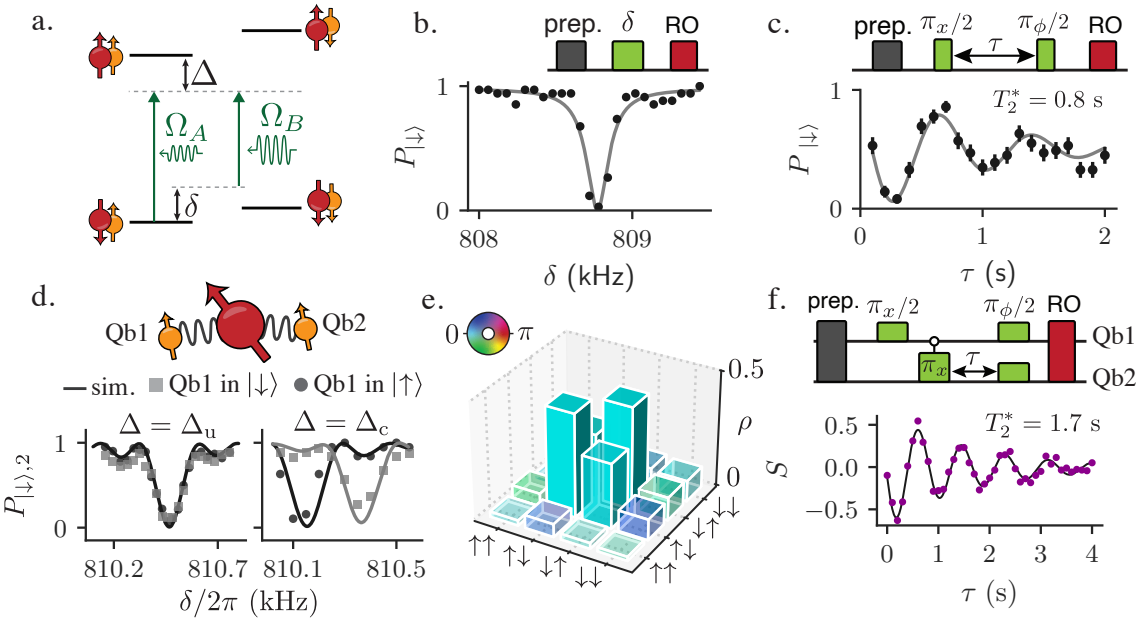

Figure 1.4.: Registre de qubits à deux spins nucléaires. **a.** Schéma Raman stimulé micro-onde dans le système de spins Er^{3+}–^{183}W. Les deux impulsions micro-ondes ont des amplitudes $\Omega_{A,B}$ et la différence de fréquence entre les deux impulsions est définie comme δ. Δ est le désaccord (detuning) entre l'excitation A et la transition du spin électronique lorsque le spin nucléaire est dans $|\uparrow\rangle$. **b.** Spectroscopie Raman stimulée. Spectroscopie d'un spin nucléaire ^{183}W à l'aide d'impulsions Raman stimulées avec un désaccord $\Delta/2\pi = -404.8$ kHz. Les lignes continues sont des ajustements lorentziens. **c.** Mesure de Ramsey d'un spin nucléaire ^{183}W individuel. L'ajustement (ligne continue) donne $T_2^* = 0.8(2)$ s et les barres d'erreur indiquent l'erreur standard sur la moyenne. La phase de la dernière impulsion est $\phi = \omega^{\text{art}} \cdot \tau$, où ω^{art} est un désaccord artificiel. La différence entre la fréquence du spin nucléaire et le désaccord artificiel est à l'origine des oscillations observées dans les données. **d.** Mise en œuvre d'une porte à deux qubits. *(haut)* Schéma du système mesuré. Un spin Er^{3+} unique est couplé simultanément à deux spins nucléaires ^{183}W, qui forment le registre quantique : Qb1 et Qb2. *(bas)* Spectroscopie de Qb2 en fonction de l'état de Qb1. Dans le graphe de gauche (droite), les impulsions Raman sont appliquées dans le régime inconditionnel (conditionnel). La ligne continue correspond à une simulation d'évolution temporelle hamiltonienne réalisée avec le logiciel `QuTiP`. **e.** Tomographie d'un état de Bell. Représentation « city plot » des matrices de densité reconstruites par tomographie de l'état de Bell $|\Psi^+\rangle = \frac{1}{\sqrt{2}}(|\downarrow\uparrow\rangle + |\uparrow\downarrow\rangle)$. La fidélité extraite après correction des erreurs SPAM est de 0,79. **f.** Sous-espace sans décohérence. Mesure de cohérence de Ramsey de l'état $|\Psi^+\rangle$. Un ajustement cosinus amorti exponentiellement donne $T_2^* = 1.7(2)$ s. Les deux dernières impulsions $\pi/2$ portent une phase ϕ jouant le rôle d'un désaccord artificiel, à l'origine des oscillations.

Un registre de deux qubits de spins nucléaires

Dans le Chapitre 8, nous exploitons les méthodes de lecture et de polarisation développées au Chapitre 7 afin de démontrer le fonctionnement d'un registre de qubits constitué de deux spins nucléaires. Les spins nucléaires dans des cristaux magnétiquement silencieux ont montré des temps de cohérence allant de la seconde à l'heure [29–31] et constituent, à ce titre, des candidats qubits particulièrement intéressants. Différentes architectures de calcul quantique fondées sur des spins électroniques et nucléaires à l'état solide ont été proposées [32–34]. La capacité à détecter et à contrôler de façon cohérente, avec une haute fidélité, l'état de spins nucléaires au sein d'un registre quantique a été démontrée dans une série de systèmes [35, 36]. L'excitation des spins nucléaires est généralement réalisée par l'application d'impulsions radiofréquence (rf) résonantes [10, 37]. Toutefois, dans notre dispositif, les spins Er^{3+} sont adressés par un résonateur micro-onde, couplé capacitivement aux lignes micro-ondes, et toutes les impulsions rf sont donc filtrées.

[29]: Saeedi et al. (2013), 'Room-Temperature Quantum Bit Storage Exceeding 39 Minutes Using Ionized Donors in Silicon-28'
[30]: Muhonen et al. (2014), 'Storing Quantum Information for 30 Seconds in a Nanoelectronic Device'
[31]: Zhong et al. (2015), 'Optically Addressable Nuclear Spins in a Solid with a Six-Hour Coherence Time'
[35]: Pla et al. (2013), 'High-Fidelity Readout and Control of a Nuclear Spin Qubit in Silicon'
[36]: Song et al. (2026), 'Entanglement of a Nuclear Spin Qubit Register in Silicon Photonics'
[10]: Bradley et al. (2019), 'A Ten-Qubit Solid-State Spin Register with Quantum Memory up to One Minute'
[37]: van der Sar et al. (2012), 'Decoherence-Protected Quantum Gates for a Hybrid Solid-State Spin Register'

En raison de ces contraintes, nous démontrons dans cette thèse une méthode nouvelle permettant d'exciter les spins nucléaires en n'utilisant que des micro-ondes. Le principe de cette technique est illustré sur la Figure 2.4a. Deux impulsions micro-ondes désaccordées, d'amplitudes Ω_A et Ω_B, sont appliquées au système. Les impulsions sont désaccordées l'une par rapport à l'autre de δ, et l'impulsion A est désaccordée de la transition EPR permise lorsque le spin nucléaire est dans $|\downarrow\rangle$ de Δ. Comme les impulsions sont désaccordées par rapport à la transition EPR, aucune population significative n'est transférée vers l'état excité du spin électronique. En revanche, un processus du second ordre peut exciter l'état du spin nucléaire si δ est résonant avec la fréquence du spin nucléaire $\sim \omega_I$. Puisque les impulsions ne peuplent pas de manière significative les niveaux excités du spin électronique, le processus préserve les propriétés de cohérence des spins nucléaires. Cela est mis en évidence par la spectroscopie NMR de la Figure 2.4b, qui trace la population $\downarrow$ du spin nucléaire en fonction de la fréquence des impulsions. La largeur de raie de la transition ($\sim$ 200 Hz) est beaucoup plus petite que la largeur de raie électronique, comme attendu pour une transition Raman. Nous mesurons le temps de cohérence du spin nucléaire au moyen d'une séquence de Ramsey et trouvons $T_2^* = 0.5$–1 s, comme montré sur la Figure 2.4c. Ce résultat confirme que $CaWO_4$ est un bon matériau hôte pour des qubits à spin nucléaire, comme cela avait déjà été établi pour des spins électroniques [26].

[26]: Le Dantec et al. (2021), 'Twenty-Three–Millisecond Electron Spin Coherence of Erbium Ions in a Natural-Abundance Crystal'

Dans le Chapitre 8, nous nous concentrons sur un système dans lequel un spin Er^{3+} est couplé à deux spins nucléaires ^{183}W voisins, notés Qb1 et Qb2. En exploitant les décalages AC-Zeeman induits par des impulsions Raman désaccordées, nous développons un protocole permettant d'implémenter une porte à deux qubits. Le désaccord Raman Δ fixe l'amplitude des décalages AC-Zeeman et conduit à deux régimes de fonctionnement distincts. La Figure 2.4d illustre ces deux régimes : à gauche, un régime inconditionnel, dans lequel la fréquence de transition de Qb2 est indépendante de l'état de Qb1, et à droite, un régime conditionnel, dans lequel cette fréquence dépend de l'état de Qb1.

Le bruit magnétique corrélé entre les deux spins peut être supprimé en préparant le système dans des états singulet ou triplet spécifiques, de moment magnétique moyen nul [10, 38]. À l'aide de spins nucléaires ^{183}W, nous préparons l'état de Bell $\frac{1}{\sqrt{2}}(|\downarrow\uparrow\rangle + |\uparrow\downarrow\rangle)$, vérifié par tomographie d'état (Figure 2.4e), et mesurons son temps de cohérence. Nous observons

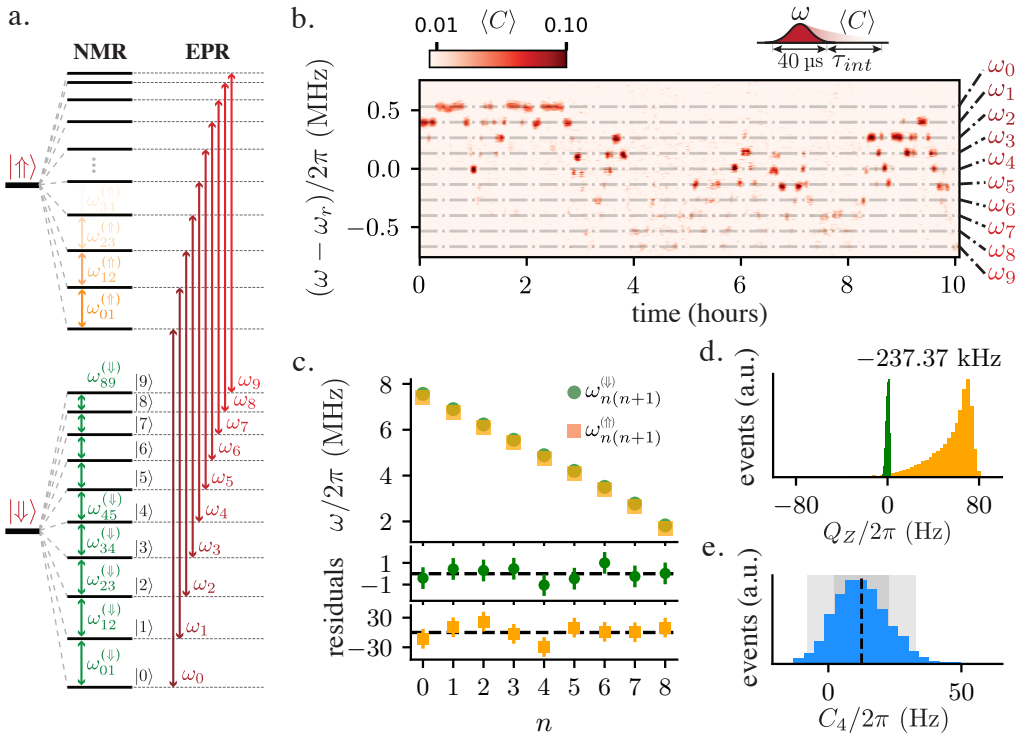

Figure 1.5.: Spectroscopie NMR de précision d'un spin nucléaire ^{93}Nb . **a.** Spectre des niveaux d'énergie d'un spin Er^{3+} couplé à un spin nucléaire ^{93}Nb de spin $I = 9/2$. Les dix transitions EPR permises sont indiquées en rouge. Les dix-huit transitions NMR permises sont mises en évidence en vert et en orange, selon l'état du spin Er^{3+} . **b.** Spectroscopie par comptage de photons d'un spin Er^{3+} unique couplé à un spin nucléaire ^{93}Nb en fonction du temps. La fréquence de détection du SMPD est accordée dynamiquement afin de correspondre à la fréquence ω de l'impulsion micro-onde appliquée. Les comptages moyennés sur l'ensemble $\langle C \rangle$ sont tracés en fonction de la fréquence de l'impulsion et du temps de mesure. Les dix fréquences EPR permises sont mises en évidence par une ligne grise pointillée. La séquence d'impulsions est indiquée en haut à droite. **c.** Spectre NMR et ajustement hamiltonien. *(haut)* Les spectres NMR des transitions ^{93}Nb dans l'état fondamental (excité) du spin Er^{3+} sont tracés en vert (orange) en fonction de l'indice de transition n. *(bas)* Résidus de l'ajustement hamiltonien. On obtient $\chi^2_\nu = 1.2$, ce qui indique un ajustement satisfaisant. Les barres d'erreur correspondent à l'incertitude sur la fréquence et la ligne noire pointillée marque le zéro. **d.** Observation d'un quadrupôle dépendant du spin. Distribution a posteriori de la composante principale du tenseur quadrupolaire le long de l'axe Z pour les ajustements de l'état fondamental et de l'état excité (vert et orange respectivement). Les distributions sont normalisées à la même hauteur pour une meilleure lisibilité. **e.** Intensité du couplage hexadécapolaire. Distributions a posteriori de la constante de couplage hexadécapolaire C_4. La ligne verticale indique la moyenne de la distribution et les zones ombrées les intervalles de confiance à 1 et 2 σ.

un gain d'un facteur deux par rapport au temps de cohérence d'un qubit unique, ce qui indique une suppression efficace du bruit magnétique au sein d'un sous-espace sans décohérence.

Spectroscopie de précision d'un spin 9/2

Une autre application des méthodes développées au Chapitre 7 consiste à caractériser un atome inconnu situé à proximité d'un spin électronique. C'est l'objet du Chapitre 9, dans lequel nous caractérisons complètement une impureté inconnue de spin nucléaire 9/2 proche d'un spin Er^{3+} . Nous réalisons en outre une spectroscopie hyperfine de précision de cet atome ^{93}Nb et mettons en évidence des termes jusque-là inconnus dans l'Hamiltonien de spin.

La Figure 2.5a représente les vingt niveaux d'énergie du système couplé ^{93}Nb–Er^{3+} ainsi que l'ensemble des transitions EPR, de fréquences ω_n, et des transitions NMR permises, séparées en deux familles selon l'état m_S du spin Er^{3+} et de fréquences $\omega^{(m_S)}_{n,n+1}$. Nous caractérisons d'abord le système par spectroscopie EPR en mesurant des traces temporelles

similaires à celles du Chapitre 7. La Figure 2.5b montre les dix transitions EPR permises du spin électronique, régulièrement espacées, signature caractéristique d'un spin électronique couplé à un spin nucléaire $I = 9/2$.

Nous utilisons les méthodes développées dans les chapitres précédents (lecture single-shot, DNP par effet solide et excitation Raman stimulée) pour mesurer le spectre NMR du spin ^{93}Nb . En comparant la fréquence de Larmor de l'impureté aux rapports gyromagnétiques de différents spins nucléaires, nous l'identifions comme étant un spin ^{93}Nb . Nous tirons parti de la longue cohérence du spin nucléaire pour mesurer son spectre hyperfin avec une résolution de l'ordre du hertz, présenté sur la Figure 2.5c en fonction de l'indice de transition. La grande séparation des niveaux indique que l'intensité de l'interaction quadrupolaire du spin nucléaire est du même ordre de grandeur que celle de l'interaction de Zeeman.

Nous ajustons le spectre NMR à un modèle hamiltonien dans les deux manifolds Er^{3+} avec une précision au hertz, comme le montrent les résidus de l'ajustement (présentés sur la Figure 2.5c). Nous utilisons ces résultats pour reconstruire le quadrupôle de ^{93}Nb et le comparer à des simulations DFT. La reconstruction du quadrupôle ainsi que le résultat DFT sont présentés sur la Figure 2.6. Nous trouvons un accord quantitatif entre les deux, tant en amplitude qu'en orientation angulaire, ce qui indique une attribution correcte du site.

De plus, nous observons que l'intensité de l'interaction quadrupolaire diffère entre les deux manifolds, comme l'illustre la Figure 2.5d à travers la différence statistiquement significative entre les distributions a posteriori de la force de couplage quadrupolaire obtenues pour les deux ajustements. Nous attribuons cette différence à un nouveau type d'interaction entre spins électronique et nucléaire. Nous avançons que l'origine de cette interaction réside dans le couplage entre le dipôle électrique induit magnétiquement du spin Er^{3+} et l'interaction quadrupolaire nucléaire [39, 40].

Enfin, nous parvenons à contraindre l'interaction hexadécapolaire avec des bornes environ un ordre de grandeur plus strictes que les mesures précédemment à l'état de l'art [41], comme le montre la Figure 2.5e.

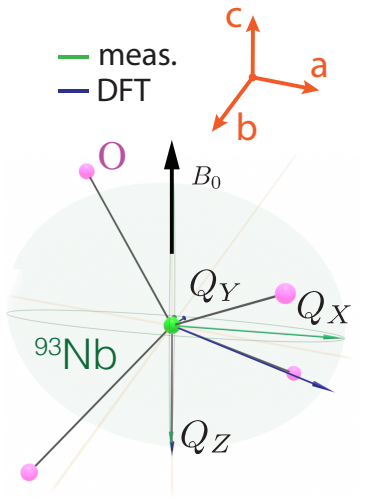

Figure 1.6.: Représentation tridimensionnelle du tenseur quadrupolaire. Le spin nucléaire ^{93}Nb (vert) se situe au centre, entouré par les atomes d'oxygène voisins (rose). Les axes cristallins a, b et c sont indiqués par des lignes orange. Les axes principaux quadrupolaires mesurés X, Y et Z sont représentés par des flèches vertes, qui définissent les demi-axes d'un ellipsoïde, représenté en vert. Les vecteurs principaux obtenus par simulations DFT sont tracés en bleu foncé.

[39]: Bloembergen (1961), 'Linear Stark Effect in Magnetic Resonance Spectra'
[40]: Mims (1964), 'Electric Field Effects in Spin Echoes'

[41]: Liao et al. (1994), 'The Nuclear Hexadecapole Interaction of Iodine-127 in Cadmium Iodide Measured Using Zero-field Two Dimensional Nuclear Magnetic Resonance'

2. Introduction

Magnetic resonance is a spectroscopic technique that uses the coupling between spins and electromagnetic radiation to probe microscopic properties of matter. The field is broadly divided into Electron Paramagnetic Resonance (EPR) [1] and Nuclear Magnetic Resonance (NMR) [2] depending on the type of spin being studied, either unpaired electron spins or nuclear spins respectively. Owing to the ubiquity of spins in matter, magnetic resonance techniques have a wide range of applications ranging from medical imaging [3] to materials science [4], biology [5] and pharmaceutical quality control [6].

An important limitation of conventional magnetic resonance techniques is their low sensitivity. Because the interaction between spins and electromagnetic fields is weak, large ensembles of spins are required to generate a detectable signal. Consequently, most measurements yield ensemble-averaged quantities, while microscopic and local variations are difficult to access.

By using quantum limited amplifiers and superconducting resonators, the sensitivity has been pushed to the extreme, sufficient to detect ten electron spins [7]. Single-spin detection has been achieved in a small number of solid state systems, such as NV centers in diamond [8] and donor impurities in silicon [9]. This has been possible thanks to system-specific mechanisms, including spin-selective optical transitions and spin-to-charge conversion. The results in these systems demonstrate how individual electron and nuclear spins in the solid state can be used for quantum computing [10, 11] and precision spectroscopy [12, 13].

Recently, our group has demonstrated how individual paramagnetic impurities in a dielectric can be detected via microwave fluorescence of their electron spin transition at 10 mK [14]. This method is, in principle, applicable to a large number of paramagnetic species and substrates, as it only requires to enhance the spontaneous emision rate of the electron spin beyond the non-radiative relaxation rate at cryogenic temperatures. **This thesis reports how microwave photon counting can be used to detect and coherently control individual nuclear spins coupled to a single electron spin.** Furthermore, we demonstrate precision spectroscopy of the NMR transitions and how nuclear spins can find applications in quantum computing.

The thesis is divided into three parts. The first part of the thesis describes the physical system and the experimental setup. We introduce the spin Hamiltonian for Er^{3+} electron spins in $CaWO_4$, the nuclear spins present in the crystal and their interaction. We describe how coupling the Er^{3+} spin to a resonator enhances the spontaneous relaxation rate through the Purcell effect and the detection device: the single microwave photon detector. In addition, we describe the microwave techniques used to control the nuclear spin state. The second part of this work focuses on the detection and control of ^{183}W nuclear spins. We measure quantum jumps of the nuclear spin state and demonstrate hyperfine spectroscopy and deterministic preparation using only microwave pulses. In addition, we use microwave stimulated Raman driving to demonstrate single- and two-qubit gates in a two-qubit register of ^{183}W nuclear spins. We also measure coherence times on the order of one second, which are among the longest measured in the solid state. In the third part of the thesis

[1]: Abragam (1986), *The Principles of Nuclear Magnetism*

[2]: Slichter (1996), *Principles of Magnetic Resonance*

[3]: Lauterbur (1973), 'Image Formation by Induced Local Interactions'

[4]: Haworth et al. (2022), 'Solid-State NMR Studies of Coatings and Interfaces in Batteries'

[5]: Wüthrich (1989), 'Protein Structure Determination in Solution by Nuclear Magnetic Resonance Spectroscopy'

[6]: Holzgrabe (2010), 'Quantitative NMR Spectroscopy in Pharmaceutical Applications'

[7]: Ranjan et al. (2020), 'Electron Spin Resonance Spectroscopy with Femtoliter Detection Volume'

[8]: Jelezko et al. (2002), 'Single Spin States in a Defect Center Resolved by Optical Spectroscopy'

[9]: Morello et al. (2010), 'Single-Shot Readout of an Electron Spin in Silicon'

[10]: Bradley et al. (2019), 'A Ten-Qubit Solid-State Spin Register with Quantum Memory up to One Minute'

[11]: Edlbauer et al. (2025), 'An 11-Qubit Atom Processor in Silicon'

[12]: Abobeih et al. (2019), 'Atomic-Scale Imaging of a 27-Nuclear-Spin Cluster Using a Quantum Sensor'

[13]: Breitweiser et al. (2024), 'Quadrupolar Resonance Spectroscopy of Individual Nuclei Using a Room-Temperature Quantum Sensor'

[14]: Wang et al. (2023), 'Single-Electron Spin Resonance Detection by Microwave Photon Counting'

we address an ^{93}Nb impurity with nuclear spin-9/2. We generalize the techniques presented above and perform precision spectroscopy of the nuclear spin transitions.

2.1. Measuring the fluorescence of individual electron spins

Conventional pulsed EPR spectrometers measure the transverse magnetization of electron spin ensembles, which cooperatively radiates a coherent field detected by a proximal antenna. Efforts to increase the sensitivity of EPR spectroscopy for the detection of small samples have led to the design of detection resonators with small mode volume, which is conveniently achieved using planar metallic resonators. Normal-metal electrodes lead to quality factors in the 10–100 regime [15, 16], while higher quality factors and smaller mode volumes can be reached using superconducting resonators [17]. Our group has pushed these efforts to the extreme limit by cooling down the sample to millikelvin temperatures and using microwave superconducting amplifiers that reach the quantum limit of sensitivity [18], achieving sensitivity sufficient to detect 10 spins in 1 second of integration time [7]. Ultimately, the remaining noise is entirely due to vacuum fluctuations of the microwave field. While the latter can be slightly reduced using microwave squeezed states [19], this was not sufficient to reach single-spin sensitivity.

A new detection method for EPR spectroscopy that overcomes these limitations was recently demonstrated in our group, shown in Figure 2.1a. The method is based on detecting the microwave fluorescence of the electron spins when they relax to their ground state, similar to photon-counting techniques in the optical regime [20]. To measure the fluorescence we use a Single Microwave Photon Detector (SMPD), a superconducting device that maps an incoming photon to the state of a transmon qubit [21]. By detecting the photon energy instead of detecting

[15]: Narkowicz et al. (2008), 'Scaling of Sensitivity and Efficiency in Planar Microresonators for Electron Spin Resonance'

[16]: Dayan et al. (2018), 'Advanced Surface Resonators for Electron Spin Resonance of Single Microcrystals'

[17]: Wallace et al. (1991), 'Microstrip Resonators for Electron-spin Resonance'

[18]: Bienfait et al. (2016), 'Reaching the Quantum Limit of Sensitivity in Electron Spin Resonance'

[7]: Ranjan et al. (2020), 'Electron Spin Resonance Spectroscopy with Femtoliter Detection Volume'

[19]: Bienfait et al. (2017), 'Magnetic Resonance with Squeezed Microwaves'

[20]: Albertinale et al. (2021), 'Detecting Spins by Their Fluorescence with a Microwave Photon Counter'

[21]: Lescanne et al. (2020), 'Irreversible Qubit-Photon Coupling for the Detection of Itinerant Microwave Photons'

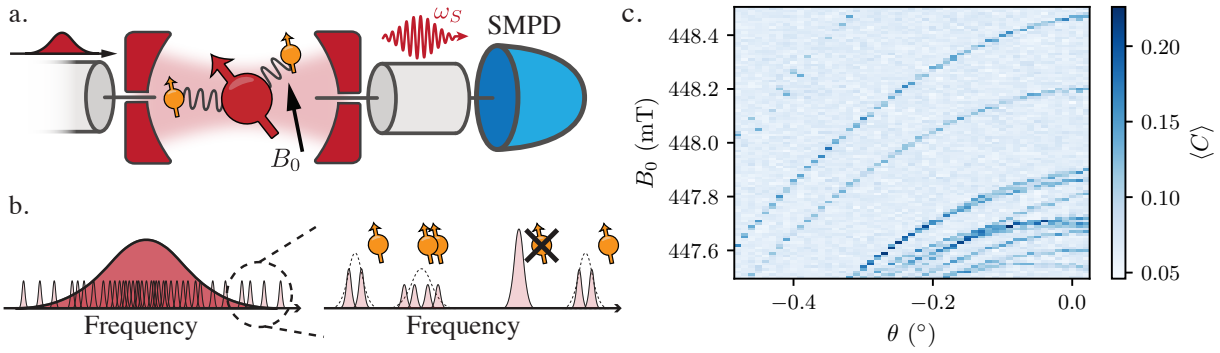

Figure 2.1.: Experimental setup and measurement principle. **a.** The physical system consists of individual electron spins (red) that are magnetically coupled to their nuclear spin environment (orange) and to a superconducting cavity. The electron spin (with frequency ω_S) is brought into its excited state with a microwave pulse (red Gaussian). The spontaneous relaxation rate is enhanced through the Purcell effect, and the microwave fluorescence (red line) is collected by a single microwave photon detector (SMPD). **b.** Inhomogeneous broadening and nuclear dipolar broadening. *(left)* The gyromagnetic ratio of each Er^{3+} spin is modified by the local environment and the ensemble signal is therefore broadened. This effect is known as inhomogeneous broadening and is present in the solid state due to local strain and charge-compensation mechanisms at each ion's position. *(right)* At the tail of the inhomogeneously broadened signal, individual spins can be resolved. At the single-spin level, the resonance frequency depends on the nuclear spin bath, which couples through magnetic dipole interaction. If the coupling between the electron and the nuclear spins is stronger than the decoherence rate of the electron spin, several peaks can be resolved. **c.** Photon counting spectroscopy as a function of the magnetic field amplitude and angle. The increase in detected number of counts $\langle C \rangle$ corresponds to the fluorescence signal of one or more spins. Individual spins can be resolved and the differences in gyromagnetic ratio due to inhomogeneous broadening are made evident.

the magnetic field in quadrature, the technique is insensitive to vacuum fluctuations. However, detecting electron spins through their microwave fluorescence has to overcome a major obstacle: the spontaneous emission rate of a spin in free space is vanishingly low (10^{-12} s^{-1}), and in the solid state, non-radiative decay via phonon interaction is the dominant mechanism.

By inductively coupling the electron spins to a low-mode-volume, high-quality resonator, the radiative relaxation rate can be enhanced through the Purcell effect [22]. Superconducting resonators have demonstrated Purcell factors on the order of 10^{14}, reaching radiative relaxation rates on the order of 10^3 s^{-1}. This extreme enhancement is possible thanks to the superconducting nature of the devices, which greatly suppresses internal losses, and by focusing the magnetic field into a small region through inductive lumped elements such as nanowires [14].

[22]: Purcell (1946), 'Spontaneous Emission Probabilities at Radio Frequencies'

[14]: Wang et al. (2023), 'Single-Electron Spin Resonance Detection by Microwave Photon Counting'

In addition, two problems can be addressed when operating at cryogenic temperatures. First, microwave blackbody radiation is exponentially suppressed, which results in a reduced number of thermal photons at the SMPD input, thereby enhancing the detection SNR. Second, the phonon bath is frozen and the non-radiative relaxation rate is reduced. Under these conditions, it was possible to demonstrate single-spin detection via microwave photon counting [23–25]

[23]: Wang (2023), 'Addressing Individual Electronic Spins with a Microwave Superconducting Resonator'
[24]: Balembois (2023), 'Magnetic Resonance of a Single Electron Spin and Its Magnetic Environment by Photon Counting'
[25]: Pallegoix (2025), 'High Performance Microwave Photon Counter and Application to Single Spin Magnetic Resonance'

The measurement scheme is depicted in Figure 2.1a. An electron spin is coupled to a resonant cavity (both in red). The cavity is coupled to two ports, input and output. A microwave excitation (red Gaussian) brings the electron spin to the excited state. The spin rapidly relaxes through the Purcell effect and emits an incoherent photon into the output port, which is routed toward the SMPD, where it is detected. The electron spin is also coupled to the nuclear spins in the environment (in orange) via hyperfine interaction. Therefore, the state of the nuclear spin influences the electron spin frequency, and resolving these shifts would permit single nuclear spin detection.

Electron spins in solids have different Larmor frequencies due to variations in their electrostatic or magnetic local environment. As a result, the spectral width of the spin ensemble is much larger than the width of its individual spin components (see Figure 2.1b). This so-called inhomogeneous broadening poses limitations to the spectral resolution in EPR spectroscopy, and is one of the motivations for single-spin EPR. In the experiments reported in this thesis, inhomogeneous broadening helps us to address individual spins which are found at the edges of the inhomogeneous distribution, as shown in Figure 2.1b.

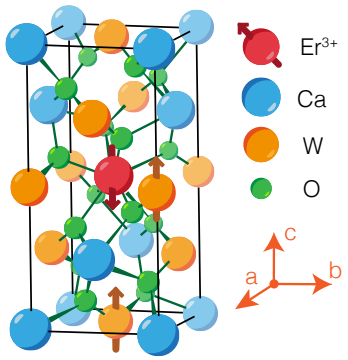

Figure 2.2.: Unit cell of a $CaWO_4$ crystal, centered around a substitutional Er^{3+} ion.

To perform our experiments we use the spin degree of freedom of an Er^{3+} ion in $CaWO_4$. The unit cell of the crystal is shown in Figure 2.2 with the Er^{3+} ion in the center. These ions are paramagnetic impurities in the crystal lattice with an unpaired electron spin. They can be effectively treated as an electron spin $S = 1/2$ with frequency ω_S with an anisotropic gyromagnetic factor. The host material is chosen due to the low nuclear magnetic moment density, which enables long coherence times for the electron spin [26]. A single-spin-resolved rotation pattern is shown in Figure 2.1c. The figure shows the measured number of counts $\langle C \rangle$ after microwave excitation as a function of the magnetic field amplitude and angle. An increase in $\langle C \rangle$ indicates the presence of one or more Er^{3+} spins. Each parabola corresponds to a single Er^{3+} spin with a different gyromagnetic factor and can be followed independently as a function of θ. In this thesis we investigate the nuclear spin environment of these spins and probe their interactions with neighboring nuclear spins.

[26]: Le Dantec et al. (2021), 'Twenty-Three–Millisecond Electron Spin Coherence of Erbium Ions in a Natural-Abundance Crystal'

2.2. Detection of individual nuclear spins and dynamical nuclear polarization

In the second part of the thesis, we report the main experimental results obtained in this thesis. In Chapter 7, we demonstrate methods to read out, measure the spectrum of, and polarize nuclear spins in close proximity to the electron spins. We leverage the single-electron spin sensitivity and the long coherence of Er^{3+} spins to detect proximal nuclear spins. The nuclear bath in $CaWO_4$ is dominated by ^{183}W nuclear spins with $\sim$ 14% abundance. Consequently, each Er^{3+} spin might have a different environment: some will have no neighboring[1] ^{183}W spins, while others might have several. As shown in Figure 2.3a, when an Er^{3+} spin is coupled to a ^{183}W nuclear spin, the hyperfine coupling splits the electron spin transition frequencies depending on the state of the ^{183}W nuclear spin, $\omega_S^{\uparrow}$ and $\omega_S^{\downarrow}$.

1: We use neighboring to refer to lattice sites in the first unit cell of the crystal, centered around the impurity

In Chapter 7 we probe the nuclear spin environment through high-resolution EPR spectroscopy at a fixed magnetic field where a single Er^{3+} is resonant with the cavity. We measure the number of counts after a microwave pulse as a function of pulse frequency and time (see Figure 2.3b). For some Er^{3+} spins, the frequency displays telegraphic behavior, which we associate with quantum jumps in the state of a neighboring

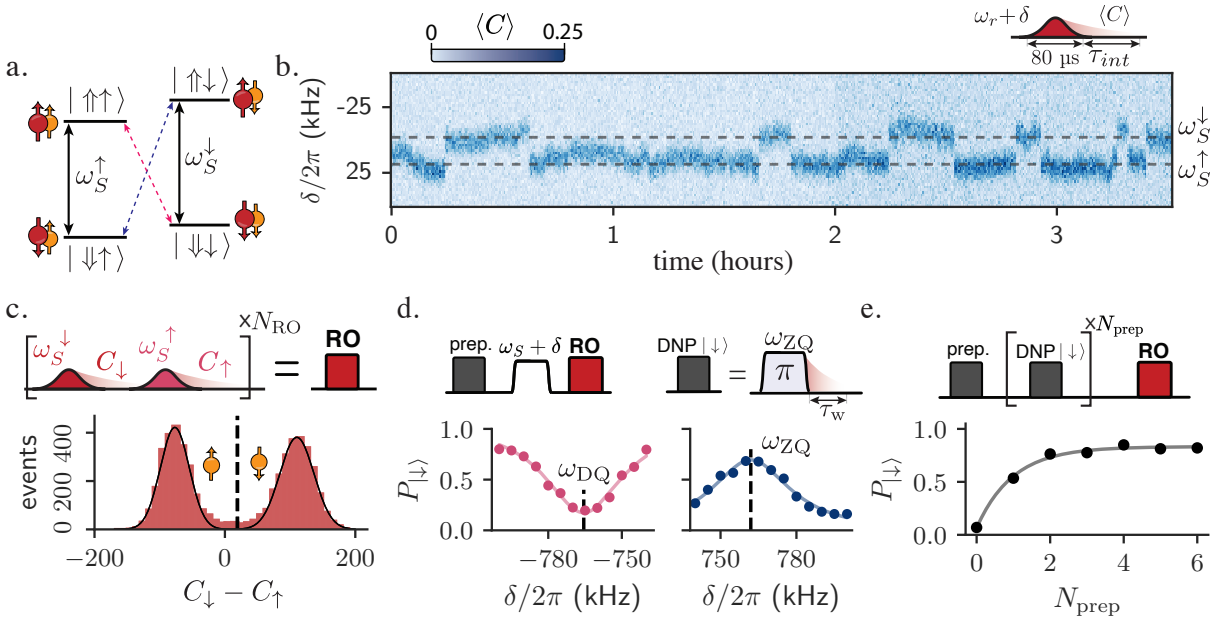

Figure 2.3.: Detection of individual nuclear spins and dynamical nuclear polarization. **a.** Energy level system of an Er^{3+} electron spin coupled to a ^{183}W nuclear spin. The states associated with the energy levels have been pictorially represented. The two EPR-allowed transitions are marked with black arrows and the ZQ and DQ transitions with blue and red dashed arrows. **b.** Photon counting spectroscopy of a single Er^{3+} spin as a function of time. The Er^{3+} spin is tuned to the frequency of the resonator and a microwave pulse at frequency $\omega_r + \delta$ is applied to the sample, followed by count integration with the SMPD. The ensemble-average counts $\langle C \rangle$ are plotted as a function of the pulse frequency and measurement time. The two EPR-allowed frequencies are highlighted with a dashed gray line. The pulse sequence is shown at the bottom right. **c.** Single-shot readout of the nuclear spin state. *(top)* Readout pulse sequence. The number of counts after exciting each EPR-allowed transition are measured for N_{RO} iterations to obtain $C_\downarrow$ and $C_\uparrow$. *(bottom)* Distribution of $C_\downarrow$ - $C_\uparrow$ for $N_{RO} = 10^3$ with events. The vertical dashed line gives the threshold for nuclear spin readout. **d.** Single spin EDNMR spectroscopy. *(top left)* EDNMR pulse sequence. After preparation of the nuclear spin in either $|\downarrow\rangle$ or $|\uparrow\rangle$, a pulse with frequency $\omega_S + \delta$ is applied on the sample, followed by nuclear readout. *(top right)* DNP pulse definition. A π-pulse is applied at the frequency of the ZQ sideband followed by a wait time τ_w = 5 ms. *(bottom)* Nuclear spin population as a function of the EDNMR pulse frequency δ. The nuclear spin was prepared in $|\downarrow\rangle$ ($|\uparrow\rangle$) for the left (right) plot. Dots indicate the measurement data and solid line a Lorentzian fit. **e.** Single spin DNP. *(top)* Pulse sequence. The spin is prepared in state $|\uparrow\rangle$ followed by N_{prep} DNP pulses and nuclear readout. *(bottom)* Population of the nuclear spin as a function of the number of DNP pulses N_{prep}. The data (markers) are fit to an exponential curve (line).

^{183}W nuclear spin in real time.

By leveraging the spectral separation of the electron spin transition we obtain single-shot quantum-non-demolition readout of the nuclear spin state. The readout protocol applies two interleaved microwave pulses at each of the EPR-allowed transitions and collects the fluorescence counts after each pulse. The histogram of the count difference shows two symmetric and well resolved peaks (see Figure 2.3c) which enables single-shot readout of the nuclear spin state.

The zero- and double-quantum transitions (represented in Figure 2.3a with dashed arrows) are weakly allowed due to the anisotropic term in the hyperfine interaction and simultaneously change the state of the electron and nuclear spin. In ensemble EPR, these weakly-allowed transitions are measured using electron-electron double resonance (ELDOR) detected NMR (EDNMR) measurements to probe the hyperfine spectra [27]. Here we demonstrate single spin EDNMR by driving the ZQ/DQ transitions on a single Er^{3+} spin. We use the resulting spectra (shown in Figure 2.3d) to identify the coupled nuclear spin as a ^{183}W .

[27]: Schosseler et al. (1994), 'Pulsed ELDOR Detected NMR'

A key requirement for single-spin spectroscopy and quantum computing is deterministic preparation of individual nuclear spins in an arbitrary state. We achieve deterministic single-spin polarization to $|\downarrow\rangle$ ($|\uparrow\rangle$) by exciting the ZQ (DQ) transitions and waiting for the electron spin to relax. After several iterations, the nuclear spin should always end up

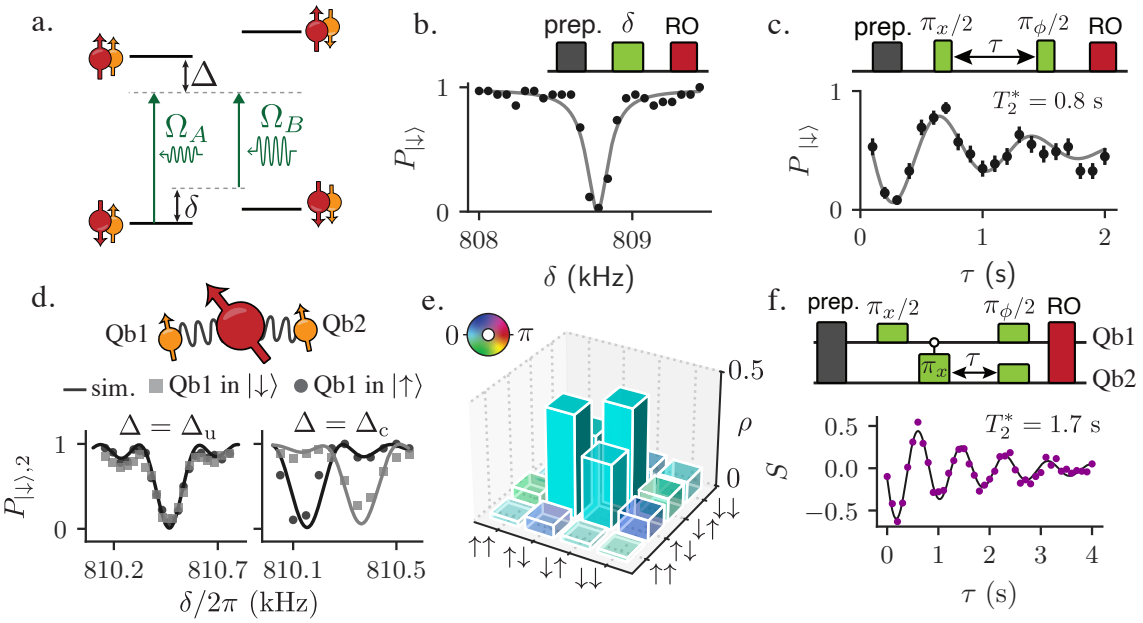

Figure 2.4.: A two nuclear spin qubit register. **a.** Microwave Stimulated Raman scheme in the Er^{3+} –^{183}W spin system. The two microwave pulses have amplitudes $\Omega_{A,B}$ and the frequency difference between the two pulses is defined as δ. Δ is the detuning between drive A and the electron spin transition when the nuclear spin is in $|\uparrow\rangle$. **b.** Stimulated Raman spectroscopy. Spectroscopy of a ^{183}W nuclear spin using stimulated Raman pulses with detuning $\Delta/2\pi = -404.8$ kHz. Continuous solid lines are Lorentzian fits. **c.** Ramsey measurement of an individual ^{183}W nuclear spin. The fit (solid line) returns $T_2^* = 0.8(2)$ s and error bars indicate the standard error of the mean. The phase of the last pulse is $\phi = \omega^{\text{art}} \cdot \tau$, where ω^{art} is an artificial detuning. The difference between the nuclear spin frequency and the artificial detuning gives rise to the oscillations in the measured data. **d.** Two-qubit gate implementation. *(top)* Sketch of the measured system. A single Er^{3+} spin is simultaneously coupled to two ^{183}W nuclear spins, which form the quantum register: Qb1 and Qb2. *(bottom)* Spectroscopy of Qb2 as a function of the state of Qb1. In the left (right) plot the Raman pulses are applied in the unconditional (conditional) regime. The solid line corresponds to a Hamiltonian time-evolution simulation performed using the `QuTiP` package. **e.** Bell state tomography. City plot of tomographically reconstructed density matrices of $|\Psi^+\rangle = \frac{1}{\sqrt{2}}(|\downarrow\downarrow\rangle + |\uparrow\uparrow\rangle)$ Bell state. Extracted fidelity after SPAM error correction is 0.79. **f.** Decoherence free subspace. Ramsey coherence measurement of the $|\Psi^+\rangle$ state. Exponentially decaying cosine fit yields $T_2^* = 1.7(2)$ s. The final two $\pi/2$-pulses carry a phase ϕ as an artificial detuning which gives rise to the oscillations.

in the desired state, as evidenced by the level diagram in Figure 2.3a. As shown in Figure 2.3e, after the application of a few ZQ π-pulses resonant with the ZQ transition, we observe that the ^{183}W nuclear spin is deterministically prepared in $|\downarrow\rangle$. This polarization scheme is the single-spin version of a method invented by Abragam and Proctor for ensembles of spins and called solid-effect dynamical nuclear polarization (DNP) [28].

[28]: Abragam, A., Procto, W. (1958), 'Une Nouvelle Méthode de Polarisation Des Noyaux Atomiques Dans Les Solides'

2.3. A register of two nuclear spin qubits

In Chapter 8, we harness the readout and polarization methods developed in Chapter 7 to demonstrate the operation of a two-nuclear-spin-qubit register. Nuclear spins in magnetically silent crystals have demonstrated coherence times ranging from seconds to hours [29–31] and, as such, are interesting qubit candidates. Different architectures for quantum computing using electron and nuclear spins in the solid state have been proposed [32–34]. The ability to detect and coherently control the state of nuclear spins with high fidelity in a quantum register has been demonstrated in a series of systems [35, 36]. Nuclear spin driving is usually done by application of resonant radiofrequency (rf) pulses [10, 37]. However, the Er^{3+} spins in our setup are addressed by a microwave resonator, capacitively coupled to the microwave lines, and therefore all rf pulses are filtered.

[29]: Saeedi et al. (2013), 'Room-Temperature Quantum Bit Storage Exceeding 39 Minutes Using Ionized Donors in Silicon-28'
[30]: Muhonen et al. (2014), 'Storing Quantum Information for 30 Seconds in a Nanoelectronic Device'
[31]: Zhong et al. (2015), 'Optically Addressable Nuclear Spins in a Solid with a Six-Hour Coherence Time'
[35]: Pla et al. (2013), 'High-Fidelity Readout and Control of a Nuclear Spin Qubit in Silicon'
[36]: Song et al. (2026), 'Entanglement of a Nuclear Spin Qubit Register in Silicon Photonics'
[10]: Bradley et al. (2019), 'A Ten-Qubit Solid-State Spin Register with Quantum Memory up to One Minute'
[37]: van der Sar et al. (2012), 'Decoherence-Protected Quantum Gates for a Hybrid Solid-State Spin Register'

Due to these limitations we demonstrate in this thesis a novel method to drive the nuclear spins with only microwaves. The principle of this technique is shown in Figure 2.4a. Two detuned microwave pulses with amplitudes Ω_A and Ω_B are applied to the system. The pulses are detuned from each other by δ, and pulse A is detuned from the EPR-allowed transition when the nuclear spin is in $|\downarrow\rangle$ by Δ. As the pulses are detuned from the EPR transition, no significant population is driven to the electron spin excited state. However, a second-order process can drive the nuclear spin state if δ is resonant with the nuclear spin frequency $\sim \omega_I$. Since the pulses do not significantly populate the electron spin excited levels, the process preserves the coherence properties of the nuclear spins. This is demonstrated in the NMR spectroscopy of Figure 2.4b, which plots the nuclear spin $\downarrow$ population as a function of the pulse frequency. The linewidth of the transition ($\sim$ 200 Hz) is much smaller than the electron linewidth, as expected for a Raman transition. We measure the coherence time of the nuclear spin through a Ramsey sequence and find $T_2^* = 0.5$–1 s, as shown in Figure 2.4c. This result confirms that $CaWO_4$ is a good host for nuclear spin qubits, as already shown for electron spins [26].

[26]: Le Dantec et al. (2021), 'Twenty-Three–Millisecond Electron Spin Coherence of Erbium Ions in a Natural-Abundance Crystal'

In Chapter 8 we focus on a system where an Er^{3+} spin is coupled to two neighboring ^{183}W nuclear spins, named Qb1 and Qb2. By exploiting the AC-Zeeman shifts induced by detuned Raman pulses, we develop a protocol for implementing a two-qubit gate. The Raman detuning Δ determines the magnitude of the AC-Zeeman shifts and gives rise to two distinct operating regimes. Figure 2.4d shows the two: on the left an unconditional regime, where the transition frequency of Qb2 is independent of the state of Qb1, and on the right a conditional regime, where this frequency depends on the state of Qb1.

Magnetic noise that is correlated between the two spins can be suppressed by preparing the system in specific singlet or triplet states with zero-average magnetic moment [10, 38]. Using ^{183}W nuclear spins, we prepare the Bell state $\frac{1}{\sqrt{2}}(|\downarrow\uparrow\rangle + |\uparrow\downarrow\rangle)$, verified by state tomography (Fig. Figure

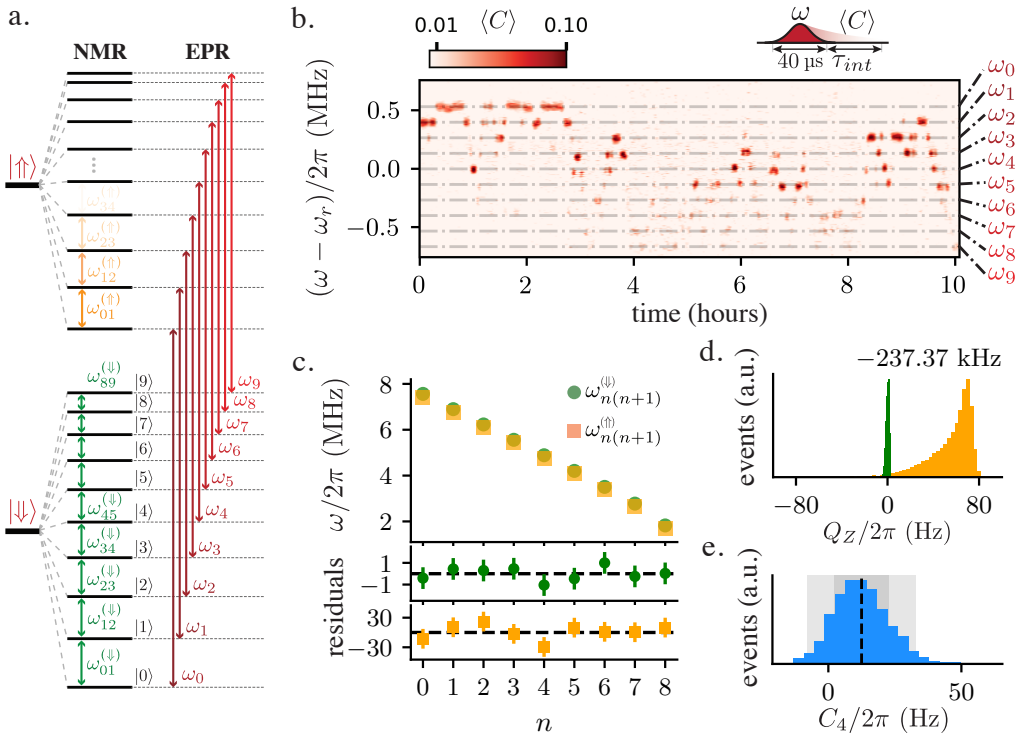

Figure 2.5.: Precision NMR spectroscopy of a ^{93}Nb nuclear spin. **a.** Energy level spectrum of an Er^{3+} spin coupled to a ^{93}Nb nuclear spin $I = 9/2$. The ten EPR-allowed transitions are marked in red. The eighteen NMR-allowed transitions are highlighted in green and orange, depending on the state of the Er^{3+} spin. **b.** Photon counting spectroscopy of a single Er^{3+} spin coupled to a ^{93}Nb nuclear spin as a function of time. The SMPD detection frequency is dynamically tuned to match the frequency of the applied microwave pulse ω. The ensemble-average counts $\langle C \rangle$ are plotted as a function of the pulse frequency and measurement time. The ten EPR-allowed frequencies are highlighted with a dashed gray line. The pulse sequence is shown at the top right. **c.** NMR spectrum and Hamiltonian fit. *(top)* NMR spectra for the ^{93}Nb transitions in the Er^{3+} spin ground (excited) state are plot in green (orange) as a function of the transition index n. *(bottom)* Residuals of the Hamiltonian fit. The $\chi^2_\nu = 1.2$ which indicates a successful fit. Errorbars correspond to the uncertainty of the frequency and black dashed line marks zero. **d.** Spin dependent quadrupole observation. Posterior distribution of the quadrupole tensor principal component along the Z-axis for the ground and excited state fits (green and orange resp.). The distributions are normalized to the same height for visual clarity. **e.** Hexadecapole coupling strength. Posterior distributions for the hexadecapole coupling constant C_4. Vertical line marks the mean of the distribution and the shaded areas the $1-$ and $2-\sigma$ confidence intervals.

2.4e), and measure its coherence time. We find a twofold increase relative to the single-qubit coherence time, indicating effective magnetic-noise suppression within a decoherence-free subspace.

2.4. Precision spectroscopy on a 9/2 nuclear spin

Another application of the methods developed in Chapter 7 is to characterize an unknown atom near an electron spin. This is the topic of Chapter 9, where we fully characterize an unknown nuclear spin-9/2 impurity near an Er^{3+} spin. We moreover perform precision hyperfine spectroscopy of this ^{93}Nb atom and find previously unknown terms in the spin Hamiltonian.

Figure 2.5a represents the twenty energy levels of the ^{93}Nb–Er^{3+} coupled system as well as all EPR transitions, with frequencies ω_n, and NMR-allowed transitions, split into two manifolds depending on the state m_S of the Er^{3+} spin and with frequencies $\omega^{(m_S)}_{n,n+1}$. We initially characterize the system through EPR spectroscopy by measuring similar time traces as in Chapter 7. Figure 2.5b shows the ten different EPR-allowed transitions of the electron spin equally spaced from each other, characteristic of an electron spin coupled to a nuclear spin $I = 9/2$.

We use the methods developed in the previous chapters (single-shot readout, solid-effect DNP, and stimulated Raman driving) to measure the NMR spectrum of the ^{93}Nb spin. By comparing the Larmor frequency of the impurity with the gyromagnetic ratios of nuclear spins, we identify it as a ^{93}Nb spin. We leverage the long coherence of the nuclear spin to measure its hyperfine spectrum with hertz resolution, shown in Figure 2.5c as a function of the transition index. The large splitting of the levels indicates that the quadrupolar interaction strength of the nuclear spin is of similar magnitude to the Zeeman interaction strength.

We fit the NMR spectrum to a Hamiltonian model in both Er^{3+} manifolds with hertz accuracy, as demonstrated by the residuals of the fit (shown in Figure 2.5c). We use these results to reconstruct the ^{93}Nb quadrupole and compare it with DFT simulations. Both the quadrupole reconstruction and the DFT result are shown in Figure 2.6. We find quantitative agreement between the two, both in magnitude and angular orientation, indicating correct site assignment.

In addition, we observe that the quadrupole interaction strength is different between the two manifolds, as shown in Figure 2.5d through the statistically significant difference between the posterior distributions for the quadrupolar interaction strength between the two fits. We assign this difference to a new type of interaction between electron and nuclear spins. We theorize that the origin of the interaction lies on the coupling between the magnetically-induced electric dipole of the Er^{3+} spin and the nuclear quadrupole interaction [39, 40].

Finally, we are able to set bounds on the hexadecapolar interaction that are an order of magnitude tighter than previous state-of-the-art measurements [41], as shown in Figure 2.5e.

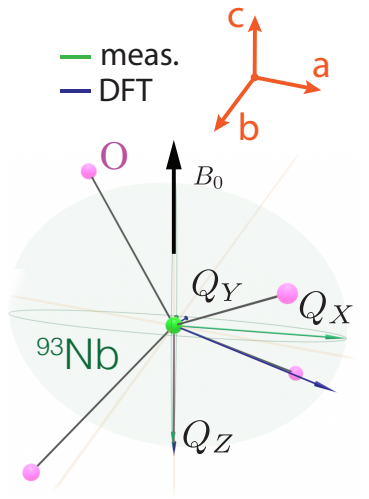

Figure 2.6.: Three-dimensional representation of the quadrupole tensor. The ^{93}Nb nuclear spin (green) lies in the center surrounded by the neighboring oxygen atoms (pink). The crystalline axes *a*, *b*, and *c* are shown as orange lines. The measured quadrupole principal axes *X*, *Y*, and *Z* are represented as green arrows, which define the semi-axes of an ellipsoid, represented in green. The principal vectors obtained via DFT simulations have been plotted in dark blue.

[39]: Bloembergen (1961), 'Linear Stark Effect in Magnetic Resonance Spectra'
[40]: Mims (1964), 'Electric Field Effects in Spin Echoes'
[41]: Liao et al. (1994), 'The Nuclear Hexadecapole Interaction of Iodine-127 in Cadmium Iodide Measured Using Zero-field Two Dimensional Nuclear Magnetic Resonance'

Background

Electron spins, nuclear spins and their interaction

3.

In this chapter, we introduce the spin Hamiltonian, which describes how an electron spin interacts with nearby nuclear spins and with external electric and magnetic fields, with a focus on Er^{3+} impurities in $CaWO_4$. We derive the approximations that let us treat the Er^{3+}:$CaWO_4$ ion as an effective spin-1/2 system at cryogenic temperatures, and we highlight how this differs from the behavior of a free electron. We then look at how Er^{3+}:$CaWO_4$ interacts with its surrounding nuclear spins, especially the hyperfine coupling to nearby ^{183}W nuclei. Finally, we discuss how Er^{3+} couples to a ^{93}Nb nuclear spin and the energy level structure of the system.

3.1 An electron in free space . 19
3.2 Er^{3+} ions in $CaWO_4$ 20
Free-ion Hamiltonian . . . 20
$CaWO_4$ crystal 21
Crystal-field Hamiltonian . 22
Spin-1/2 approximation . . 24
Linear electric field effect . 25
Summary 26
3.3 Nuclear spins in $CaWO_4$. 27
Nuclear Zeeman interaction 27
Electric Quadrupole interaction 27
3.4 Hyperfine interaction . . . 29
3.5 The spin Hamiltonian . . . 30
3.6 Nuclear spin $\frac{1}{2}$: Energy states and wavefunctions . 32
3.7 Quadrupolar nucleus: Energy states and wavefunctions 34

3.1. An electron in free space

We begin this chapter by describing the properties of a single electron spin in a magnetic field. This simple system introduces key concepts of the spin Hamiltonian, and its behavior provides a useful baseline for comparison with the effective spin-1/2 nature of Er^{3+}:$CaWO_4$.

Electrons are elementary particles with negative charge and an inherent magnetic moment arising from their spin,

$$\hat{\boldsymbol{\mu}}_e = \gamma_e \hat{\mathbf{S}} \tag{3.1}$$

where $\hat{\mathbf{S}} = (\hat{S}_x, \hat{S}_y, \hat{S}_z)$ correspond to the spin-1/2 operators and $\gamma_e/2\pi = 28.024\,\mathrm{GHz/T}$ is the gyromagnetic ratio of the electron spin. In a constant magnetic field $\mathbf{B_0}$, an electron in free space can be described by the Zeeman effect:

$$\hat{\mathcal{H}}_e/\hbar = -\mathbf{B_0} \cdot \hat{\boldsymbol{\mu}}_e = \omega_e \hat{S}_{z'}. \tag{3.2}$$

where $\omega_e = -\gamma_e\,\mathbf{B_0}$ is the Larmor frequency of the electron spin and z' corresponds to the quantization axis of the spin, parallel to $\mathbf{B_0}$. The two states of the system are labeled $|\Downarrow\rangle$ and $|\Uparrow\rangle$ and their energy difference depends linearly on $|B_0|$. We highlight the following properties:

- **Isotropy**. The electron's gyromagnetic factor is isotropic. As a result, the quantization axis is aligned with the external magnetic field ($z' \parallel \mathbf{B_0}$).
- **Opposite magnetic moments.** The two eigenstates have opposite magnetic moments μ_e and $-\mu_e$, which correspond to parallel and antiparallel orientations of the spin with respect to B_0.
- **No electric dipole**. An electron spin in free space does not exhibit a permanent electric dipole, as it is a single, point-like charge.

In the following section, we explore how some paramagnetic centers in solids, in particular Er^{3+} in $CaWO_4$, can be treated as an effective spin-1/2 at cryogenic temperatures. However, these are complex, multielectron systems with strong spin-orbit coupling, which lead to deviations from the simple free electron system.

3.2. Er^{3+} ions in $CaWO_4$

The next few pages discuss the properties of Er^{3+} ion impurities in $CaWO_4$, and compare them to those of an electron spin in free space. A summary of the main results of this analysis can be found in this section's conclusion and in ref. [42]. Readers seeking an overview of the essential findings may wish to consult the Conclusion first, as it contains the results needed for the remainder of this thesis.

[42]: Liu et al. (2005), *Spectroscopic Properties of Rare Earths in Optical Materials*

Erbium belongs to the family of lanthanides. In solids, it typically forms a trivalent ion whose common property is a partially filled $4f$ shell. Its electronic configuration is based on xenon plus an additional N electrons in the $4f$ shell: $\{[\mathrm{Xe}], 4f^N\}$. For erbium, $N = 11$. Due to this electronic structure, the $4f$ shell is shielded by the $5s$ and $5p$ closed shells from interactions with ligand electrons. This allows one to treat the electronic level structure using the free-ion energy levels. In the solid state, the electrostatic fields generated by the surrounding ions can be treated as a perturbation of the free ion.

Free-ion Hamiltonian

Here, we sketch a derivation of the Free-Ion Hamiltonian of Er^{3+} , based on [43, 44]. The free-ion Hamiltonian that describes an N-electron ion in free space can be expressed as

[43]: Weissbluth (2012), *Atoms and Molecules*
[44]: Abragam et al. (2012), *Electron Paramagnetic Resonance of Transition Ions*

$$\hat{\mathcal{H}}_{\mathrm{fi}} = \underbrace{-\sum_{i=1}^{N} \frac{\hbar^2}{2m}\nabla_i^2 - \sum_{i=1}^{N} \frac{Ze^2}{r_i}}_{\hat{\mathcal{H}}_0 \rightarrow \text{Kinetic and Potential}} + \underbrace{\sum_{i<j}^{N} \frac{e^2}{r_{ij}}}_{\hat{\mathcal{H}}_{\mathrm{C}} \rightarrow \text{Coulomb}} + \underbrace{\sum_{i=1}^{N} \xi(r_i)\, \hat{\mathbf{L}}_i \cdot \hat{\mathbf{S}}_i}_{\hat{\mathcal{H}}_{\mathrm{SO}} \rightarrow \text{Spin-Orbit}} . \tag{3.3}$$

where r_i is the distance of each electron to the nucleus and r_{ij} are the distances between electrons. In order, the terms describe the kinetic and potential energy, the electron–electron Coulomb interaction, and the spin–orbit coupling. For light ions, the spin–orbit coupling can be considered as a perturbation to the dominant electron–electron interaction. However, the Hamiltonian defined by the remaining terms cannot be directly solved, as it involves the coupling between N independent electrons. This problem is solved by introducing the mean-field approximation, where the electron–electron interaction is described with a single-electron potential averaged over all electron interactions.

$$\hat{\mathcal{H}}_{\mathrm{fi}} = \underbrace{\hat{\mathcal{H}}_0 + \left\langle \sum_{\mathrm{pairs}} \frac{e^2}{r_{ij}} \right\rangle}_{\hat{\mathcal{H}}_{\mathrm{c}} \rightarrow \text{Central}} + \underbrace{\hat{\mathcal{H}}_{\mathrm{C}} - \left\langle \sum_{\mathrm{pairs}} \frac{e^2}{r_{ij}} \right\rangle}_{\hat{\mathcal{H}}_{\mathrm{nc}} \rightarrow \text{Non-central}} + \hat{\mathcal{H}}_{\mathrm{SO}}. \tag{3.4}$$

From this expression, it is clear that the non-central term $\hat{\mathcal{H}}_{\mathrm{nc}}$ is merely a perturbation to the central term $\hat{\mathcal{H}}_{\mathrm{c}}$. Importantly, $\hat{\mathcal{H}}_{\mathrm{c}}$ can be described by single-electron equations with the same angular properties as the hydrogen atom. Each electron i can be described by the four quantum numbers (n, l, m_l, m_s), respectively the principal quantum number, the angular momentum quantum number $(0 \leq l < n - 1)$, the magnetic

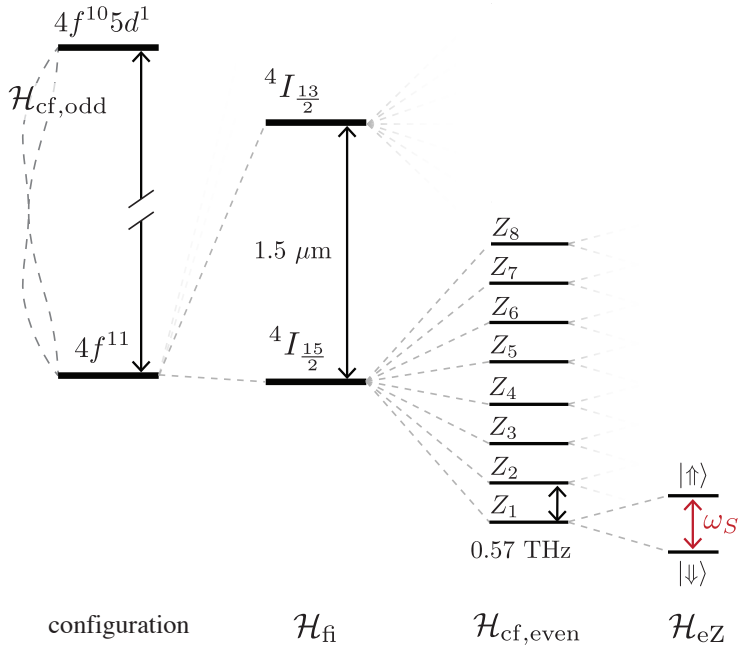

Figure 3.1.: Energy splitting diagram from the electronic configuration to the effective spin-1/2. The electronic $4f$ shell is split into optically addressable states by electron–electron interaction and spin–orbit coupling. The free-ion ground state corresponds to $^4I_{15/2}$, a 16-fold degenerate level, and the first excited level is separated by an optical transition at 1.5 µm. In $CaWO_4$, the $J = 15/2$ ground state is split into eight doublets ($Z_{1,\dots,8}$) due to the crystal field. Finally, a magnetic field lifts the doublet degeneracy through the Zeeman effect. We note that the odd-parity terms of the crystal field do not modify the energy spectrum, but create a small mixing between the configuration states (marked as a gray dashed line) which allows optical driving in non-centrosymmetric crystals.

quantum number ($-l \leq m_l \leq +l$) and the spin quantum number ($m_s = \pm\frac{1}{2}$). For lanthanides, the valence shell is located in the $n = 4$ and $l = 3$ configuration and is generally referred to as the $4f$ shell [1]. The final electronic configuration of Er^{3+} is shown in Figure 3.1. The averaged electron interaction term is not known, but it can be treated using the Hartree–Fock approximation (see [43]).

To calculate the effect of the non-central Hamiltonian $\hat{\mathcal{H}}_{\mathrm{nc}}$, the matrix elements of the Hamiltonian are calculated in a shared diagonal basis. This basis exploits the fact that both the angular momentum operators $\hat{\mathbf{L}}$ and the spin operators $\hat{\mathbf{S}}$ commute with $\hat{\mathcal{H}}_{\mathrm{fi}}$. This allows one to define a common basis with the set of eigenvectors of $\hat{\mathbf{L}}^2$ and $\hat{\mathbf{S}}^2$ (Russell–Saunders coupling).

Lastly, we consider the effects of the spin–orbit Hamiltonian $\hat{\mathcal{H}}_{\mathrm{SO}}$. For light ions, this term is smaller than the rest of the interactions and can be treated as a perturbation. $\hat{\mathcal{H}}_{\mathrm{SO}}$ commutes only with the total angular momentum, defined as $\hat{\mathbf{J}} = \hat{\mathbf{L}} + \hat{\mathbf{S}}$. Thus, the perturbation splits the degeneracy of the Russell–Saunders ground state into levels with a specific value of J, which are $(2J + 1)$-degenerate. The labels are given by Russell–Saunders notation as $^{2S+1}L_J$.

In the case of Er^{3+} , the free-ion ground state corresponds to $^4I_{15/2}$, a 16-fold degenerate level. The first excited level is separated by 1.5 µm as shown in Figure 3.1. In the following work, the $CaWO_4$ crystal and the ions are cooled down to 10 mK. Consequently, only the ground state will be populated, which can be described as a spin $J = 15/2$.

1: The actual electronic wavefunctions are given by a Slater determinant, which enforces the Pauli exclusion principle and the antisymmetric behavior under electron exchange that is characteristic of fermionic particles.

[43]: Weissbluth (2012), *Atoms and Molecules*

$CaWO_4$ crystal

Calcium tungstate ($CaWO_4$), also known as scheelite, is a tetragonal crystal appearing as dipyramidal pseudo-octahedra and belongs to the $I4_1/a$ symmetry group. The unit cell of $CaWO_4$ is shown in Figure 3.2. It consists of Ca^{2+} and W^{6+} ions coordinated by O^{2-} ions. Each Ca^{2+} ion is surrounded by eight O^{2-} ions, forming a distorted dodecahedral

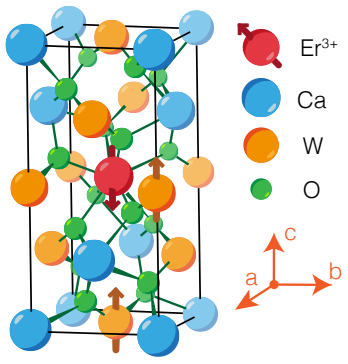

Figure 3.2.: First unit cell of a $CaWO_4$ crystal, centered around a substituting Er^{3+} ion.

environment, while each W^{6+} ion is tetrahedrally coordinated by four O^{2-} ions. The arrangement of these polyhedra leads to orthogonal principal axes (labeled as a, b and c). Due to the symmetry of the crystal, the a- and b-axes are equivalent. The unit cell parameters at cryogenic temperature are $a = b = 5.23643$ Å and $c = 11.3381$ Å [45].

[45]: Senyshyn et al. (2004), 'Lattice Dynamics and Thermal Properties of CaWO4'

Er^{3+} ions are found to substitute Ca^{2+} ions in $CaWO_4$. The substitution sites exhibit an S_4 point-symmetry along the c-axis of the crystal. Sites with this symmetry are invariant under a combination of a rotation of 90° around the c-axis followed by an inversion operation.

Due to the charge difference between the two ions, charge compensation mechanisms take place inside the crystal [46], which can take the form of interstitial ions, vacancies, or other defects. However, the EPR spectrum of Er^{3+}:$CaWO_4$ shows S_4 symmetry [26, 47, 48], indicating that this charge compensation does not happen in close proximity to the ion.

[46]: Cornacchia et al. (2007), 'Growth and Spectroscopic Characterization of Er3+'
[26]: Le Dantec et al. (2021), 'Twenty-Three–Millisecond Electron Spin Coherence of Erbium Ions in a Natural-Abundance Crystal'
[47]: Antipin et al. (1968), 'Paramagnetic Resonance and Spin-Lattice Relaxation of Er3+ and Tb3+ Ions in CaWO4 Crystal Lattice'
[48]: Billaud et al. (2025), 'Electron Paramagnetic Resonance Spectroscopy of a Scheelite Crystal Using Microwave-Photon Counting'

Crystal-field Hamiltonian

Inside the crystal, the energy levels of the Er^{3+} ion are perturbed by the electrostatic potential V at the ion's location produced by the neighboring atoms of the lattice. This potential can be expressed as a multipole expansion and written by separating terms that are even and odd under inversion symmetry ($r \leftrightarrow -r$), $V = V_{\text{odd}} + V_{\text{even}}$. Because the Er^{3+} insertion site (of symmetry S_4) does not have inversion symmetry, $V_{\text{odd}} \neq 0$.

Due to the shielding provided by the more external $5s$ and $5p$ closed shells, the electrostatic interaction between the ion and the crystal can be treated as a perturbation to the free-ion Hamiltonian. The crystal-field Hamiltonian is used to describe the interaction between the ion and the crystal and is generally described in terms of the extended Stevens operators $\hat{O}_k^q$ with $k = 1, 2, 3, \ldots$ and $q \in \{-k, \ldots, k\}$ [44, 49]

[44]: Abragam et al. (2012), *Electron Paramagnetic Resonance of Transition Ions*
[49]: Stevens (1952), 'Matrix Elements and Operator Equivalents Connected with the Magnetic Properties of Rare Earth Ions'

$$\hat{\mathcal{H}}_{\text{cf}}/\hbar = \sum_{k=0}^{\infty} \sum_{q=-k}^{k} B_k^q \hat{O}_k^q \tag{3.5}$$

where the coefficients B_k^q are real-valued crystal-field parameters[2]. Terms with even and odd rank (the k index) belong to the even and odd electrostatic potentials (V_{even} and V_{odd}), respectively.

2: The terms with $k > 6$ are rarely considered as they are practically irrelevant.

The extended Stevens operators are constructed as polynomial combinations of the J_z, J_+ and J_- operators, and a full list of the operators can be found in [50]. The indices k and q encode the symmetry properties of the crystal field: k specifies the rank of the operator (i.e., the maximum total power of angular momentum operators in the polynomial). The index q determines the projection onto the quantization axis (i.e. the maximum power of the non-diagonal terms). For example,

[50]: Al'tshuler et al. (1964), *Electron Paramagnetic Resonance*

$$\begin{aligned} \hat{O}_2^0 &= 3\hat{J}_z^2 - J\,\hat{\mathbb{1}}, \\ \hat{O}_4^4 &= \tfrac{1}{2}\left(\hat{J}_+^4 + \hat{J}_-^4\right). \end{aligned} \tag{3.6}$$

The maximum power of the angular momentum operators in the polynomial expansion of the Stevens operator is given by the k index, while the maximum power of the $J_\pm$ operators is given by the q index. This allows

the crystal field to encode the symmetry properties of the crystal site in a reduced number of terms.

Odd-parity crystal-field terms The effect of the odd terms (and thus V_{odd}) has been discussed in [51, 52]. This term couples electrons in the $4f$ shell with shells of opposite parity, for instance the $5d$. Because of the large energy difference, the wave-function admixture is small; nevertheless, its consequences are important. First, it allows a non-zero electric dipole matrix element between Kramers doublets (and in particular, it allows electric-dipole driving of the optical transition at 1.5 µm as shown in Figure 3.1) [52]. Second, and very relevant for this work, it means that the energy states of Er^{3+} may present a finite electric dipole moment. This moment is suppressed at zero magnetic field by Kramers degeneracy, however the latter is lifted under a finite magnetic field. Therefore, in finite magnetic fields, Er^{3+} energy levels present a non-zero electric dipole, whose magnitude is moreover approximately proportional to the magnetic field strength.

[51]: Kiel (1966), 'Theory of Electric Shifts of the Optical and Magnetic Resonance Properties of Paramagnetic Ions in Crystals'
[52]: Judd (1962), 'Optical Absorption Intensities of Rare-Earth Ions'

Even-parity crystal-field terms We now neglect the effect of the odd crystal-field terms, and consider only the main $4f$ part of the Er^{3+} level wavefunction. Non-zero matrix elements between $4f$ states require even parity operators; hence, the wavefunctions and energy levels are determined by V_{even}. The following level of approximation is to neglect the admixture between levels of well-defined angular momentum J. This is justified by the large energy difference between the J manifolds due to the large spin-orbit interaction ($J = 1.5\mu$m between 15/2 and $J = 13/2$). We go back to the effects of the odd terms in the Hamiltonian and their interaction with an external electric field in the following section.

To accurately describe the Er^{3+} energy level system, we rely on the crystal-field Hamiltonian derived by Bernal [53] for Er^{3+}:$CaWO_4$ through a series of optical spectroscopy measurements:

$$\hat{\mathcal{H}}_{\text{cf}}/\hbar = \alpha\, B_2^0 \hat{O}_2^0 + \beta \left(B_4^0 \hat{O}_4^0 + B_4^4 \hat{O}_4^4 \right) + \gamma \left(B_6^0 \hat{O}_6^0 + B_6^4 \hat{O}_6^4 + B_6^{-4} \hat{O}_6^{-4} \right) \tag{3.7}$$

Where the normalization parameters for the Stevens operators (α, β, γ) are given by [54] and the crystal-field parameters are given in Table 3.1.

B_2^0	231 cm^{-1}
B_4^0	-90 cm^{-1}
B_4^4	852 cm^{-1}
B_6^0	-0.6 cm^{-1}
B_6^4	396 cm^{-1}
B_6^{-4}	75 cm^{-1}

Table 3.1.: Crystal field parameters for Er^{3+}:$CaWO_4$ measured in [53] with the operator normalization as defined in [54]

Energy levels The electronic structure of the Er^{3+} ground-multiplet ($J = 15/2$) under an external magnetic field $\mathbf{B_0}$ is described by the following Hamiltonian:

$$\hat{\mathcal{H}}_{\text{J}}/\hbar = \mu_B\, g_J \mathbf{B_0} \cdot \hat{\mathbf{J}} + \hat{\mathcal{H}}_{\text{CF}}, \tag{3.8}$$

where the first term represents the Zeeman interaction. Here, $g_J = 6/5$ is the Landé factor for the Er^{3+} ground state and $\mu_B/2\pi = 13.996$ GHz/T is the Bohr magneton.

The crystal-field interaction mixes states with different J_z, lifting the 16-fold degeneracy of the ${}^4I_{15/2}$ state. For Er^{3+} (an $N = 11$ electron system), Kramers' theorem [55] dictates that in the absence of a magnetic field, all levels must remain at least doubly degenerate due to time-reversal

[55]: Kramers (1930), 'General Theory of Paramagnetic Rotation in Crystals'

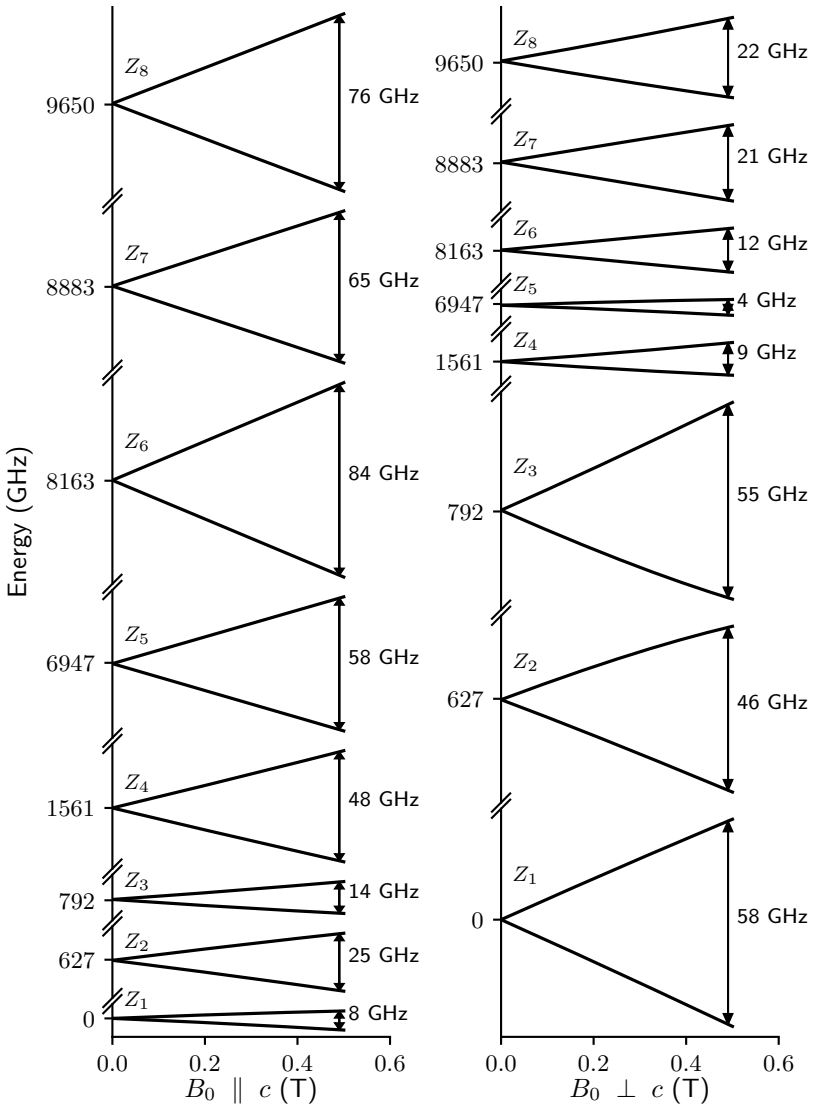

Figure 3.3.: Energy levels for all Z_i doublets under a magnetic field parallel (perpendicular) to the *c*-axis. The y-axis is broken to better show the magnetic splitting of the levels. The energy difference between the states of each doublet at 500 mT is shown as vertical double arrows, along with the approximate frequency of the transition.

symmetry. Consequently, the ground state splits into eight distinct *Kramers doublets* ($Z_{1,\ldots,8}$), as shown in Figure 3.1.

The dependence of these levels as a function of the applied field, calculated via direct diagonalization of Eq. 3.8, is illustrated in Figure 3.3. Each doublet behaves as an effective spin-1/2 system characterized by an anisotropic gyromagnetic factor. This anisotropy is physically manifested in the shift of transition frequencies when the orientation of a 500 mT field is rotated from parallel to perpendicular relative to the *c*-axis.

Crucially, the energy gap between the two lowest doublets (Z_1 and Z_2) is approximately 0.6 THz ($\approx$ 30 K). At cryogenic temperatures (generally between 10 mK and 100 mK), the thermal energy is insufficient to populate higher levels. Thus, only the Z_1 doublet will be populated and the system can be treated as a spin-1/2. During much of this work, this approximation will be used.

Spin-1/2 approximation

The energy separation between the Z_1 and Z_2 doublets is approximately 650 GHz, which corresponds to a temperature of 50 K. Thus, at the

working temperature of 10 mK, only the Z_1 doublet will be populated. This doublet can be effectively treated as a spin-1/2 with an anisotropic gyromagnetic tensor. Under a magnetic field, the Hamiltonian of the spin is

$$\hat{\mathscr{H}}_{\mathrm{eZ}}/\hbar = -\mathbf{B_0} \cdot \bar{\bar{\gamma}}_{^{3+}\mathrm{Er}} \cdot \hat{\mathbf{S}} = \omega_S \, \hat{S}_{z'} \tag{3.9}$$

where $\omega_S = -\mathbf{B_0} \cdot \bar{\bar{\gamma}}_{^{3+}\mathrm{Er}}$ is the Larmor frequency of the spin and z' corresponds to its quantization axis. The two eigenstates of the system are labeled $|\Downarrow\rangle$ and $|\Uparrow\rangle$. The effective gyromagnetic tensor $\bar{\bar{\gamma}}_{^{3+}\mathrm{Er}}$ is diagonal along the principal axes of the crystal, with values [56]

[56]: Antipin, A.A. et al. (1981), 'Anisotropy of Er3+ Spin-Lattice Relaxation in LiYF4 Crystals'

$$\begin{aligned} \gamma_a = \gamma_b = \gamma_\perp &= -2\pi \times 17.3 \ \mathrm{GHz/T}, \\ \gamma_c = \gamma_\parallel &= -2\pi \times 17.45 \ \mathrm{GHz/T}. \end{aligned} \tag{3.10}$$

Because the effective gyromagnetic tensor is anisotropic, the spin quantization axis of the spin is not in general parallel to the applied magnetic field. Indeed, the unitary vector of the quantization axis is given by

$$\mathbf{u}_{z'} = \frac{\mathbf{B_0} \cdot \bar{\bar{\gamma}}_{^{3+}\mathrm{Er}}}{\| \mathbf{B_0} \cdot \bar{\bar{\gamma}}_{^{3+}\mathrm{Er}} \|}. \tag{3.11}$$

This axis coincides with $\mathbf{B_0}$ only when the field is aligned with one of the crystal principal axes a, b or c.

We note that in the solid state, local charge compensation mechanisms or strain effects can lead to shifts of the gyromagnetic tensor of individual ions. This leads to broadening of the ensemble lines, as each spin experiences a different environment. This is known as inhomogeneous broadening.

Linear electric field effect

As discussed in Section 3.2, paramagnetic ions in solids, occupying non-centrosymmetric sites, display a gyromagnetic tensor that depends on both the magnitude and direction of an applied static electric field [57]. This linear electric field effect is proportional to the spin-orbit coupling of the ion and is generally observed in paramagnetic ions in the solid state, where the orbital momentum is not quenched.

[57]: Ham (1961), 'Linear Effect of Applied Electric Field in Electron Spin Resonance'

Ensemble spin coherence measurements in Er^{3+}:$CaWO_4$ have revealed the effects of this interaction even in the absence of externally applied electric fields. Local strain in the crystal lattice induces different electric fields at individual ion sites. Because the sensitivity to electric fields depends on the orientation of the external magnetic field [58], the ensemble spin coherence exhibits a corresponding dependence [26].

[58]: Mims (1965), 'Electric Field Shift in Paramagnetic Resonance for Four Ions in a Calcium Tungstate Lattice'

[26]: Le Dantec et al. (2021), 'Twenty-Three–Millisecond Electron Spin Coherence of Erbium Ions in a Natural-Abundance Crystal'

As noted earlier, Er^{3+}:$CaWO_4$ occupies a site with S_4 symmetry, which lacks inversion symmetry. This allows odd terms ($k = 1, 3, 5, \ldots$) to appear in the crystal-field Hamiltonian. As discussed in ref. [59], these terms can be modeled by a magneto-electric Hamiltonian:

[59]: Kiel et al. (1970), 'Electric-Field-Induced g Shifts for Loose Yb Ions in Three Scheelite Lattices'

$$\hat{\mathscr{H}}_{\mathrm{m\text{-}e}}/\hbar = \sum_{i,j,k}^{\{a,b,c\}} T_{k,i,j} \hat{S}_i B_j E_k \tag{3.12}$$

where $i, j, k \in \{x, y, z\}$ and $T_{k,i,j}$ is a third-rank tensor which is symmetric in the $\{i, j\}$ indices. The tensor captures the linear mixing of the levels as a function of the electric and magnetic fields. The values for the tensor in Er^{3+}:$CaWO_4$ were experimentally determined by Mims [58] and are displayed in Table 3.2. The effect can be described with only four independent parameters, and the rest of the elements of the tensor are obtained by enforcing S_4 and $\{i, j\}$ index symmetry.

param.	value	S_4 symm.
$T_{a,c,a}$	1.4	$-T_{b,c,b}$
$T_{a,c,b}$	1.0	$-T_{b,c,a}$
$T_{c,a,a}$	5.4	$-T_{c,b,b}$
$T_{c,b,a}$	2.9	(-)

Table 3.2.: Magneto-electric parameters for Er^{3+}:$CaWO_4$ given in $(10^{-32} \times \frac{\mathrm{J/T}}{\mathrm{V/m}})$. The values were measured by Mims in ref. [58]. The third column indicates the relation between the parameters that originate from the S_4 symmetry of the ion site. The rest of the values of the tensor can be obtained by enforcing $\{i, j\}$ index symmetry $T_{k,i,j} = T_{k,j,i}$.

[58]: Mims (1965), 'Electric Field Shift in Paramagnetic Resonance for Four Ions in a Calcium Tungstate Lattice'

Even if the energy shifts are zero in the absence of an electric field, this interaction can be understood as an induced electric dipole **d** due to an external magnetic field; if **B** is fixed, the interaction can be effectively rewritten as

$$\begin{aligned} \hat{\mathcal{H}}_{\text{m-e}}/\hbar &= \sum_k -d_k E_k = -\mathbf{d}\cdot\mathbf{E}, \\ d_k &= -\sum_{i,j} T_{k,i,j}\langle \hat{S}_i\rangle B_j. \end{aligned} \tag{3.13}$$

where $\langle \hat{S}_i \rangle$ corresponds to the expectation value of the electron spin. In conclusion, the Er^{3+} spin states display an electric dipole, whose magnitude is proportional to the applied magnetic field, and whose orientation is spin-dependent.

Summary

We can summarize the results of this section by comparing the properties of the effective spin-1/2 of Er^{3+}:$CaWO_4$ to a free electron, described at the beginning of the chapter:

- **Anisotropy**. In the crystalline axis basis, the gyromagnetic tensor of Er^{3+}:$CaWO_4$ is given by

$$\bar{\bar{\gamma}}_{^{3+}\text{Er}} = \begin{pmatrix} -117.3 & 0 & 0 \\ 0 & -117.3 & 0 \\ 0 & 0 & -17.45 \end{pmatrix} \frac{\text{GHz}}{\text{T}}$$

  This tensor is anisotropic, in contrast to that of the free electron spin. In addition, the gyromagnetic factor along the a and b axes is four times larger than γ_e, which is key to achieving large inductive coupling strengths. Finally, the quantization axis is in general not parallel to the external magnetic field, unless $\mathbf{B_0}$ is applied along one of the crystalline axes.
- **Average magnetic moment.** As the magnetic field increases, mixing between the doublets (Z_1, Z_2, ...) leads to deviations from the effective spin-1/2 approximation. This effect is illustrated in Figure 3.4, where the energy levels of the Z_1 doublet are shown as a function of the applied magnetic field along the c-axis. They show clear deviations from the linear Zeeman Hamiltonian, resulting in a field-dependent average magnetic moment. This induces a pseudo-Zeeman shift on nearby nuclear spins by modifying the effective magnetic field at their location, thereby shifting their resonant frequency [60, 61].
- **Induced electric dipole**. The non-centrosymmetric nature of the insertion site (of symmetry S_4) yields non-zero odd terms in the crystal-field Hamiltonian. These terms do not contribute to the energy splitting of the free-ion eigenstates but are responsible

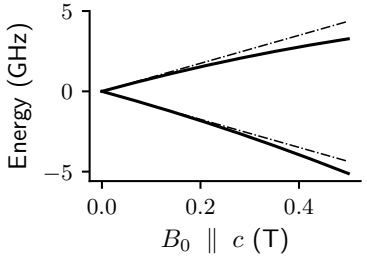

Figure 3.4.: Energy levels of the Z_1 doublet as a function of magnetic field along the c-axis. The curves were obtained by direct diagonalization of Eq. 3.8 and Eq. 3.9 (solid and dot-dashed resp.).

[60]: Baker et al. (1958), 'Paramagnetic Resonance in Some Lanthanon Ethyl Sulphates'
[61]: Sottini et al. (2012), 'A Comment on the Pseudo-Nuclear Zeeman Effect'

for the appearance of a spin-dependent electric dipole, whose magnitude is proportional to the applied magnetic field.

3.3. Nuclear spins in $CaWO_4$

In contrast to electrons, nuclei are not elementary particles but a combination of protons and neutrons, bound together by the strong nuclear force. What we refer to as the *nuclear spin* I is actually the total angular momentum of the ground state of the nuclear Hamiltonian [62]. The combination of both spin and orbital angular momentum in the nucleus can yield nuclear spin numbers as large as $I = 7$ for the case of ^{176}Lu.

[62]: Kuprov (2023), *Spin*

In Chapters 7 and 8 we report the detection and coherent control of individual ^{183}W nuclear spins, and in Chapter 9 we identify a nearby impurity as ^{93}Nb with nuclear spin $I = 9/2$ via spectroscopy. This section summarizes how external magnetic and electric fields couple to nuclear moments. We focus on the interactions that dominate our experiments: the nuclear Zeeman effect and the electric quadrupole coupling. We describe their influence on the level structure and transition frequencies of ^{183}W and ^{93}Nb .

Nuclear Zeeman interaction

A nuclear spin $I = 1/2$ in an external magnetic field is described by the Zeeman Hamiltonian, analogous to the electron case:

$$\hat{\mathcal{H}}_{\mathrm{nZ}}/\hbar = -\gamma_n \, \mathbf{B_0} \cdot \hat{\mathbf{I}} = \omega_I \, \hat{I}_{z'}, \tag{3.14}$$

where γ_n is the isotropic nuclear gyromagnetic factor, $\hat{\mathbf{I}} = (\hat{I}_x, \hat{I}_y, \hat{I}_z)$ are the nuclear spin operators, $\omega_I = \gamma_n \, \mathbf{B_0}$ is the Larmor frequency, and z' is the quantization axis of the nuclear spin. This term splits the nuclear manifold into $2I + 1$ energy levels, uniquely described by the magnetic quantum number $m_I \in \{-I, -I + 1, \ldots, I\}$. For the species relevant to this work, the gyromagnetic ratios are $\gamma_{^{183}\mathrm{W}}/2\pi = 1.77394$ MHz/T and $\gamma_{^{93}\mathrm{Nb}}/2\pi = 10.4213$ MHz/T [63].

[63]: Knight et al. (1986), 'Solid-State Tungsten-183 Nuclear Magnetic Resonance Spectroscopy'

These values lie in the MHz/T range, which is roughly 10^{-3} times smaller than an electron. In addition, we note that the sign of the gyromagnetic ratios is generally positive[3], which means that the Zeeman ground state is $m_I = I$ and parallel to the applied magnetic field, in contrast to the electron spin.

3: Given that the nuclear spin is a complex combination of the spin and orbital momentum of nucleons, the gyromagnetic ratio can also be negative under particular circumstances, as is the case for ^{15}N.

Electric Quadrupole interaction

For nuclei with $I \geq 1$, the ground-state charge distribution is not spherically symmetric, and the nucleus therefore possesses an electric quadrupole moment. In the presence of a non-zero electric-field gradient (EFG) at the nuclear site, this quadrupole moment couples to the EFG, giving rise to the nuclear quadrupole interaction which must be included in the spin Hamiltonian. The quadrupole interaction arises from the non-sphericity of the nuclear wavefunctions of $I \geq 1$ nuclear spins. The charge distribution inside the nucleus is elongated, and when subject to an external electric-field gradient, certain orientations of the

charge are favored. Figure 3.5 sketches this intuition by placing an elongated positively charged distribution between four charges, two $+q$ on the x-axis and two $-q$ on the y-axis. Due to the electrostatic attraction between the positive and negative charges, the vertical orientation is energetically favored.

We now proceed to sketch the derivation of the quadrupole interaction in terms of the spin operators, based on ref. [2]. We begin by considering the classical case of a charge distribution $\rho(\mathbf{r})$ under an electric potential $V(\mathbf{r})$. The energy associated with this system is given by

$$E = \int \rho(\mathbf{r})\, V(\mathbf{r})\, d\mathcal{V}. \tag{3.15}$$

We can approach this problem through the multipole expansion, which consists of writing the potential as a Taylor series at the center of mass of the nucleus and treating each term independently:

$$V(\mathbf{r}) = V(0) + \sum_{\alpha} x_\alpha \left.\frac{\partial V}{\partial x_\alpha}\right|_{\mathbf{r}=0} + \frac{1}{2!}\sum_{\alpha,\beta} x_\alpha x_\beta \left.\frac{\partial^2 V}{\partial x_\alpha \partial x_\beta}\right|_{\mathbf{r}=0} + \cdots \tag{3.16}$$

Consequently, the energy will be written as [4]

$$\begin{aligned} E = V(0)\int \rho\, d\mathcal{V} + \sum_{\alpha} V_\alpha \int x_\alpha \rho\, d\mathcal{V} + \\ + \frac{1}{2!}\sum_{\alpha,\beta} V_{\alpha\beta}\int x_\alpha x_\beta \rho\, d\mathcal{V} + \cdots \end{aligned} \tag{3.17}$$

Respectively, each term corresponds to the electrostatic energy of a point-charge nucleus, the energy due to the dipole moment [5] and the quadrupolar term. Higher-order energy terms correspond to the octupole and hexadecapole interactions, which can induce minute shifts on the energy levels. To describe the quadrupole interaction, it is particularly useful to introduce the following quantities:

$$Q_{\alpha\beta} = \int \left(3x_\alpha x_\beta - \delta_{\alpha\beta} r^2\right) \rho\, d\mathcal{V} \tag{3.18}$$

as the energy of the quadrupole can be written in a compact form

$$E_{\mathrm{Q}} = \tfrac{1}{6}\sum_{\alpha,\beta} Q_{\alpha\beta} V_{\alpha\beta}. \tag{3.19}$$

To quantize this expression one must take the quantum mechanical expression for the charge density of the constituting protons of the nucleus and apply the Wigner-Eckart theorem to evaluate the resulting integrals and express the interaction in terms of the nuclear spin operator $\mathbf{I}$

$$\hat{\mathcal{H}}_{\mathrm{Q}}/\hbar = \frac{e\mathbb{Q}}{6I(2I-1)}\sum_{\alpha,\beta} V_{\alpha\beta}\left[\tfrac{3}{2}\left(\hat{I}_\alpha\hat{I}_\beta + \hat{I}_\beta\hat{I}_\alpha\right) - \delta_{\alpha\beta}\hat{I}^2\right]. \tag{3.20}$$

[2]: Slichter (1996), *Principles of Magnetic Resonance*

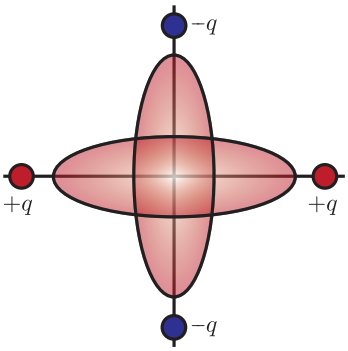

Figure 3.5.: Non-spherical charge distribution with four charges, two $+q$ in the x-axis and two $-q$ in the y-axis. The positively charged distribution has two orientations: perpendicular and horizontal. The perpendicular orientation is energetically more favorable.

4: We have introduced the notation

$$V_\alpha = \frac{\partial V}{\partial x_\alpha}, \quad V_{\alpha\beta} \equiv \frac{\partial^2 V}{\partial x_\alpha \partial x_\beta},$$

which correspond to the electric field and the EFG respectively.

5: Given that the center of mass and the center of charge coincide, the dipole energy is strictly zero

where $\mathbb{Q}$ denotes the quadrupole moment, obtained from the integral of the nuclear charge distribution and measured in Barns. The quadrupole Hamiltonian can be written as

$$\hat{\mathcal{H}}_{\mathrm{Q}}/\hbar = \hat{\mathbf{I}} \cdot \bar{\bar{Q}} \cdot \hat{\mathbf{I}}, \tag{3.21}$$

where $\bar{\bar{Q}}$ is the quadrupole tensor, proportional to the EFG. The EFG satisfies Laplace's equation, so its components obey $V_{xx} + V_{yy} + V_{zz} = 0$, and by electrostatic symmetry $V_{\alpha\beta} = V_{\beta\alpha}$. Consequently, the EFG (and thus $\bar{\bar{Q}}$) is a real, symmetric, traceless rank-2 tensor and can be diagonalized to obtain the principal-axis frame (X, Y, Z) and the corresponding principal values (V_X, V_Y, V_Z). Choosing the Z axis so that $|V_X| \leq |V_Y| \leq |V_Z|$, one defines the conventional asymmetry parameter

$$\eta = \frac{V_Y - V_X}{V_Z}, \qquad 0 \leq \eta \leq 1, \tag{3.22}$$

and the Hamiltonian in the principal-axis system can be expressed as

$$\hat{\mathcal{H}}_{\mathrm{Q}}/\hbar = \frac{C_q}{4I(2I-1)} \left[3\hat{I}_Z^2 - I(I+1) + \eta(\hat{I}_Y^2 - \hat{I}_X^2) \right], \tag{3.23}$$

where $C_q \equiv e\mathbb{Q}V_{ZZ}$ is the quadrupole interaction strength,

Therefore, the quadrupolar interaction is completely described by five parameters: C_q, η and the three Euler angles that define the principal axis system.

3.4. Hyperfine interaction

When an electron and a nuclear spin are close to each other, they interact magnetically via two distinct mechanisms. The Fermi contact term is an isotropic, short-range interaction that appears when the nuclear and electron spin wavefunctions overlap. The magnetic dipole-dipole interaction is a long-range and anisotropic coupling between two magnetic dipole moments.

In this manuscript, we focus on the interaction between Er^{3+} isotopes with zero nuclear spin and distant nuclear spins. As such, we neglect the Fermi contact contribution for three reasons. First, the electronic wavefunctions of Er^{3+}:$CaWO_4$ are localized $4f$ orbitals, screened by the outer $5s$ and $5p$ shells. Second, in the crystal the Er^{3+} and ^{183}W ions are separated and coordinated by intervening oxygen ligands (see Figure 3.2), which prevents direct overlap of their electronic wavefunctions. Third, the typical interatomic separations in our samples are large enough that any residual contact contribution is orders of magnitude smaller than the dipolar coupling. For studies of the hyperfine interaction between the electron spin of ^{167}Er and its own nuclear spin, the Fermi contact interaction constitutes an important contribution and cannot be neglected.

Treating the nucleus and Er^{3+} as point dipole moments, the magnetic dipole-dipole interaction is given by [44]

[44]: Abragam et al. (2012), *Electron Paramagnetic Resonance of Transition Ions*

$$\hat{\mathcal{H}}_{\mathrm{hf}}/\hbar = \frac{\mu_0}{4\pi} r^{-3} \left[\boldsymbol{\mu}_1 \cdot \boldsymbol{\mu}_2 - 3r^{-2}(\boldsymbol{\mu}_1 \cdot \mathbf{r})(\boldsymbol{\mu}_2 \cdot \mathbf{r}) \right] \tag{3.24}$$

where $\mathbf{r}$ is the vector separating the two spins and $\boldsymbol{\mu}_1 = g_J \mu_B \hat{\mathbf{J}}$ and $\boldsymbol{\mu}_2 = \gamma_n \hat{\mathbf{I}}$ are the magnetic moments of Er^{3+} and the neighboring nuclear spin. Expanding the expression in terms of the spin operators yields

$$\begin{aligned}\hat{\mathcal{H}}_{\mathrm{hf}} = g_J \mu_B \gamma_n \frac{\mu_0}{4\pi} r^{-3} \Big[& \hat{J}_x \hat{I}_x \left(1 - 3\sin^2\theta_r \cos^2\phi_r\right) \\ & + \hat{J}_y \hat{I}_y \left(1 - 3\sin^2\theta_r \sin^2\phi_r\right) \\ & + \hat{J}_z \hat{I}_z \left(1 - 3\cos^2\theta_r\right) \\ & - 3\sin^2\theta_r \cos\phi_r \sin\phi_r \left(\hat{J}_x \hat{I}_y + \hat{J}_y \hat{I}_x\right) \\ & - 3\sin\theta_r \cos\phi_r \cos\theta_r \left(\hat{J}_x \hat{I}_z + \hat{J}_z \hat{I}_x\right) \\ & - 3\sin\theta_r \sin\phi_r \cos\theta_r \left(\hat{J}_y \hat{I}_z + \hat{J}_z \hat{I}_y\right) \Big]\end{aligned} \tag{3.25}$$

where θ_r and ϕ_r are, respectively, the polar and azimuthal angles of the vector $\mathbf{r}$ and the spin operators are expressed in the crystal axis basis. This interaction can be written in a more compact form:

$$\hat{\mathcal{H}}_{\mathrm{hf},J}/\hbar = \hat{\mathbf{J}} \cdot \bar{\bar{A}}_J \cdot \hat{\mathbf{I}}, \tag{3.26}$$

where the complexity of the dipolar interaction is encoded in the hyperfine tensor $\bar{\bar{A}}_J$.

3.5. The spin Hamiltonian

We now summarize the previous derivations and assemble a compact spin Hamiltonian for a single Er^{3+} :$CaWO_4$ ion coupled to one nearby nuclear spin. The model below applies to both to ^{183}W and ^{93}Nb . The nuclear quadrupole term is included generally and set to zero for ^{183}W (which has $I = 1/2$). We employ three nested levels of approximations, each appropriate in different parameter regimes and used throughout this thesis:

Full J-manifold

The most general description retains the entire $J = 15/2$ manifold and includes the crystal-field, Zeeman, nuclear Zeeman, nuclear quadrupole and the full hyperfine coupling:

$$\hat{\mathcal{H}}_{15/2}/\hbar = g_J \mu_B B_0 \hat{J}_{z'} + \hat{\mathcal{H}}_{\mathrm{cf}} + \omega_I \hat{I}_{z'} + \hat{\mathbf{I}} \cdot \bar{\bar{Q}} \cdot \hat{\mathbf{I}} + \hat{\mathbf{J}} \cdot \bar{\bar{A}}_J \cdot \hat{\mathbf{I}}. \tag{3.27}$$

We note that, at this level of approximation, the two Zeeman terms are isotropic and the operators $J_{z'}$ and $I_{z'}$ refer to the same axis z', parallel to the magnetic field B_0.

Effective spin-1/2

In the effective spin-1/2 model, the magnetic dipole Hamiltonian is obtained by expressing $\boldsymbol{\mu}_1 = \bar{\bar{\gamma}}_{^{3+}\mathrm{Er}} \cdot \mathbf{S}$ in Eq. 3.24:

$$\begin{aligned}\hat{\mathcal{H}}_{\mathrm{hf}}/\hbar = \frac{\mu_0 \gamma_{^{183}\mathrm{W}}}{4\pi r^3}\Big[&\gamma_\perp S_a I_a \left(1 - 3\sin^2\theta_r \cos^2\phi_r\right) \\ &+ \gamma_\perp S_b I_b \left(1 - 3\sin^2\theta_r \sin^2\phi_r\right) \\ &+ \gamma_\parallel S_c I_c \left(1 - 3\cos^2\theta_r\right) \\ &- 3\sin^2\theta_r \cos\phi_r \sin\phi_r \left(\gamma_\perp S_a I_b + \gamma_\perp S_b I_a\right) \\ &- 3\sin\theta_r \cos\phi_r \cos\theta_r \left(\gamma_\perp S_a I_c + \gamma_\parallel S_c I_a\right) \\ &- 3\sin\theta_r \sin\phi_r \cos\theta_r \left(\gamma_\perp S_b I_c + \gamma_\parallel S_c I_b\right)\Big] = \mathbf{S}\cdot\bar{\bar{A}}_S\cdot\mathbf{I}\end{aligned} \tag{3.28}$$

Note that this Hamiltonian is written in the basis of the crystalline axes. The effective spin-1/2 Hamiltonian becomes

$$\hat{\mathcal{H}}_{\frac{1}{2}}/\hbar = \omega_S\, S_{z''} + \omega_I\, I_{z'} + \mathbf{I}\cdot\bar{\bar{Q}}\cdot\mathbf{I} + \mathbf{S}\cdot\bar{\bar{A}}_S\cdot\mathbf{I} \tag{3.29}$$

We note that, given the anisotropy of the electron spin gyromagnetic factor, the quantization axis of the nuclear spin z' and of the electron spin z'' are not necessarily parallel to each other.

Pseudosecular approximation

When ω_S is much larger than the hyperfine interaction strength[6] , $S_{x''}$ and $S_{y''}$ terms have a negligible effect on the wavefunctions. In this pseudosecular approximation, the hyperfine Hamiltonian writes:

$$\hat{\mathcal{H}}_{\mathrm{hf}}/\hbar \approx A_\perp S_{x''} I_{z'} + A_\parallel S_{z''} I_{z'} \tag{3.30}$$

where the x''-axis has been chosen to be parallel to the direction of the perpendicular hyperfine coupling. Intuitively, the pseudosecular approximation can be understood by considering the effects of each term in the Er^{3+} spin Bloch sphere. The dominant Zeeman term induces a precession of the electron spin around the z''-axis with frequency ω_S. By contrast, the hyperfine terms involving $S_{x''}$ and $S_{y''}$ correspond to rotations around the x''- and y''-axes, with much smaller frequencies. Because of the large difference in frequency scales, the transverse rotations effectively average to zero and can be neglected.

We note that the terms $A_\parallel$ and $A_\perp$ appear in the quantization axes basis, which is different from the one in Eq. 3.28. These parameters play an essential role in the experiments as they can be measured through EPR spectroscopy. We compare the measured values with a numerical estimation to perform site assignment of the nuclear spins coupled to the Er^{3+} spin. The numerical estimate is obtained by calculating $\hat{\mathcal{H}}_{\mathrm{hf}}$ and projecting the Hamiltonian into the quantization axes basis using the Frobenius inner product:

$$A_\parallel = \frac{\mathrm{Tr}\{H_{\mathrm{hf}}(S_{z''}I_{z'})^\dagger\}}{\mathrm{Tr}\{S_{z''}I_{z'}(S_{z''}I_{z'})^\dagger\}}, \quad A_\perp = \frac{\mathrm{Tr}\{H_{\mathrm{hf}}(S_{x''}I_{z'})^\dagger\}}{\mathrm{Tr}\{S_{x''}I_{z'}(S_{x''}I_{z'})^\dagger\}}. \tag{3.31}$$

The final spin-1/2 Hamiltonian is

6: This corresponds to

$$|\bar{\bar{\gamma}}_{^{3+}\mathrm{Er}}\cdot\mathbf{B_0}| \gg \bar{\bar{A}}.$$

If the separation between the spins is a, the condition can be approximated as

$$|\mathbf{B_0}| \gg \frac{\gamma_{^{183}\mathrm{W}}\mu_0}{8\pi a^3} \approx 1\ \mathrm{mT}.$$

$$\hat{\mathscr{H}}/\hbar = \omega_S S_{z''} + \omega_I I_{z'} + \mathbf{I}\cdot\bar{\bar{Q}}\cdot\mathbf{I} + A_\perp S_{x''} I_{z'} + A_\parallel S_{z''} I_{z'}, \tag{3.32}$$

In the following two sections we describe the energy level system of this Hamiltonian for the case of ^{183}W and ^{93}Nb nuclear spins respectively. For notational simplicity, the rest of this thesis will denote the spin quantization axes simply by z, omitting the primes used above (z' and z'').

3.6. Nuclear spin $\frac{1}{2}$: Energy states and wavefunctions

We now consider the Hamiltonian of an Er^{3+} spin-1/2 coupled via hyperfine interaction to a ^{183}W nuclear spin while under a magnetic field B_0 (see Figure 3.6a). As described in this chapter, the Hamiltonian of this system is

$$\hat{\mathscr{H}}/\hbar = \omega_S\hat{S}_z + \omega_I\hat{I}_z + A_\parallel\hat{S}_z\hat{I}_z + A_\perp\hat{S}_z\hat{I}_x. \tag{3.33}$$

This Hamiltonian defines a four-level system and the analytical solution is derived in ref. [64]. The resulting energy levels of the system can be described as an admixture of the uncoupled spin states $|\Downarrow\uparrow\rangle$, $|\Downarrow\downarrow\rangle$, $|\Uparrow\uparrow\rangle$, $|\Uparrow\downarrow\rangle$:

[64]: Schweiger et al. (2001), *Principles of Pulse Electron Paramagnetic Resonance*

$$\begin{aligned}
|1\rangle &= \cos\left(\tfrac{\eta_\Uparrow}{2}\right)|\Uparrow\uparrow\rangle - \sin\left(\tfrac{\eta_\Uparrow}{2}\right)|\Uparrow\downarrow\rangle,\\
|2\rangle &= \sin\left(\tfrac{\eta_\Uparrow}{2}\right)|\Uparrow\uparrow\rangle + \cos\left(\tfrac{\eta_\Uparrow}{2}\right)|\Uparrow\downarrow\rangle,\\
|3\rangle &= \cos\left(\tfrac{\eta_\Downarrow}{2}\right)|\Downarrow\uparrow\rangle - \sin\left(\tfrac{\eta_\Downarrow}{2}\right)|\Downarrow\downarrow\rangle,\\
|4\rangle &= \sin\left(\tfrac{\eta_\Downarrow}{2}\right)|\Downarrow\uparrow\rangle + \cos\left(\tfrac{\eta_\Downarrow}{2}\right)|\Downarrow\downarrow\rangle.
\end{aligned} \tag{3.34}$$

where $\eta_\Uparrow$ and $\eta_\Downarrow$ correspond to the mixing angles

$$\eta_\Uparrow = \arctan\left(\frac{-A_\perp}{A_\parallel + 2\omega_I}\right), \qquad \eta_\Downarrow = \arctan\left(\frac{-A_\perp}{A_\parallel - 2\omega_I}\right). \tag{3.35}$$

However, in the high-field regime, both $\eta_\Uparrow \approx -\eta_\Downarrow \approx -A_\perp/2\omega_I \ll 1$ and the energy levels are close to the unperturbed states (see Figure 3.6b).

It is useful to separate the transitions of this system into three groups.

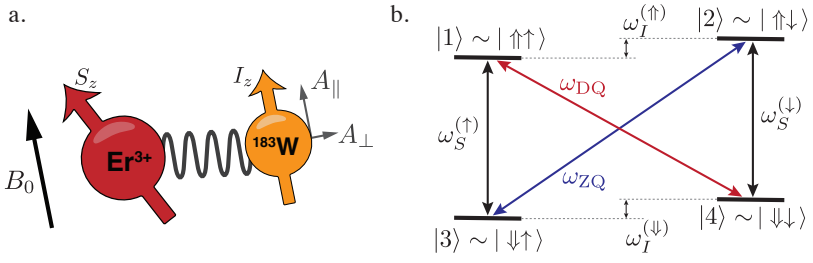

Figure 3.6.: a. ^{183}W-Er^{3+} coupled system. The Er^{3+} spin (red) interacts with a ^{183}W spin (orange) through the hyperfine interaction. The quantization axis of the spins S_z and I_z differ from each other due to the anisotropy of the Er^{3+} gyromagnetic tensor. **b.** Energy level diagram of the coupled system in the high field regime approximation. Allowed EPR transitions are shown with a black arrow while zero-quantum and double-quantum transitions are shown with blue and red arrows respectively.

NMR transitions These correspond to $|1\rangle \leftrightarrow |2\rangle$ and $|3\rangle \leftrightarrow |4\rangle$. The state of the nuclear spin can be controlled by resonantly driving these transitions, with frequencies given by

$$\begin{aligned}\omega_I^{(\Uparrow)} &= \left(\omega_I + \frac{A_\parallel}{2}\right)\cos\eta_\Uparrow - \frac{A_\perp}{2}\sin\eta_\Uparrow \approx \omega_I + \frac{A_\parallel}{2},\\ \omega_I^{(\Downarrow)} &= \left(\omega_I - \frac{A_\parallel}{2}\right)\cos\eta_\Downarrow - \frac{A_\perp}{2}\sin\eta_\Downarrow \approx \omega_I - \frac{A_\parallel}{2}.\end{aligned} \tag{3.36}$$

The frequency of these transitions generally lies in the radio-frequency range. We note that the two frequencies differ by $A_\parallel$, depending on whether the electron spin is in the excited or the ground state, respectively.

EPR transitions The EPR-allowed transitions couple $|1\rangle \leftrightarrow |3\rangle$ and $|2\rangle \leftrightarrow |4\rangle$ and have the following frequencies,

$$\begin{aligned}\omega_S^{(\uparrow)} &= \omega_S + \frac{1}{2}\left(\omega_I^{(\Uparrow)} - \omega_I^{(\Downarrow)}\right) \approx \omega_S + \frac{A_\parallel}{2},\\ \omega_S^{(\downarrow)} &= \omega_S - \frac{1}{2}\left(\omega_I^{(\Uparrow)} - \omega_I^{(\Downarrow)}\right) \approx \omega_S - \frac{A_\parallel}{2}.\end{aligned} \tag{3.37}$$

Analogously to the NMR-allowed transitions, they are spectrally separated and depend on the state of the nuclear spin, which we denote with a superscript.

Zero- and double-quantum transitions Historically named "forbidden" transitions[7], the admixture of the wavefunctions weakly allows transitions that simultaneously change the state of the two spins. Depending on their frequency with respect to the EPR transitions, they receive the name of zero-quantum (ZQ) and double-quantum (DQ) transitions or simply blue and red sidebands. The names ZQ and DQ indicate the net change in the total magnetic quantum number: in a ZQ transition the electron and nuclear spins flip in opposite directions, while for a DQ transition they flip in the same direction. The transitions couple $|3\rangle \leftrightarrow |2\rangle$ and $|1\rangle \leftrightarrow |4\rangle$ and are shown in Figure 3.6b as blue and red arrows respectively. Their frequency is given by

$$\begin{aligned}\omega_{\mathrm{ZQ}} &= |\omega_S^{(\uparrow)}| + |\omega_I^{(\Uparrow)}| \approx \omega_S + \omega_I,\\ \omega_{\mathrm{DQ}} &= |\omega_S^{(\downarrow)}| - |\omega_I^{(\Uparrow)}| \approx \omega_S - \omega_I.\end{aligned} \tag{3.38}$$

The ZQ and DQ transitions are approximately detuned from the electron spin transitions by the Larmor frequency of the nuclear spin. As such, it is possible to drive the nuclear spin transitions with a microwave pulse [27]. Electron-Electron-Double-Resonance (ELDOR) detected NMR (EDNMR) techniques routinely leverage these transitions to probe hyperfine structure in a broad range of systems [65].

In conclusion, the ^{183}W -Er^{3+} coupled system displays two EPR and two NMR-allowed transitions which individually change the state of the electron and nuclear spins, respectively. In addition, the perpendicular

7: We refrain from using this nomenclature, as they can be evidently driven, which makes them "unforbidden" transitions.

[27]: Schosseler et al. (1994), 'Pulsed ELDOR Detected NMR'

[65]: Goldfarb (2017), 'ELDOR-Detected NMR'

hyperfine coupling mixes the nuclear spin wavefunctions, which enables driving of the ZQ and DQ transitions and modifies the state of the electron and nuclear spin simultaneously.

3.7. Quadrupolar nucleus: Energy states and wavefunctions

In Chapter 9 we report the observation of an Er^{3+} electron spin coupled to a ^{93}Nb nuclear spin $I = 9/2$. The Hamiltonian for this system extends the ^{183}W–Er^{3+} model by including the nuclear electric quadrupole interaction, which is present for all nuclei with $I \geq 1$ (see Section 3.3), and is given by

$$\hat{\mathcal{H}}/\hbar = \omega_S \hat{S}_z + \omega_I \hat{I}_z + A_\parallel \hat{S}_z \hat{I}_z + A_\perp \hat{S}_z \hat{I}_x + \hat{\mathbf{I}} \cdot \bar{\bar{Q}} \cdot \hat{\mathbf{I}}. \tag{3.39}$$

This Hamiltonian yields twenty energy levels, illustrated in Figure 3.7. Under the pseudosecular approximation the electron spin projection m_S is a good quantum number, so the full manifold effectively separates into two submanifolds ($m_S = \Uparrow, \Downarrow$) of ten nuclear spin levels each. By contrast, the nuclear spin states are influenced by both the hyperfine coupling and the electric quadrupole interaction, which mix states with different m_I.

In Chapter 9 the nuclear Zeeman term still dominates the interaction, so most eigenstates are well approximated by the magnetic quantum number m_I, but the quadrupolar interaction produces noticeable mixing for the lower-frequency levels. We label the nuclear eigenstates by $n \in \{0, 1, \ldots, 9\}$ in order of increasing energy (see Figure 3.7).

We now describe the energy levels and provide approximate analytical expressions for the transition frequencies that shall be useful in Chapter 5 & 9. Furthermore, we simplify the interaction by taking the specific quadrupole interaction measured in Chapter 9, where one of the principal axes is approximately parallel to both the c-axis and B_0. Under this approximation, the quadrupole Hamiltonian (given by Eq. 3.23) can be written as

$$\begin{aligned} \hat{\mathcal{H}}_Q/\hbar &= \frac{\omega'_Q}{6}\left[3\hat{I}_z^2 + \frac{\eta'}{2}(e^{-2i\alpha}\hat{I}_+^2 - e^{2i\alpha}\hat{I}_-^2)\right] \\ \omega'_Q &= -\frac{\eta+1}{2}\,\omega_Q, \\ \eta' &= \frac{\eta-3}{1+\eta}. \end{aligned} \tag{3.40}$$

where α is the angle between the Z-axis and the x-axis. The Hamiltonian of the system can be approximated by

$$\begin{aligned} \hat{\mathcal{H}}/\hbar = \omega_S \hat{S}_z + \omega_I \hat{I}_z + A_\parallel \hat{S}_z \hat{I}_z + A_\perp \hat{S}_z \hat{I}_x + \\ + \frac{\omega'_Q}{6}\left[3\hat{I}_z^2 + \frac{\eta'}{2}(e^{-2i\alpha}\hat{I}_+^2 - e^{2i\alpha}\hat{I}_-^2)\right]. \end{aligned} \tag{3.41}$$

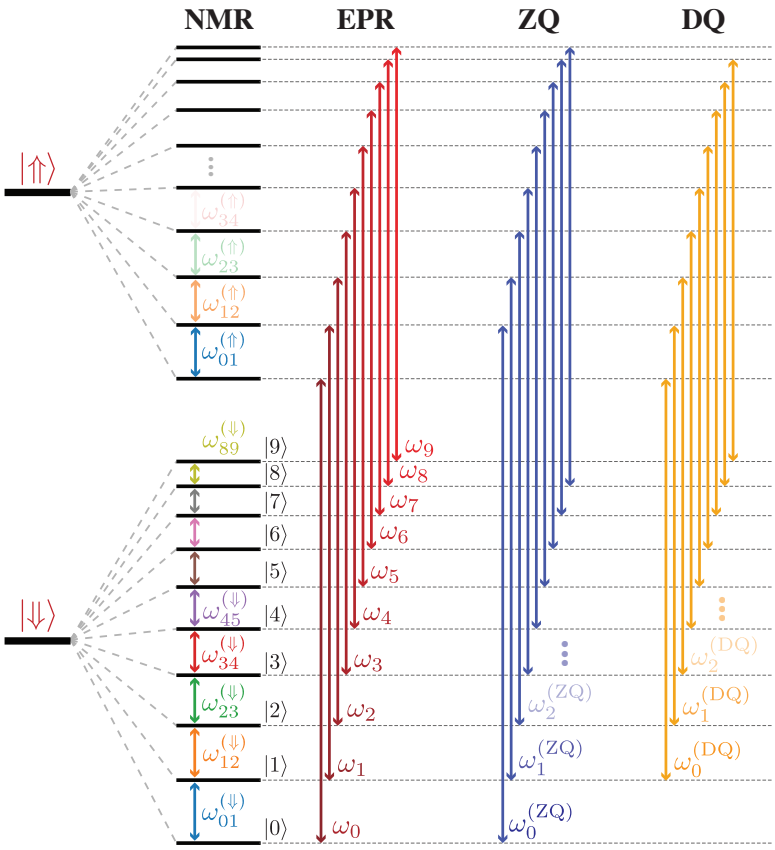

Figure 3.7.: Energy level diagram of an Er^{3+} coupled to a ^{93}Nb nuclear spin-9/2. The twenty energy levels are separated into two manifolds, depending on the state of the electron spin. In order, the following transitions are represented as arrows: NMR-allowed in multiple colors, EPR-allowed in red, ZQ in blue, and DQ in orange.

We now give an estimation of the electron and nuclear spin allowed transition frequencies at first order. In this limit, the nuclear spin wavefunctions are well approximated by the magnetic spin number $m_I = 9/2 - n$. There are ten allowed transitions for the electron spin whose frequency depends on the nuclear spin state n,

$$\omega_n \approx \omega_S + m_I A_\parallel = \omega_S + \left(\tfrac{9}{2} - n\right) A_\parallel , \tag{3.42}$$

Second-order corrections to these frequencies arise from quadrupolar mixing of the nuclear states, but are considerably smaller than the linewidth of the transitions and are not considered in this work.

There are eighteen allowed nuclear spin transitions separated into two manifolds, depending on the state of the Er^{3+} spin. These transitions couple two adjacent nuclear spin levels (n and $n+1$) and, at first order, their frequency is given by[8]

8: Note that $\omega_I < 0$

$$\begin{aligned} \omega_{n(n+1)}^{(\Downarrow)} &= -\omega_I + A_\parallel/2 - \omega'_Q \left((9/2 - n) - \tfrac{1}{2}\right) , \\ \omega_{n(n+1)}^{(\Uparrow)} &= -\omega_I - A_\parallel/2 - \omega'_Q \left((9/2 - n) - \tfrac{1}{2}\right) . \end{aligned} \tag{3.43}$$

In the absence of quadrupole coupling, all nuclear spin transitions would occur at the same frequency, independent of n. In the weak-quadrupole regime, the quadrupole interaction lifts this degeneracy, shifting the transition frequencies linearly with the nuclear spin projection. The state-dependent transition frequencies allow coherent control of the nuclear

spin population between adjacent nuclear spin states without leakage into the rest of the space.

The ZQ and DQ transitions can also be driven in this system, enabled by the perpendicular hyperfine coupling. Each nuclear spin state n has one ZQ and one DQ transition with frequencies $\omega_n^{(\mathrm{ZQ,\,DQ})}$. The exceptions are the edges of the nuclear spin state ladder, $n = 0$ and $n = 9$, for which there is no DQ or ZQ transition, respectively. The transition frequencies are given by

$$\begin{aligned} \omega_n^{\mathrm{ZQ}} &= \omega_n + \omega_{n(n+1)}^{(\Uparrow)} \\ \omega_n^{\mathrm{DQ}} &= \omega_n - \omega_{(n-1)(n)}^{(\Uparrow)} \end{aligned} \tag{3.44}$$

In conclusion, for the ^{93}Nb-Er^{3+} coupled system, there are ten EPR and eighteen NMR-allowed transitions which individually change the state of the electron and nuclear spins, respectively. In the weak-quadrupole regime, the electron spin transitions are spectrally separated by $A_\parallel$ and the nuclear spin transitions are linearly split by the quadrupole. We separate the eighteen nuclear spin transitions into two manifolds, depending on the Er^{3+} state. In addition, the perpendicular hyperfine coupling mixes the nuclear spin wavefunctions, which weakly allows eight ZQ and eight DQ transitions.

Er^{3+} spin coupled to a cavity | 4.

In this chapter we describe the methods used to achieve single spin resolution. Our detection scheme relies on a single microwave photon detector (SMPD) designed and fabricated in-house. By inductively coupling the Er^{3+} spins to a superconducting resonator, we enhance the radiative decay rate of the spins via the Purcell effect. The spontaneously emitted microwave photons are routed into the SMPD, where they are detected.

We begin with a discussion of a superconducting circuit inductively coupled to an Er^{3+} spin, and describe the Purcell effect. We then follow with a qualitative description of the detector and its performance metrics.

4.1 Quantum circuits 37
4.2 Spin-resonator coupling . . 38
Driving the Er^{3+} spin . . . 40
4.3 The effect of the environment 41
Resonator losses 41
Spin losses 42
4.4 Microwave photon counting 44
4.5 Single-spin detection by microwave photon counting 45

4.1. Quantum circuits

We consider a lumped element resonator [66], where the capacitance C and the inductance L can be considered as separate elements (see Figure 4.1). Classically, the energy of the system is given by the voltage V that accumulates on the capacitor and the current I that goes through the inductor

$$E = \frac{1}{2}LI^2 + \frac{1}{2}CV^2 \tag{4.1}$$

This results in a resonant frequency $\omega_r = 1/\sqrt{LC}$ with an impedance of $Z_r = \sqrt{L/C}$, and the Hamiltonian of the classical system is

$$H_r = \frac{Q^2}{2C} + \frac{\phi^2}{2L}, \tag{4.2}$$

where Q is the charge on the capacitor and ϕ is the flux of the inductor[1] the quantization of this Hamiltonian is performed by replacing Q and ϕ with the charge and phase operators ($\hat{Q}$ and $\hat{\phi}$), which obey the following commutation relation: $[\hat{Q}, \hat{\phi}] = i\hbar$. By introducing the creation and annihilation operators ($\hat{a}$ and $\hat{a}^\dagger$) we can write the Hamiltonian of the resonator in second quantization

$$\begin{aligned} \hat{\mathcal{H}}_r/\hbar &= \omega_r(\hat{a}^\dagger\hat{a} + 1/2), \\ \hat{\phi} &= \sqrt{\frac{\hbar Z_r}{2}}(\hat{a}^\dagger + \hat{a}) = \delta\phi(\hat{a}^\dagger + \hat{a}), \\ \hat{Q} &= i\sqrt{\frac{\hbar}{2Z_r}}(\hat{a}^\dagger - \hat{a}) = i\delta Q(\hat{a}^\dagger - \hat{a}), \end{aligned} \tag{4.3}$$

and the eigenstates of the system are the Fock states $|n\rangle$ with associated energy $\hat{\mathcal{H}}_r|n\rangle = \hbar\omega_r(\hat{n} + 1/2)$. The potential as a function of the flux and the energy diagram are represented in Figure 4.2. The Zero Point Fluctuations (ZPF) of the phase and the charge inside of the resonator

[66]: Blais et al. (2020), 'Circuit Quantum Electrodynamics'

1: The charge and flux are related to the voltage and current as

$$I = -\frac{dQ}{dt} = -C\frac{dV}{dt},$$
$$V = \frac{d\phi}{dt} = L\frac{dI}{dt}$$

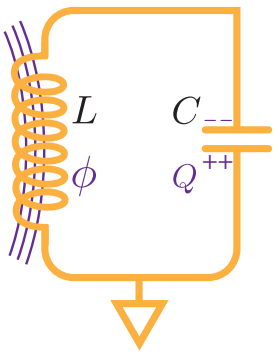

Figure 4.1.: Sketch of a lumped element resonator. The capacitor is defined by the capacitance to ground C and the charge accumulated Q while the inductor by its inductance to ground L and the flux threading the loops ϕ.

($\delta\phi$ and δQ) correspond to the root-mean-square vacuum fluctuations of these quantities. Similarly, the electric and magnetic field generated by the resonator will be given by

$$\begin{aligned}\hat{\mathbf{B}}(\mathbf{r}) &= \boldsymbol{\delta}\mathbf{B}_1(\mathbf{r})\,(\hat{a}^\dagger + \hat{a}),\\ \hat{\mathbf{E}}(\mathbf{r}) &= i\boldsymbol{\delta}\mathbf{E}(\mathbf{r})\,(\hat{a}^\dagger + \hat{a}).\end{aligned} \tag{4.4}$$

The electric and magnetic field have their associated ZPF ($\boldsymbol{\delta}\mathbf{E}(\mathbf{r})$ and $\boldsymbol{\delta}\mathbf{B}_1(\mathbf{r})$). These quantities have a spatial distribution: the magnetic field ZPF will be located close to the inductor and the electric field ZPF will be stronger between the capacitor plates.

Throughout this work, the thermal energy of the system $k_B T$ is consistently lower than the energy of the resonator $\hbar\omega_r$, which ensures that the oscillator is in its vacuum state at thermal equilibrium.

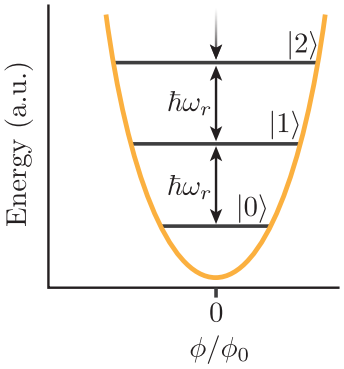

Figure 4.2.: Energy diagram (black) and potential (orange) of a harmonic oscillator with $\phi_0 = h/2e$. The levels are all separated by $\hbar\omega_r$

4.2. Spin-resonator coupling

We now consider a resonator coupled to an individual Er^{3+} spin in the $S = 1/2$ approximation, as described in Section 3.2. The Hamiltonian modeling the interaction between the two can be written as [67]:

[67]: Haroche et al. (2006), *Exploring the Quantum*

$$\hat{\mathscr{H}}/\hbar = \omega_r(\hat{a}^\dagger\hat{a} + 1/2) + \omega_S\hat{S}_z + \hat{\mathscr{H}}_{\text{int}}, \tag{4.5}$$

where $\omega_S = |\mathbf{B_0}\cdot\bar{\bar{\gamma}}_{Er^{3+}}|$ is the Larmor frequency of the spin, and we have arbitrarily chosen the z-axis as the orientation of $\mathbf{B}_0$. The spin couples inductively to the magnetic field generated by the resonator $\mathbf{B}_1$, and the interaction Hamiltonian $\hat{\mathscr{H}}_{\text{int}}$ is given by

$$\hat{\mathscr{H}}_{\text{int}}/\hbar = \hat{\mathbf{B}}_1\cdot\bar{\bar{\gamma}}_{Er^{3+}}\cdot\hat{\mathbf{S}} = (\hat{a}^\dagger + \hat{a})\,\boldsymbol{\delta}\mathbf{B}_1\cdot\bar{\bar{\gamma}}_{Er^{3+}}\cdot\hat{\mathbf{S}}, \tag{4.6}$$

where $\boldsymbol{\delta}\mathbf{B}_1$ are the zero-point fluctuations of the magnetic field at the Er^{3+} spin's position. The Hamiltonian can be re-formulated in terms of the raising and lowering operators [2],

2: Which are defined as
$$\hat{S}_+ = |\Uparrow\rangle\langle\Downarrow|,$$
$$\hat{S}_- = |\Downarrow\rangle\langle\Uparrow|.$$

$$\hat{\mathscr{H}}_{\text{int}}/\hbar = (\hat{a}^\dagger + \hat{a})\,(g_0\hat{S}_+ + g_0\hat{S}_- + \alpha_\Downarrow|\Downarrow\rangle\langle\Downarrow| + \alpha_\Uparrow|\Uparrow\rangle\langle\Uparrow|), \tag{4.7}$$

where g_0 is the coupling strength between the resonator and the spin and $\alpha_\Uparrow$ and $\alpha_\Downarrow$ are energy shifts of the electron spin states, given by

$$\begin{aligned}g_0 &= \langle\Uparrow|\,\boldsymbol{\delta}\mathbf{B}_1\cdot\bar{\bar{\gamma}}_{Er^{3+}}\cdot\hat{\mathbf{S}}\,|\Downarrow\rangle,\\ \alpha_\Uparrow &= \langle\Uparrow|\,\boldsymbol{\delta}\mathbf{B}_1\cdot\bar{\bar{\gamma}}_{Er^{3+}}\cdot\hat{\mathbf{S}}\,|\Uparrow\rangle,\\ \alpha_\Downarrow &= \langle\Downarrow|\,\boldsymbol{\delta}\mathbf{B}_1\cdot\bar{\bar{\gamma}}_{Er^{3+}}\cdot\hat{\mathbf{S}}\,|\Downarrow\rangle.\end{aligned} \tag{4.8}$$

Therefore, g_0 depends on the orientation of $\mathbf{B_1}$, and is maximal when perpendicular to $\mathbf{B_0}$. The Hamiltonian takes a more intuitive form in the rotating frame of the resonator and the spin [67]:

[67]: Haroche et al. (2006), *Exploring the Quantum*

$$\hat{\mathcal{H}}_{\text{int}}/\hbar \approx g_0\left(\hat{a}\hat{S}_+ e^{i(\omega_s-\omega_r)t} + \hat{a}^\dagger \hat{S}_- e^{-i(\omega_s-\omega_r)t}\right). \tag{4.9}$$

where we have considered that the spin and the resonator are close to resonance ($\omega_s - \omega_r$) $\ll \omega_s, \omega_r$, and we have taken the rotating-wave approximation.[3]. In the laboratory frame, the resulting Hamiltonian is given by

$$\hat{\mathcal{H}}_{\text{JC}}/\hbar = \omega_r(\hat{a}^\dagger\hat{a} + 1/2) + \omega_S\hat{S}_z + g_0\left(\hat{a}\hat{S}_+ + \hat{a}^\dagger\hat{S}_-\right), \tag{4.10}$$

also known as the Jaynes-Cummings Hamiltonian [68], which can be used to accurately describe the interaction of a two-level system (be it an atom, a transmon or an electron spin) with a single electromagnetic mode of light. The effect of the interaction term is the coherent exchange of photons between the spin and the resonator.

3: For the rotating-wave approximation to be valid, the interaction strength must also be small compared to the energies of the resonator and the spin

$$g_0 \ll (\omega_s + \omega_r)$$

[68]: Jaynes et al. (1963), 'Comparison of Quantum and Semiclassical Radiation Theories with Application to the Beam Maser'

Coupling strength

As discussed in Section 6.1, the resonator takes the form of two superconducting electrodes shunted by a nanowire. As shown in Eq. 4.8, g_0 is proportional to the gyromagnetic factor of the Er^{3+} along the direction of B_1. Given that the gyromagnetic factor in the (a, b)-plane is ~7 times larger compared to the c-axis (see Eq. 3.10), the inductive element of the resonator is designed as a nanowire parallel to the c-axis. For this geometry, the magnetic field of the nanowire is confined in the (a, b)-plane.

The ZPF of the magnetic field generated by the nanowire can be estimated using the Biot-Savart law,

$$\begin{aligned} \boldsymbol{\delta}\mathbf{B}_1(r) &= \frac{\mu_0}{2\pi r}\delta I \mathbf{u}_\theta, \\ \delta I &= \frac{\delta\phi}{L} = \omega_r\sqrt{\frac{\hbar}{2Z_r}}. \end{aligned} \tag{4.11}$$

where δI are the ZPF of the current and $\mathbf{u}_\theta$ is a unit vector confined to the (a, b)-plane. In the experiments, the $\mathbf{B}_0$ is applied approximately parallel to the c-axis. From Eq. 4.8 we have that the coupling strength is then given by

$$g_0 = \frac{\gamma_\perp\mu_0}{2\pi r}\delta I \langle\Uparrow| \mathbf{u}_\theta \cdot \hat{\mathbf{S}} |\Downarrow\rangle = \frac{\gamma_\perp\mu_0}{4\pi r}\omega_r\sqrt{\frac{\hbar}{2Z_r}}. \tag{4.12}$$

From this equation we conclude the following. First, the closer the spin is to the wire, the more strongly it will be coupled. Second, given that the coupling is inversely proportional to the impedance of the resonator, the design should maximize the capacitance and minimize the inductance, while maintaining the frequency constant. These considerations are addressed in Chapter 6, where we describe the resonator design and characterization.

Driving the Er^{3+} spin

In this section, we derive how a coherent drive on the resonator induces Rabi oscillations of the spin, which naturally reveals the role of the cavity as a Lorentzian filter. We begin by considering the Jaynes-Cummings Hamiltonian, where the resonator is under the effect of a drive with complex amplitude ϵ_d and frequency ω_d

$$\hat{\mathcal{H}}_{\text{JC}}/\hbar = \omega_r\,\hat{a}^\dagger\hat{a} + \frac{\omega_S}{2}\hat{S}_z + g_0(\hat{a}\hat{S}_+ + \hat{a}^\dagger\hat{S}_-) + (\epsilon_d e^{-i\omega_d t}\hat{a}^\dagger + \epsilon_d^* e^{i\omega_d t}\hat{a}), \quad (4.13)$$

where we have dropped the constant 1/2 factor from the resonator energy. In the rotating frame of the drive[4], and applying the rotating-wave approximation, the Hamiltonian becomes time independent and can be written as

$$\hat{\mathcal{H}}_{\text{JC}}/\hbar = \Delta_r\,\hat{a}^\dagger\hat{a} + \frac{\Delta_S}{2}\hat{S}_z + g_0(\hat{a}\hat{S}_+ + \hat{a}^\dagger\hat{S}_-) + (\epsilon_d\hat{a}^\dagger + \epsilon_d^*\hat{a}), \quad (4.14)$$

where $\Delta_r = \omega_r - \omega_d$ and $\Delta_S = \omega_S - \omega_d$. The driving term in the Hamiltonian will induce the cavity to develop a large coherent field α which translates as a non-zero photon occupation. From input-output theory [66], the equation of motion for the coherent state of the resonator under drive is given by

$$\dot{\alpha} = -\left(i\Delta_r + \frac{\kappa}{2}\right)\alpha - i\epsilon_d. \quad (4.15)$$

For the steady state $\dot{\alpha} = 0$,

$$\alpha = -\frac{\epsilon_d}{\Delta_r - i\kappa/2}. \quad (4.16)$$

From this equation, we can see that the resonator behaves as a Lorentzian filter: the coherent amplitude of the resonator is damped at large detunings compared to κ. Given the non-zero cavity field, it is convenient to displace the Hamiltonian to be centered around α by introducing the displacement operator

$$D(\alpha) = \exp\left(\alpha\hat{a}^\dagger - \alpha^*\hat{a}\right), \quad (4.17)$$

which redefines the annihilation operator so that $\hat{a}$ describes only quantum fluctuations around the coherent amplitude. After the transformation, the Hamiltonian becomes

$$\hat{\mathcal{H}}_{\text{JC}}/\hbar = \Delta_r\,\hat{a}^\dagger\hat{a} + \frac{\Delta_S}{2}\hat{S}_z + g_0\left((\hat{a}+\alpha)\hat{S}_x + (\hat{a}^\dagger+\alpha^\dagger)\hat{S}_y\right), \quad (4.18)$$

By reorganizing terms we can distinguish three contributions:

$$\hat{\mathcal{H}}_{\text{JC}}/\hbar = \underbrace{\Delta_r\,\hat{a}^\dagger\hat{a}}_{\text{resonator}} + \underbrace{\frac{\Delta_S}{2}\hat{S}_z + g_0\left(\alpha\hat{S}_+ + \alpha^\dagger\hat{S}_-\right)}_{\text{spin}} + \underbrace{g_0\left(\hat{a}\hat{S}_+ + \hat{a}^\dagger\hat{S}_-\right)}_{\text{coupling}}. \quad (4.19)$$

4: The unitary of the transformation is given by

$$\hat{U}(t) = \exp\left\{i\omega_d t\left(\hat{a}^\dagger\hat{a} + \frac{1}{2}\hat{\sigma}_z\right)\right\}$$

[66]: Blais et al. (2020), 'Circuit Quantum Electrodynamics'

If the amplitude of the coherent state is sufficiently large ($|\alpha| \gg 1$), the coupling interaction between the resonator and the spin can be treated as a perturbation and the dynamics of the spin and the resonator can be disentangled. The resulting Hamiltonian for the spin is

$$\hat{\mathcal{H}}_\mathrm{d}/\hbar = \frac{\Delta_S}{2}\hat{S}_z + \frac{\Omega}{2}\left(\cos\phi\hat{S}_x + \sin\phi\hat{S}_y\right), \tag{4.20}$$

where $\alpha = |\alpha|e^{i\phi}$ and Ω is the Rabi frequency of the drive, given by

$$\Omega = 2g_0|\alpha| = \frac{2g_0\epsilon_d}{\sqrt{\Delta_r^2 + \kappa^2/4}} \propto \frac{\langle\Uparrow|\, S_x\, |\Downarrow\rangle}{\sqrt{\Delta_r^2 + \kappa^2/4}}. \tag{4.21}$$

This corresponds to a driven two-level system Hamiltonian. We note that Ω scales proportionally to the S_x matrix element between the two relevant states and is filtered by a Lorentzian function centered around the cavity frequency. These considerations will be relevant in the following chapter, when treating weakly allowed transitions with small oscillator strength.

If the spin is initially in the ground state, the excited-state population at time t is

$$P_e(t) = \frac{\Omega^2}{\Omega^2 + \Delta_S^2}\sin^2\left(\tfrac{1}{2}\sqrt{\Omega^2 + \Delta_S^2}\, t\right). \tag{4.22}$$

At resonance ($\Delta_S = 0$), this reduces to simple Rabi oscillations

$$P_e(t) = \sin^2\left(\tfrac{\Omega}{2}\, t\right), \tag{4.23}$$

with resonant Rabi frequency given by $\Omega = 2g_0|\alpha| = 4g_0\epsilon_d/\kappa$.

Figure 4.3 shows the quantum trajectory of the spin in the Bloch sphere under the influence of a detuned drive with phase $\phi = 0$. The state evolves from the ground state $|\Downarrow\rangle$ and is coherently excited. Full population transfer to the excited state is only possible when $\Delta_S = 0$.

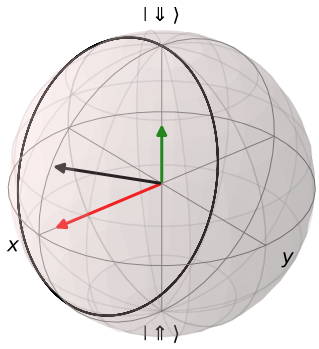

Figure 4.3.: Quantum trajectory of the spin in the Bloch sphere under a coherent drive. The detuning Δ_S and the drive Ω are represented as green and red arrows respectively and the resulting drive vector is shown in black. The trajectory is shown as a black curve.

4.3. The effect of the environment

So far, we have considered a resonator coupled to a spin isolated from the environment. In reality, both the spin and the resonator interact with their environment, which can be modeled with an open-system description. These external degrees of freedom effectively induce energy losses on both the resonator and the spin, as shown in Figure 4.4.

Resonator losses

The resonator is fabricated on the surface of a dielectric and the electromagnetic mode will be partially contained inside the material. Therefore, the energy of the resonator is subject to dielectric losses and will be lost at a rate κ_i. In addition, the resonator is coupled to microwave transmission lines, with which it exchanges energy at a rate κ_c. Therefore, the total loss rate of the resonator is $\kappa = \kappa_i + \kappa_c$. We say the resonator is overcoupled when the total loss is dominated by the capacitive coupling ($\kappa_c > \kappa_i$),

undercoupled when the internal damping dominates ($\kappa_c < \kappa_i$), and critically coupled when they are balanced ($\kappa_c = \kappa_i$).

Spin losses

We differentiate two types of loss mechanisms for the spins: relaxation and decoherence. We now proceed to describe how they manifest on electron and nuclear spins, in particular Er^{3+} and ^{183}W in $CaWO_4$.

Spin relaxation and the Purcell effect

When excited, a spin will spontaneously relax into the ground state by releasing energy to the environment at rate Γ_1, which defines the lifetime $T_1 = \Gamma_1^{-1}$. The spontaneous emission rate of a spin in free space is vanishingly low, $\sim 10^{-12}$ s^{-1} for an electron spin and $\sim 10^{-21}$ s^{-1} for a nuclear spin, which is effectively infinite.

In a crystal, the spin relaxation is dominated by non-radiative decay, where spins exchange energy with the crystal phonons at a rate Γ_{NR}. The strength of this interaction depends on the temperature of the crystal and the frequency of the spins. The non-radiative decay of Er^{3+} at 8 GHz and 10 mK with B_0 along the c-axis has been measured to be $\Gamma_{NR} = 5$ s^{-1} [69]. For ^{183}W nuclear spins in similar conditions, it was in the order of several weeks [70].

[69]: Le Dantec (2022), 'Electron Spin Dynamics of Erbium Ions in Scheelite Crystals, Probed with Superconducting Resonators at Millikelvin Temperatures'

[70]: Wang et al. (2024), *Month-Long-Lifetime Microwave Spectral Holes in an Erbium-Doped Scheelite Crystal at Millikelvin Temperature*

We now consider how coupling the Er^{3+} spin to the resonator modifies the radiative relaxation rate. Depending on the relative magnitude of the coupling g_0 and the resonator loss rates, two regimes can be distinguished.

- *Strong coupling regime*: $g_0 \gg \kappa, \Gamma_2$, where the system coherently exchanges excitations between the spin and the resonator multiple times before dissipating.
- *Weak coupling regime*: $g_0 \ll \kappa, \Gamma_2$, where energy is damped before any coherent oscillations can occur.

As measured in Chapter 6, the total losses of the resonator used in this work are $\kappa/2\pi \approx 700$ kHz. By comparing the losses to the expected coupling to the spins, $g_0/2\pi \approx 10$ kHz $\ll \kappa$, we conclude we are deep in the weak-coupling regime. Nevertheless, the resonator enhances the density of states at the resonant frequency, therefore enhancing the radiative decay rate of any resonant Er^{3+} spin via the Purcell effect [71]. The Purcell radiative relaxation rate[5] is given by

[71]: Purcell et al. (1946), 'Resonance Absorption by Nuclear Magnetic Moments in a Solid'

5: An in-depth derivation of the Purcell effect can be found in [67].

$$\Gamma_R(\omega_S) = \frac{g_0^2 \kappa}{(\omega_r - \omega_S)^2 + \kappa^2/4}. \tag{4.24}$$

Moreover, the spin undergoes a frequency shift (the Lamb shift)

$$\Delta\omega(\omega_S) = (\omega_r - \omega_S) \frac{g_0^2}{(\omega_r - \omega_S)^2 + \kappa^2/4}. \tag{4.25}$$

At exact resonance ($\omega_r = \omega_S$) the shift vanishes and the Purcell rate is given by $\Gamma_R = 4g_0^2/\kappa$. Using the parameter estimates above gives $\Gamma_R \sim 10^3$ s^{-1}, which is several orders of magnitude larger than Γ_{NR}. Consequently, the main relaxation mechanism for resonant Er^{3+} spins

becomes radiative. The resulting microwave photons can either be dissipated due to material losses or sent to the coupled microwave lines, depending on the ratio between κ_i and κ_c.

Spin decoherence

In the solid state, both electron and nuclear spins interact magnetically with one another, as discussed in Section 3.4. These interactions can be described as an effective magnetic field generated by the surrounding spin bath at the position of the central spin. Due to the dynamics of the bath, such as spin flip-flop processes or slow environmental fluctuations, this effective field varies in time. As a consequence, the Larmor frequency of the central spin becomes time-dependent, which results in a loss of phase coherence and an effective broadening of the single-spin resonance linewidth. In addition, fluctuations on the static magnetic field will also induce a similar effect. This phenomenon is known as spectral diffusion and is associated with a dephasing time given by T_2^*, which can be measured through a Ramsey sequence.

Given that magnetic noise spans multiple timescales, the measured value of T_2^* depends on the total measurement duration. To illustrate this, consider a magnetic field that fluctuates on the timescale of hours. A Ramsey experiment averaged over only a few minutes will effectively experience a static magnetic field and therefore will not suffer additional dephasing from these slow fluctuations. In contrast, if the same measurement is averaged over several days, successive averages will sample different magnetic field values. This results in an increase in spectral diffusion and a reduced value of T_2^*.

A way to suppress the effect of slow noise is to refocus the spin coherence using a Hahn echo sequence. This yields an echo coherence time T_2 that is longer than the Ramsey dephasing time, $T_2 \geq T_2^*$. Therefore, one can define a transverse decoherence rate $\Gamma_2 = 1/T_2$. Since energy relaxation contributes to decoherence, Γ_2 is bounded by $\Gamma_2 \geq \Gamma_1/2$. When $\Gamma_2 \approx \Gamma_1/2$ the spin is said to be lifetime-limited, as it does not visibly suffer any decoherence before energy relaxation.

Spectral diffusion can be suppressed by reducing the density of paramagnetic impurities and nuclear spins. In this context, Er^{3+} :$CaWO_4$ has demonstrated extraordinarily long ensemble coherence times of 23 ms [26]. In the single-spin regime with a Purcell-limited lifetime of approximately 1 ms, the decoherence time was lifetime limited. This achievement was possible due to two factors. First, the low concentration of erbium and other paramagnetic impurities, on the order of parts per billion (ppb). In

[26]: Le Dantec et al. (2021), 'Twenty-Three–Millisecond Electron Spin Coherence of Erbium Ions in a Natural-Abundance Crystal'

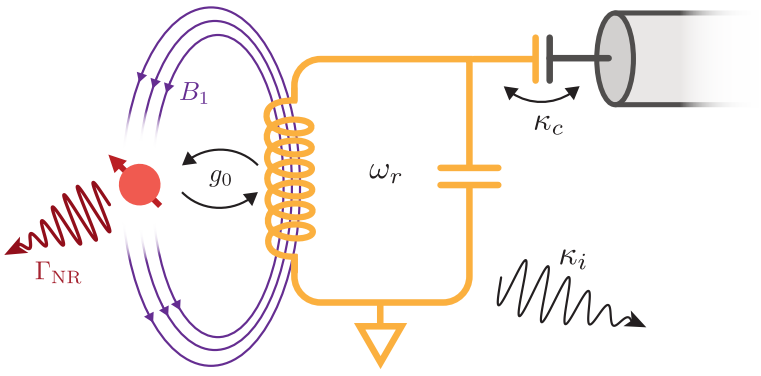

Figure 4.4.: Resonator inductively coupled to a single electron spin. The resonator has two loss mechanisms: internal losses κ_i and energy exchange with the capacitively coupled lines κ_c and interacts with a spin with coupling strength g_0. The spin can decay via phonon relaxation with a rate κ_{phonon}

this regime, the average distance between impurities is much larger than the magnetic dipole interaction range and their contribution to spectral diffusion can be neglected. Second, $CaWO_4$ has one of the lowest nuclear magnetic moment densities among natural-abundance crystals. Only the ^{183}W isotope has a non-negligible abundance (14.4%), with nuclear spin $I = 1/2$ and a relatively weak gyromagnetic ratio (see Section 3.3).

Based on the electron decoherence time in $CaWO_4$, we expect second-long coherence times for the ^{183}W nuclear spins, given the ratio of their gyromagnetic ratios ($\sim 10^3$). In Chapter 8, we measure the nuclear spin coherence and find $T_2^* \approx 1\ s$, in agreement with the expected value.

In addition, nuclear polarization can be used to reduce spectral diffusion when the nuclear spin flip-flop rate is smaller than the measurement rate. In Section 7.6, we explore dynamical nuclear polarization (DNP) using a single spin and in Chapter 9 we demonstrate the decoherence reduction using DNP.

Finally, an additional source of spectral diffusion is fluctuations of the static magnetic field, which arise from the intrinsic noise of the current source driving the coil. We mitigate this by using superconducting coils that are set in persistent-current mode, where the current source is effectively disconnected (see Section 6.2). This results in a substantial increase in field stability.

4.4. Microwave photon counting

Single-electron spin sensitivity has been recently demonstrated in our group through the use of a unique device known as the Single Microwave Photon Detector (SMPD) [23]. The device is based on a superconducting circuit, designed to detect individual microwave photons with high efficiency in a narrow frequency bandwidth [21]. The device consists of a transmon qubit coupled to two coplanar waveguide resonators, called the *buffer* and the *waste* resonators. The incoming photon arrives in the buffer resonator and is converted to an excitation in the qubit and the waste through a parametric process controlled by a pump tone. The waste is strongly coupled to the microwave lines and the excitation on this resonator is rapidly dissipated, rendering the process irreversible. Finally, the state of the qubit is measured via dispersive readout through the waste resonator. The qubit is conditionally reset with a π-pulse and subsequently read out until it is measured in its ground state. This process is repeated cyclically.

[23]: Wang (2023), 'Addressing Individual Electronic Spins with a Microwave Superconducting Resonator'

[21]: Lescanne et al. (2020), 'Irreversible Qubit-Photon Coupling for the Detection of Itinerant Microwave Photons'

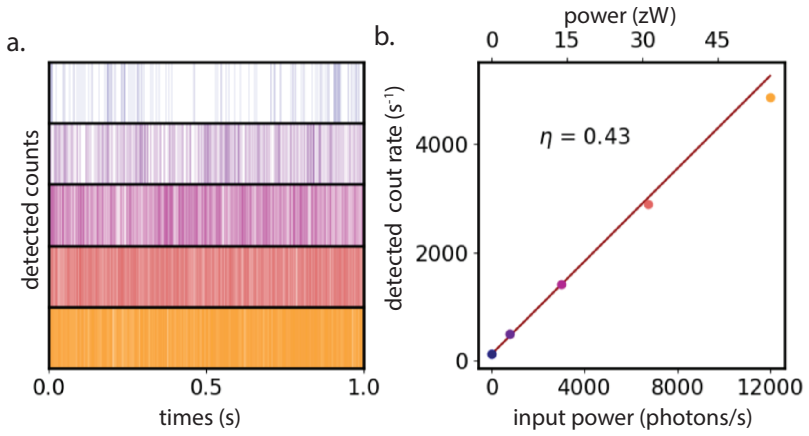

Figure 4.5.: Operational efficiency of an SMPD. The figure was taken from [72]. **a.** Time traces representing one second of detection (≈80000 cycles) for different powers applied to the buffer. Each line represents a click. **b.** Number of clicks per second as the function of the number of incoming photons. The fit (orange line) allows to extract the overall efficiency $\eta_d = 0.43$.

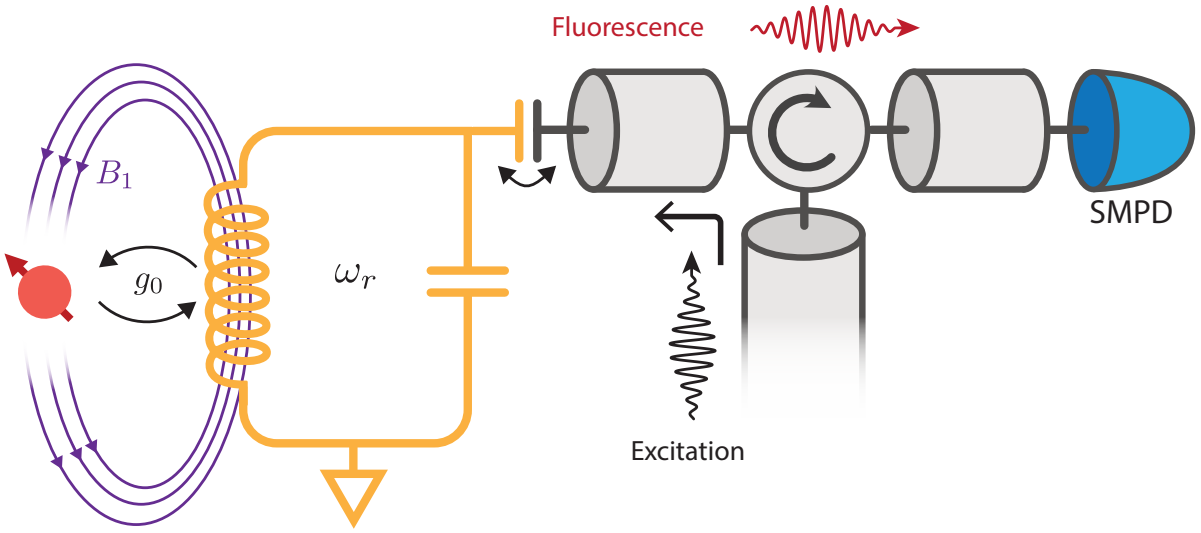

Figure 4.6.: Detection Scheme. A microwave pulse (black arrow) is sent to the superconducting resonator (orange), fabricated on the surface of a $CaWO_4$ crystal, which excites a resonant Er^{3+} spin (red). Via the Purcell effect, the spontaneous microwave emission (red arrow) is collected in the microwave lines and routed through a circulator to the SMPD where it is detected as a count.

For our purposes, we now discuss the relevant performance metrics: the dark count rate Γ_{DC} and the detection efficiency η_d. Appendix B gives a concise explanation of the operation and characteristics of the device.

The quantum efficiency of the detector is the ratio between the number of counts and the number of incoming photons. The dark count rate is the count rate when the device is operated without any input signal. Its origin can be traced back to two main effects: spurious qubit excitations and thermal photons on the microwave lines. Figure 4.5a shows a series of traces as a function of calibrated input power: at zero power, the detection events correspond to the dark count rate of the detector, as the power increases, the number of counts also does so, until the detector saturates. We measure the efficiency of the detector by fitting the number of detection events as a function of the calibrated input power with a linear curve (see Figure 4.5b).

The data shown in Figure 4.5 correspond to the previous generation SMPD fabricated by Leo Balembois [72]. The detector used in this work was designed, fabricated and characterized by Louis Pallegoix and an in depth study can be found in [25, 73]. The main improvement of this design with respect to the previous generation is the tunable input bandwidth between ~100 kHz and ~1 MHz. In this work we operate at ~ 300 kHz, where the detection efficiency is approximately $\eta_d \approx 0.8$ and the dark count rate fluctuates between $\Gamma_{DC} \approx 50$–100 counts/s.

[72]: Balembois et al. (2024), 'Cyclically Operated Microwave Single-Photon Counter with Sensitivity of 10^(-22) W / √Hz'

[25]: Pallegoix (2025), 'High Performance Microwave Photon Counter and Application to Single Spin Magnetic Resonance'

[73]: Pallegoix et al. (2025), *Enhancing the Sensitivity of Single Microwave Photon Detection with Bandwidth Tunability*

4.5. Single-spin detection by microwave photon counting

Most of the measurements shown in this manuscript are performed by monitoring the Purcell enhanced microwave fluorescence of the Er^{3+} spin after a resonant excitation using the SMPD. Unlike traditional single-spin readout methods that rely on spin-dependent optical fluorescence [74] or on transport-based spin-to-charge conversion (STM [75] or quantum-dot readout [76]), microwave photon counting operates entirely in the

[74]: Wrachtrup et al. (1993), 'Optical Detection of Magnetic Resonance in a Single Molecule'

[75]: Elzerman et al. (2004), 'Single-Shot Read-out of an Individual Electron Spin in a Quantum Dot'

[76]: Rugar et al. (2004), 'Single Spin Detection by Magnetic Resonance Force Microscopy'

microwave regime and does not require system specific mechanisms like optical transitions or spin-to-charge conversion.

The measurement scheme is summarized by the diagram presented in Figure 4.6. The crystalline $CaWO_4$ sample, where the Er^{3+} spins are hosted, takes the form of a rectangular monocrystalline slab. On the surface of the crystal, a superconducting Nb thin film resonator is fabricated. The Er^{3+} spins are inductively coupled to the resonator through the magnetic field generated by the nanowire inductive element, thereby enhancing their radiative relaxation rate via the Purcell effect. A microwave pulse is generated at room temperature with a frequency that is resonant with the cavity. If an Er^{3+} spin is resonant with the cavity, it will be excited by the pulse. Following the excitation, the spin will spontaneously relax into a microwave photon, routed with a microwave circulator to the SMPD, where it is detected. The *spin-to-click* efficiency η_{spin} depends on the SMPD efficiency, the ratio between the coupling and total loss of the resonator and the attenuation of the microwave line connecting the two.

Nuclear spin control via microwaves

5.

This chapter is focused on the specific techniques used to achieve coherent control of a nuclear spin coupled to an Er^{3+} spin. We distinguish two sections in this chapter: the first part focuses on an Er^{3+} spin coupled to a single ^{183}W nuclear spin, which constitutes the bulk of the nuclear spin environment in $CaWO_4$. We discuss resonant driving of the ZQ/DQ transition and introduce microwave stimulated Raman transitions for the case of a nuclear spin $I = 1/2$. The second part generalizes these results to a quadrupolar nuclear spin $I > 1/2$, which will be used in Chapter 9 to control a ^{93}Nb nuclear spin with $I = 9/2$.

5.1 Driving a ^{183}W nuclear spin through the Er^{3+} spin . . . 47
Zero- and double-quantum transitions 47
AC-Zeeman shifts 48
Cross-relaxation probability 49
Stimulated Raman driving 50
5.2 High-spin generalization . 52
Zero- and double-quantum transitions 52
Cross-relaxation rates . . . 54
Stimulated Raman driving 55
5.3 Summary 55

This chapter is focused on the derivation of the Rabi rates for the different nuclear spin driving techniques. Readers seeking an overview of the essential results may wish to consult Section 5.3 first, as it contains a summary of the results of this chapter.

5.1. Driving a ^{183}W nuclear spin through the Er^{3+} spin

If one wishes to drive the state of a nuclear spin, the most straightforward way is to apply a radiofrequency (rf) pulse resonant with the allowed NMR transitions. However, the superconducting resonator in our setup acts as a narrow band-pass filter centered around $\omega_r \approx 7.7$ GHz, as detailed in Section 4.2. Consequently, all rf drives applied to the sample will be reflected from the resonator and direct driving of a nuclear spin is impossible in our setup. We now proceed to discuss two different methods that can be used to drive a nuclear spin using only microwave pulses.

Zero- and double-quantum transitions

The Er^{3+} spin is resonant with the cavity when the magnitude of the magnetic field along the c-axis is $B_0 \approx 0.45$ T. At this field, the Larmor frequency of ^{183}W is $\omega_I \approx 800$ kHz. The ZQ and DQ transitions are detuned from the EPR-allowed transitions by this frequency, and can therefore be driven with a microwave tone (see Figure 5.1b). As these transitions simultaneously change the state of both spins, resonant driving of the ZQ and DQ transitions is a valid strategy to control the coupled nuclear spin.

We now proceed to derive the Rabi rate of ZQ and DQ transitions when resonantly driven. We begin by recalling the spin Hamiltonian in the high-field regime derived in Section 3.6:

$$\hat{\mathcal{H}}/\hbar = \omega_S \hat{S}_z + \omega_I \hat{I}_z + A_\parallel \hat{S}_z \hat{I}_z + A_\perp \hat{S}_z \hat{I}_x. \tag{5.1}$$

As seen in Section 3.6, this Hamiltonian defines a four level system, shown in Figure 5.1a. The energy levels are given by

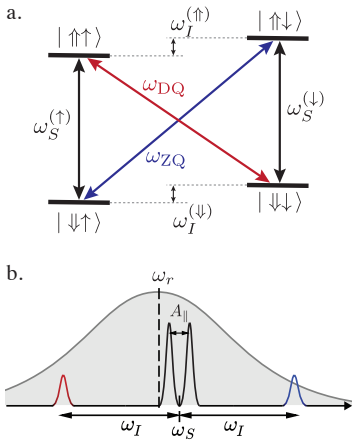

Figure 5.1.: a. Energy level diagram of an Er^{3+} coupled to a nuclear spin-1/2. Electron spin transitions are marked with a black arrow while zero and double quantum transitions are marked with blue and red arrows respectively. **b.** Schematic of the transitions, superimposed with the resonator response shown as a gray Lorentzian of FWHMκ. Allowed transitions (black peaks) are quasi-resonant with ω_r, forbidden transitions (red and blue) are detuned by $\sim \omega_I$

$$
\begin{aligned}
|1\rangle &\approx \tfrac{1}{\mathcal{N}}\left(|\Uparrow\uparrow\rangle + \tfrac{A_\perp}{4\omega_I}|\Uparrow\downarrow\rangle\right),\\
|2\rangle &\approx \tfrac{1}{\mathcal{N}}\left(|\Uparrow\downarrow\rangle - \tfrac{A_\perp}{4\omega_I}|\Uparrow\uparrow\rangle\right),\\
|3\rangle &\approx \tfrac{1}{\mathcal{N}}\left(|\Downarrow\uparrow\rangle - \tfrac{A_\perp}{4\omega_I}|\Downarrow\downarrow\rangle\right),\\
|4\rangle &\approx \tfrac{1}{\mathcal{N}}\left(|\Downarrow\downarrow\rangle + \tfrac{A_\perp}{4\omega_I}|\Downarrow\uparrow\rangle\right),
\end{aligned}
\tag{5.2}
$$

where $\mathcal{N}$ is a normalization constant. The eigenstates therefore correspond to the uncoupled product states with a small admixture of the opposite nuclear spin component. This mixing produces a small, but nonzero, $\hat{S}_x$ matrix elements:

$$
\langle 1|\,\hat{S}_x\,|4\rangle \approx -\langle 2|\,\hat{S}_x\,|3\rangle \approx \frac{A_\perp}{4\omega_I} \ll 1. \tag{5.3}
$$

Therefore, the zero- and double-quantum transitions $|1\rangle \leftrightarrow |4\rangle$ and $|2\rangle \leftrightarrow |3\rangle$, which are strictly forbidden in the absence of mixing, become weakly allowed with oscillator strength on the order of $A_\perp/(4\omega_I)$, much smaller than that of the allowed EPR transitions:

$$
\langle 1|\,\hat{S}_x\,|3\rangle \approx \langle 2|\,\hat{S}_x\,|4\rangle \approx 1/2, \tag{5.4}
$$

The Rabi rate of an allowed EPR transition when resonant with the cavity is given in Section 4.2 by $\Omega = 4g_0\epsilon_d/\kappa$, where ϵ_d is the applied microwave amplitude. To obtain the ZQ and DQ Rabi rates at the *same* drive amplitude, we simply rescale Ω by the ratio of the relevant matrix elements. Including the cavity filtering (the sideband is detuned from the cavity by $\sim \omega_I$) gives the final ZQ/DQ Rabi rate

$$
\Omega_{\mathrm{ZQ}} \approx \Omega_{\mathrm{DQ}} \approx \Omega \cdot \frac{A_\perp}{2\omega_I} \cdot \frac{1}{\sqrt{1 + 4\omega_I^2/\kappa^2}}. \tag{5.5}
$$

Because the matrix elements and the cavity filtering are nearly the same for the ZQ and DQ sidebands, their driven Rabi rates are essentially equal. This equation will be used in the analysis of the experimental results to extract the value of $A_\perp$.

We note that sideband driving necessarily involves populating the electron spin excited state, so the operation is limited by the much faster electron dephasing time T_2^* rather than by the long nuclear coherence. Consequently, the electron spin decoherence rate imposes a fundamental limit on the fidelity of nuclear spin gates implemented via sideband drives.

AC-Zeeman shifts

When the drive amplitude on a two-level system becomes large enough, the fast-rotating terms that are ignored in the rotating-wave-approximation (see (refsec)) will shift the energy levels [77]. This is known as the Bloch-Siegert shift. In the case when the drive is not resonant from the transition frequency it also receives the name of AC-Stark shift. Given that, in our

[77]: Cohen-Tannoudji et al. (2024), *Atom - Photon Interactions*

system, the driving is performed through a magnetic field, we will refer to this effect as the AC-Zeeman shift.

When a microwave pulse with amplitude[1] Ω and frequency $\omega_d = \omega_S + \Delta$ is applied to a single electron spin, the transition frequency is shifted by

$$\delta\omega_{\mathrm{AC}} = -\frac{\Omega^2}{2\Delta}, \tag{5.6}$$

This results in a smaller frequency when $\Delta > 0$ and *vice versa*.

We now address the AC-Zeeman shifts occurring when driving the forbidden ZQ or DQ transitions. As described in Section 3.6, there are six different transitions in this system: two EPR-allowed, two NMR-allowed, and the ZQ and DQ transitions. Under an off-resonant drive, *all* the transitions are shifted following Eq. 5.6. The total shift of the ZQ and DQ transitions can be calculated by independently considering the effect of the drive on each transition:

- Both EPR-allowed transitions are shifted by the presence of the off-resonant drive by

$$\delta\omega_{\mathrm{AC}}^{\uparrow} = -\frac{\Omega^2}{2\Delta - A_{\parallel}}, \quad | \quad \delta\omega_{\mathrm{AC}}^{\downarrow} = -\frac{\Omega^2}{2\Delta + A_{\parallel}}, \tag{5.7}$$

- The AC-Zeeman shift is proportional to the matrix element of the transition [67]. As calculated in Section 3.6, the matrix elements of the ZQ and DQ transitions are very small compared to the EPR-allowed transitions. Therefore, the *direct* shift is negligible.
- The NMR-allowed transitions are not significantly shifted as they are far too detuned with respect to the frequency of the drive.

Even if the direct shift of the ZQ and DQ transitions is negligible, the effect of the drive on the EPR-allowed transitions creates an effective shift on the ZQ and DQ transition frequencies, as shown in Figure 5.2. This shift is given by

$$\delta_{ZQ,DQ}(\Omega) = \mp\frac{1}{2}\left(\delta\omega_{\mathrm{AC}}^{(\uparrow)} + \delta\omega_{\mathrm{AC}}^{(\downarrow)}\right) \approx \mp\frac{1}{2}\left(\frac{\Omega^2}{2\omega_I^{(\Uparrow)}} + \frac{\Omega^2}{2\omega_I^{(\Downarrow)}}\right). \tag{5.8}$$

This approximation holds when the induced AC-Zeeman shifts are small compared to the intrinsic sideband detuning, ($|\delta_{ZQ,DQ}| \ll \omega_I$) so that the drive frequency remains effectively unchanged with respect to the unperturbed ZQ/DQ transitions.

1: From here onwards, we characterize the amplitude of a microwave pulse by the equivalent Rabi frequency on resonance

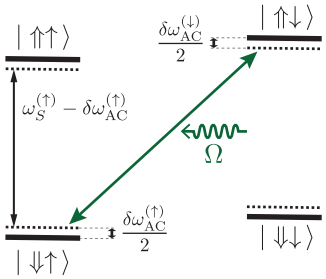

Figure 5.2.: AC Zeeman shift diagram. Driving the ZQ transition induces AC-Zeeman shifts on the electron spin transitions ($\delta\omega_{\mathrm{AC}}^{(\uparrow)}$, $\delta\omega_{\mathrm{AC}}^{(\downarrow)}$), which modify the resonance condition for the sideband transition.

Cross-relaxation probability

We now consider all possible relaxation mechanisms for the electron spin in the ^{183}W–Er^{3+} coupled system. Due to the coupling to the superconducting resonator, the main relaxation mechanism is spontaneous emission through the EPR-allowed transitions. The decay rate of this process is given by $\Gamma_{\mathrm{R}} = 4g_0^2/\kappa$ when the spin is in resonance with the cavity $\omega_S = \omega_r$ (see Section 4.2). In this event the state of the nuclear spin is preserved as these transitions only involve the electron spin. However, the small ZQ and DQ matrix elements allow the Er^{3+} spin to relax through any of these transitions, albeit with a much reduced decay

rate. Through any of these cross-relaxation events, the state of both spins is simultaneously changed. Spontaneous emission through the ZQ and DQ transitions is also strongly enhanced by the Purcell effect. Their decay rate can be estimated by considering the Purcell effect on the ZQ and DQ transitions and rescaling by the relevant matrix element

$$\begin{aligned}\Gamma_{\mathrm{ZQ}} &= \frac{g_0^2\kappa}{(\omega_r-\omega_{\mathrm{ZQ}})^2+\kappa^2/4}\,\frac{\langle\Downarrow\uparrow|\,\hat{S}_x\,|\Uparrow\downarrow\rangle}{\langle\Downarrow\downarrow|\,\hat{S}_x\,|\Uparrow\downarrow\rangle},\\ \Gamma_{\mathrm{DQ}} &= \frac{g_0^2\kappa}{(\omega_r-\omega_{\mathrm{DQ}})^2+\kappa^2/4}\,\frac{\langle\Downarrow\downarrow|\,\hat{S}_x\,|\Uparrow\uparrow\rangle}{\langle\Downarrow\uparrow|\,\hat{S}_x\,|\Uparrow\uparrow\rangle},\\ \Gamma_{\mathrm{DQ}} &\approx \Gamma_{\mathrm{DQ}} \approx \frac{\Gamma_{\mathrm{R}}}{1+4\omega_I^2/\kappa^2}\,\frac{A_\perp^2}{4\omega_I^2}.\end{aligned} \tag{5.9}$$

We define the probability of a cross-relaxation event after the electron spin has been excited as

$$p_{\mathrm{ZQ,\,DQ}} = \frac{\Gamma_{\mathrm{ZQ,\,DQ}}}{\Gamma_{\mathrm{ZQ,\,DQ}}+\Gamma_{\mathrm{R}}} \approx \frac{\Gamma_{\mathrm{ZQ,\,DQ}}}{\Gamma_{\mathrm{R}}} = \frac{1}{1+4\omega_I^2/\kappa^2}\,\frac{A_\perp^2}{4\omega_I^2}. \tag{5.10}$$

Stimulated Raman driving

As discussed in the previous section, a pulse resonant with a ZQ/DQ transition can be used to coherently drive the nuclear spin state. As explained earlier, ZQ/DQ driving is not an efficient way to coherently drive a nuclear spin in our setup. In this section, we explain how a nuclear spin can be driven by the simultaneous application of two off-resonant microwave tones. This so-called Raman scheme is commonly used in optics to drive hyperfine transitions in atoms [78], and we transpose it here to spin systems at microwave frequencies. In this section, we derive the effective nuclear spin driving strength (the so-called Raman Rabi frequency Ω_{Ram}). We also derive formulas for the differential AC-Zeeman shifts undergone by the nuclear spin levels in the presence of the Raman drives, which will be useful in Chapter 8 to construct a two-qubit gate.

As a starting point, we consider a three-level system with a Λ-structure: two uncoupled ground states (named $|a\rangle$ & $|b\rangle$) and an excited state (named $|c\rangle$), as shown in Figure 5.3a. The two ground-to-excited transitions are off-resonantly driven by microwave tones with Rabi rates Ω_{A} and Ω_{B}. The frequency difference between the $|a\rangle \leftrightarrow |c\rangle$ transition and drive A is given by Δ, and the detuning between the two drives by δ. In the dispersive regime ($|\Delta| \gg |\Omega_{\mathrm{A,B}}|$) the excited state can be adiabatically eliminated [77]. When δ is resonant with the NMR-allowed transition frequency, the nuclear spin population is driven with Rabi frequency given by

$$\Omega_{\mathrm{Ram}} = \frac{\Omega_{\mathrm{A}}\Omega_{\mathrm{B}}}{2\Delta}. \tag{5.11}$$

We now apply the Raman drive concept to the coupled electron-nuclear spin system. The level diagram in Figure 5.3b now displays two Λ-systems, instead of a single one. In addition, the cavity filters the microwave amplitude as

[78]: Kasevich et al. (1991), 'Atomic Interferometry Using Stimulated Raman Transitions'

[77]: Cohen-Tannoudji et al. (2024), *Atom - Photon Interactions*

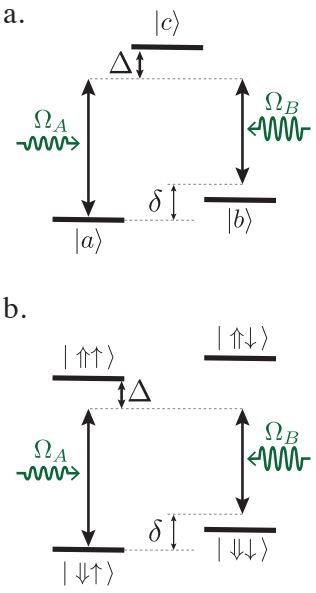

Figure 5.3.: Stimulated Raman Scheme. The two microwave pulses have amplitudes $\Omega_{\mathrm{A,\,B}}$. The frequency difference between the two pulses is defined as δ. **a.** Λ-level system. Δ is defined as the detuning between drive A and the $|a\rangle \leftrightarrow |c\rangle$ transition. **b.** ^{183}W–Er^{3+} coupled system. Δ is defined as the detuning between drive A and the electron spin transition when the nuclear spin is in state $\uparrow$.

$$\Omega_{\mathrm{A}} = \frac{\Omega_e}{\alpha_{\mathrm{A}}} \cdot \frac{1}{\sqrt{1 + 4\frac{(\omega_r - (\omega_S^{(\uparrow)} - \Delta))^2}{\kappa^2}}},$$
$$\Omega_{\mathrm{B}} = \frac{\Omega_e}{\alpha_{\mathrm{B}}} \cdot \frac{1}{\sqrt{1 + 4\frac{(\omega_r - (\omega_S^{(\uparrow)} - \Delta - \delta))^2}{\kappa^2}}}, \tag{5.12}$$

where $\alpha_{\mathrm{A,B}}$ is a linear scaling factor to account for differences in pulse amplitudes. Because each Raman pulse can couple the ground states to either of two excited states, $|\Uparrow\uparrow\rangle$ or $|\Uparrow\downarrow\rangle$ (see Figure 5.3), the stimulated Raman transition is mediated by both paths. The total Rabi rate results from the combination of the independent rates, rescaled by the corresponding relative matrix elements,

$$\Omega_{\mathrm{Ram}} = \Omega_{\mathrm{Ram},1} + \Omega_{\mathrm{Ram},2} \approx -\frac{\Omega_A \Omega_B}{2\Delta}\frac{A_\perp}{2\omega_I} + \frac{\Omega_A \Omega_B}{2(\Delta + \omega_I^{(\Uparrow)})}\frac{A_\perp}{2\omega_I}. \tag{5.13}$$

Because the ZQ and DQ matrix elements have opposite signs (Eq. 5.3), the resulting Raman Rabi rates necessarily carry opposite signs as well. The sign difference can be compensated for by driving "in the middle" of the two excited state levels, as the sign of the denominator will also be opposite in these conditions. The optimal point corresponds to $\Delta = -\omega_I^{(\Uparrow)}/2$, since it results in the maximal frequency detuning of the drives with respect to the EPR-allowed transitions. This allows one to increase their microwave amplitude without breaking the Raman condition $\Omega_{\mathrm{A,B}} \ll \Delta$, which would significantly populate the Er^{3+} excited state. The Raman Rabi frequency at this condition is given by

$$\Omega_{\mathrm{Ram}} = \frac{\Omega_A \Omega_B}{\omega_I^{(\Uparrow)}}\frac{A_\perp}{\omega_I} \approx \frac{\Omega_A \Omega_B A_\perp}{\omega_I^2} \tag{5.14}$$

Figure 5.4 shows Ω_{Ram} as a function of Δ for $\alpha_{\mathrm{A,B}} = 1$, $\Omega/2\pi = 200$ kHz and $A_\perp/2\pi = 50$ kHz, which are close to experimental conditions.

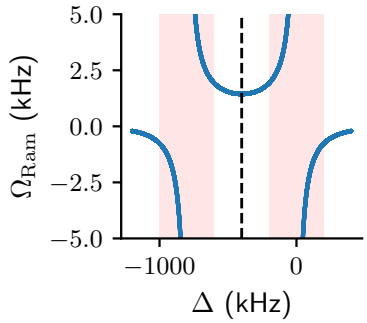

Figure 5.4.: Raman Rabi frequency as a function of Δ. Data in blue is calculated with Eq. 5.13 by considering $\alpha_{\mathrm{A,B}} = 1$, $\Omega/2\pi = 200$ kHz and $A_\perp/2\pi = 50$ kHz. Dashed vertical line marks $\Delta = -\omega_I^{(\Uparrow)}/2$. The red shaded area indicates the hard limit beyond which the Raman approximation breaks down, i.e., $\Omega_{\mathrm{A,B}} \gtrsim \Delta$.

Differential AC-Zeeman shift As described in the previous section, the presence of an off-resonance microwave drive shifts the energy levels of the system and induces an AC-Zeeman shift on the EPR-allowed transitions. In turn, this effectively shifts the resonance of the ZQ/DQ transition. Similarly, the two drives used for the stimulated Raman driving will shift the energy levels and create an effective shift δ_{AC} of the NMR transition which modifies the resonant condition of the stimulated Raman drive to $\delta = \omega_I^{(\Downarrow)} + \delta_{\mathrm{AC}}$. The shift can be by considering the independent effect of each drive in each EPR-allowed transition,

$$\delta_{\mathrm{AC}} = \frac{\Omega_A^2}{4}\cdot\left(\frac{1}{\Delta} - \frac{1}{\Delta + \omega_I^{(\Uparrow)} - \omega_I^{(\Downarrow)}}\right) + \frac{\Omega_B^2}{4}\cdot\left(\frac{1}{\Delta + \omega_I^{(\Downarrow)}} - \frac{1}{\Delta + \omega_I^{(\Uparrow)}}\right). \tag{5.15}$$

In this equation, the first term corresponds to the shift induced by drive A on the EPR-allowed transition when the nuclear spin is in $\uparrow$ and $\downarrow$,

respectively, and the second term corresponds to the shift induced by drive B on the same electron transitions.

5.2. High-spin generalization

In Chapter 9 we experimentally identify a strongly coupled spin $I = 9/2$, which we spectroscopically identify as ^{93}Nb. Our goal is to derive analytical formulas for the sideband driving, cross-relaxation rates, and Raman Rabi frequencies between pairs of nuclear spin levels $n, n+1$. These results will be used in Chapter 9 to analyze the results and extract the hyperfine parameters. As discussed in Section 3.7, the main differences between the two systems are the larger Hilbert space, which spans twenty energy levels, and the introduction of the nuclear-quadrupole interaction, which couples the nuclear spin to the electric field gradient at the ^{93}Nb position.

Zero- and double-quantum transitions

As derived in Section 3.7, the Hamiltonian of the system is given by

$$\begin{aligned}\hat{\mathcal{H}}/\hbar = \omega_S \hat{S}_z + \omega_I \hat{I}_z + A_\parallel \hat{S}_z \hat{I}_z + A_\perp \hat{S}_z \hat{I}_x + \\ + \frac{\omega'_Q}{6}\left[3\hat{I}_z^2 + \frac{\eta'}{2}(e^{-2i\alpha}\hat{I}_+^2 - e^{2i\alpha}\hat{I}_-^2)\right].\end{aligned} \tag{5.16}$$

In the secular approximation, the electron wavefunctions are well described by the magnetic number m_S. However, the nuclear spin states are mixed to varying degree due to the hyperfine and the electric quadrupole interaction. In order to calculate the relevant matrix element we will treat the wavefunctions of the Hamiltonian in first-order perturbation theory. We consider as a perturbation $\hat{V}$ all terms that do not commute with $\hat{S}_z$ and $\hat{I}_z$, that is,

$$\begin{aligned}\hat{\mathcal{H}} &= \hat{\mathcal{H}}_0 + \hat{V} \\ \hat{\mathcal{H}}_0 &= \omega_S \cdot \hat{S}_z + \omega_I \cdot \hat{I}_z + A_\parallel \hat{S}_z \hat{I}_z + \omega'_Q/2 \cdot \hat{I}_z^2 \\ \hat{V} &= A_\perp \hat{S}_z \hat{I}_x + \frac{\omega'_Q \eta'}{12}(e^{-2i\alpha}\hat{I}_+^2 - e^{2i\alpha}\hat{I}_-^2),\end{aligned} \tag{5.17}$$

The eigenstates of the unperturbed system $\hat{\mathcal{H}}_0$ correspond to $|m_S m_I\rangle$, where $m_I \in \{-9/2, \ldots, 9/2\}$ are the nuclear spin quantum numbers. At first order, the hyperfine and quadrupole perturbations will mix terms with $m_I \pm 1$ and $m_I \pm 2$ respectively and the wavefunctions are given by

$$\left|\psi_{m_S,m_I}\right\rangle \approx |m_S, m_I\rangle + \sum_{i\in\{\pm1,\pm2\}} M_i^{(m_S,m_I)} \cdot |m_S, m_I + i\rangle \tag{5.18}$$

where

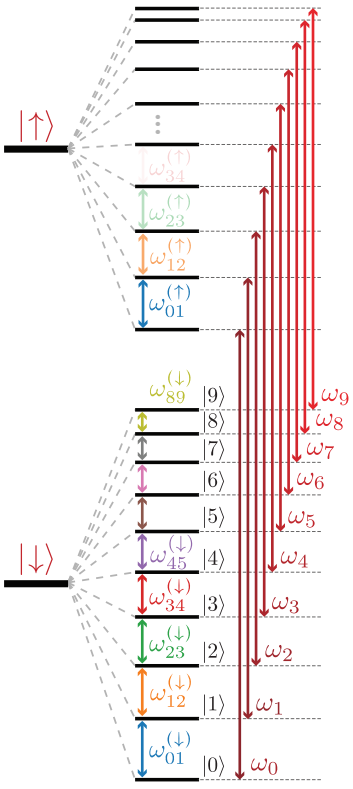

Figure 5.5.: Energy level diagram of an Er^{3+} coupled to a nuclear spin-9/2

$$M_{\pm1}^{(m_S,m_I)} = \mp\frac{C_{m_I}^{\pm}\cdot A_\perp m_S/2}{\omega_I + A_\parallel m_S + \omega'_Q(m_I \pm 1/2)},$$
$$M_{\pm2}^{(m_S,m_I)} = \mp\frac{e^{\mp 2i\alpha} D_{m_I}^{\pm}\cdot \omega'_Q\eta'/12}{2(\omega_I + A_\parallel m_S + \omega'_Q(m_I \pm 1))}. \tag{5.19}$$

$$C_{m_I}^{\pm} = \langle m_I \pm 1|\,\hat{I}_\pm\,|m_I\rangle = \sqrt{I(I+1) - m_I(m_I\pm 1)},$$
$$D_{m_I}^{\pm} = \langle m_I \pm 2|\,\hat{I}_\pm\,|m_I\rangle = C_{m_I}^{\pm}\ \cdot\ C_{m_I+1}^{\pm}\,.$$

Due to the hyperfine- and quadrupole-induced mixing, the nuclear spin magnetic numbers are not good quantum numbers anymore, and we introduce the notation $|m_S, n\rangle = \left|\psi_{m_S,9/2-m_I}\right\rangle$ with $n \in \{0,\dots,9\}$ in ascending order of energy. Due to the admixing of the nuclear spin wavefunctions, the matrix elements for the EPR-allowed and ZQ/DQ transitions are given by

$$\langle\downarrow n|\,\hat{S}_x\,|\uparrow n\rangle \approx 1/2$$
$$\langle\downarrow n\pm1|\,\hat{S}_x\,|\uparrow n\rangle \approx \mp\frac{1}{4}\frac{A_\perp C_n^{\pm}}{\omega_I + \omega'_Q\left(n\pm\frac{1}{2}\right)} \tag{5.20}$$

.

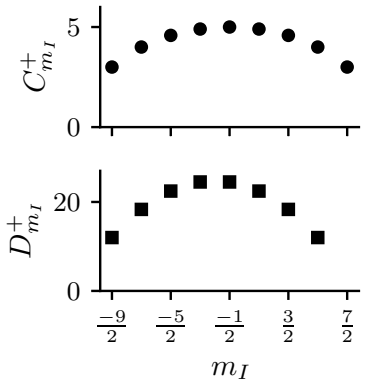

Figure 5.6.: Spin ladder operators for a spin $I = 9/2$ as a function of the spin magnetic number m_I. We note that $C^+_{m_I} = C^-_{m_I+1}$ and $D^+_{m_I} = D^-_{m_I+2}$.

We note that $\Delta n = \pm2$ matrix elements are nonzero, which means that higher-order sideband driving is permitted thanks to the quadrupole mixing. In the weak-quadrupole regime these $\Delta m_I = \pm2$ matrix elements are much smaller than their $\Delta m_I = \pm1$ counterparts. Moreover, the $\Delta m_I = \pm2$ lines are typically farther detuned from the resonator center, so cavity filtering further suppresses the effective drive amplitude. The net effect is that driving $\Delta m_I = \pm2$ transitions requires higher microwave power with much slower Rabi rates, and we do not treat them in the following.

Analogous to the $I = 1/2$ case, the nuclear population of the $I = 9/2$ system can be addressed by resonantly driving the weakly allowed sideband transitions. The perpendicular hyperfine term is responsible for the dominant $\Delta m_I = \pm1$ ZQ and DQ sidebands, while the non-diagonal quadrupole terms open additional $\Delta m_I = \pm2$ paths.

We arbitrarily consider the ZQ transitions from state n to $n+1$ with frequency $\omega_n^{(+1)}$, but the following derivation is analogous for the DQ transitions. As in the previous section, the oscillation frequency $\Omega_{\mathrm{ZQ}}^{(n)}$ depends on two factors: the matrix element of the transition and the amplitude of the applied microwave field, quantified by an electron Rabi frequency Ω measured at a reference pulse amplitude. Using Ω as a calibration point, we express the drive amplitude for any pulse as a relative factor α. The corresponding sideband Rabi frequency is then

$$\Omega_{\mathrm{ZQ}}^{(n)} = \frac{\Omega}{\alpha}\,\frac{A_\perp\, C_n^{+}}{2\left(\omega_I + \omega'_Q\left(n+\frac{1}{2}\right)\right)}\,\frac{1}{\sqrt{1+4\frac{(\omega_r-\omega_n^{(+1)})^2}{\kappa^2}}} \tag{5.21}$$

As for the case of the nuclear spin $I = 1/2$, the oscillation frequency is proportional to the coupling strength. However, the ladder factors C_n^+ will modulate the driving speed depending on the state of the nuclear spin, with the highest factor for the $n = 4$ to $n = 5$ transition which approximately corresponds to the $m_I = 1/2$ to $m_I = -1/2$ transition (see Figure 5.6). In addition, when driving the ZQ and DQ transitions, the energy levels will experience an AC-Zeeman shift, as described in the spin-1/2 case.

Cross-relaxation rates

Using the calculated matrix elements, we now proceed to give an estimate of the relaxation rate of the electron spin through all the available mechanisms. The main relaxation channel for the electron spin comes from the EPR-allowed transitions, which leave the nuclear spin invariant, and the matrix element for these transitions is approximately 1/2 no matter the state of the nuclear spin. However, the hyperfine interaction shifts the frequency of these transitions ($\omega_0, \dots, \omega_9$) depending on the state of the nuclear spin. Experimentally, we tune the spin such that $\omega_0 = \omega_r$, which results in different Purcell factors for every transition. The electron relaxation rate when the nuclear spin is in state n, $\Gamma_R^{(n)}$, is given by

$$\Gamma_R^{(n)} = \frac{\kappa g_0^2}{\kappa^2/4 + (\omega_r - \omega_n)^2} = \Gamma_R^{(0)} \cdot \frac{1}{1 + 4\frac{(\omega_r - \omega_n)^2}{\kappa^2}} \tag{5.22}$$

where $\Gamma_R^{(0)}$ is the electron decay rate when $n = 0$. We denote the frequency for a cross-relaxation where the state of the nuclear spin is changed from n to $n + i$ as $\omega_n^{(i)}$. The decay rate is obtained by rescaling the relaxation rate given by the Purcell effect by the matrix element

$$\begin{aligned}\Gamma_i^{(n)} &= \frac{\kappa g_0^2}{\kappa^2/4 + (\omega_r - \omega_n^{(i)})^2} \cdot \frac{|\langle\downarrow n + i|\, \hat{S}_x\, |\uparrow n\rangle|^2}{|\langle\downarrow n|\, \hat{S}_x\, |\uparrow n\rangle|^2} = \\ &= 2\,\Gamma_R^{(0)} \cdot \frac{|\langle\downarrow n + i|\, \hat{S}_x\, |\uparrow n\rangle|^2}{1 + 4\frac{(\omega_r - \omega_n^{(i)})^2}{\kappa^2}}\end{aligned} \tag{5.23}$$

The total relaxation rate for $|\uparrow n\rangle$ is given by $\Gamma^{(n)} = \Gamma_R^{(n)} + \sum_i \Gamma_i^{(n)}$. We naturally introduce the cross-relaxation probability.

$$p_{x,i}^{(n)} = \frac{\Gamma_i^{(n)}}{\Gamma^{(n)}} \approx \frac{\Gamma_i^{(n)}}{\Gamma_R^{(n)}} = \frac{2|\langle\downarrow n + i|\, \hat{S}_x\, |\uparrow n\rangle|^2}{1 + 4\frac{(\omega_r - \omega_i^{(n)})^2}{\kappa^2}}. \tag{5.24}$$

Due to the difference in scale of the matrix elements between the $\Delta m_I \pm 1$ and $\Delta m_I \pm 2$ transitions, the dominant contribution to the relaxation dynamics arises from the ZQ and DQ transitions, while the probability of a cross-relaxation event with $\Delta m_I = \pm 2$ is orders of magnitude weaker.

Stimulated Raman driving

In this section we derive the expressions for the Rabi frequency of a Raman drive for the case of a nuclear spin $I = 9/2$ by generalizing the results obtained in the previous section for a spin $I = 1/2$. As in the previous section, the stimulated Raman scheme allows one to transfer the population between the two adjacent nuclear spin levels $|\Downarrow n\rangle$ and $|\Downarrow n+1\rangle$ through the use of two off-resonant microwave drives with amplitudes Ω_A and Ω_B (see Eq. 5.12). When the difference in frequency between the two drives matches the nuclear spin transition frequency, a two-photon process enables the coherent control of the nuclear spin population between the two levels. This is possible by leveraging the coupling of the two levels of interest to their electron excited counterparts: $|\Uparrow n\rangle$ and $|\Uparrow n+1\rangle$. As in the previous section, the presence of two electron excited states creates two possible paths for the scheme, which interfere with each other,

$$\begin{aligned}
\Omega_{\text{Ram}} &= \Omega_{\text{Ram},1} + \Omega_{\text{Ram},2} \\
\Omega_{\text{Ram},1} &\approx -\frac{\Omega_A \Omega_B}{4\Delta} \frac{A_\perp C_n^+}{\omega_I + \omega'_Q\left(n+\frac{1}{2}\right)} \\
\Omega_{\text{Ram},2} &\approx +\frac{\Omega_A \Omega_B}{4\left(\Delta+\omega_n\right)} \frac{A_\perp C_n^+}{\omega_I + \omega'_Q\left(n+\frac{1}{2}\right)},
\end{aligned} \tag{5.25}$$

where we have used that $C^+_{m_I} = C^-_{m_I+1}$. As in the case of $I = 1/2$, the matrix elements have opposite signs and constructive interference is only achieved while driving between the two excited state levels. Similarly, the optimal driving point is given for $\Delta = -\omega_n/2$, as it maximizes the detuning between the drives and the EPR-allowed transitions. The Raman Rabi frequency in this regime is given by

$$\Omega_{\text{Ram}} = \frac{\Omega_A \Omega_B}{\omega_n} \frac{A_\perp C_n^+}{\omega_I + \omega'_Q\left(n+\frac{1}{2}\right)} \approx A_\perp C_n^+ \frac{\Omega_A \Omega_B}{\omega_n^2} \tag{5.26}$$

We note that the final value of Ω_{Ram} is the same as in the $I = 1/2$ case, but scaled by the ladder-operator factor C_n^+.

5.3. Summary

This chapter has established the theoretical framework for nuclear spin control mediated by an electron spin using microwave drives. We have discussed two mechanisms, resonant driving of the ZQ/DQ transition and microwave stimulated Raman driving. The discussion was separated into two parts: first, the case of nuclear spins $I = 1/2$, which will be used in Chapters 7 and 8, and second, the generalization to high-spin nuclei ($I > 1/2$) used in Chapter 9.

Zero- and double-quantum transitions. Direct driving of the ZQ/DQ transitions allows simultaneous control of the electron and nuclear spin state. The matrix element of the transition is small compared to the EPR-allowed transitions, and large microwave amplitude pulses are required to effectively drive Rabi oscillations. The use of large microwave amplitudes induces AC-Zeeman shifts of the EPR-allowed transitions which translate to effective shifts of the ZQ and DQ transition frequencies. However, even at large microwave amplitudes the scheme is limited by electron spin decoherence since the excited state is populated by the drive.

Cross-relaxation events. Due to the non-zero ZQ and DQ matrix elements, the electron spin can spontaneously decay through a ZQ or DQ transition, changing the state of the nuclear spin in the process. The probability for this cross-relaxation event scales proportionally to the square of the perpendicular hyperfine coupling, $A_\perp$.

Stimulated Raman driving. Control of the nuclear spin can be achieved by applying two off-resonant microwave tones with a mutual detuning equal to the NMR-allowed transition frequency [77]. This microwave stimulated Raman scheme does not significantly populate the electron spin excited state and preserves the coherence time of nuclear spins. The two microwave drives shift the energy levels of the system, which result in a *differential* AC-Zeeman shift of the NMR-allowed transition.

[77]: Cohen-Tannoudji et al. (2024), *Atom - Photon Interactions*

6. Sample and setup

In this chapter we describe the setup and methods used in the experimental chapters. We describe the $CaWO_4$ sample and the superconducting micro-resonator. We describe the assembly of the sample and its mounting in the dilution refrigerator along with the SMPD. Then, we present the resonator characterization at zero field and the protocol we use to tune the detection frequency of the SMPD to the resonator frequency. After this preliminary characterization, we summarize the magnetic-field alignment procedure and ensemble Er^{3+} spectroscopy using microwave photon counting. Finally, we outline the methods used to detect, address, and coherently control individual Er^{3+} spins, as well as characterize their relaxation and decoherence times.

6.1 Sample 57
Resonator design and fabrication 57
6.2 Measurement setup 60
6.3 Superconducting resonator characterization 61
Magnetic field alignment . 61
6.4 SMPD frequency tuning . 63
6.5 Erbium ensemble spectroscopy 64
6.6 Individual Er^{3+} spins . . . 66

6.1. Sample

The experiments reported in this thesis were all carried out on one monocrystalline $CaWO_4$ sample on the surface of which a superconducting thin-film resonator was fabricated.

The sample originates from a large single-crystal *boule* grown by Philippe Goldner using the Czochralski [79] method from CaCO3 (99.95% purity) and WO3 (99.9% purity). No paramagnetic impurities were added during crystal growth. Standard EPR measurements performed by Sylvain Bertrana on a sample from the same *boule* yield a residual Er^{3+} concentration of 3.1(2) ppb [69]. The average distance between Er^{3+} ions at this concentration is 300 nm, far enough to suppress dipolar interactions between the Er^{3+} spins.

[79]: Erb et al. (2013), 'Growth of High-Purity Scintillating CaWO4 Single Crystals for the Low-Temperature Direct Dark Matter Search Experiments CRESST-II and EURECA'

[69]: Le Dantec (2022), 'Electron Spin Dynamics of Erbium Ions in Scheelite Crystals, Probed with Superconducting Resonators at Millikelvin Temperatures'

The sample used in this work was cut into a rectangular slab. Its dimensions are 7 mm by 4 mm by 2 mm, with its surface approximately along the (a, c)-plane of the crystal and the c-axis along the short edge. The polishing of the surface, performed by SurfaceNet GmbH, reduced the thickness to 0.5 mm.

Resonator design and fabrication

As discussed in Chapter 4, the purpose of the resonator is to enhance the radiative relaxation of the spins via the Purcell effect. To achieve this, the coupling strength g_0 must be maximized. From Eq. 4.12, we observe that the coupling strength scales inversely with the resonator impedance. Consequently, reducing the resonator impedance provides a direct route to increasing the coupling rate. We achieve this through a design that maximizes the resonator capacitance while keeping the resonator inductance to a minimum.

The resonator is made of a 50-nm-thick niobium film and takes the form of two superconducting electrodes separated by an interdigitated capacitor and shunted by a small constriction: a nanowire with a length of 50 µm and a width of 300 nm parallel to the c-axis. A micrograph of one of the resonators is shown in Figure 6.1a. Each of the fingers has

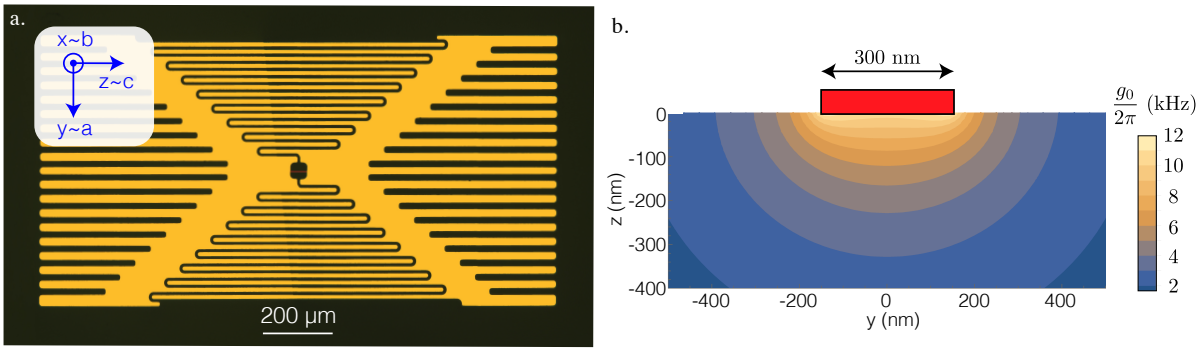

Figure 6.1.: Sample micrograph and coupling map. **a.** False color micrograph of a Nb thin-film resonator of the same design fabricated on a $CaWO_4$ crystal. The nanowire is colored in red while the rest of the resonator is colored yellow. The picture is stitched from 2 independent images. The laboratory frame axes x, y and z approximately coincide with the crystal axes. The z-axis is parallel to the nanowire and the x-axis is perpendicular to the plane. **b.** Spatial map for the coupling g_0 between Er^{3+} and the superconducting resonator calculated with COMSOL by André Pscherer. The map is shown as a transversal cut around the nanowire (in red).

an associated geometric inductance as the current needs to travel from one side of the capacitor plate to the other. The geometric inductance increases the impedance of the resonator without contributing to the magnetic field generated by the nanowire and is therefore important to minimize. To reduce the effect of the finger's geometric inductance the "bow tie" design shown in the micrograph was adopted.

We use finite element simulations using `HFSS` to target the frequency and impedance of the resonators. The simulations follow the procedure developed by Zhiren Wang and Marianne le Dantec, which is described in detail in refs. [23, 69]. The key modification implemented in this work was the reduction of the nanowire width from 500 nm to 300 nm, resulting in an increased magnetic coupling strength to the Er^{3+} spins.

We measure the impedance of the resonator by introducing a small lumped element with inductance δL. We run the simulation for different values of inductance and obtain the frequency as a function of δL, which is then fit to $1/\sqrt{(L+\delta L)\,C}$ [80]. From the values of L and C we obtain $Z_r = 13\,\Omega$.

The simulations also yield the current density through the nanowire, which was used by André Pscherer to create a spin coupling map based on the magnetic field generated by the rectangular nanowire using COMSOL (see Figure 6.1b). For an Er^{3+} spin located 10–100 nm away, we expect $g_0/2\pi$ = 8–12 kHz, about twice as large as in the previous design (see Figure 3.4b in ref. [23]).

Three superconducting resonators of similar design are fabricated on top of the $CaWO_4$ sample. The target frequencies of the resonators are separated by 50 MHz, to increase the probability that at least one of them lies within the SMPD range. The fabrication also follows the process developed by Zhiren Wang and Marianne le Dantec, which is outlined in the following.

- Surface cleaning with a mixture of sulfuric acid and hydrogen peroxide.
- Sputtering of a 50 nm thick Nb film.
- A double layer of PMMA and MMA positive resist is spin coated on top of the chip. The respective thicknesses are 340 nm and 110 nm.
- A single electron beam lithography step patterns the resonator on the sample. The exposed resist is subsequently removed.

[23]: Wang (2023), 'Addressing Individual Electronic Spins with a Microwave Superconducting Resonator'
[69]: Le Dantec (2022), 'Electron Spin Dynamics of Erbium Ions in Scheelite Crystals, Probed with Superconducting Resonators at Millikelvin Temperatures'

[80]: Eichler et al. (2017), 'Electron Spin Resonance at the Level of $1{0}^{4}$ Spins Using Low Impedance Superconducting Resonators'

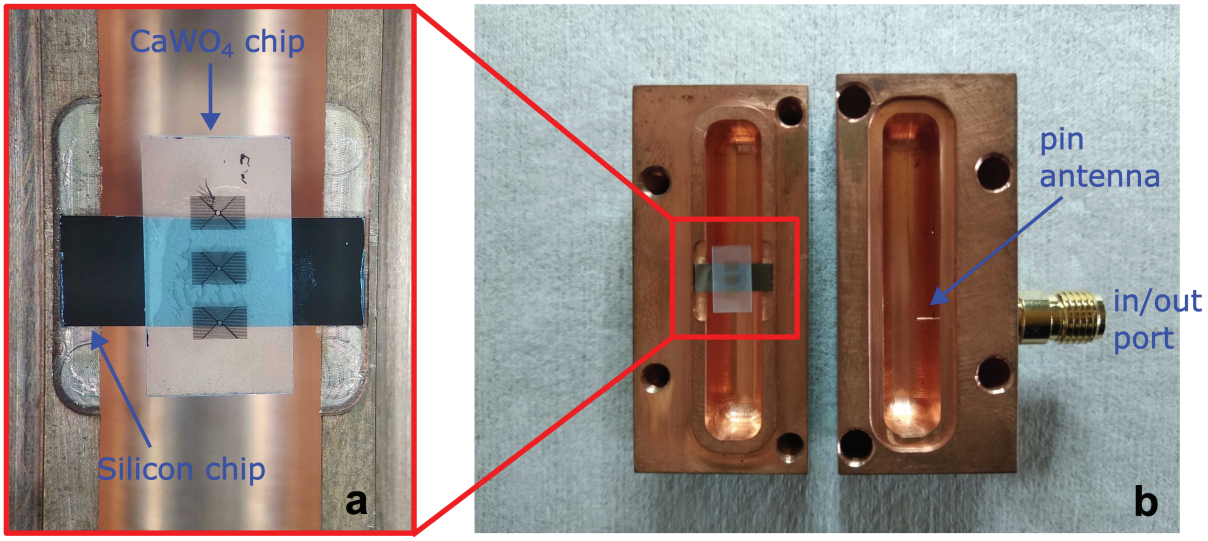

Figure 6.2.: Resonator and copper cavity assembly. Since the sample remains in the fridge at the time of writing this manuscript, the image was taken from ref. [23], which used a similar assembly. **a.** Zoomed view of the sample. The $CaWO_4$ sample in the figure is 4×7 mm and three resonators have been fabricated on top. We note that in the real sample used for this work, the chip broke during fabrication but left one resonator unharmed. The sample is affixed to a silicon bridge (dark rectangle) supported by the copper cavity. **b.** Open copper cavity. The cavity is set up in the reflection configuration, where only one metallic antenna is present. The antenna is soldered to a SMA port which connects to the microwave lines. A second hole (visible as a small speck on top of the antenna) is used to introduce a second antenna in the transmission configuration. The hole is covered with copper tape on the outside in the reflection setup.

- A 30 nm film of aluminum is evaporated on the sample to act as a hard mask.
- Aluminum lift-off.
- Reactive ion etching removes the unmasked Nb film.
- Aluminum removal through wet-etching.

When characterizing the resonators we found that their frequencies were ~ 100 MHz higher than the target ones and therefore outside the SMPD range. We reworked the resonators by removing Nb from the fingers, therefore increasing the distance between the capacitors and reducing their frequency. The rework had to be performed twice. During one of these reworks, the sample was snapped into two halves, leaving one resonator unharmed, which was then found to have the appropriate frequency. We qualitatively note that the quality factor of the resonator was significantly reduced after the rework.

Sample assembly

The sample is mounted in a copper sample holder as shown in Figure 6.2. The sample is affixed with vacuum grease to a silicon chip that plays the role of a bridge by suspending it in the center of the cavity. The silicon chip is held in place by compression between the cavity halves. The resonator is capacitively coupled to an antenna that is soldered to an SMA connector. The antenna protrudes through a small pinhole in the cavity wall, and coupling to the resonator is tuned by adjusting the insertion depth. The copper cavity is then mounted on the fridge with a three-axis magnet surrounding the assembly.

During this work, two different setups were used: first, in Chapters 7 & 8 we use a reflection configuration with a single pin antenna. The coupling of the antenna to the resonator is tuned to achieve critical coupling. Second, in Chapter 9 a transmission setup is used, where the resonator

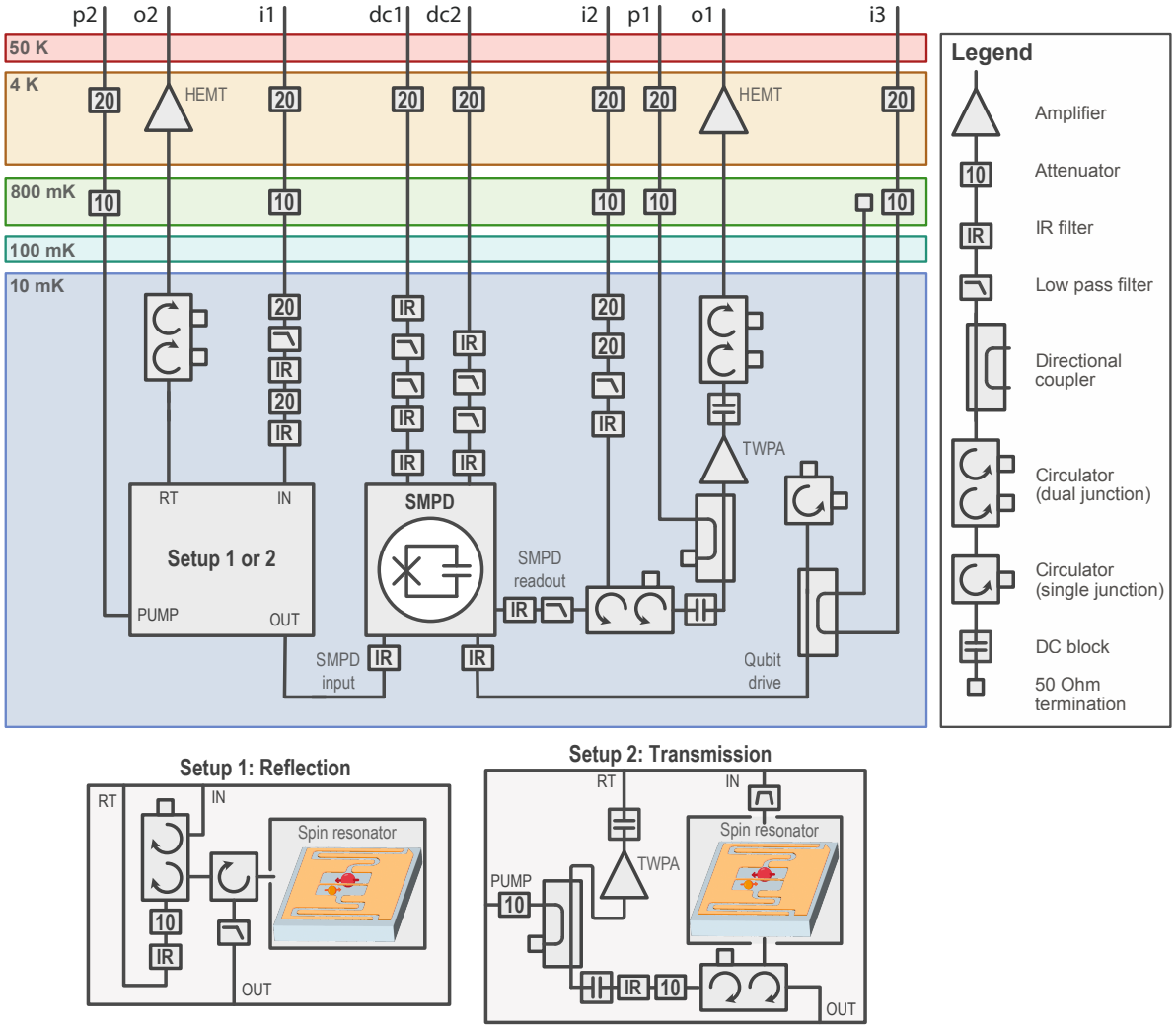

Figure 6.3.: Cryogenic wiring diagram with the two configurations used in this work. Two different setups were used during the course of this thesis. The main changes are outlined in the bottom separating the components between the reflection and the transmission setups. Line names are marked at the top which indicate: *i* for input, *o* for output, *p* for TWPA pumping and *dc* for DC bias lines. For the transmission setup, a large µ-metal shield surrounding the dilution fridge at room temperature was introduced to shield the interior from stray magnetic fields.

is coupled with two antennas to separate lines, one for input and one for output. The coupling rates of the two antennas are dissimilar by a factor ~ 10, with the larger one being the output line, so that most of the fluorescent photons are directed towards the detector.

6.2. Measurement setup

Both the sample and the SMPD are mounted at the 10 mK stage of a dilution refrigerator. The wiring diagram of the fridge is presented in Figure 6.3. Line *i*1 is directly connected to the SMPD input and is therefore well attenuated (-20 dB at 4 K, -10 dB at 800 mK, -40 dB at 10 mK) to reduce the number of thermal photons per mode. Reducing the thermal population at the input of the detector is required to achieve low dark counts and high SNR, as discussed in Appendix B.

Two configurations were used to measure the sample: in reflection (Chapters 7 & 8), and in transmission (Chapter 9). For the transmission setup, a large μ-metal shield surrounding the dilution fridge at room temperature was installed to shield the interior from stray magnetic fields.

The sample is surrounded by a 1T/1T/1T superconducting vector magnet, which can produce an arbitrary vector field along the three orthogonal directions X, Y and Z. The coils are independently driven by three current sources which can be individually shunted on demand with superconducting wires, turning on the so-called magnet persistent mode in which field stability is greatly enhanced. All measurements reported in the experimental chapters on individual spins were taken in this persistent mode.

The SMPD (described in Section 4.4) is placed inside a light-tight container with a μ-metal shield to protect the device from stray magnetic fields. The SMPD pump is sent through line $i3$. The frequency and bandwidth are tuned by sending current through lines $dc1$ and $dc2$, respectively. In the reflection setup, we use $i1$ to tune the SMPD parameters (pump frequency and amplitude) to achieve maximum detection efficiency. In the transmission setup, the SMPD input line is filtered by the resonator. We instead use the qubit drive line ($i3$), which is weakly capacitively coupled to the buffer for characterization. Qubit readout pulses are sent through line $i2$, and the reflected signals are directed to output line $o1$, which contains a Traveling Wave Parametric Amplifier (TWPA) pumped through line $p1$.

6.3. Superconducting resonator characterization

The resonator is first characterized at zero magnetic field using a Vector Network Analyzer in the reflection configuration. Figure 6.4a shows the complex reflection parameter as a function of frequency. By fitting the model, we obtain the internal and coupling losses of the resonator, $\kappa_i/2\pi = 255$ kHz and $\kappa_c/2\pi = 621$ kHz. The quality factor of the resonator is given by

$$Q = \frac{\omega_r}{\kappa_i + \kappa_c} = 8.8 \times 10^5 \tag{6.1}$$

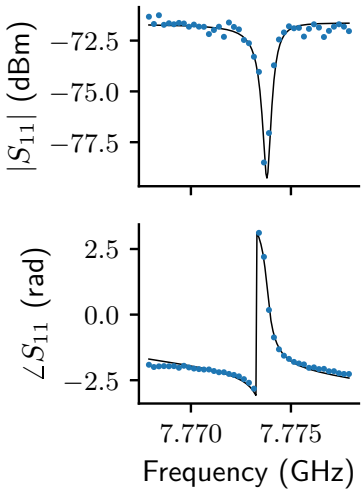

Figure 6.4.: Resonator fit at zero field. Reflection signal of the resonator at zero magnetic field. The data is fit to a standard reflection model (black lines) which yields $\omega_r/2\pi = 7.74845$ GHz and a quality factor of $Q = 8.8 \times 10^5$.

Magnetic field alignment

During the mounting process, the resonator assembly is fixed such that the Y and Z axes of the magnet are close to the plane of the resonator. Due to the limited precision of manual alignment, we begin the experimental run by measuring the relative alignment between these coordinate frames. We follow the procedure described in ref. [81], which we briefly summarize below.

The working principle of the alignment procedure is the strong dependence of the resonator frequency on any out-of-plane component of the magnetic field [1]. By measuring the dependence of the frequency on the components of the field we can map a rotation from the magnetic-field axes X, Y, and Z to the resonator-plane axes x, y, and z (see Figure 6.1). The steps of the procedure, shown in a diagram in Figure 6.5, are:

[81]: Dantec (2022), 'Electron Spin Dynamics of Erbium Ions in Scheelite Crystals, Probed with Superconducting Resonators at Millikelvin Temperatures'

1: A magnetic field increases the penetration depth, and therefore the kinetic inductance. This results in a reduction of the resonator frequency. This effect is also present for in-plane fields but is drastically stronger for out-of-plane components.

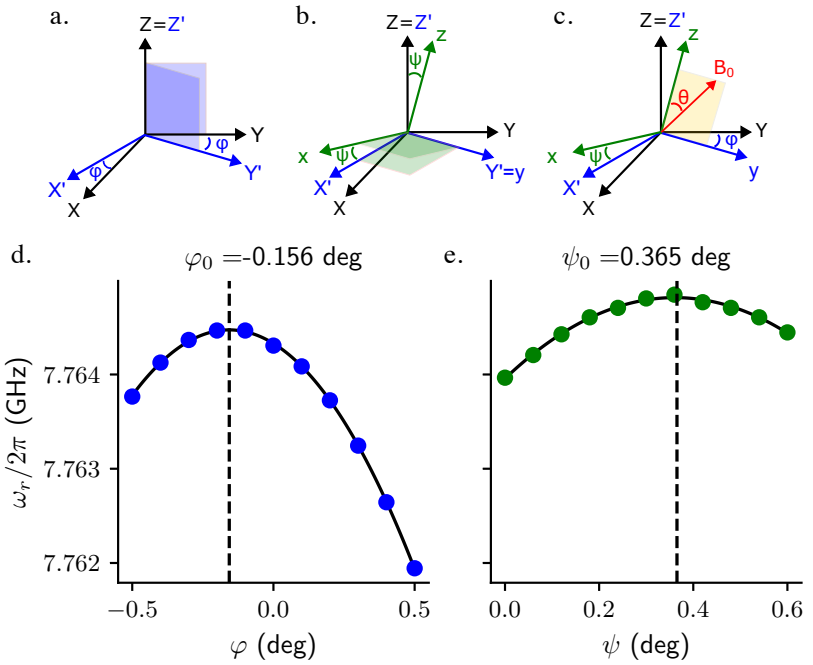

Figure 6.5.: Magnetic field alignment scheme and data. Figures a, b and c show the subsequent rotations performed to arrive to the resonator reference frame. Figures d and e plot the frequency of the resonator as a function of the out-of-plane angle during steps 2 and 5 of the aligning procedure (see text). The data were fit to a parabola and the alignment angles φ_0 and ψ_0 correspond to the top of the parabolic fit.

1. Apply a 50 mT field along the Y axis.
2. Sweep the amplitude of a small magnetic field along the X axis and measure the frequency of the resonator. The combined field makes an angle φ with respect to the (Y, Z)-plane. We measure the angle for which the resonator frequency is maximized, φ_0, which defines the intermediate coordinate frame X', Y', and Z (see Figure 6.5a).
3. Ramp down the magnetic field along Y to 0 mT.
4. Ramp up the magnetic field along Z to 50 mT.
5. Repeat the procedure described in step 2. The angle ψ_0 in the (Y', Z)-plane defines the aligned coordinate system x, y, and z (see Figure 6.5b).
6. Define θ as the angle in the resonator plane with respect to the z axis (see Figure 6.5c).

The resonator frequency as a function of φ and ψ is plotted in Figure 6.5d and Figure 6.5e, respectively. The data were fit to a parabola and the top gives the values of φ_0 and ψ_0. The applied magnetic field in the resonator plane can then be expressed in the laboratory frame as

$$\mathbf{B}_0 = B_0 \begin{pmatrix} \sin\theta\ \sin\phi_0 - \cos\theta\ \sin\psi_0\ \cos\phi_0 \\ \sin\theta\ \cos\phi_0 + \cos\theta\ \sin\psi_0\ \sin\phi_0 \\ \cos\theta\ \cos\psi_0 \end{pmatrix} \tag{6.2}$$

In the following, the magnetic field will always be applied in the plane of the resonator, unless otherwise stated.

We then measure the frequency and quality factor as a function of the applied field. The data are shown in Figure 6.6. The resonance frequency is quadratically shifted as a function of the in-plane field. At 450 mT it drops approximately 40 MHz with respect to the zero field values. Due to the field alignment, the quality factor of the resonator remains approximately constant as a function of the magnetic field. We note that the sharp peaks correspond to paramagnetic impurities previously observed in similar samples [48, 69].

[48]: Billaud et al. (2025), 'Electron Paramagnetic Resonance Spectroscopy of a Scheelite Crystal Using Microwave-Photon Counting'
[69]: Le Dantec (2022), 'Electron Spin Dynamics of Erbium Ions in Scheelite Crystals, Probed with Superconducting Resonators at Millikelvin Temperatures'

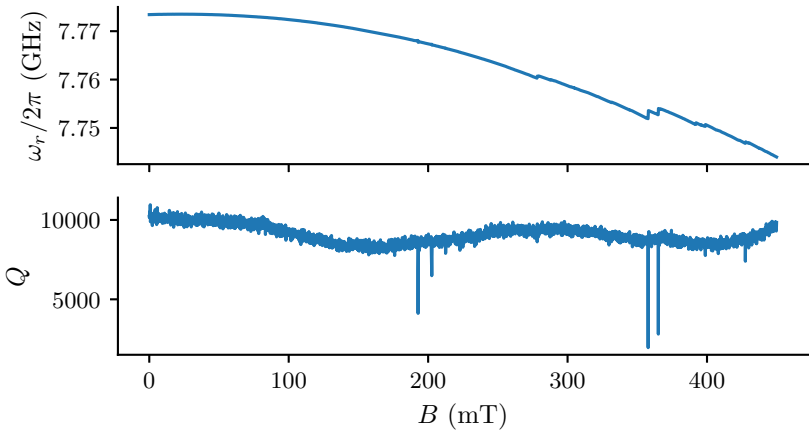

Figure 6.6.: Resonator response to in-plane magnetic field. Frequency and quality factor as a function of in-plane magnetic field amplitude. The data was taken in transmission mode.

6.4. SMPD frequency tuning

The first step of the measurements is to tune the SMPD frequency to the resonator frequency ω_r. The procedure is fully automated, as explained below. This is needed in particular when large magnetic field sweeps are launched, since ω_r then changes with field, thus necessitating repeated SMPD tuning during the sweep.

To achieve this, we sweep a weak probe tone around the resonator frequency on $i1$ while varying the voltage applied to the DC tuning line $dc1$ to tune the input frequency of the detector. In the reflection measurement, the signal reflected on the resonator reaches the SMPD input. In the transmission measurement, the probe tone is filtered by the resonator before reaching the SMPD input.

We now show an example of frequency tuning, performed with the transmission setup. Figure 6.7a shows the SMPD response for different DC voltages which appears as a set of narrow resonance lines with linewidths of approximately 300 kHz (the SMPD bandwidth). Each individual trace is well described by a Lorentzian lineshape, and the extracted peak positions (red triangles) form a broader envelope corresponding to the resonator response. Fitting this envelope yields a resonator linewidth of 740 kHz. We observe a slight asymmetry in the envelope lineshape, which we attribute to weak parasitic transmission between the two antennas interfering with the resonant response. This asymmetry is well captured by a Fano model; however, the extracted linewidth agrees with the Lorentzian fit within uncertainty, and the large Fano asymmetry

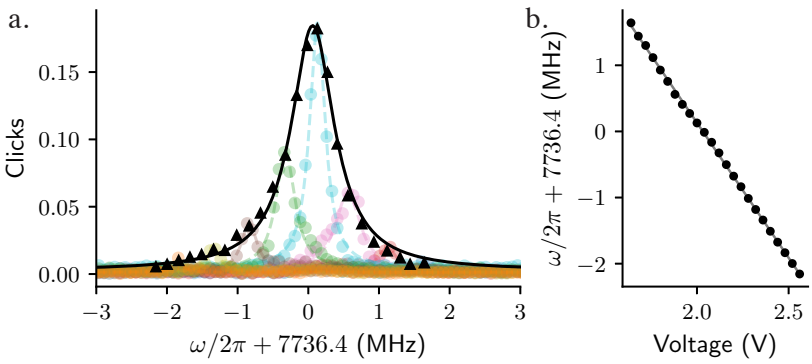

Figure 6.7.: SMPD buffer resonator frequency calibration in transmission configuration. **a.** Response of the SMPD as a function of probe frequency for different DC tuning voltages (faintly colored circles). For clarity only a few have been plotted. Each trace is fitted to a Lorentzian (faint dashed lines), yielding narrow linewidths of approximately 300 kHz. The extracted peak centers (black triangles) form an envelope reflecting the resonator response. Fitting the envelope to a Fano resonance yields a resonator linewidth of 740 kHz. **b.** SMPD resonance frequency as a function of DC bias voltage, showing a linear dependence used to tune the SMPD to the resonator frequency.

parameter indicates that the parasitic contribution is weak and does not affect the linewidth determination.

In Figure 6.7b, the SMPD resonance frequency is plotted as a function of the applied DC voltage and fitted with a linear relation. Using this calibration, we set the DC voltage corresponding to the resonator frequency, thereby aligning the SMPD to the resonator.

6.5. Erbium ensemble spectroscopy

We now perform spectroscopy of the Er^{3+} spin ensemble. Given the gyromagnetic ratio of Er^{3+} spins (see Section 3.2), the expected magnetic field along the c-axis for which the resonator is tuned to the ensemble is given by

$$B_0 = -\frac{\omega_r}{\gamma_{\parallel}} \approx 440 \text{ mT} \tag{6.3}$$

We ramp the magnetic field along the z-axis (which is close to the c-axis) to this value and perform photon counting spectroscopy. We apply a strong microwave pulse with a duration of 100 µs at the frequency of the resonator ω_r. After the pulse, we measure the number of counts on the SMPD during an integration window of $\tau_{\text{int}} = 200$ ms. We average the total number of counts during the integration time over a number of iterations to obtain the ensemble average counts $\langle C \rangle$. We repeat this measurement while sweeping the magnetic field. Due to the dependence of the resonator frequency on the applied magnetic field, we apply the SMPD frequency tuning procedure for every value of B_0 (0.15 mT steps).

Figure 6.8 shows $\langle C \rangle$ as a function of B_0. We observe a peak at $B_0^{\max} = 441.5$ mT of width 0.6 mT, which corresponds to the resonance of Er^{3+} spins. The inset plot shows the count rate $\langle \dot{C} \rangle$ after the excitation pulse at $t = 0$ for two different magnetic fields (marked as red and green markers in the main figure). When the resonator is not resonant with the ensemble (red curve), the count rate is flat and equal to the dark count rate of the SMPD, shown as a black dashed line. The first point of the curve escapes that trend, and we attribute this increase in

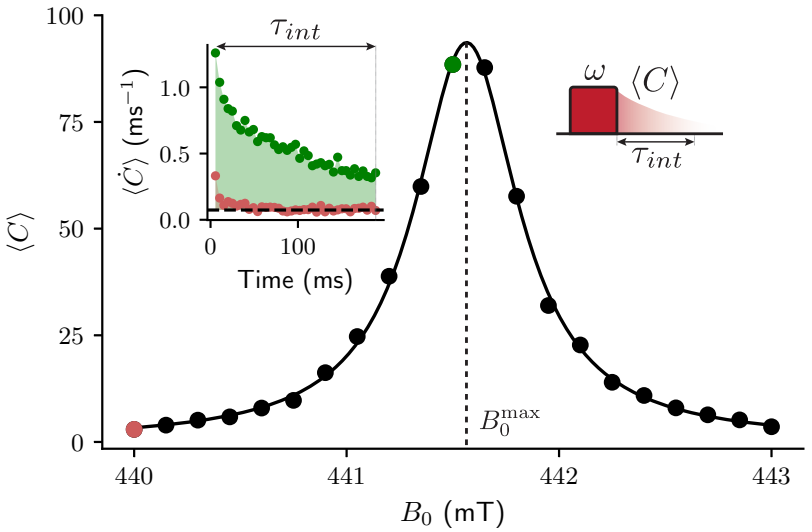

Figure 6.8.: High power spectroscopy. Ensemble average of counts after microwave excitation $\langle C \rangle$ as a function of the magnetic field along the z-axis. The data points are fit to a Lorentzian curve (black line) centered at $B_0^{\max}$. *Top right inset.* Pulse sequence. *Top left inset.* Microwave count rate as a function of time for the green and red data points. The integral of the curve, which corresponds to $\langle C \rangle$, is highlighted with the respective colors. The dark count rate of the SMPD is plotted as a dashed horizontal line.

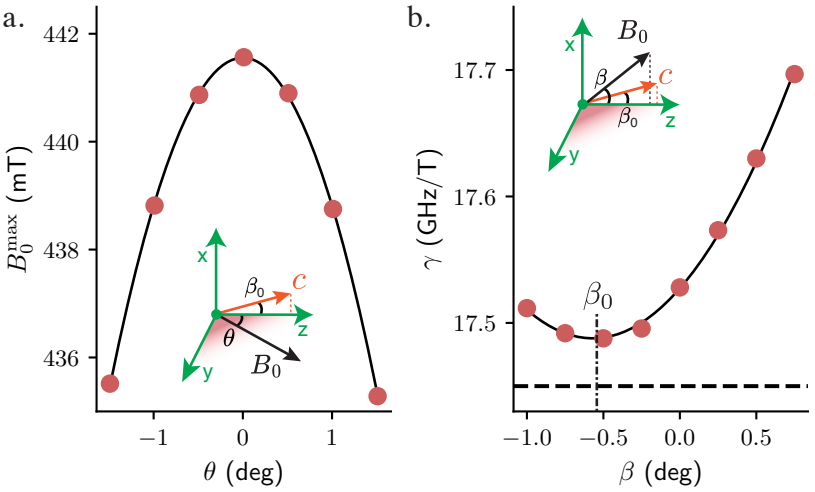

Figure 6.9.: Sample Field Alignment. **a.** Er^{3+} main line resonant field as a function of the in-plane angle θ. The data is fit to a parabola (black line). **b.** Gyromagnetic factor γ as a function of the out-of-plane angle β for $\theta = 0$. The parabolic fit (black line) gives $\beta_0 = -0.57°$ marked with a dash-dot line. Dashed horizontal line shows the literature value for $\gamma_\parallel$.

counts to the emission of unknown degrees of freedom in the resonator, such as TLS [23]. In contrast, when the ensemble is resonant the count rate displays a non-exponential decay over a period of time longer than 200 ms. This non-exponential behavior is consistent with the excitation of an ensemble of Er^{3+} spins with different coupling strength, and therefore relaxation rate. This phenomenon is quantitatively described in ref. [48].

[23]: Wang (2023), 'Addressing Individual Electronic Spins with a Microwave Superconducting Resonator'

[48]: Billaud et al. (2025), 'Electron Paramagnetic Resonance Spectroscopy of a Scheelite Crystal Using Microwave-Photon Counting'

Due to finite precision when cutting the sample, the crystal c-axis is not perfectly parallel to the surface plane (which corresponds to the (y, z)-plane). We define θ as the angle of B_0 with respect to the projection of the c-axis on the (y, z)-plane. In addition, we define β as the angle made by B_0 with the (y, z)-plane. Finally, we define β_0 as the angle between the c-axis and the z-axis (see Figure 6.9 inset).

The orientation of the c-axis is determined by a parabolic fit of B_0^{max} as a function of θ, shown in Figure 6.9a. To measure β_0, we apply an out-of-plane component along the x-axis and measure the center frequency of the resonance as a function of the out-of-plane angle β. As discussed above, an out-of-plane magnetic field will significantly modify the resonator frequency. Therefore, we define an effective gyromagnetic rate,

$$\gamma \equiv -\frac{\omega_r(B_0^{max})}{B_0^{max}}. \tag{6.4}$$

Figure 6.9b plots γ as a function of β, and the data is fit to a parabola which yields $\beta_0 = -0.57°$.

By comparing the measured gyromagnetic factor along the c-axis (see Eq. 3.10), we find that the magnetic field in the transmission setup is miscalibrated by a factor 1.002. This effect can be explained by the partial magnetization of the magnetic shield surrounding the cryostat, which introduces a constant shift on the field. This correction is taken into account as a global factor in all the measurements of Chapter 9, so that we estimate the uncertainty on the applied field to less than $\sim 10^{-3}$.

After this characterization, the sample is brought to 10 K and then cooled down again to remove any magnetic vortices in the superconducting film, which reduce the quality factor of the resonator. For all following measurements in this thesis, the field is always applied along the (y, z)-plane,

but the characterization of these angles is crucial for the understanding of the experimental results.

6.6. Individual Er^{3+} spins

Single-spin resolution is achieved by addressing Er^{3+} spins located far from the ensemble central frequency. Because individual detection is not feasible within the main line due to the high density of spins, we focus on the spins that are detuned 4–5 mT above the ensemble center. To detect single spins, we reduce the amplitude of the driving pulse by a factor ~ 50, its duration to 10 µs and the integration time is set to $\tau_{\text{int}} = 10$ ms. In addition, we switch B_X and B_Z to persistent mode and sweep the field with B_Y. Figure 6.10a plots $\langle C \rangle$ as a function of the magnetic field and shows a constant background with a distribution of narrow and reproducible peaks. Previous work performed by Zhiren Wang demonstrated that each peak corresponds to a single Er^{3+} spin through instensity-instensity correlation analysis [14].

[14]: Wang et al. (2023), 'Single-Electron Spin Resonance Detection by Microwave Photon Counting'

We systematically characterize each Er^{3+} spin with the following measurements:

Rabi oscillations We measure $\langle C \rangle$ as a function of the duration of the driving microwave pulse (see Figure 6.10b). On top of the Rabi oscillations, we note a linearly increasing background that we attribute the emission of unknown degrees of freedom [23]. The data is fit to a cosine oscillation with a linearly increasing background. The fit yields the Rabi frequency Ω for the specific microwave amplitude.

[23]: Wang (2023), 'Addressing Individual Electronic Spins with a Microwave Superconducting Resonator'

Fluorescence We measure the count rate $\langle \dot{C} \rangle$ as a function of the time t after the microwave pulse (see Figure 6.10c). After the pulse, we wait a time $\tau_w = 120$ µs before measuring. The data is fit to a single exponential decay with a constant background. Given that the signal comes from a single emitter, the integral of the signal minus the background rate gives the *spin-to-click* efficiency η_{spin}. During the experiments presented in this thesis, $\eta_{\text{spin}} \approx 0.3 - 0.4$, a considerable improvement from previous demonstrations [14], thanks to the increased sensitivity of the SMPD used in this work [73].

[14]: Wang et al. (2023), 'Single-Electron Spin Resonance Detection by Microwave Photon Counting'

[73]: Pallegoix et al. (2025), *Enhancing the Sensitivity of Single Microwave Photon Detection with Bandwidth Tunability*

In addition, the fit yields the relaxation time of the spin T_1. For spins where the relaxation rate is completely dominated by the Purcell effect, we calculate the coupling to the resonator as

$$g_0 = \frac{1}{2}\sqrt{\frac{\kappa}{T_1}} \tag{6.5}$$

In this work we measure $g_0/2\pi$ up to 9 kHz, a noticeable increase compared to ref. [23] where typical couplings ranged between 1–4 kHz. The enhanced coupling can be attributed to the narrower nanowire (see Section 6.1). This results in faster measurements, as the repetition time of the experiment is limited by the relaxation time of the spin T_1, which is proportional to g_0^2.

[23]: Wang (2023), 'Addressing Individual Electronic Spins with a Microwave Superconducting Resonator'

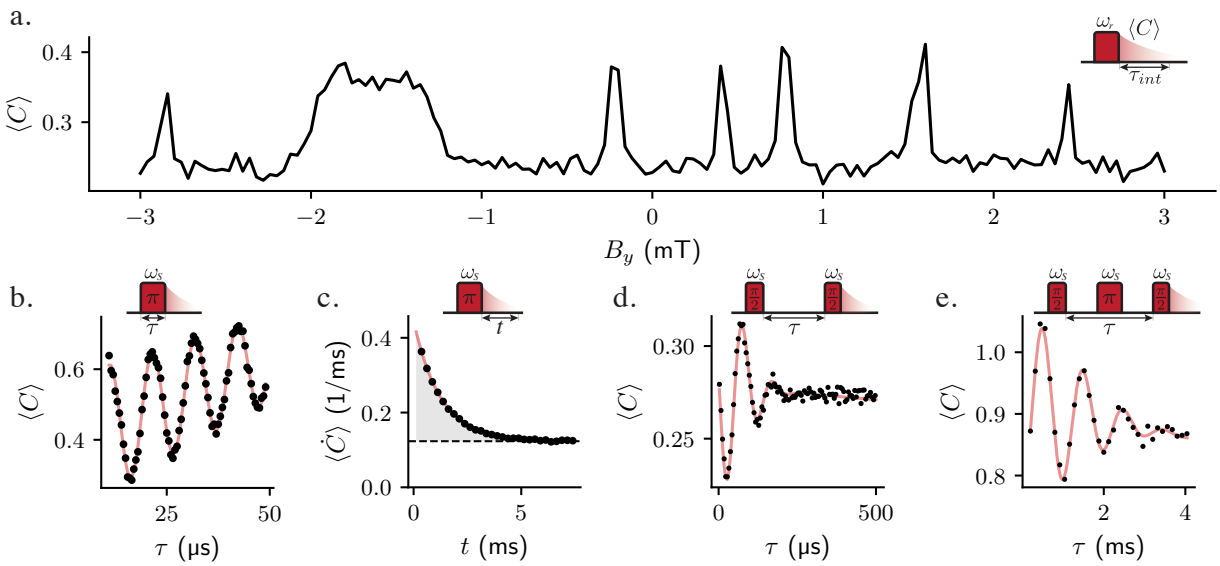

Figure 6.10.: Low power spectroscopy and electron spin characterization. Pulse sequences are shown as an inset in all subplots. **a.** Single spin spectroscopy. Ensemble average counts $\langle C \rangle$ as a function of B_y measured with an integration time $\tau_{\text{int}} = 10$ ms. The measurement data have been connected with a line for visual clarity. **b.** Rabi sequence. $\langle C \rangle$ as a function of the duration of the driving pulse. The measurement was done with an integration time of 1 ms. The data is fit to a cosine oscillation with a linearly increasing background **c.** Single spin fluorescence. Count rate $\langle \dot{C} \rangle$ as a function of the time t after a π pulse. The data is fit to an exponential decay with a constant background. The integral of the data minus the background (gray area and dashed line respectively) gives a *spin-to-click* efficiency $\eta_{\text{spin}} = 0.39$. The fit yields $T_1 = 1.24$ ms from which we calculate the coupling $g_0/2\pi = 4.5$ kHz. **d. & e** Ramsey and Hahn echo sequence. $\langle C \rangle$ as a function of the interpulse delay τ between the two $\pi/2$-pulses. The exponentially decaying cosine fits yield $T_2^* = 81$ µs and $T_2 = 1.3$ ms respectively.

Ramsey and Hahn echo coherence . We measure $\langle C \rangle$ after a Ramsey and a Hahn echo sequence as a function of the interpulse delay between the two $\pi/2$ pulses (see Figure 6.10d & e). The data are fit to an exponentially decaying cosine which yield the T_2^* and T_2 respectively (see Section 4.3). In the experiments we consistently observe $T_2^* \sim 100$ µs and $T_2 \sim 1$ ms. Therefore, the coherence time is generally lifetime-limited. These extraordinary coherence times are consistent with the measurements performed by Marianne le Dantec in ensembles, where they achieve coherence times of ~ 20 ms [26]. As discussed in Section 4.3, this is possible thanks to the combination of low impurity concentration and the low nuclear magnetic moment density of $CaWO_4$.

[26]: Le Dantec et al. (2021), 'Twenty-Three–Millisecond Electron Spin Coherence of Erbium Ions in a Natural-Abundance Crystal'

Finally, we measure a single-spin-resolved rotation pattern around $\theta = 0°$. Figure 6.11 presents a wide-range spectroscopic map concatenated from several measurement sets. We note that the span of the map is considerably larger than ones performed in ref. [23]. This increase is facilitated by the enhanced detection SNR granted by the larger coupling to the spin and improvements on the SMPD.

[23]: Wang (2023), 'Addressing Individual Electronic Spins with a Microwave Superconducting Resonator'

Individual Er^{3+} resonances are clearly resolved and each Er^{3+} spin has a slightly different gyromagnetic ratio. We associate this with inhomogeneous broadening discussed in Section 1. The origin of the shifts likely originates from local strain conditions, which arise due to differential thermal contractions from the metallic wire. Consequently, different spins are subject to different strain tensors depending on their spatial location with respect to the resonator wire.

We note that the top of the parabolas of each spin do not lie at the same value of θ. The strain distorts the γ-tensor, which likely loses its axial character. Nevertheless, there is a direction of minimal effective gyromagnetic tensor, but this direction can be slightly different for each

Er^{3+} spin. In the following, we will call this direction the "local c-axis" of each spin.

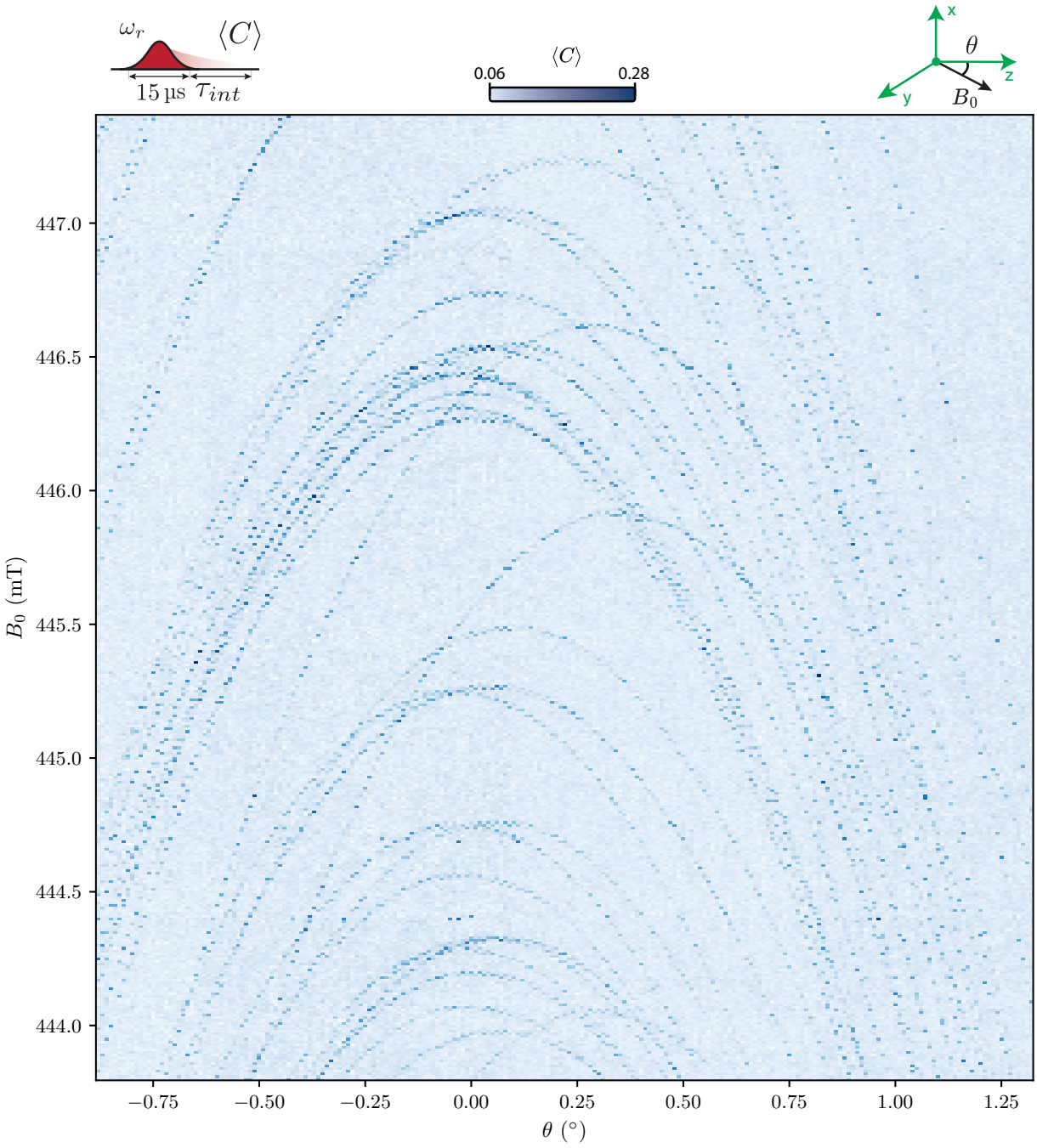

Figure 6.11.: 2D single spin spectroscopy. The map is created by stitching several individual measurements. Each measurement sweeps both the amplitude and the in-plane angle θ of the magnetic field. The SMPD is re-tuned to the resonator approximately every 0.5 mT. The total acquisition time was approximately 1 week

^{183}W NUCLEAR SPINS

All-microwave detection and control of individual ^{183}W nuclear spins

7.

In this chapter, we experimentally demonstrate single ^{183}W nuclear spin detection, spectroscopy, and polarization using a local Er^{3+} spin probe in an all-microwave setup. We begin by reporting the observation of nuclear spin quantum jumps, measured through high-resolution spectroscopy of the Er^{3+} spin. By analyzing the spectral separation of the electron spin frequencies and the quantum-jump rate, we estimate the hyperfine couplings and identify the lattice sites of the ^{183}W nuclear spins relative to the Er^{3+} probe. The strong hyperfine coupling between the Er^{3+} and ^{183}W spins enables single-shot readout of the nuclear spin state by monitoring the EPR-allowed transition frequency via single microwave photon counting. We perform single-spin EDNMR spectroscopy on a ^{183}W nuclear spin by driving the zero- and double-quantum transitions. Through the combination of driving these transitions and electron spin relaxation, we achieve deterministic nuclear spin polarization, also known as solid-effect dynamical nuclear polarization.

The measurements and analysis of the data in this section were performed by me and James O'Sullivan.

7.1 State-of-the-art 70
7.2 Single Er^{3+} spins characterization 73
7.3 Nuclear spin quantum jumps 74
Time trace analysis 74
Tracking procedure 77
7.4 Single-shot readout 79
7.5 Sideband driving and nuclear spin identification 83
7.6 Solid effect DNP 85
7.7 Conclusion and outlook . . 87

7.1. State-of-the-art

Single nuclear spin detection has been achieved in a variety of physical systems. In this section, we focus on two landmark experiments that laid the foundation for readout techniques now routinely implemented and adapted to other defect centers and solid-state systems, including the detection schemes presented in this Chapter.

Single-shot readout of a ^{14}N nuclear spin in diamond

Nitrogen-vacancy (NV) centers are point defects consisting of a substitutional nitrogen atom adjacent to a vacancy in the diamond lattice, as shown in Figure 7.1. This defect forms a localized electronic state within the diamond band gap. In its negatively charged state, the NV center possesses a paramagnetic ground state with total spin $S = 1$. The corresponding energy levels as a function of magnetic field are shown in Figure 7.2a. The electron spin levels are further split by the hyperfine coupling to the ^{14}N nuclear spin.

The optical transitions exhibit spin-dependent fluorescence intensity, a property that enabled the detection of the spin state of an individual NV center using optical excitation [8], followed shortly by the detection of nearby single ^{13}C nuclear spins [83].

Single-shot readout of the ^{14}N nuclear spin was achieved by Neumann *et al.* in 2010 [82]. In the experiment, the electron spin is initialized in the $m_S = 0$ state. A nuclear-spin-selective microwave π-pulse is then applied, transferring the electron population to the $m_S = -1$ state conditional on the nuclear spin state. This selective mapping is possible because the hyperfine splitting of the EPR-allowed transitions is stronger than the

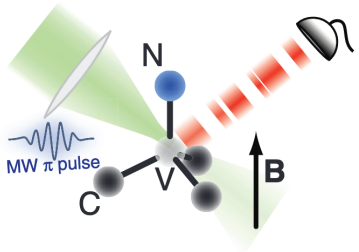

Figure 7.1.: Sketch of an NV center in diamond. A nitrogen and a vacancy (blue and gray respectively) combine in a diamond substrate (black C atoms). In its negatively charged state, the system has $S = 1$ and can be controlled with microwave pulses (in blue). Single-shot readout is performed by measuring the spin-selective optical fluorescence (in red). A green laser is used to readout and prepare the state of the NV center (in green). The figure was taken from [82].

[8]: Jelezko et al. (2002), 'Single Spin States in a Defect Center Resolved by Optical Spectroscopy'

[83]: Jelezko et al. (2004), 'Observation of Coherent Oscillation of a Single Nuclear Spin and Realization of a Two-Qubit Conditional Quantum Gate'

[82]: Neumann et al. (2010), 'Single-Shot Readout of a Single Nuclear Spin'

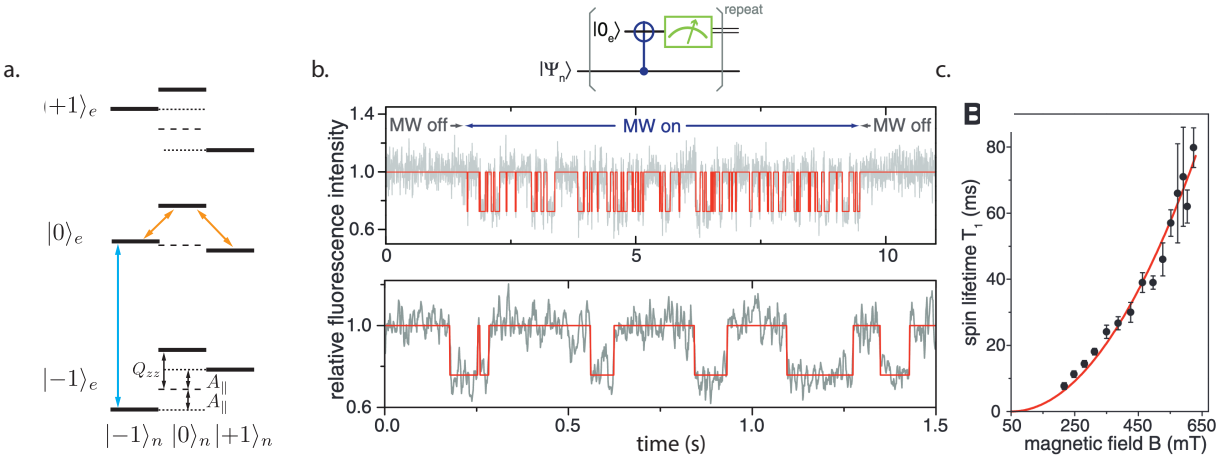

Figure 7.2.: Single-shot readout of a ^{14}N nuclear spin. The figures were taken from [82]. **a.** Complete energy level scheme including magnified ^{14}N hyperfine structure. The EPR-allowed transition is shown in blue. The NMR-allowed transitions are shown as orange arrows. The nuclear spin quadrupole and hyperfine splitting Q and A respectively are depicted as well. The nuclear Zeeman energy has been considered in the diagram. **b.** Normalized fluorescence time traces (gray) as a function of time. The microwave pulses are applied during the time interval defined by the blue arrow. Low fluorescence intensity corresponds to the nuclear spin in state $m_I = -1$, and high fluorescence intensity indicates $m_I = 0, 1$. **c.** Nuclear spin effective lifetime T_1 as a function of the magnetic field intensity along the NV axis. The data are fit to a model of cross-relaxation due to the electron spin scrambling after excitation by a green laser.

decoherence rate of the electron spin. Then, the electron spin is read out optically by measuring the photoluminescence under pulsed green-laser excitation. Therefore, if the ^{14}N is in state $m_I = -1$ the PL should be low, whereas it should be high if the ^{14}N is in state $m_I = 0$ or $m_I = +1$. The fluorescence trace shown in Figure 7.2b reveals real-time quantum jumps of the nuclear spin state.

The time trace shows that the nuclear spin can be interrogated repeatedly before a state change occurs. Under laser excitation, the electron spin is reset in the ground state. Nevertheless, the nuclear spin state remains stable for many cycles. Therefore, the protocol is a projective, single-shot, Quantum Non-Demolition (QND) measurement of the nuclear spin state [84]. The average number of readout cycles before a nuclear spin flip defines an effective nuclear T_1 under measurement.

[84]: Imoto et al. (1985), 'Quantum Nondemolition Measurement of the Photon Number via the Optical Kerr Effect'

This effective lifetime ultimately limits both the readout fidelity and the degree to which the measurement can be considered truly QND. Nuclear spin flips are induced by cross-relaxation through the ZQ/DQ transitions, occurring mostly in the optically-excited state since the hyperfine coupling is ~ 10 times stronger than in the ground-state. As discussed in Section 5.1, the probability of such cross-relaxation events scales inversely with the nuclear Larmor frequency. Consequently, increasing the applied magnetic field enhances the nuclear spin lifetime. Figure 7.2c shows the measured effective nuclear T_1 as a function of magnetic field and is in good agreement with a model that describes cross-relaxation via ZQ/DQ transitions in the optical excited state. A similar mechanism will be present in our system, as ^{183}W nuclear spins will cross-relax through the ZQ/DQ transitions when the electron spin is excited.

^{31}P nuclear spin in silicon

In contrast to optical fluorescence-based readout, electrical detection schemes exploit spin-to-charge conversion mechanisms. One such technique couples a neutral phosphorus donor in silicon to a single-electron transistor (SET). The SET current depends on the charge state of the donor.

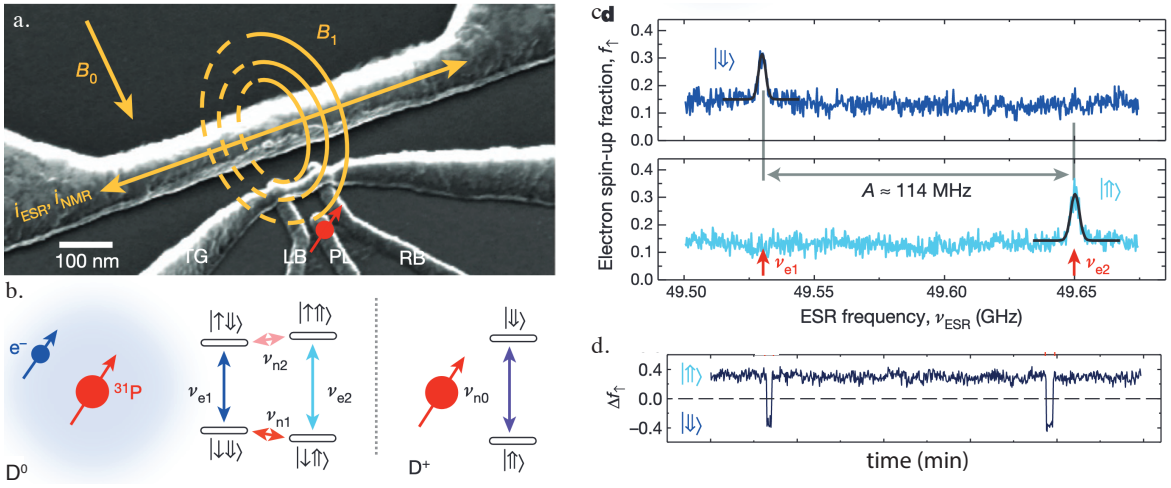

Figure 7.3.: Single-shot readout of a ^{31}P nuclear spin in silicon. The figures were taken from [35]. **a.** Scanning electron micrograph of the device used for the demonstration, showing the SET and the position of the ^{31}P donor. The static and oscillating magnetic fields (B_0 and B_1 respectively) are shown in red. A series of gates used to control the electron spin are highlighted. **b.** *(left)* Energy levels of the neutral ^{31}P donor system, named D^0. In this system, $\omega_S > A > \omega_I$. The EPR-allowed transitions are marked in blue and the NMR-allowed transitions in red. *(right)* Energy levels of the ionized ^{31}P donor system, named D^+. The NMR-allowed transitions are marked in blue. **c.** Spectroscopy of the EPR-allowed transitions. The electron spin up fraction $f_\uparrow$ is plotted as a function of the frequency of the microwave pulse. The top (bottom) plot corresponds to the nuclear spin in $|\Downarrow\rangle$ ($|\Uparrow\rangle$). **d.** Electron spin up fraction difference, $\Delta f_\uparrow = f_\uparrow(\nu_{e2}) - f_\uparrow(\nu_{e1})$ as a function of time, where $f_\uparrow(\nu_{e1,2})$ are the electron spin up fraction at the EPR-allowed frequencies. $\Delta f_\uparrow > 0$ indicates nuclear in $|\uparrow\rangle$, and vice versa.

By applying a strong magnetic field B_0, spin-dependent tunneling can be engineered, as the Zeeman effect lifts the degeneracy of the electron spin states. Therefore, current flowing through the device signals the state of the electron spin, enabling single-shot electron spin readout [9].

The first detection of an individual nuclear spin using this architecture was demonstrated by J. Pla *et al.* in 2013 [35]. The device used in their work is shown in Figure 7.3a. Four electrostatic gates control the potential of the donor. The electron spin is driven using a microwave magnetic field B_1 generated by an on-chip transmission line.

In its neutral state, the donor hosts both an electron and a nuclear spin, coupled via the Fermi contact interaction. The energy level diagram of the coupled system is shown in Figure 7.3b. Compared to the regime discussed in Section 3.6, the hyperfine interaction strength exceeds the nuclear Zeeman splitting, such that $\omega_S > A > \omega_I$. When the donor is ionized, the electron is removed and only the nuclear spin remains.

Figure Figure 7.3c shows electron spin resonance spectroscopy. After applying a microwave π-pulse, two well-resolved peaks in the excited-state population $f_\uparrow$ are observed. The resonance frequency depends on the state of the coupled nuclear spin. These peaks correspond to the two EPR-allowed transitions and are separated by the hyperfine coupling strength, $A \approx 120$ MHz.

By monitoring the difference in excited-state population between the two resonance frequencies, $\Delta f_\uparrow = f_\uparrow(\nu_{e2}) - f_\uparrow(\nu_{e1})$, the nuclear spin state can be discriminated with a fidelity exceeding 0.998. Observation of the nuclear spin dynamics (shown in Figure 7.3d) reveals the presence of a shorter-lived spin state. This effect is attributed to electron-nuclear flip-flop processes occurring during electron spin readout. The authors mitigate this mechanism by increasing the donor ionization rate, thereby suppressing unwanted spin exchange during measurement.

[9]: Morello et al. (2010), 'Single-Shot Readout of an Electron Spin in Silicon'

[35]: Pla et al. (2013), 'High-Fidelity Readout and Control of a Nuclear Spin Qubit in Silicon'

Discussion

The two experiments rely on the hyperfine interaction between a nuclear spin and a proximal electron spin to enable single-shot nuclear spin readout. Fundamentally, they resolve the hyperfine splitting of the EPR-allowed transitions. In both approaches, successful discrimination of the nuclear spin state requires that the hyperfine coupling exceed the electron spin linewidth, ensuring that the EPR transitions are spectrally resolvable.

Such strong hyperfine interactions are typically achieved when the electron and nuclear spins are coupled through the Fermi contact interaction, leading to coupling strengths on the order of several megahertz. In contrast, dipolar interactions with more distant nuclear spins are significantly weaker and therefore more challenging to resolve spectroscopically. Nevertheless, advances in dynamical decoupling have enabled the detection of large ensembles of weakly coupled distant ^{13}C spins using a single NV center [85].

[85]: van de Stolpe et al. (2024), 'Mapping a 50-Spin-Qubit Network through Correlated Sensing'

Using magnetically silent substrates is a promising path towards single nuclear spin detection. In this context, $CaWO_4$ has demonstrated exceptionally long electron spin coherence times in ensembles [26]. Such narrow intrinsic linewidths relax the requirement for large hyperfine coupling strengths. Consequently, ^{183}W nuclear spins that are coupled through magnetic dipole interaction to an Er^{3+} impurity should, in principle, be spectroscopically resolvable even without resorting to dynamical decoupling techniques. This is the topic of the present chapter.

[26]: Le Dantec et al. (2021), 'Twenty-Three–Millisecond Electron Spin Coherence of Erbium Ions in a Natural-Abundance Crystal'

7.2. Single Er^{3+} spins characterization

In this chapter we focus on five different Er^{3+} ions, which we label Er_i with $i = \{1, 2, 3, 4, 5\}$. After identifying an individual Er^{3+} spin, we set the magnetic field amplitude and angle such that the electron spin frequency is close to the resonator frequency, *i.e.* $\omega_r \approx \omega_S$, and set the coils on persistent mode. We proceed by characterizing the spin following the procedure described in Section 6.6. This yields the values shown in Table 7.1. Due to time constraints, some coherence times were not measured for certain ions.

As discussed in Section 6.6, the measured coherence times are remarkably long when compared to other single electron spins in the solid-state discussed in the *state-of-the-art* section. In fact, the decoherence time is generally lifetime-limited. In addition, given that $T_2^* \sim 100$ µs, hyperfine couplings in the order of 10 kHz should be resolved, enabling the detection of single ^{183}W nuclear spins.

	Er_1	Er_2	Er_3	Er_4	Er_5
T_1 (ms)	2.0(3)	0.71(1)	0.90(1)	0.80(3)	1.24(1)
$g_0/2\pi$ (kHz)	3.6(2)	6.0(2)	5.3(2)	5.6(2)	4.5(1)
T_2^* (µs)	-	53(5)	-	170(5)	81(2)
T_2 (ms)	-	-	-	2.05(3)	1.3(1)

Table 7.1.: Electron spin characterization for 5 different ions Er_i. Dashes are in place when the measurement was not performed.

7.3. Nuclear spin quantum jumps

After identifying and characterizing individual Er^{3+} ions, we perform high-resolution spectroscopy by exciting the spin with an 80 µs long Gaussian-shaped microwave π-pulse, with frequency ω, followed by microwave fluorescence detection, sweeping $\delta = \omega - \omega_r$ over $2\pi \times 100$ kHz. Each sweep is averaged 200 times to obtain the ensemble-averaged number of counts $\langle C \rangle(\delta)$. Figure 7.4a shows such spectra measured repeatedly during 150 minutes for $Er_1 - Er_5$. Ion Er_1 displays a single line, whose center frequency fluctuates on a timescale of several minutes and on a frequency scale of ~ 20 kHz. This spectral diffusion is attributed to a combination of B_0 drift, charge noise, and rearrangements of the weakly coupled nuclear spin bath, and was observed for all measured ions, although with varying intensity (see discussion below). Because the drift is slow, it can be compensated by various frequency-tracking strategies (see discussion below) that are used in all the measurements reported later in this chapter. In contrast, the electron spin frequencies of ions Er_2, Er_3, and Er_5 display a clear telegraphic noise between two frequencies (four, in the case of Er_4). Similar to the systems discussed in Section 7.1, these jumps occur when one nearby ^{183}W nuclear spin changes state. Quantum jumps are a hallmark of the measurement of individual quantum systems, and, aside from nuclear spins, they have been observed for trapped ions [86–88], photons in a high-Q microwave cavity [89, 90], and superconducting circuits [91]. Here, we report their observation in individual ^{183}W nuclear spins by microwave fluorescence detection.

The transition frequency of each spectrum $\tilde{\delta}(t)$ is obtained from a Lorentzian fit, shown as a histogram in Figure 7.4b for the five ions. Each histogram presents a different number of resolved distributions. For Er_2, Er_3 and Er_5, the two resolved distributions indicate the presence of a strongly coupled neighboring nuclear spin. In contrast, Er_4 shows four resolved distributions, which correspond to two strongly coupled nuclear spins. The pair will be referred to as $Er_4^{(1)}$ and $Er_4^{(2)}$ in the following. We note that the standard deviation of the individual distributions is significantly different for each ion, indicating that part of the drift originates from their local environment, likely from unresolved nuclear spin jumps.

[86]: Nagourney et al. (1986), 'Shelved Optical Electron Amplifier'
[87]: Bergquist et al. (1986), 'Observation of Quantum Jumps in a Single Atom'
[88]: Sauter et al. (1986), 'Observation of Quantum Jumps'
[89]: Gleyzes et al. (2007), 'Quantum Jumps of Light Recording the Birth and Death of a Photon in a Cavity'
[90]: Guerlin et al. (2007), 'Progressive Field-State Collapse and Quantum Non-Demolition Photon Counting'
[91]: Vijay et al. (2011), 'Observation of Quantum Jumps in a Superconducting Artificial Atom'

Time trace analysis

The energy level structure presented in Section 3.6 dictates that the difference in frequency between the two EPR-allowed transitions is a good estimate of the parallel hyperfine coupling $|A_\parallel|$ in the high-field regime. To extract this value, we measure the difference in frequency between each time window,

$$\Delta\tilde{\delta}(\tau) = \tilde{\delta}(\tau) - \tilde{\delta}(\tau - \Delta t), \tag{7.1}$$

where Δt is the difference in time between subsequent traces. $\Delta\tilde{\delta}$ is plotted in Figure 7.5a as a function of time for Er_2. Depending on the number of strongly coupled nuclear spins, the value distribution of $\Delta\tilde{\delta}$ will show a different number of peaks (see Figure 7.5b). The peak centered at 0 arises when no resolved jump occurs between two consecutive traces. A Gaussian fit yields a full width at half maximum varying from 4.5 to

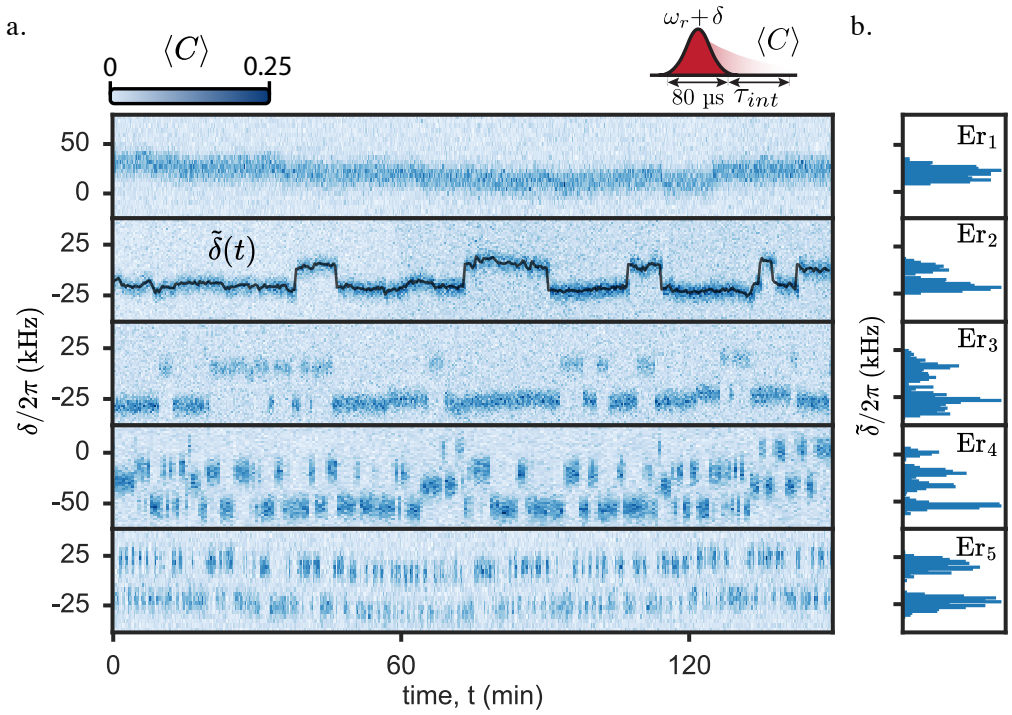

Figure 7.4.: Er^{3+} time traces. **a.** *(top)* Fluorescence detection spectroscopy pulse scheme. A Gaussian π-pulse of duration 80 µs and frequency $\omega_r + \delta$ is applied to the sample. The ensemble-averaged number of counts $\langle C \rangle$ is subsequently measured during an integration time window, τ_{int}. The sequence is then repeated without any delay, with the excitation pulse frequency updated. *(bottom)* High-resolution spectra of five Er^{3+} ion spins, measured consecutively during 150 minutes. Each spectrum is recorded by averaging 200 sweeps of δ, yielding the ensemble-averaged number of counts $\langle C \rangle(\delta)$. The integration time τ_{int} is 1.6 ms for Er_1, 2.0 ms for $Er_{2,3}$ and 3.6 ms for $Er_{4,5}$. The increase in counts corresponds to the detected fluorescence after exciting an EPR-allowed transition. The resonance frequency evolves in time with a slow drift and sudden telegraphic jumps. Each spectrum is fitted as a Lorentzian and the center $\tilde{\delta}$ is shown as a function of time for Er_2 as a black continuous line. **b.** Histograms of $\tilde{\delta}$ for the five ions.

10 kHz, indicating that the short-term noise (at the minute scale) also varies significantly from ion to ion. The extra peaks observed for Er_{2-5} arise from resolved nuclear spin quantum jumps. Gaussian fits to these peaks yield the mean frequency jump size, which corresponds to $|A_\parallel|$. The measured values are shown in Table 7.3. We note that the standard deviation of the satellite peaks is similar in value to the central peak, as expected.

The direct relaxation rate of ^{183}W nuclear spins proximal to Er^{3+} impurities in $CaWO_4$ is exceedingly slow at 10 mK, with an upper bound of approximately 10^{-6} s^{-1} [70]. Therefore, we attribute the origin of the quantum jumps to cross-relaxation events, during which the electron spin relaxes through the weakly allowed ZQ and DQ transitions. We define the cross-relaxation probability as

[70]: Wang et al. (2024), *Month-Long-Lifetime Microwave Spectral Holes in an Erbium-Doped Scheelite Crystal at Millikelvin Temperature*

$$p_{\text{ZQ, DQ}} = \frac{N_{ZQ,DQ}}{N_{\text{ex}}}, \tag{7.2}$$

where $N_{\text{ZQ, DQ}}$ is the number of ZQ and DQ transitions and N_{ex} is the number of electron excitations.

$N_{\text{ZQ, DQ}}$ is straightforward to obtain from the histograms presented in Figure 7.5b as each event under the satellite peaks corresponds to a single cross-relaxation event.

The number of electron excitations N_{ex} depends on the step-size of the

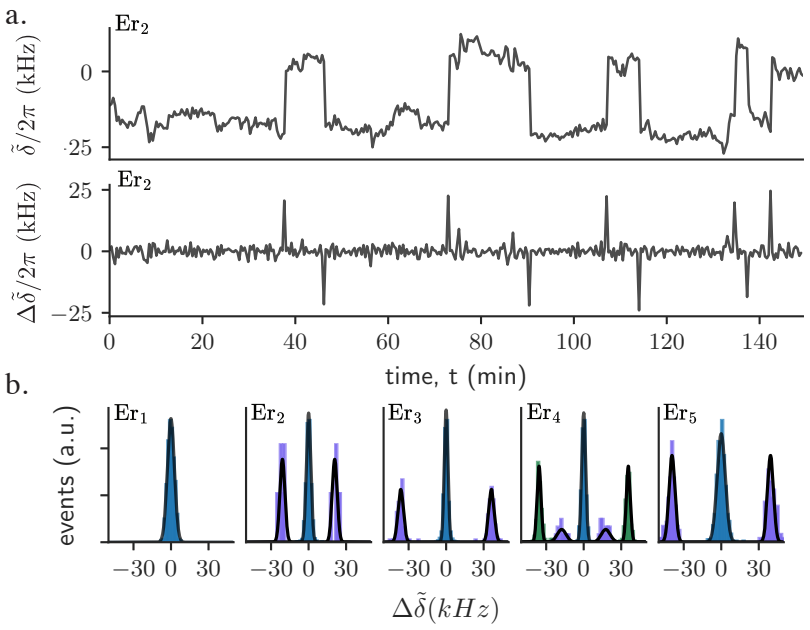

Figure 7.5.: a. *(top)* Lorentzian fit center $\tilde{\delta}$ as a function of time for Er_2. *(bottom)* Difference between consecutive values of the fitted frequency $\Delta\tilde{\delta}$ as a function of time. **b.** Histograms of $\Delta\tilde{\delta}$ for the five ions. The satellite peaks have been rescaled by an arbitrary factor for visibility. Each peak has been fit to a Gaussian distribution (black line). The difference between their centers yields the parallel hyperfine coupling constant of each nuclear spin, $A_\parallel$.

frequency sweep. Because detuned π-pulses still drive the electron spin when they fall within the linewidth, every pulse contributes with a weight set by the lineshape. Thus, the total excitation count per sweep can be estimated by summing over all applied pulses, each weighted by a Lorentzian profile with the fitted linewidth.

Table I shows the cross-relaxation probabilities for the coupled nuclear spins of Er_{2-5}. The measured values were extracted from longer traces, this is particularly important when the cross-relaxation rate is low as significant statistics require long measurement time. We note that, for $Er_4^{(1)}$, there is significant difference between p_{ZQ} and p_{DQ}. This is consistent with the nuclear spin spending a considerably longer amount of time in one of the states compared to the other, as noted through visual inspection of Figure 7.4. A large detuning with respect to the resonator center can induce this effect, as the Purcell enhancement of the two transitions is equal only when $\omega_S = \omega_r$. However, the measured detuning is not enough to explain the large disagreement between the two cross-relaxation rates. Further studies are needed to understand the origin of this difference, but a working hypothesis is the existence of an extra, non-radiative relaxation channel mediated through another Er^{3+} spin.

	$p_{ZQ} \cdot 10^5$	$p_{DQ} \cdot 10^5$
Er_2	1.5(7)	0.8(3)
Er_3	5.8(6)	4.2(4)
$Er_4^{(1)}$	18(2)	9(1)
$Er_4^{(2)}$	1.6(7)	0.7(3)
Er_5	24(2)	24(2)

Table 7.2.: Cross-relaxation probability measured through the time-trace analysis. The uncertainties of the cross-relaxation probabilities are estimated through the Wald method with a 1 sigma confidence interval.

Finally, we compare the measured data to the analytical equation derived in Section 5.1 for $p_{ZQ,\,DQ}$, which we remind here:

$$p_{ZQ,\,DQ} = \frac{1}{1 + 4\omega_I^2/\kappa^2} \frac{A_\perp^2}{4\omega_I^2}. \tag{7.3}$$

From this equation, we estimate $A_\perp$ by averaging both probabilities. The results are presented alongside the measured values of $A_\parallel$ in Table 7.3.

	Er_2	Er_3	$Er_4^{(1)}$	$Er_4^{(2)}$	Er_5
$\lvert A_\parallel\rvert/2\pi$ (kHz)	21(1)	36.3(6)	38.5(8)	19(1)	39.6(5)
$\lvert A_\perp\rvert/2\pi$ (kHz)	12(3)	27(3)	40(5)	11(3)	72(5)
θ (deg)	-0.3	-0.2	- 0.1	-0.1	0.1
type	3	1 | 2	1 | 2	3	1

Table 7.3.: Hyperfine coupling between the neighbouring ^{183}W of each Er^{3+} spin and site assignment.

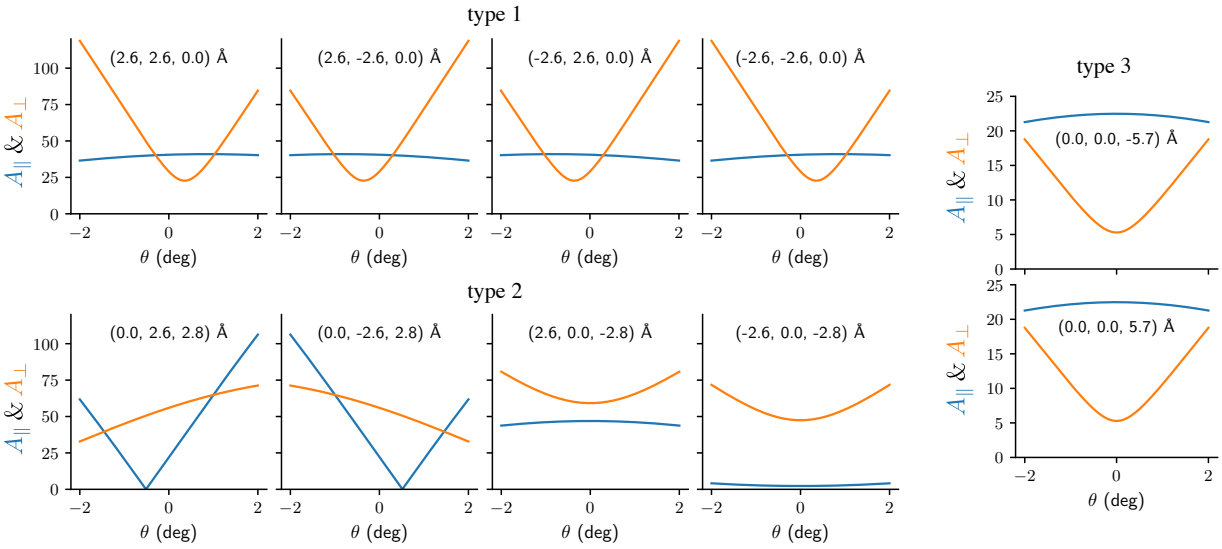

Figure 7.6.: Hyperfine coupling $A_\parallel$ and $A_\perp$ obtained through a dipole-dipole Hamiltonian simulation as a function of the in-plane angle θ. The calculation considers the measured out-of-plane angle $\beta = -0.57°$. The position of the ions is specified in angstroms. The plots are organized depending on the relative position of the nuclear spin with respect to the Er^{3+} spin, as shown in Figure 7.7.

By comparing the measured values of $A_\parallel$ and $A_\perp$ to magnetic dipole simulations, shown in Figure 7.6, we can tentatively assign the crystalline site of each nuclear spin. When the magnetic field is applied approximately parallel to the c-axis, we can distinguish three types of magnetically similar sites within a unit cell centered around the Er^{3+} impurity, as shown in Figure 7.7. The assignment of each nuclear spin is shown in Table 7.3.

For the nuclear spins coupled to Er_2 and $Er_4^{(2)}$, the measured values of $A_\parallel$ and $A_\perp$ are close to those expected from type 3 sites, making this site assignment likely. The other nuclear spins have larger values of $|A_\parallel|$ and $|A_\perp|$, implying that they are either type 1 or type 2 sites; however, the match is not quantitative with any of the sites. Several reasons could explain this. First, local deformations of the crystal could be caused by the larger positive charge of Er^{3+} compared to the original Ca^{2+}. Second, the measured ions are notably strained, as evidenced by the fact that they are found several mT above the center of the ensemble line (as discussed in Section 6.6). In the case of the nuclear spin coupled to Er_5, the value of $|A_\perp|$ measured is notably larger than the range predicted both for type 1 and type 2; however, for larger angles, type 1 spins reach such large $|A_\perp|$ values (see Figure 7.6), motivating a tentative assignment of Er_5 to a type 1 site. We finally note that site assignment should be made easier by the measurement of the angular dependence of $A_\parallel$ and $A_\perp$.

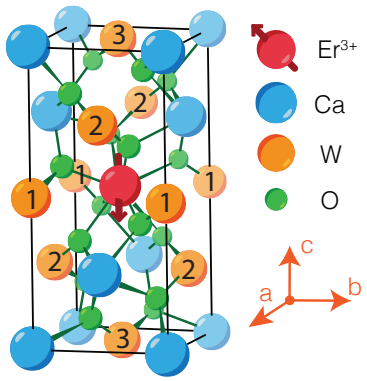

Figure 7.7.: $CaWO_4$ crystal with magnetically similar sites when the field is applied along the c-axis, grouped into three types.

Tracking procedure

As discussed in the previous section, the frequency drift on the EPR-allowed frequencies is on the same order of magnitude as the linewidth of the transition. Without active tracking and compensation of the drift, the fluorescent intensity of the transition will not be constant, resulting in a reduction of SNR. However, the noise has a characteristic timescale of minutes, which is slow when compared to the duration of our pulse sequences. Therefore, it is possible to track the drift between averages, which allows us to compensate it during the next sequence.

A rudimentary but straightforward tracking protocol can be implemented by performing high-resolution spectroscopy with a small sweeping range around the electron transition frequency[1]. The ensemble averaged number of counts $\langle C \rangle(\delta)$ is then fitted to a Lorentzian, as shown in Figure 7.8 The center of the fit yields the new electron spin transition frequency and the pulse frequencies are updated for the next measurement. This algorithm is straightforward and reliable, but the main drawback is the time it takes to obtain a reasonable fit, approximately 1 minute. Therefore, it can only be realistically run a limited number of times, resulting in poor tracking.

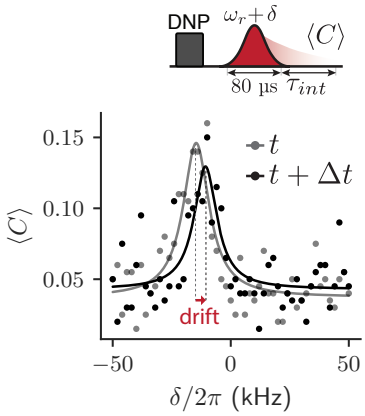

Figure 7.8.: Rudimentary tracking scheme. Ensemble average number of counts $\langle C \rangle$ as a function of the pulse frequency $\omega_r + \delta$ after polarization of the neighboring ^{183}W spins (see text). The two traces are separated by $\Delta t \sim 2$ minutes and the data (dots) are fit to a Lorentzian (line). The red arrow indicates the drift in the EPR-allowed transition after the waiting time.

Due to the limitations of the direct tracking procedure, we envisioned a second algorithm focused on speed rather than fine control. This method exploits the properties of a Ramsey measurement as a frequency sensor. One possible strategy for tracking the drift would be to measure the full Ramsey fringe and fit the oscillation frequency, but this method will again be limited by the data acquisition time. Instead, the tracking can be greatly accelerated by probing only a single time point on the Ramsey curve, chosen for maximal sensitivity. This point corresponds to the zero crossing of the Ramsey oscillation, where the population of the electron spin is linear in the instantaneous drift $\delta\omega$. For this single-point Ramsey sensor, sensitivity is maximized when $\tau \sim T_2^*$ as it balances long phase accumulation time with low information loss due to decoherence.

In practice, fluctuating dark counts introduce a varying offset in the measured counts C. We remove this offset by phase cycling: the Ramsey sequence is repeated with an added π phase shift on the second pulse, producing a second measurement $\bar{C}$. Subtracting the two, $C - \bar{C}$, cancels the offset and yields a signal that is linear in $\delta\omega$, provided that $\tau \ll 2\pi/\Delta\omega$ (see Figure 7.9a).

The quantity $C - \bar{C}$ can be used as the process variable of a Proportional-Integral (PI) loop with a setpoint at zero, integrated within the FPGA logic. In practice, we define the variable Y_i which carries a short memory by filtering the values of the sensor output for every iteration i of the PI

1: To account for nearby nuclear spins, we perform dynamical nuclear polarization before tracking (see Section 7.6)

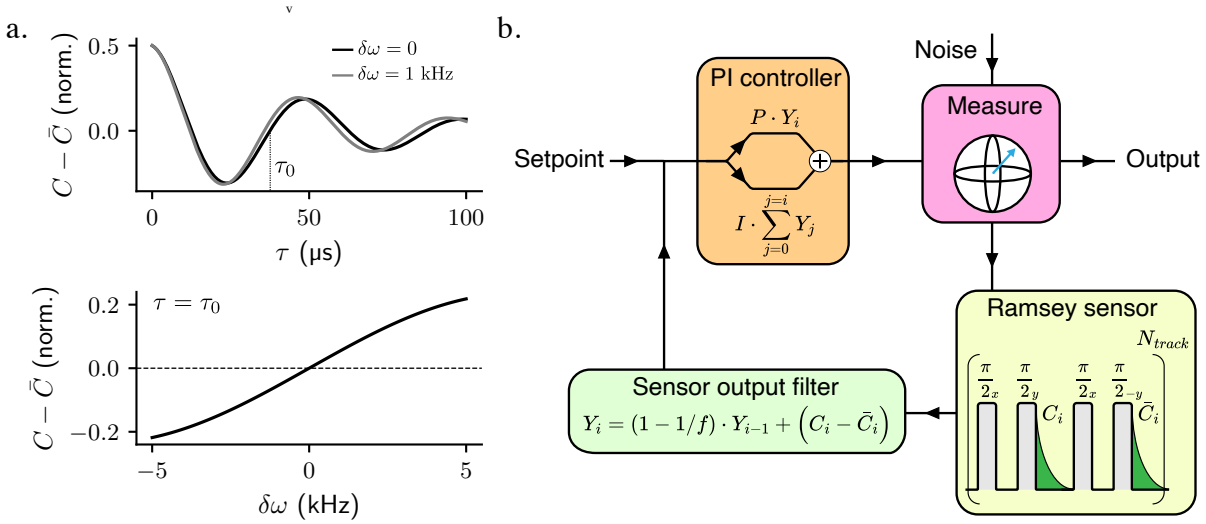

Figure 7.9.: Ramsey tracking scheme. **a.** *(top)* Simulated Ramsey measurement under phase cycling. The signal was generated with a dephasing time of 50 µs and artificial detuning of 20 kHz and 21 kHz (red and gray respectively). The resulting quantity, $C - \bar{C}$, is plotted as a function of the interpulse delay τ. *(bottom)* A single-point Ramsey at $\tau = \tau_0$ as a function of $\delta\omega$. This quantity has a stable setpoint at zero (dashed horizontal line) and is linear in the detuning for small values of $\delta\omega$. **b.** Feedback loop diagram. The PI loop is run after every measurement to correct any shift in the frequencies of the system.

loop,

$$Y_i = \sum_{j=0}^{i} (C_j - \bar{C}_j)\, e^{-(j-i)/f} \approx (1 - 1/f)\, Y_{i-1} + (C_i - \bar{C}_i), \qquad (7.4)$$

where $f = 2000$ is the memory of the system. Finally, the PI controller calculates the frequency correction to be applied on the pulses through a proportional and an integral channel,

$$\delta\omega_i = P\, Y_i + I \sum_{j=0}^{i} Y_j. \qquad (7.5)$$

The values for P and I were set by manually optimizing the convergence time after artificially detuning the pulse frequency. Figure 7.9b shows a block diagram with the control loop.

The second tracking procedure is used to compensate for the drift in all measurements presented in this chapter and the next, unless explicitly stated.

7.4. Single-shot readout

We leverage the ability to spectrally resolve the different allowed transition frequencies of the electronic spin to perform a projective, QND, single-shot measurement of the nuclear spin state (see Figure 7.11a). We apply sequences of frequency-resolved excitation pulses at $\omega_S - A/2$ and $\omega_S + A/2$. The pulses are Gaussian-shaped, 80 µs long and spaced by an integration time τ_{int} during which the fluorescence counts are measured; repeating this N_{RO} times yields the number of counts after each sequence $C_\uparrow$ and $C_\downarrow$. Figure 7.11b shows the described pulse sequence.

We continuously record $C_\uparrow$ and $C_\downarrow$ for ion Er_2 over a 7-hour period using $N_{\text{RO}} = 10^3$ readout pulses per sequence. The two time traces appear in Figure 7.10a, and show strongly anti-correlated behavior. The measurement did not include any tracking, which results in a drift of the maximum counts over time.

The photon-counting histograms for each trace are shown in Figure 7.10b. They present two well-separated distributions. We note that the

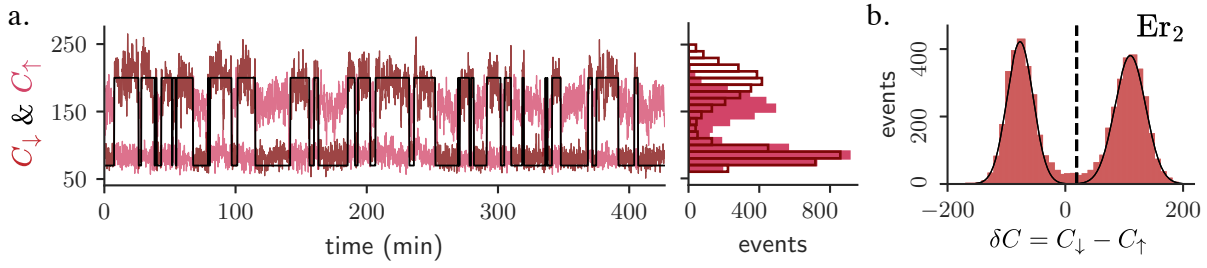

Figure 7.10.: Single-shot readout trace. The measurement in this figure did not include tracking. **a.** *Left* Integrated counts $C_\downarrow$ (resp. $C_\uparrow$) as a function of time as a dark red (resp. light red) solid line. The data were taken for Er_2 with integration time $\tau_{\text{int}} = 1.6$ ms and $N_{\text{RO}} = 10^3$. Quantum jumps appear as abrupt changes in the number of counts with a telegraphic trajectory. The two traces are anti-correlated and the state of the nuclear spin can be mapped to $|\downarrow\rangle$ when $C_\downarrow > C_\uparrow$, represented by a black solid line. *Right* Readout histograms of $C_\downarrow$ and $C_\uparrow$. The lower number of counts in state $\uparrow$ is attributed to imperfect SMPD frequency tuning, resulting in different fluorescence intensities. **b.** Histogram of $\delta C \equiv C_\downarrow - C_\uparrow$. A bimodal Gaussian distribution fit is plotted as a solid black line. The vertical black dashed line shows the threshold for single-shot readout.

distribution centers are not identical, and we measure a lower count signal for $C_\uparrow$. We attribute this difference to imperfect tuning of the SMPD center frequency and the resulting bias in detector efficiency.

The histogram of the count difference $\delta C \equiv C_\downarrow - C_\uparrow$ shows two symmetric and well-resolved peaks (see Figure 7.10b). We define a threshold at the minimum of the distribution, which enables single-shot readout of the nuclear spin state.

We characterize the fidelity of the readout of the ^{183}W nuclear spin of Er_5 as a function of N_{RO} by deterministically preparing the nuclear spin in a specific state (see the following section) and measuring the population of the prepared state as a function of N_{RO} (see Figure 7.12). At first, the probability of a correct assignment increases with N_{RO}, due to the increase in Signal-to-Noise Ratio (SNR). After reaching a maximum value, the probability exponentially decreases with N_{RO}, due to the finite cross-relaxation probability $p_{ZQ,DQ}$ at each readout step. In the following, we present a model that computes the ^{183}W state readout fidelity resulting from these two phenomena.

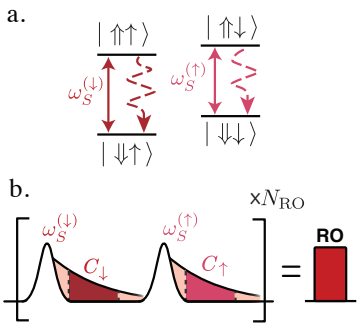

Figure 7.11.: a. Energy level diagram of an ^{183}W-Er^{3+} coupled system. EPR-allowed transitions are represented as solid bright and dark red lines and the respective radiative decays in dashed lines of the same color. **b.** Single-shot nuclear readout pulse sequence. Resonant pulses are applied on each EPR-allowed transition and the counts are recorded independently for the two frequencies. The sequence is repeated N_{RO} times, yielding the number of counts after each sequence, $C_\downarrow$ and $C_\uparrow$.

SNR of the measurement We consider a nuclear spin prepared in $|\downarrow\rangle$. Since the spin is completely polarized, the measured counts $C_\uparrow$ will arise solely from detector dark-counts and can be modelled as a Poissonian random variable with rate $N_{RO}\,\Gamma_{DC}\,t_d$ where Γ_{DC} is the detector dark-count rate and t_d is the duration of each detection window (see Section 4.4).

In contrast, the measured counts $C_\downarrow$ contain contributions from both detector dark counts and real fluorescence events. We model the fluorescence contribution as a binomial random variable with sample size N_{RO} and success probability η, where η denotes the spin-to-click detection efficiency. The total distribution of $C_\downarrow$ is therefore given by the sum of a Poisson-distributed dark-count process and a binomially distributed fluorescence process. Direct addition of these two distributions does not have a simple form, but it can be significantly simplified in the experimentally relevant regime.

When the Poisson rate and the binomial sample size are sufficiently large, both distributions can be well approximated by Gaussian distributions according to the central limit theorem. In this limit, their sum is also

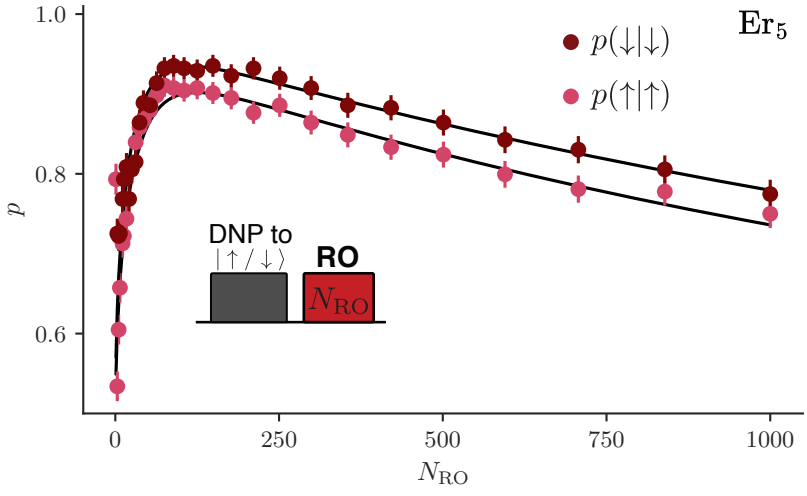

Figure 7.12.: Single-shot readout fidelity for Er_5. Probability of measuring state $|\downarrow\rangle$ and $|\uparrow\rangle$ (resp. dark and light red) as a function of N_{RO}, after preparation in the respective state. Experimental data are shown as red dots and the fit is shown as a solid black line. The data were obtained for Er_5 with integration time τ_{int} = 2 ms. *Inset.* Pulse sequence. The nuclear spin is initialized into state $\downarrow$ (resp. $\uparrow$) through a DNP sequence (see Section 7.6) followed by state readout with variable N_{RO}.

Gaussian, with mean and variance equal to the sum of the respective means and variances of the individual contributions.

The distributions for $C_\uparrow$ and $C_\downarrow$ are then

$$\begin{aligned} C_\uparrow &\sim \mathcal{N}(\mu_\uparrow, \sigma_\uparrow^2) \\ \mu_\uparrow &= \sigma_\uparrow^2 = N_{\mathrm{RO}}\,\Gamma_{\mathrm{DC}}\,t_{\mathrm{d}} \end{aligned} \tag{7.6}$$

$$\begin{aligned} C_\downarrow &\sim \mathcal{N}(\mu_\downarrow, \sigma_\downarrow^2) \\ \mu_\downarrow &= N_{\mathrm{RO}}\left(\eta + \Gamma_{\mathrm{DC}}\,t_{\mathrm{d}}\right) \\ \sigma_\downarrow^2 &= N_{\mathrm{RO}}\left(\eta\,(1-\eta) + \Gamma_{\mathrm{DC}}\,t_{\mathrm{d}}\right) \end{aligned} \tag{7.7}$$

The quantity used for single-shot readout corresponds to the difference in counts $\delta C = C_\downarrow - C_\uparrow$, which is given by

$$\begin{aligned} \delta C &\sim \mathcal{N}(\mu_\delta, \sigma_\delta^2) \\ \mu_\delta &= \mu_\downarrow - \mu_\uparrow = N_{\mathrm{RO}}\eta \\ \sigma_\delta^2 &= \sigma_\downarrow^2 + \sigma_\uparrow^2 = N_{\mathrm{RO}}\left(\eta\,(1-\eta) + 2\Gamma_{\mathrm{DC}}\,t_{\mathrm{d}}\right) \end{aligned} \tag{7.8}$$

The threshold-based nuclear spin state assignment translates to an integral of the probability density function of the δC distribution from the threshold and ∞. As the model does not include detector bias, we take the threshold at zero. The probability of measuring the prepared state is

$$p_{\mathrm{SNR}}(\downarrow \mid \downarrow, N_{\mathrm{RO}}) = \int_0^\infty \frac{1}{\sigma_\delta\sqrt{2\pi}}\, e^{-\frac{(x-\mu_\delta)^2}{2\sigma_\delta^2}}\, dx = \frac{1}{2}\left(1 + \mathrm{Erf}\left[\frac{\mathrm{SNR}}{\sqrt{2}}\right]\right) \tag{7.9}$$

where SNR corresponds to the Signal-to-Noise Ratio,

$$\mathrm{SNR} = \frac{\mu_\delta}{\sigma_\delta} = \frac{\eta}{\sqrt{\eta\cdot(1-\eta) + 2\Gamma_{\mathrm{DC}}\,t_{\mathrm{d}}}} \cdot \sqrt{N_{\mathrm{RO}}}. \tag{7.10}$$

The SNR is proportional to $\sqrt{N_{\mathrm{RO}}}$ and the prefactor contains detector specific parameters which can be measured from the fluorescence curve of the spin as detailed in Section 6.5. For the measurement shown in Figure 7.12 we estimate $\eta = 0.18$, $\Gamma_{\mathrm{DC}} = 150\ \mathrm{s}^{-1}$, $t_{\mathrm{d}} = 2.6$ ms.

Population evolution due to cross-relaxation The cross-relaxation events introduce a dynamic change in the population of the nuclear spin states. The population evolution can be modeled through a system of discrete rate equations by considering the finite probabilities of cross-relaxation $p_{\mathrm{ZQ,DQ}}$,

$$\begin{aligned} \frac{\Delta P_\downarrow}{\Delta N_{\mathrm{RO}}} &= p_{\mathrm{DQ}} P_\uparrow - p_{\mathrm{ZQ}} P_\downarrow, \\ \frac{\Delta P_\uparrow}{\Delta N_{\mathrm{RO}}} &= p_{\mathrm{ZQ}} P_\downarrow - p_{\mathrm{DQ}} P_\uparrow, \\ P_\uparrow + P_\downarrow &= 1. \end{aligned} \tag{7.11}$$

In our specific case, $p_{\mathrm{ZQ,DQ}} \ll 1$ and the dynamics of the system are much slower than the step size. Therefore we can approximate the discrete evolution as a continuous derivative, $\frac{\Delta P_\downarrow}{\Delta N_{\mathrm{RO}}} \approx \frac{dP_\downarrow}{dN_{\mathrm{RO}}}$. We solve the equations by considering the initial condition $P_\downarrow(0) = P_0 < 1$ which yields

$$P_\downarrow(N_{\mathrm{RO}}) \;=\; (P_0 - \frac{p_{\mathrm{DQ}}}{p_{\mathrm{DQ}} + p_{\mathrm{ZQ}}}) \cdot e^{-(p_{\mathrm{DQ}} + p_{\mathrm{ZQ}}) \cdot N_{\mathrm{RO}}} + \frac{p_{\mathrm{DQ}}}{p_{\mathrm{DQ}} + p_{\mathrm{ZQ}}}. \tag{7.12}$$

The populations exponentially converge to a stable state which depends on the relative cross-relaxation probabilities. In the following, we consider that both cross-relaxation rates are equal $p_{\mathrm{ZQ}} \approx p_{\mathrm{DQ}} = p_{\mathrm{x}}$, and complete polarization of the nuclear spin state at the beginning of the sequence $P_0 = 1$ and the equation can be simplified to

$$P_\downarrow(N_{\mathrm{RO}}) \;\approx\; \frac{1}{2}\left(1 + e^{-2p_{\mathrm{x}} N_{\mathrm{RO}}}\right), \tag{7.13}$$

In conclusion, cross-relaxation drives the system into an unpolarized state when $N_{\mathrm{RO}} \gg p_{\mathrm{x}}^{-}1$; larger p_x gives faster deterioration of the prepared nuclear population and thus limits the number of usable readout pulses.

Total fidelity of the measurement The final readout fidelity is set by a combination of the two processes described above, which have different scaling on N_{RO}.

As shown in Figure 7.12, the two effects operate in different timescales. The assignment probability rapidly converges after approximately $N_{RO} \approx 10^2$, while, the effective nuclear spin lifetime due to cross-relaxation events is $N_{RO} \approx 10^3$. Therefore, we consider both processes independent, and we model the total assignment probability by weighting the discrimination success by the population remaining in the target level:

$$p(\downarrow \mid \downarrow, N_{\mathrm{RO}}) \approx p_{\mathrm{SNR}}(\downarrow \mid \downarrow, N_{\mathrm{RO}})\, P_\downarrow(N_{\mathrm{RO}}), \tag{7.14}$$

This model contains a single free parameter, namely the cross-relaxation probability p_x. An analogous expression can be derived for the complementary sequence in which the system is initialized in $|\uparrow\rangle$. Fitting the model to the experimental data shown in Figure 7.12 yields an average value of $p_x \approx 2.9(3) \times 10^{-4}$. However, the dataset presented in Figure 7.12 does not extend to the full decay of the exponential dependence. As a result, the extracted value of p_x should be taken as an estimate. The quoted uncertainty likely underestimates the true error, since fitting an exponential decay without access to the exponential tail is inherently ill-conditioned and sensitive to noise.

Using Eq. 5.10, we convert this value into a perpendicular hyperfine coupling of $A_\perp/2\pi \approx 71(7)$, kHz, in agreement to the one measured in Section 7.3.

From the assignment probability, we can define readout fidelity as

$$\mathcal{F}_{\mathrm{RO}} = \frac{1}{2}\left[p\left(\downarrow \mid \downarrow, N_{\mathrm{RO}}\right) + p\left(\uparrow \mid \uparrow, N_{\mathrm{RO}}\right)\right]. \tag{7.15}$$

The upper bound for the fidelity can be obtained by optimizing N_{RO} to balance SNR gain and cross-relaxation loss. For the parameters of our detector and the fitted p_x, this optimal fidelity is given by

$$\mathcal{F}_{\mathrm{RO}} = \frac{1}{2}\left[p\left(\downarrow \mid \downarrow, N_{\mathrm{RO}}^{(\mathrm{max})}\right) + p\left(\uparrow \mid \uparrow, N_{\mathrm{RO}}^{(\mathrm{max})}\right)\right] = 0.93. \tag{7.16}$$

Similar to the initial detection of ^{14}N discussed in Section 7.1, the fidelity of the readout is ultimately limited by the nuclear spin cross-relaxation rate. To increase the readout fidelity, two strategies are possible: increasing detection SNR and suppressing the cross-relaxation probability.

Enhancing the SMPD performance will yield an increase of detection SNR. In the ideal limit of unit efficiency and vanishing dark counts ($\eta = 1$, $\Gamma_{\mathrm{DC}} = 0$), a single electron excitation would suffice for nuclear spin single-shot readout. In this regime, the only remaining source of infidelity is the probability of a cross-relaxation event occurring during the measurement, p_x, which therefore sets the fundamental upper bound on the achievable fidelity.

Alternatively, the cross-relaxation probability itself can be reduced. By decreasing the resonator linewidth κ, one can suppress the Purcell enhancement of the ZQ/DQ transitions, thereby reducing the cross-relaxation probability. Consequently, the fabrication of higher-quality resonators provides a direct route towards improved readout fidelity.

7.5. Sideband driving and nuclear spin identification

We now perform hyperfine spectroscopy by resonantly driving the ZQ/DQ transitions. As described in Section 5.1, the ZQ/DQ transitions are weakly allowed thanks to the perpendicular hyperfine interaction. This enables the cross-relaxation effect described in the previous section, whereby the state of the nuclear spin can change during an electron spin relaxation. These transitions can be resonantly driven with a pulse at frequency $\sim \omega_S \pm \omega_I$, opening a path for coherent nuclear spin control with microwaves.

This corresponds to the single-spin equivalent of an EDNMR sequence [27, 65]. In traditional ensemble EPR, if the inhomogeneous broadening is larger than the nuclear spin Larmor frequency, a strong microwave pulse will simultaneously drive the EPR-allowed transitions of some spins, as well as the ZQ/DQ transitions of others. Therefore, the EPR signal measured by a weaker pulse will show two sidebands detuned by the Larmor frequency of the driven nuclear spins. This in turn gives information about the nuclear spins in the system and their hyperfine coupling.

[27]: Schosseler et al. (1994), 'Pulsed ELDOR Detected NMR'
[65]: Goldfarb (2017), 'ELDOR-Detected NMR'

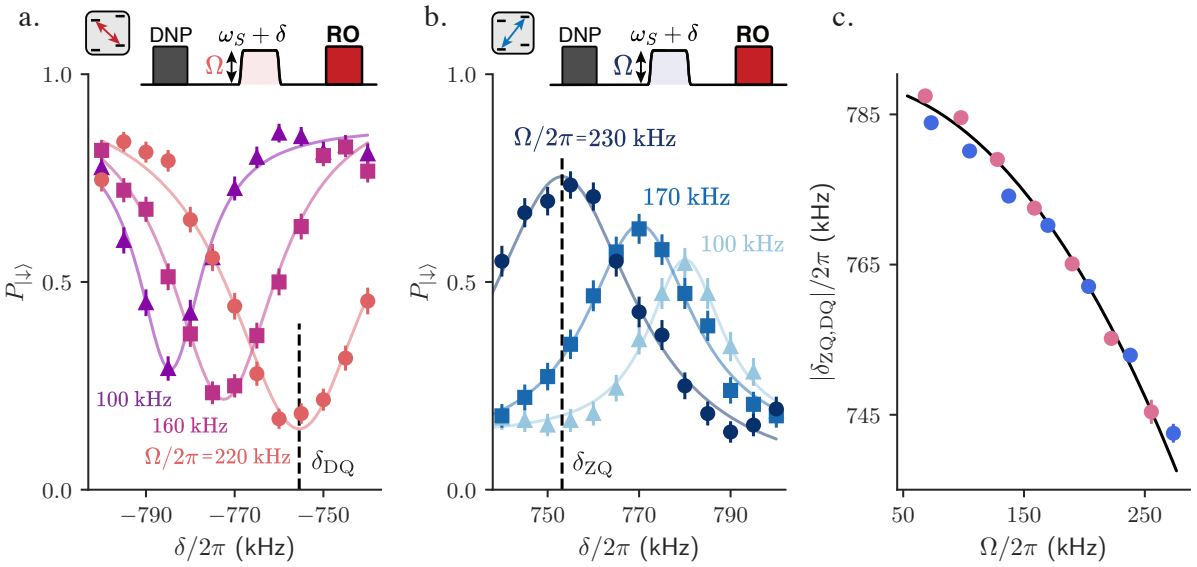

Figure 7.13.: EDNMR spectroscopy for Er_5. **a & b**. Nuclear spin ↓ probability as a function of δ for three values of Ω with pulse duration τ_f equal to 60 µs, 32 µs and 22 µs in increasing order of Ω. Panels *a* and *b* respectively show the DQ and ZQ transitions. Markers correspond to measured data and solid lines are Lorentzian fits, yielding the measured transition frequencies δ_{DQ} and δ_{ZQ} respectively. Pulse sequences are shown above the data. **c.** Measured ZQ and DQ frequency $|\delta_{ZQ,DQ}|$ (blue and red respectively) as a function of Ω. Markers are obtained from the Lorentzian fit in subplots a & b and the solid line is obtained by fitting the data to the AC-Zeeman shift model described in Section 5.1 with one free parameter, ω_I.

In the single-spin case, inhomogeneous broadening is no longer relevant, and the ZQ/DQ transitions can be driven directly. We begin the pulse sequence by deterministically preparing the nuclear spin state (see Section 7.6). We then apply a flat-top[2] microwave pulse at frequency $\omega_S + \delta$. The amplitude of the pulse is characterized by the maximum electron Rabi frequency Ω (see Section 5.1). Spectroscopy data are shown in Figure 7.13a & b for 3 values of Ω after preparation in state $|\downarrow\rangle$ (resp. $|\uparrow\rangle$). A reduction (resp. increase) in the down-state population $P_\downarrow$ is observed when $\omega_S + \delta$ matches the DQ (resp. ZQ) transition. The measurement shows that the frequency and linewidth of the resonance depend on the pulse amplitude.

2: A flat-top pulse is a square pulse with a Gaussian rise and fall shape. This shape reduces the spectral artifacts generated by the sharp edges of a flat pulse.

The fitted frequencies for the ZQ and DQ transitions, $\delta_{ZQ,\,DQ}$, are shown in Figure 7.13c as a function of Ω. As discussed in Section 5.1, $\delta_{ZQ,\,DQ}$ depend quadratically on the driving amplitude. The shift originates in the off-resonant driving of the allowed transitions, which leads to AC-Zeeman shifts of the energy levels. The measured data are fit to the expression derived in Section 5.1, which we remind here,

$$\delta_{ZQ,DQ}(\Omega) = \mp\frac{1}{2}\left(\delta\omega_{AC}^{(\uparrow)} + \delta\omega_{AC}^{(\downarrow)}\right) \approx \mp\frac{1}{2}\left(\frac{\Omega^2}{2\omega_I^{(\Uparrow)}} + \frac{\Omega^2}{2\omega_I^{(\Downarrow)}}\right). \qquad (7.17)$$

The fit yields the nuclear spin Larmor frequency, $\omega_I/2\pi = -788.1(4)$ kHz. The corresponding gyromagnetic factor of 1.767(1) MHz/T is close to the value expected for ^{183}W in $CaWO_4$, $\gamma_W/2\pi = 1.774$ MHz/T [63], thus confirming the nature of the nuclear spin. The residual difference is attributed to a combination of pseudo-nuclear Zeeman, chemical shift, and possibly error in field calibration.

[63]: Knight et al. (1986), 'Solid-State Tungsten-183 Nuclear Magnetic Resonance Spectroscopy'

We coherently control the nuclear spin state by modifying the pulse duration and the resulting Rabi oscillations are plotted in Figure 7.14.

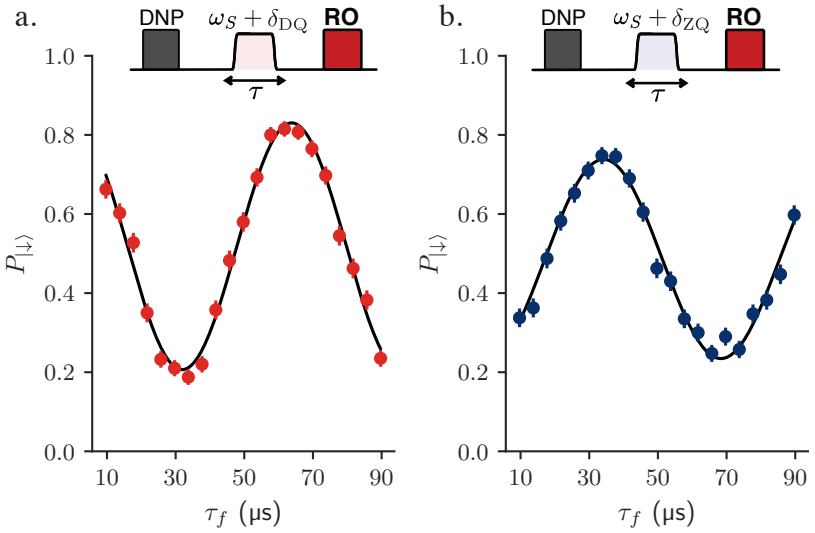

Figure 7.14.: a & b. Measured nuclear spin ↓ probability as a function of τ for the DQ and ZQ Rabi measurement (*a* and *b* side-panels), with δ set at resonance, for $\Omega/2\pi = 220$ kHz. Black solid lines are cosine fits, yielding a Rabi frequency $\Omega_{ZQ,DQ}/2\pi \sim 15$ kHz for both of them. Pulse sequences are shown on top.

This control is enabled by the long coherence of the Er^{3+} spin, as the matrix elements of the transition are considerably small. Fitting the Rabi frequency provides an alternative method to determine $A_\perp$, as discussed in Section 5.1. Indeed, the ZQ and DQ Rabi frequency $\Omega_{ZQ,\,DQ}$ are related to the allowed-transition Rabi frequency as

$$\Omega_{ZQ} \approx \Omega_{DQ} \approx \Omega \frac{A_\perp}{2\omega_I} \frac{1}{\sqrt{1 + 4\omega_I^2/\kappa^2}}. \tag{7.18}$$

From the fitted Rabi frequency the equation yields $A_\perp/2\pi = 103(7)$ kHz. This value is significantly larger than the one obtained using the time-trace analysis in Section 7.3 as well as the readout analysis of Section 7.4.

In the time-trace analysis, the difference originates from the limitations of the method. Nuclear spins with large $A_\perp$ will experience rapid changes in the nuclear spin state. Given that each spectroscopy corresponds to 200 sweeps, rapid switching will be hidden by the averaging. Therefore, the measurement of large values of $A_\perp$ will be biased towards a lower estimation. For the readout analysis, the fitted curve is restricted to low values of N_{RO}, and the tail of the exponential was not captured. Therefore, the exponential fit is not well-constrained and the uncertainty is probably larger than estimated. For these reasons, we consider the value of $A_\perp$ measured using ZQ/DQ Rabi oscillations as a more precise estimation of the hyperfine coupling, limited by the precision in the microwave amplitude.

7.6. Solid effect DNP

Driving the ZQ/DQ sidebands provides a direct mechanism to deterministically prepare the nuclear spin state. To prepare $|\downarrow\rangle$ one can apply a resonant π-pulse on the ZQ transition and wait for the electron spin relaxation. If the nuclear spin was in $|\uparrow\rangle$ the pulse drove the system to $|\Uparrow\downarrow\rangle$, but if the nuclear spin was in $|\downarrow\rangle$ the pulse was not resonant with any transition. After the wait time, the system has been deterministically prepared in $|\Downarrow\downarrow\rangle$. Equivalently, the up-state can be prepared using a π-pulse that is resonant with the DQ transition.

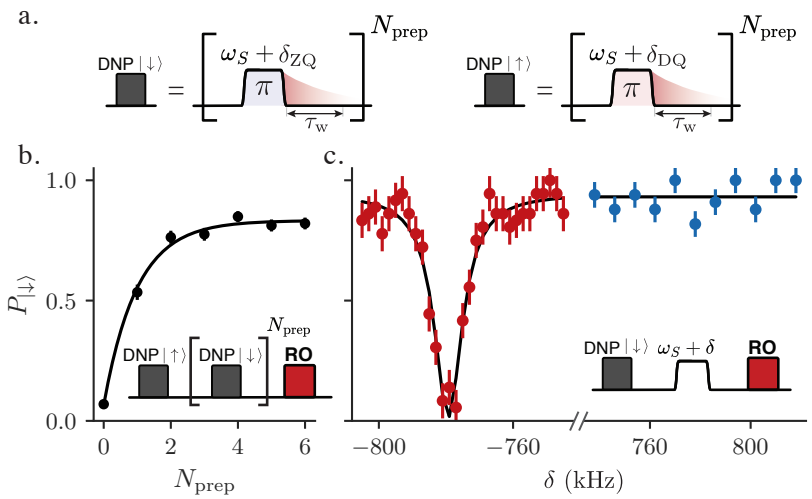

Figure 7.15.: a. Pulse sequence for preparing the nuclear spin in $\downarrow$ (respectively, $\uparrow$) through solid-effect DNP. One π-pulse at $\omega_S + \delta_{ZQ}$ (respectively, $\omega_S + \delta_{DQ}$), followed by a relaxation time τ_w, prepares the nuclear spin state to the desired state. The sequence is repeated N_{prep} times for higher efficiency. **b.** Measured (dots) nuclear spin $\downarrow$ probability as a function of the number of preparation pulses N_{prep} into this state. Solid line shows an exponential fit. *Inset.* Pulse sequence diagram. The nuclear spin is initialized into the $\uparrow$ state. Then, the preparation sequence for different N_{prep} and $\tau_w = 3$ ms is applied, followed by nuclear spin readout. **c.** Probability of measuring the nuclear spin in state $\downarrow$ in an EDNMR experiment for the ZQ and DQ transitions after preparation in the $\downarrow$ state. *Inset.* EDNMR sequence. $N_{prep} = 10$ pulses and $\tau_w = 5$ ms are used for preparation.

This technique was first theorized and observed by Anatole Abragam in ensembles and receives the name of solid-effect dynamical nuclear polarization (DNP) [92–94]. Anatole Abragam was the founder of our laboratory and here we follow in his footsteps by adapting solid-effect DNP to the single nuclear spin case.

In practice, we require several π-pulses due to spectral drift and fluctuations of the microwave amplitude. The pulses are separated by a wait time τ_w, taken to be close to Γ_R^{-1}. Figure 7.15a shows $P_\downarrow$ as a function of the number of applied pulses N_{prep}. The population in the down-state increases rapidly, reaching ≈ 0.8 for 2 pulses (Figure 7.15b). This demonstrates single-atom solid-effect nuclear spin polarization. The maximum value is limited by nuclear spin readout errors and out-of-equilibrium excitations of the electron spin, and can likely be improved in future experiments.

State preparation is also confirmed spectroscopically. After polarizing the state of the nuclear spin to $|\downarrow\rangle$, a pulse is applied at a frequency $\omega_S + \delta$, with the amplitude corresponding to a π-pulse for the ZQ transition at resonance, followed by nuclear spin state readout. Figure 7.15c shows the probability $P_\downarrow$ as a function of δ, which shows a clear dip at the frequency corresponding to the double-quantum resonance, but no dip on the zero-quantum transition, which is further evidence for nuclear spin polarization.

The solid-effect DNP is also effective when multiple spins are present, as seen in Figure 7.16 where it is applied to Er_4. The polarization protocol into $|\downarrow\downarrow\rangle$ involves sending pulses at each of the zero-quantum transition frequencies. A 20-minute time trace of the allowed-transitions spectrum is shown in Figure 7.16 with no preparation (bottom), with polarization into $|\downarrow\downarrow\rangle$ (middle), and into $|\uparrow\uparrow\rangle$ (top). The polarization sequence is applied at the beginning of every spectrum. Whereas the trace with no polarization shows nuclear spin quantum jumps, the two other traces show predominantly the single EPR-allowed transition corresponding to the polarized state.

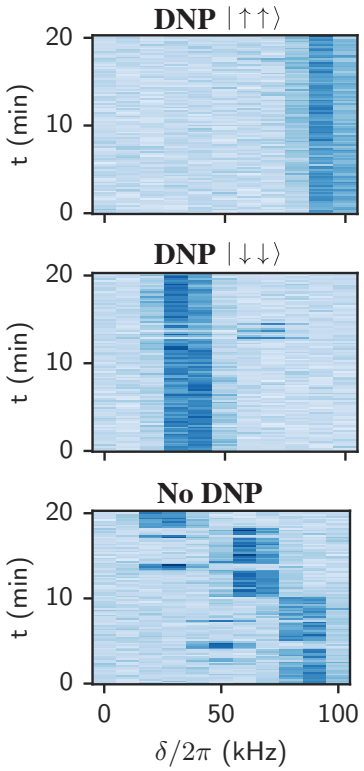

Figure 7.16.: Ensemble-averaged counts $\langle C \rangle$ measured in a fluorescence detection spectroscopy experiment as a function of frequency during 20 minutes. Data obtained for Er_4 which has 2 neighboring nuclear spins. From top to bottom, the nuclear spins are prepared through solid-effect DNP to $|\uparrow\uparrow\rangle$, $|\downarrow\downarrow\rangle$ and no preparation. When preparing the state, the electron spin frequency δ remains constant (except three spectra where preparation was unsuccessful). In absence of state preparation, the frequency δ changes after each quantum jump.

7.7. Conclusion and outlook

In summary, we have demonstrated single ^{183}W nuclear spin detection, EDNMR spectroscopy, and polarization. In contrast to previous work, the detection of the nuclear spin does not rely on system-specific mechanisms such as optical transitions or spin-to-charge conversion. Instead, it is based on detecting the microwave fluorescence of the electron spin. This method is, in principle, applicable to a range of nuclear spin systems in a large variety of samples, crystalline or not. The main requirement is that the Purcell-enhanced radiative rate is on the order of $\sim 10^3\ s^{-1}$ and larger than the non-radiative rate at 10 mK.

These methods open the way to ^{183}W -nuclear spin-based quantum registers operated and read out via the Er^{3+} spin. At present, coherent control of the nuclear spins relies exclusively on resonant driving of the ZQ/DQ transitions mediated by the electron. Consequently, the achievable control fidelity and coherence are ultimately limited by the decoherence time of the Er^{3+} spin, which is expected to be significantly shorter than the decoherence time of the ^{183}W nuclear spins. Therefore, to establish a working quantum register, it is necessary to develop a method to drive the ^{183}W nuclear spins while preserving their coherence properties.

In addition, these techniques are not limited to nuclear spin-1/2 species and can be readily generalized. By measuring the NMR spectra of a high-nuclear spin system, one can reconstruct the quadrupole interaction. The quadrupole tensor can be used to deduce structural information, as it depends on the local electric field gradients.

It is important to note that the detection and manipulation of the nuclear spins is enabled by the long decoherence times of the Er^{3+} spin, approximately $\sim 100\ \mu s$. This allowed us to measure weak hyperfine couplings on the order of ~ 20 kHz. However, as the Purcell-enhanced radiative rate is increased to achieve a faster repetition rate, it will get closer to the instantaneous dephasing time. Beyond that point, the decoherence time of the spin will be limited by the relaxation of the Er^{3+} . A possible strategy to mitigate this trade-off is the use of a resonator with tunable bandwidth, as recently demonstrated in ref. [95]. Such a design would enable dynamic control of the resonator linewidth: narrowing it during readout to enhance the Purcell factor, and broadening it during spin manipulation. This dynamic control can be performed in a timescale of nanoseconds. This approach allows one to maintain long decoherence times while still having single nuclear spin resolution.

[95]: Wen et al. (2025), *Addressing Spins at the Clock Transitions with a Frequency- and Bandwidth-Tunable Superconducting Resonator*

Dynamic Purcell tuning and radiofrequency access would also enable the use of dynamical decoupling sequences in our system, which are currently limited by the Purcell-enhanced relaxation rate of the Er^{3+} spin. This would allow one to extend the detection to weakly coupled spins that are located further from the Er^{3+} spin using the methods discussed in Section 7.1 for NV centers in diamond.

Individual nuclear spins in the solid state for quantum computing

8.

In this chapter, we approach our system from a quantum-computing perspective. We describe how to build a two-qubit register using two ^{183}W nuclear spins coupled to a single Er^{3+} impurity. Using the single-shot readout and DNP techniques demonstrated in the previous chapter, we expand on control of the spins by driving microwave-stimulated Raman transitions. We implement a two-qubit gate leveraging the frequency shifts imparted by the Raman drives on the nuclear spins and demonstrate a two-qubit CNOT gate. We measure second-long coherence times for the nuclear spins, among the longest reported for nuclear-spin qubits. Finally, we demonstrate that Bell states with zero-average magnetic moment exist in a so-called decoherence-free subspace and are protected against external magnetic noise.

The measurements and analysis of the data in this section were performed by me and James O'Sullivan.

8.1 State of the art 88
8.2 Spin system 92
8.3 Preparation and readout . 93
8.4 Stimulated Raman driving 94
Single-qubit gates 96
8.5 Nuclear spin coherence time 98
8.6 Entangling the nuclear spins 99
8.7 Bell state tomography . . 100
8.8 Decoherence-free subspace102
8.9 Conclusion and outlook . 103

8.1. State of the art

We start the chapter with a brief review of quantum computing platforms using individual nuclear spins, interfaced and read out via an electron spin ancilla, highlighting topics that are relevant for putting our results in perspective. In these systems, the electron spin acts as a central node, coupling simultaneously to all nuclear spin qubits in the register. Because direct nuclear–nuclear coupling is generally too weak to support fast two-qubit gates, these gates are instead mediated by the electron spin. We highlight two experiments that are representative of the state of the art in two-qubit gate implementations: one using NV centers in diamond and another using phosphorus donors in silicon.

^{13}C register operated by an NV center in diamond

Natural-abundance diamond hosts carbon isotopes with non-zero nuclear spin. In particular, ^{13}C has an abundance of 1.07% and a spin-1/2. Therefore, the NV center is surrounded by a bath of nuclear spins coupled through the hyperfine interaction. For the purposes of quantum computing, the nuclear spins are both a resource, as they are long-lived qubits, and sources of noise: very weakly coupled nuclear spins are not addressable but nevertheless induce decoherence of the electron spin. Two-qubit gate implementations in electron–nuclear systems leverage the splitting of the ESR-allowed spectrum due to the hyperfine interaction. Consequently, an important challenge for implementing two-qubit gates mediated by the NV electron spin is decoherence of the electron spin. This is addressed by implementing dynamical decoupling sequences on the electron spin, which extend the coherence time and therefore the spectral resolution [37, 96].

We highlight a particular implementation of this scheme by Bradley *et al.*, which was used to demonstrate single- and two-qubit gates in a nine nuclear spin register [10]. The sequence is shown in Figure 8.1a.

[37]: van der Sar et al. (2012), 'Decoherence-Protected Quantum Gates for a Hybrid Solid-State Spin Register'
[96]: Taminiau et al. (2012), 'Detection and Control of Individual Nuclear Spins Using a Weakly Coupled Electron Spin'
[10]: Bradley et al. (2019), 'A Ten-Qubit Solid-State Spin Register with Quantum Memory up to One Minute'

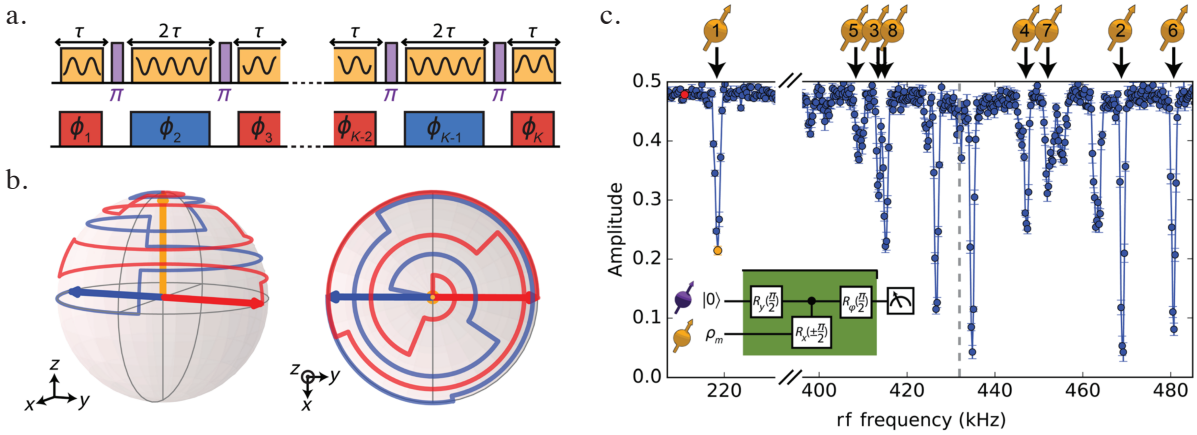

Figure 8.1.: a. *(top)* Dynamical decoupling pulses on the electron spin are interleaved with rf pulses on the nuclear spin (purple and yellow, respectively). *(bottom)* Depending on the initial state of the electron spin, even or odd pulses will be resonant with the NMR-allowed transition. For initial electron state $m_S = 0$, the even (blue) rf pulses are resonant. The phase of each rf pulse is adapted for each pulse. **b.** Nuclear spin trajectory on the Bloch sphere for a conditional rotation with $N = 8$ electron decoupling pulses. Starting from the initial nuclear state $|\uparrow\rangle$ (yellow), the red (blue) path shows the nuclear spin evolution for the case where the electron starts in the state $m_S = -1$ ($m_S = 0$). The final state vectors are antiparallel along the equator; therefore, the gate is a maximally entangling two-qubit gate. **c.** Spectroscopy of individual ^{13}C nuclear spins using DDrf sequences with single NV center probe. The coherence of the NV center dips when the interpulse delay τ matches the resonant condition for a nuclear spin. Eight different nuclear spins have been highlighted. Plots a. and b. and c. come from ref. [10].

Electron π-pulses are applied, separated by time intervals of duration 2τ. During these intervals, they apply narrowband radiofrequency (rf) pulses. The rf pulses are resonant with the NMR-allowed transition of the nuclear spin, in this case ^{13}C, when the electron spin is in state $m_S = -1$. Consequently, the initial state of the electron spin determines which rf pulses are resonant. For initial electron state $m_S = -1$, the odd (red) rf pulses are resonant. For $m_S = 0$, the even (blue) rf pulses are resonant.

To ensure that the rf pulses build up constructively, their phases need to be updated to account for the periods of nuclear spin precession between them. Figure 8.1b shows the evolution of the nuclear spin from the initial $|\uparrow\rangle$ state (in yellow). The red (blue) path shows the nuclear spin evolution for the case where the electron starts in the state $m_S = -1$ ($m_S = 0$). After eight DD pulses, the nuclear-spin states are antiparallel, which effectively constitutes a CNOT gate.

If the electron spin is prepared in a superposition, and a nuclear spin is resonant during a DDrf sequence, the entangling interaction results in a loss of coherence of the electron spin. Therefore, by sweeping the frequency of the rf pulse, they perform spectroscopy. Figure 8.1c shows the NMR spectra of eight individual ^{13}C measured with a DDrf sequence. Each of them has a unique frequency, mainly due to the hyperfine coupling with the electron spin. They measure the coherence time of ^{13}C nuclear spins and obtain $T_2^* \sim 10$ ms and $T_2 \sim 1$ s. By adding extra dynamical decoupling pulses, they are able to achieve coherence times of tens of seconds with 256 pulses. This highlights the interest of nuclear spins for quantum computing, as their coherence times are remarkably long even in natural-abundance crystals.

Moreover, they demonstrate that correlated sources of noise, mainly arising from the nuclear spin bath, can be suppressed by preparing a spatially close nuclear spin pair in a decoherence-free subspace (DFS) [97]. In particular, the Bell states $|\Phi^+\rangle = (|\downarrow\downarrow\rangle + |\uparrow\uparrow\rangle)/\sqrt{2}$ and $|\Psi^-\rangle = (|\downarrow\uparrow\rangle - |\uparrow\downarrow\rangle)/\sqrt{2}$ are triplet and singlet states of a nuclear spin pair system. The magnetic projection of the states is $m_{\Phi^+} = 1$ and $m_{\Psi^+} = 0$. Therefore, $|\Phi^+\rangle$ is, in

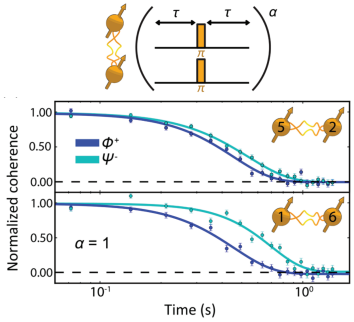

Figure 8.2.: Coherence time of the $|\Phi^+\rangle = (|\downarrow\downarrow\rangle + |\uparrow\uparrow\rangle)/\sqrt{2}$ and $|\Psi^-\rangle = (|\downarrow\uparrow\rangle - |\uparrow\downarrow\rangle)/\sqrt{2}$ with a single decoupling pulse. Nuclear spins 5 & 2(1 & 6) are spatially separated by 1.37 nm (0.96 nm).

[97]: Lidar et al. (1998), 'Decoherence-Free Subspaces for Quantum Computation'

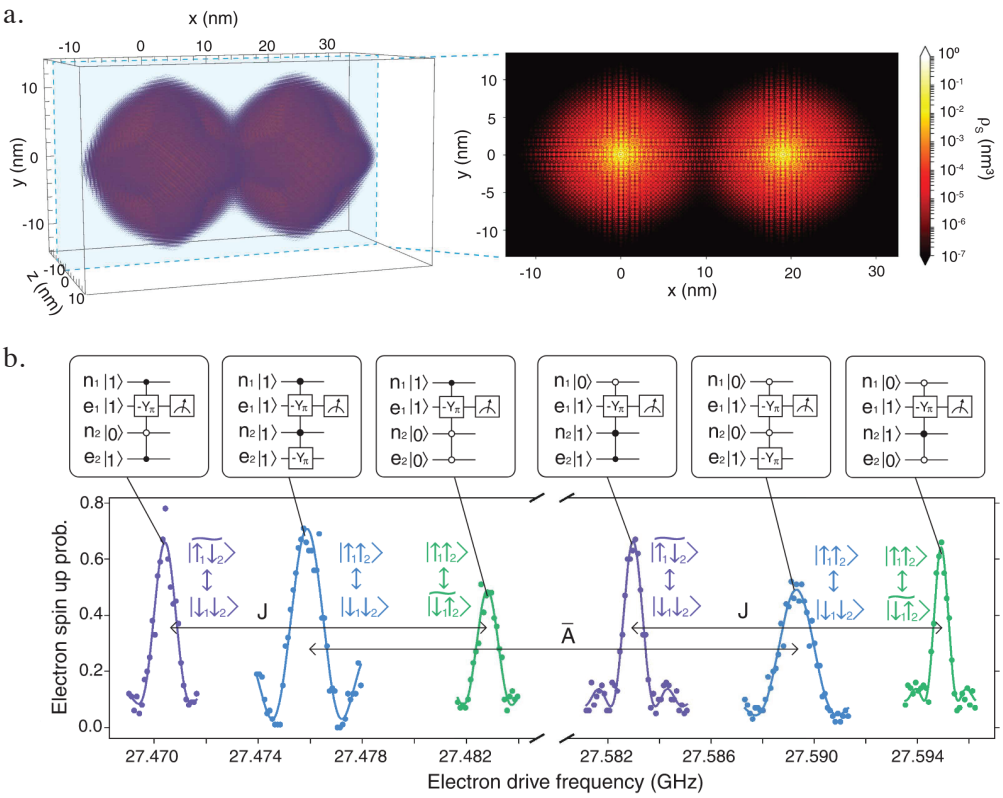

Figure 8.3.: a. *(right)* Three-dimensional (3D) rendering of the wavefunctions of the electron spins of both donors. They are exchange-coupled with a strength of 12 MHz, which corresponds to a spacing of 19 nm. *(left)* 2D plane cut of the simulation. **b.** ESR-allowed spectrum for one of the electrons in an exchange-coupled, two-donor system for the case of $J > A$, where J is the electron–electron exchange interaction strength and A is the average hyperfine coupling. Six EPR-allowed transitions are present, conditional on the state of the other electron and the two donor nuclei. Inset specifies the electron spin states driven. The top shows the effective quantum gate applied to the register when resonantly driving the transition. Figure was taken from ref. [98].

principle, twice as sensitive to correlated noise compared to single qubits while $|\Psi^-\rangle$ is only sensitive to uncorrelated noise.

They measure the coherence time of each state, which shows statistically significant differences, as shown in Figure 8.2. The magnitude of the effect is correlated with the distance between the spins in the pairs, consistent with the idea that spatially close nuclear spins experience similar bath dynamics.

^{31}P nuclear spins in silicon

The methods developed for NV centers use a single electron spin that couples to all the nuclear spins simultaneously. In contrast, a very recent work by Stemp *et al.* has demonstrated how to perform two-qubit gates between distant ^{31}P donors in silicon by leveraging the exchange coupling between their electron spins [98].

[98]: Stemp et al. (2025), 'Scalable Entanglement of Nuclear Spins Mediated by Electron Exchange'

The electronic wavefunction of a phosphorus donor in silicon extends over $\sim$ 2 nm. Therefore, when two neutral donors are separated by approximately 10 nm, their electronic wavefunctions will overlap, leading to exchange interaction between the electron spins (as shown in Figure 8.3a). This interaction splits the EPR spectrum of one electron spin depending on the state of the other. In addition, the spectrum is further split by the contact interaction with the ^{31}P nuclear spin, leading to six EPR-allowed transitions, shown in Figure 8.3b. Each of the transitions

corresponds to a different state of the hybrid qubit register. Note that, although the electron spin coherence time is approximately $T_2^* \approx 20$ µs, the strong exchange and contact interactions allow them to resolve all the different transitions.

A microwave 2π-pulse on a specific transition will induce a π phase shift on the corresponding state. Given that this operation is conditional on the state of the other electron and the two nuclear spins, this corresponds to a multi-qubit gate. The corresponding gate after a resonant 2π-pulse for each transition is shown as an inset in Figure 8.3b. They measure the coherence time of the neutral donors and obtain $T_2^* = 0.6$ ms. They are able to extend it to $T_2^* = 30$ ms by ionizing the donor, thereby removing the electron spin noise.

Discussion

Both approaches to two-qubit gates leverage the hyperfine coupling to deterministically entangle the electron and nuclear spins. In both cases, a crucial requirement is electron spin coherence. The T_2^* in both systems is relatively low, in the order of 1 µs for NVs and 20 µs for neutral ^{31}P donors. However, the approaches to solve this problem in each system are different.

In the case of NV centers, they rely on minute-long electron-spin lifetimes at cryogenic temperatures. This enables them to perform long dynamical decoupling sequences, therefore enhancing the coherence time of the electron spin. For donors in silicon, the electron spins are coupled by a strong contact interaction $\sim$ 10 MHz, which allows them to spectrally resolve all EPR-allowed transitions, even with a wide electron linewidth of $\sim$ 1 MHz.

When performing detection by microwave fluorescence, DD sequences are not well suited for extending the coherence of the electron spin, as it is bounded by the Purcell-enhanced radiative rate[1]. In addition, the electronic wavefunction of the unpaired electron in rare-earth ions is well confined by the more external $5s$ and $5p$ shells. Consequently, the interaction with distant nuclear spins is primarily mediated by magnetic dipole interaction, which is orders of magnitude weaker[2].

However, the Hahn echo coherence of Er^{3+} in magnetically silent crystals is exceedingly long, $\sim$ 23 ms in ensembles [26], and in our system is limited by $2T_1$ (see Section 6.6). As shown in the previous chapter, we are able to directly resolve individual nuclear spins with hyperfine couplings of 20 kHz. Consequently, the method demonstrated in the work of Stemp *et al.* [98] should be directly applicable, albeit with low fidelity. It is therefore appealing to develop an all-microwave technique that can be used to drive single- and two-qubit gates under these conditions. This is the objective of this chapter.

1: Also, rf pulses are incompatible with the current setup. This could be overcome with a new resonator design.

2: Especially when considering that the nuclear spins of interest, ^{183}W , have a weak gyromagnetic ratio

[26]: Le Dantec et al. (2021), 'Twenty-Three–Millisecond Electron Spin Coherence of Erbium Ions in a Natural-Abundance Crystal'

[98]: Stemp et al. (2025), 'Scalable Entanglement of Nuclear Spins Mediated by Electron Exchange'

8.2. Spin system

In the following, we focus on a single Er^{3+} spin with two strongly coupled ^{183}W nuclear spins. In the previous chapter, this system was presented as Er_4. The position of the ^{183}W spins was estimated by matching the measured hyperfine coupling to dipole-dipole simulations, and a schematic view of one of the possible configurations is shown in Figure 8.4.

The spin Hamiltonian of this system is

$$\hat{\mathcal{H}} = \omega_S \hat{S}_z + \sum_{i\in\{1,2\}} \omega_{I,i}\hat{I}_{z,i} + A_{\parallel}^{(i)}\hat{S}_z\hat{I}_{z,i} + A_{\perp}^{(i)}\hat{S}_z\hat{I}_{x,i}, \tag{8.1}$$

where ω_S is the Er^{3+} spin frequency, $\hat{\mathbf{S}} = [\hat{S}_x, \hat{S}_y, \hat{S}_z]$ is the Erbium spin operator, $\omega_{I,i}$ are the nuclear spin frequencies, $\hat{\mathbf{I}}_i = [\hat{I}_{x,i}, \hat{I}_{y,i}, \hat{I}_{z,i}]$ are the nuclear spin operators and $A_{\parallel}^{(i)}, A_{\perp}^{(i)}$ are the zz and zx hyperfine coupling constants between the electron and nuclear spins, for $i \in \{1,2\}$. Here we have kept only the hyperfine terms proportional to S_z according to the secular approximation (see Section 3.4).

The Hamiltonian gives rise to an eight-level system, represented in Figure 8.5. In the following, we utilize the two nuclear spins as qubits, designated Qb1 and Qb2, and the electron spin as an ancilla, used to control and read out the nuclear spin qubits. We remind the reader of the characteristics of the Er_4 spin, Qb1, and Qb2 in Table 8.1, measured in the previous chapter. The values of $A_\perp$ were measured by monitoring the jumps in the time traces shown in Section 7.3. As discussed in Section 7.5, this method can underestimate large values of $A_\perp$. This is the case for $A_\perp^{(1)}$, as will be discussed in Section 8.4.

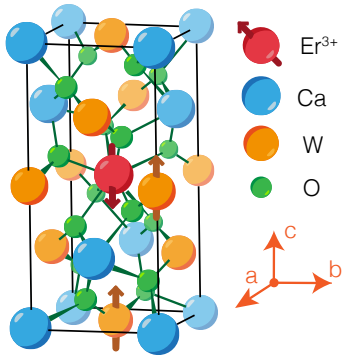

Figure 8.4.: Er^{3+}:$CaWO_4$ with two ^{183}W nuclear spins. The location of the nuclear spins corresponds to Er_4 nuclear spin positions, estimated by comparing the hyperfine coupling measurements to dipole-dipole calculations. This represents one of the possible configurations as the hyperfine coupling is degenerate. The ^{183}W located under the Er^{3+} along the c-axis could also be assigned the site related by inversion. The other ^{183}W could be located in any of the four sites in the (a,b)-plane.

T_1 (ms)	$g_0/2\pi$ (kHz)	T_2^* (µs)	T_2 (ms)
0.80(3)	5.6(2)	170(5)	2.05(3)

$A_{\parallel}^{(1)}/2\pi$ (kHz)	$A_{\perp}^{(1)}/2\pi$ (kHz)	$A_{\parallel}^{(2)}/2\pi$ (kHz)	$A_{\perp}^{(2)}/2\pi$ (kHz)
36(1)	40(5)	19(1)	11(3)

Table 8.1.: Er_4 characterization. The top table details the parameters of the Er^{3+} spin and the bottom table the parameters of the ^{183}W nuclear spin, measured in Chapter 7.

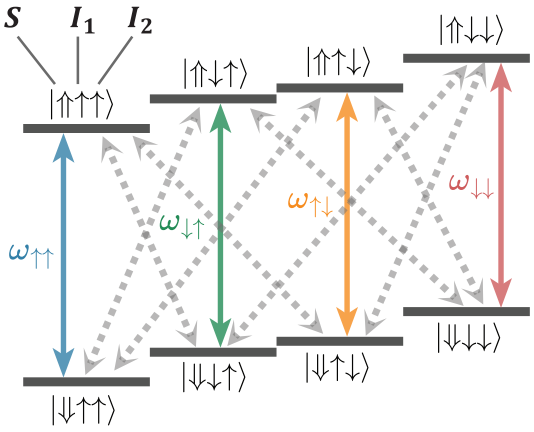

Figure 8.5.: Energy level diagram of the system of an Er^{3+} spin $\mathbf{S} = 1/2$ electron (double arrow) coupled to two ^{183}W nuclear spins $\mathbf{I}_{1,2} = 1/2$ (single arrows). EPR-allowed transitions occur at $\omega_{\uparrow\uparrow}, \omega_{\uparrow\downarrow}, \omega_{\downarrow\uparrow}$ and $\omega_{\downarrow\downarrow}$ (blue, orange, green and red, respectively) depending on the nuclear spin state. Simultaneous nuclear- and electron-spin-flip events are also possible via ZQ/DQ transitions (gray dashed arrows).

8.3. Preparation and readout

We extend the readout and preparation protocols from the previous chapter to the two-qubit system. Preparation into arbitrary nuclear spin states is done through a combination of solid-effect DNP (see Section 7.6) and single-qubit gates (see next section). Solid-effect DNP is achieved by driving the ZQ/DQ transitions (represented as gray arrows in Figure 8.5) with a $\tau_{\text{prep}} = 3.5$ ms-long square pulse followed by $\tau_{\text{w}} = 2$ ms of wait time, allowing the electron spin to decay. This sequence is then repeated $N_{\text{prep}} = 50$ times to ensure preparation. This corresponds to a very large number of repetitions compared to those needed in Section 7.6. Given that the measurement time is mostly dedicated to nuclear spin readout (see below), increasing the number of preparation pulses is not a significant time investment.

We chose $|\downarrow\downarrow\rangle$ as the target state for preparation. Therefore, during the preparation sequence we drive the ZQ transitions. To cover both Qb1 and Qb2 sidebands, the frequency of the pulse is chirped by 50 kHz around the expected sideband transition frequency (see Chapter 7). To prepare other states, we apply the appropriate single-qubit gates after initializing in $|\downarrow\downarrow\rangle$.

Qubit readout leverages the spectral separation of the EPR-allowed transitions $\omega_{\uparrow\uparrow}$, $\omega_{\uparrow\downarrow}$, $\omega_{\downarrow\uparrow}$ and $\omega_{\downarrow\downarrow}$ (blue, orange, green and red in Figure 8.5). The linewidth of the resonator $\kappa/2\pi \approx 700$ kHz and the bandwidth of the SMPD ~ 300 kHz are sufficient to span the four possible frequencies. Figure 8.6 shows four photon-counting spectra obtained by high-resolution spectroscopy with an 80 µs electron excitation pulse. The peak photon count occurs at a different frequency for each of the four nuclear spin states, which are clearly well-resolved. This enables single-shot readout of the nuclear spin register state by monitoring the spin-selective fluorescence.

The readout protocol is shown in Figure 8.7a. Four π-pulses are consecutively applied, each of the pulses resonant with one of the EPR-allowed transitions. After each pulse, we measure the number of detector counts during an integration time $\tau_{\text{int}} = 1$ ms, repeated over N_{RO} iterations. The total number of counts after each pulse is given by $C_{\uparrow\uparrow}$, $C_{\downarrow\uparrow}$, $C_{\uparrow\downarrow}$ and $C_{\downarrow\downarrow}$. We define

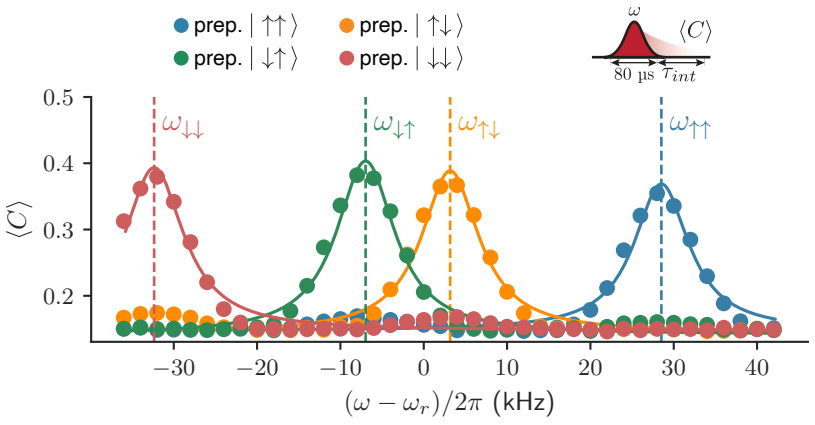

Figure 8.6.: High-resolution spectroscopy of the EPR-allowed transitions. The data are obtained from Figure 7.4 by post-selecting each spectroscopy measurement based on the nuclear spin state configuration. The original trace was obtained by measuring the ensemble-averaged counts $\langle C \rangle$ as a function of the frequency of an 80 µs excitation pulse. The data were taken with an integration time of $\tau_{\text{int}} = 1$ ms.

$$\begin{aligned}\Delta_x &= (C_{\uparrow\uparrow} + C_{\uparrow\downarrow}) - (C_{\downarrow\uparrow} + C_{\downarrow\downarrow}),\\ \Delta_y &= (C_{\uparrow\uparrow} + C_{\downarrow\uparrow}) - (C_{\uparrow\downarrow} + C_{\downarrow\downarrow}).\end{aligned} \tag{8.2}$$

Δ_x (Δ_y) effectively "traces out" the state of Qb2 (Qb1), while also cancelling the contribution of the dark counts to the photon-counting statistics. Figure 8.7b plots the measured Δ_y versus Δ_x for each possible state of the nuclear spin manifold with $N_{\mathrm{RO}} = 200$ readout pulses. The color of the points represents the state in which the system was prepared before the measurement took place. There are four well-resolved distributions, each corresponding to a different prepared state of the two-qubit system. We use a k-means algorithm to separate the space corresponding to each distribution, displayed in the plot with the corresponding background color. The boundaries approximately correspond to the $x = 0$ and $y = 0$ curves as expected. The skewness in the boundaries can be attributed to inaccurate calibration of the driving frequencies $\omega_{\uparrow\uparrow}$, $\omega_{\downarrow\uparrow}$, $\omega_{\uparrow\downarrow}$ and $\omega_{\downarrow\downarrow}$, which would result in different counting statistics for each state.

We note that the assignment of the prepared state is not perfect in Figure 8.7b, which is indicative of non-negligible State Preparation and Measurement (SPAM) errors. These errors arise from non-idealities in the preparation and measurement procedures and ultimately limit the performance of any quantum computing platform. SPAM errors can be characterized and subsequently mitigated in complex measurements, such as state tomography. One such approach is the T-matrix SPAM correction technique [99]. The T matrix has dimension $2^n \times 2^n$, where n is the size of the quantum register; in our case, $n = 2$. Each column of the T matrix corresponds to the measured probability distribution obtained after preparing a specific basis state. To correct for SPAM errors, the inverse of the T matrix is applied to the results of any measurement. From the data in Figure 8.7b, we extract the following T matrix:

$$T = \begin{pmatrix} 0.91 & 0.02 & 0.05 & 0.01 \\ 0.01 & 0.92 & 0 & 0.06 \\ 0.05 & 0 & 0.91 & 0.03 \\ 0 & 0.05 & 0.01 & 0.94 \end{pmatrix} \tag{8.3}$$

As discussed in Section 7.4, the main limiting factor of this scheme is the non-zero probability for the electron spin to relax through a nuclear spin flipping transition, which is proportional to $(A_\perp/2\omega_I)^2$. These cross-relaxation events limit the number of readout pulses that can be applied before the readout becomes non-QND and are likely the main source of SPAM errors in our system.

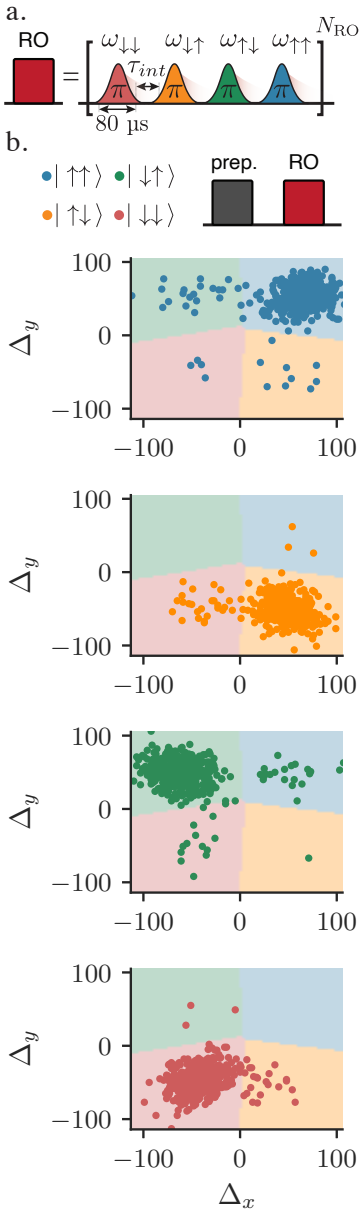

Figure 8.7.: Four-state readout of the nuclear spin state. **a.** Readout pulse sequence definition. We use $\tau_{\mathrm{int}} = 1$ ms. **b.** Each point corresponds to the value of Δ_x and Δ_y measured after preparing in a specific state. The color indicates the prepared state: blue, orange, green and red correspond to $|\uparrow\uparrow\rangle$, $|\uparrow\downarrow\rangle$, $|\downarrow\uparrow\rangle$ and $|\downarrow\downarrow\rangle$, respectively. Background color indicates the state assignment regions calculated using a k-means algorithm.

8.4. Stimulated Raman driving

As discussed in Section 8.1, the nuclear spin driving schemes used in other solid-state platforms are not readily available. The limitations mainly arise from the enhanced electron spontaneous relaxation rate, which is required for readout. In addition, direct driving of the NMR-allowed transitions through rf pulses is not possible due to setup constraints. Therefore, we require a different method to control the nuclear spins, implemented with microwave drives.

[99]: Lidar et al. (2013), *Quantum Error Correction*

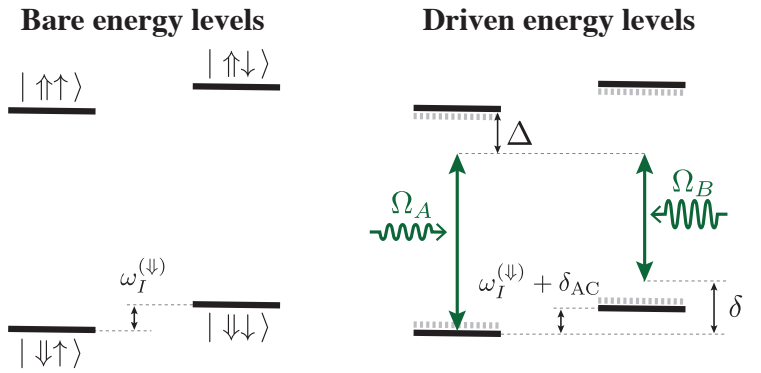

Figure 8.8.: *(left)* Bare energy levels of an Er^{3+} spin coupled to a single ^{183}W nuclear spin qubit. We highlight the nuclear spin transition in the ground state of the Er^{3+} ground state with frequency $\omega_I^{(\Downarrow)}$. *(right)* Two microwave pulses with amplitude $\Omega_{A,\,B}$ are applied on a four-level system. The detuning between drive A and the $|\Downarrow\uparrow\rangle \leftrightarrow |\Uparrow\uparrow\rangle$ is defined as Δ. The frequency difference between the two pulses is defined as δ. The bare energy levels (gray dashed lines) have been AC-Zeeman shifted by the strong off-resonance drives. The combined AC-Zeeman shift of the system results in an effective shift of the nuclear spin transition by δ_{AC}

As detailed in Chapter 5, the method of choice for coherent control of the ^{183}W nuclear spins is stimulated Raman driving. We derived the analytical Rabi frequency and discussed the origin of the *differential AC-Zeeman shift*. We now briefly remind the reader of these concepts and introduce the subtleties that arise when a second ^{183}W qubit is strongly coupled to the Er^{3+} spin, which naturally leads to two-qubit gates.

Let us first consider a single ^{183}W qubit coupled to the Er^{3+} spin. To control the state of the nuclear spin through stimulated Raman driving, we simultaneously apply two detuned microwave pulses with amplitudes Ω_A and Ω_B. The frequency detuning between the two pulses is defined as δ and the frequency detuning between drive A and the $|\Downarrow\uparrow\rangle \leftrightarrow |\Uparrow\uparrow\rangle$ transition is defined as Δ, as depicted in Figure 8.8. The population between the two lower nuclear spin levels is coherently driven when $\delta = \omega_I^{(\Downarrow)} + \delta_{\mathrm{AC}}$, where $\omega_I^{(\Downarrow)}$ is the bare NMR transition frequency and δ_{AC} corresponds to the differential AC-Zeeman shift due to the off-resonant driving of the microwave pulses given by Eq. 5.15.

We now return to the system with two ^{183}W nuclear spins. In the following, we concentrate on the control of Qb1, as the same methods apply to Qb2. We distinguish two cases, depending on the state of Qb2, highlighted in different colors in Figure 8.9a. The key difference between the two cases arises from the different Raman shifts $\Delta^{\uparrow,\downarrow}$ depending on the state of Qb2. The origin of this difference lies in the splitting of the EPR-allowed frequencies depending on the state of the nuclear spin. For the same stimulated Raman drives, $\Delta^{\uparrow} \approx \Delta^{\downarrow} + A_{\parallel}^{(2)}$.

Figure 8.9b shows the expected differential AC-Zeeman shift on the Qb1 transition as a function of $\Delta^{\uparrow}$ for both possible states of Qb2 and equal driving amplitudes $\Omega_A = \Omega_B$. The curves are calculated using Eq. 5.15 and only plot the region where $\Delta > \Omega_{\mathrm{Ram}}$. As expected, the two quantities are similar but not equal. We define

$$\delta_{2\mathrm{qb}} \equiv \delta_{\mathrm{AC}}^{\uparrow} - \delta_{\mathrm{AC}}^{\downarrow} \tag{8.4}$$

shown in Figure 8.9c as a function of $\Delta^{\uparrow}$. Based on the value of $\delta_{2\mathrm{qb}}$ we can distinguish two regimes:

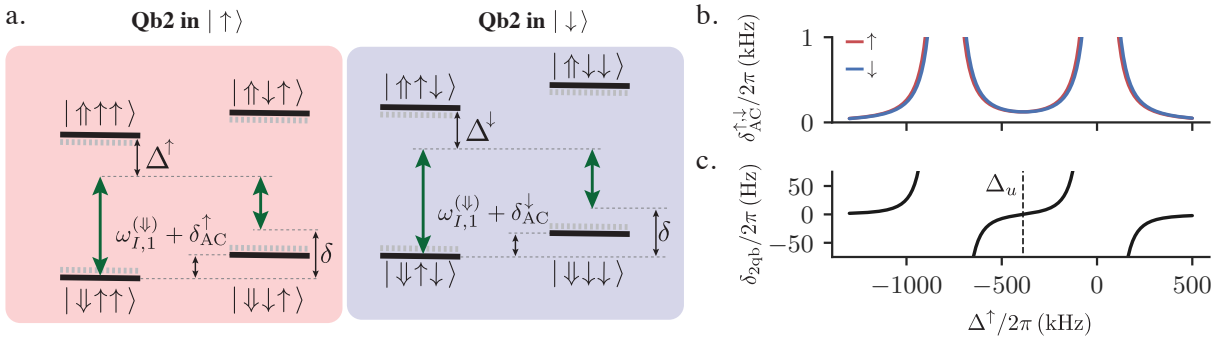

Figure 8.9.: Two-qubit stimulated Raman drive. **a** Energy level diagram under stimulated Raman drive. The bare energy levels shown in Figure 8.5 (gray dashed lines) have been AC-Zeeman shifted by the strong off-resonance drives, plotted as green arrows. The colored boxes differentiate the two possible states of Qb2. When Qb2 is in $|\downarrow\rangle$ ($|\uparrow\rangle$), the Raman detuning is given by $\Delta^{\downarrow}$ ($\Delta^{\uparrow}$) and the AC-Zeeman shift on the Qb1 transition frequency is $\delta_{\mathrm{AC}}^{\downarrow}$ ($\delta_{\mathrm{AC}}^{\uparrow}$). **b** Computed $\delta_{\mathrm{AC}}^{\uparrow}$ (red line) and $\delta_{\mathrm{AC}}^{\downarrow}$ (blue line) as a function of $\Delta^{\uparrow}$ for two drives with the same amplitude $\Omega_{\mathrm{A,\,B}}/2\pi = 10$ kHz. **c** Computed $\delta_{2\mathrm{qb}}$ as a function of $\Delta^{\uparrow}$ for the same conditions as the previous plot. A dashed vertical line shows the unconditional driving condition Δ_u, where $\delta_{2\mathrm{qb}} = 0$.

- **Unconditional driving.** In this regime $\delta_{2\mathrm{qb}} \approx 0$ and the Qb1 transition frequency is effectively independent of Qb2. It is obtained for $\Delta^{\uparrow} \approx \Delta_u \equiv -\omega_{I,1}/2 - A_{\parallel}^{(2)}/2$, where the driving speed can be maximized[3].
- **Conditional driving.** For all other values of $\Delta^{\uparrow}$, the transition frequency for Qb1 is conditioned on the state of Qb2.

3: Experimentally, the unconditional regime applies when $|\delta_{2\mathrm{qb}}| \ll \Omega_{\mathrm{Ram}}$. For $\Omega_{\mathrm{Ram}} \approx 0.1$ kHz we observe tolerance for $\Delta^{\uparrow}$ variations of order ~ 10 kHz while remaining unconditional.

These two regimes are used for the single- and two-qubit gates, respectively. In the unconditional regime, the frequency of the NMR-allowed transitions does not depend on the state of Qb2, a crucial property for implementing single-qubit gates. On the contrary, conditional driving creates a native CNOT gate, which will be explored in detail in Section 8.6.

Single-qubit gates

We now perform spectroscopy and characterization of the two ^{183}W nuclear spins via stimulated Raman driving in the unconditional regime. We first perform Raman spectroscopy using the unconditional driving condition $\Delta/2\pi = -408.8$ kHz $\approx \Delta_u/2\pi$, and $\Omega_A = \Omega_B$. The nuclear spin register is prepared in the $|\downarrow\downarrow\rangle$ state, after which a Raman pulse is applied with detuning δ, followed by nuclear spin readout. When the resonance condition is met, we observe a transfer of the nuclear spin population to either the $|\downarrow\uparrow\rangle$ or the $|\uparrow\downarrow\rangle$ state (see Figure 8.10a). The resonance linewidth is of order 100 Hz or less, two orders of magnitude narrower than the electron spin linewidth, which confirms that the Raman driving occurs through virtual transitions of the electron excited states. The ~ 2 kHz splitting between the two NMR-allowed transitions reflects different values of $A_{\parallel}, A_{\perp}$ and ω_I for the two ^{183}W nuclear spins, due to their distinct positions relative to the Er^{3+} ion.

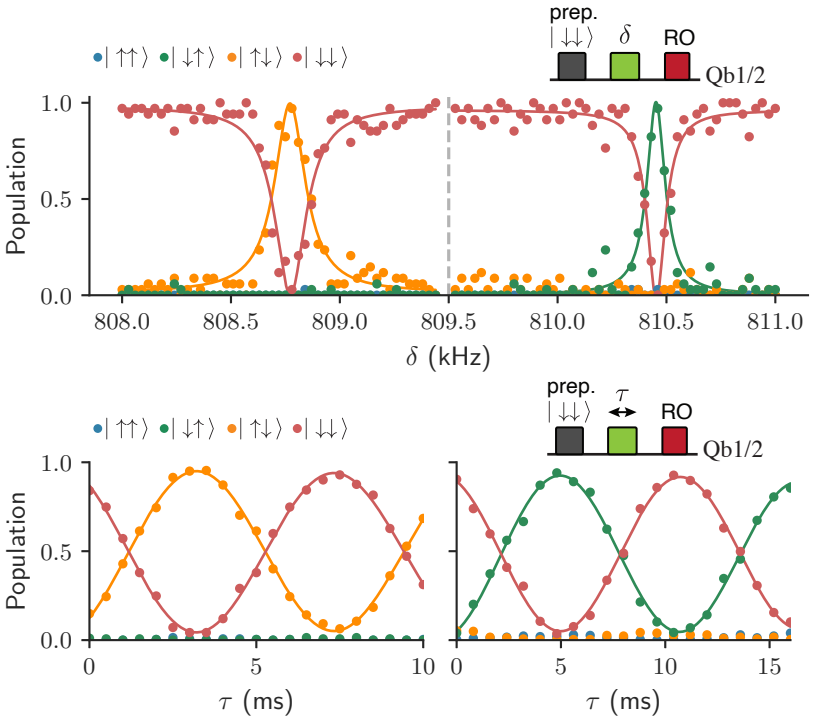

Figure 8.10.: NMR spectroscopy and Rabi driving of Qb1 and Qb2. **a.** Spectroscopy of the two nuclear spins Qb1 (left) and Qb2 (right) using unconditional Raman pulses with detuning $\Delta/2\pi = -404.8$ kHz. Drive power below (above) 809.5 kHz was tuned to match the drive amplitude corresponding to a π-pulse for Qb1 (Qb2); continuous solid lines are Lorentzian fits, error bars indicate $1-\sigma$ standard deviation of the data. **b.** Rabi oscillations of Qb1 (left) and Qb2 (right) as a function of pulse duration at $\delta/2\pi = 808.85$ kHz and 810.45 kHz, respectively; drive amplitudes were the same as those used in (a), error bars indicate $1-\sigma$ standard deviation of the data, continuous line is a sinusoidal fit.

We now confirm the unconditional nature of the drive by studying the spectrum of Qb2 after preparation of Qb1 in either the $|\downarrow\rangle$ or the $|\uparrow\rangle$ state, as shown in Figure 8.11. At $\Delta \sim \Delta_u$, the two resonances occur at the same frequency, confirming the unconditional driving condition. Additionally, both curves are quantitatively reproduced by simulations based on the spin Hamiltonian performed by Z. Huang (see Appendix C), using parameters determined by spectroscopic measurements.

Knowing the required drive frequencies, we then prepare the $|\downarrow\downarrow\rangle$ state and sweep the drive duration, giving rise to coherent Rabi oscillations of each qubit, as shown in Figure 8.10b. This allows us to measure the Rabi Raman rate $\Omega^{(1)}_{\text{Ram}}/2\pi = 121(1)$ Hz and $\Omega^{(2)}_{\text{Ram}}/2\pi = 87(1)$ Hz for a specific microwave amplitude and calibrate the π-pulses for Qb1 and Qb2, respectively.

As detailed in Section 5.1, the Rabi frequency of a stimulated Raman drive is proportional to the hyperfine coupling $A_\perp$. We can therefore use the measured values of $\Omega^{(1,2)}_{\text{Ram}}$ to estimate $A_\perp$. In the unconditional regime with both drives having the same microwave amplitude, this relation is readily expressed as

$$\Omega_{\text{Ram}} \approx \frac{\Omega_A^2 A_\perp}{\omega_I^2} \tag{8.5}$$

From the data presented in Figure 8.10b we obtain $A^{(1)}_\perp/2\pi = 71(3)$ kHz and $A^{(2)}_\perp/2\pi = 12.8(6)$ kHz. We note that there is a difference between the measured value of $A^{(1)}_\perp$ and the value inferred from time-trace statistics in the previous chapter (where we obtain ~40 kHz). For the same reasons invoked in Section 7.5, we consider the value measured by the Raman fit to be more precise, although limited by the precision in microwave amplitude.

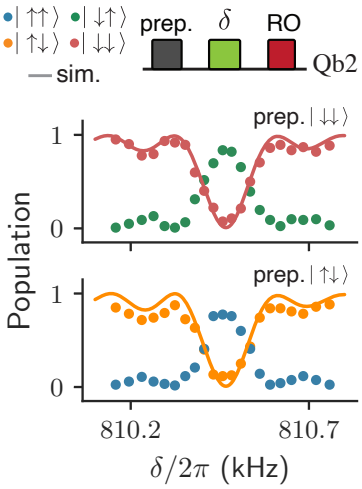

Figure 8.11.: Spectroscopy of Qb2 with unconditional pulse conditions, $\Delta/2\pi = -404.8\,\text{kHz} \approx \Delta_u/2\pi$ with Qb1 prepared in state $|\downarrow\rangle$ (top) or $|\uparrow\rangle$ (bottom). Solid line is the result of a simulation using the QuTiP package, based on the measured spin Hamiltonian parameters.

In the process of running these experiments, we realized that the application of the microwave Raman driving pulses has an impact on the nuclear spin coherence. This is shown in the following experiment. We measured Raman Rabi oscillations extending over longer times than those previously shown. In Figure 8.12, we observe that the oscillations are damped with a characteristic time $T_{2,\text{drive}} = 150(35)$ ms, much faster than T_2^* for this qubit (see next section). We attribute this to an increase in the thermal population of the electron spin $\bar{n}_{\text{th}}$ during driving, which results in excess dephasing. The measurement data in Figure 8.12 are fit to a simulation performed by Z. W. Huang (see Appendix C), which yields a thermal population $\bar{n}_{\text{th}} = 9.5 \times 10^{-3}$, several orders of magnitude larger than the expected Er^{3+} excited state population at 10–20 mK. Due to time constraints, measurement of $T_{2,\text{drive}}$ under different pulse amplitudes was not performed, which would be required to experimentally confirm the origin of this noise source.

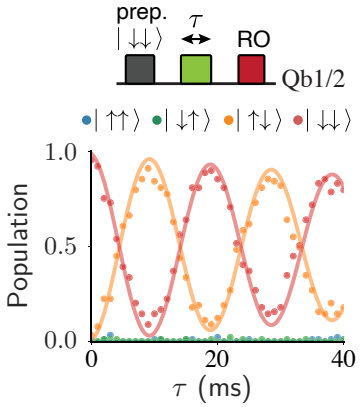

Figure 8.12.: Extended duration Raman Rabi on Qb1. The decay time of the oscillations under driving $T_{2,\text{drive}} = 150(35)$ ms was extracted from fitting. Solid line is a simulation with thermal population of the Er^{3+} ancilla adjusted to $\bar{n}_{\text{th}} = 9.5 \times 10^{-3}$ to match the decay rate to the data.

8.5. Nuclear spin coherence time

We then proceed to measure the coherence properties of the nuclear spin qubits. We perform a Ramsey experiment on each qubit as shown in Figure 8.13 and extract T_2^* times of 0.8(2) s and 1.2(3) s for Qb1 and Qb2, respectively. To our knowledge, these are the longest single-nuclear-spin Free-Induction-Decay times measured in a natural-abundance material by more than an order of magnitude. These times are on par with those measured in isotopically-enriched silicon [30] and diamond [100], which further confirms the interest of $CaWO_4$ for spin-based quantum computing [26]. The residual decay is likely caused by a combination of B_0 drift and spectral diffusion due to nuclear spin bath reconfiguration. Coupled Cluster Expansion calculations, performed by Sen Lin and Renbao Liu, predict a decay time of 0.2 s, shorter than the measurements. We interpret the longer experimental T_2^* as being due to partial polarization of the ^{183}W nuclear-spin bath by the pulses used to prepare the $|\downarrow\downarrow\rangle$ state, an effect which has been observed in similar systems [101, 102]. Additionally, the Larmor frequency of ^{183}W neighboring the Er^{3+} impurity experiences a paramagnetic shift due to the hyperfine coupling, which reduces the flip-flop interaction rate with the rest of the ^{183}W bath, also known as the frozen-core effect [103].

We performed Hahn echo measurements yielding T_2 times of 3.4(4) s and 4.4(6) s for qubits 1 and 2, respectively, as shown in Figure 8.14. Coupled Cluster Expansion calculations predict a Hahn echo decay time of 10 s due to nuclear spin bath dynamics. We believe the extra decoherence

[30]: Muhonen et al. (2014), 'Storing Quantum Information for 30 Seconds in a Nanoelectronic Device'

[100]: Bartling et al. (2025), 'Universal High-Fidelity Quantum Gates for Spin Qubits in Diamond'

[26]: Le Dantec et al. (2021), 'Twenty-Three–Millisecond Electron Spin Coherence of Erbium Ions in a Natural-Abundance Crystal'

[101]: Taminiau et al. (2014), 'Universal Control and Error Correction in Multi-Qubit Spin Registers in Diamond'

[102]: Mądzik et al. (2020), 'Controllable Freezing of the Nuclear Spin Bath in a Single-Atom Spin Qubit'

[103]: Guichard et al. (2015), 'Decoherence of Nuclear Spins in the Frozen Core of an Electron Spin'

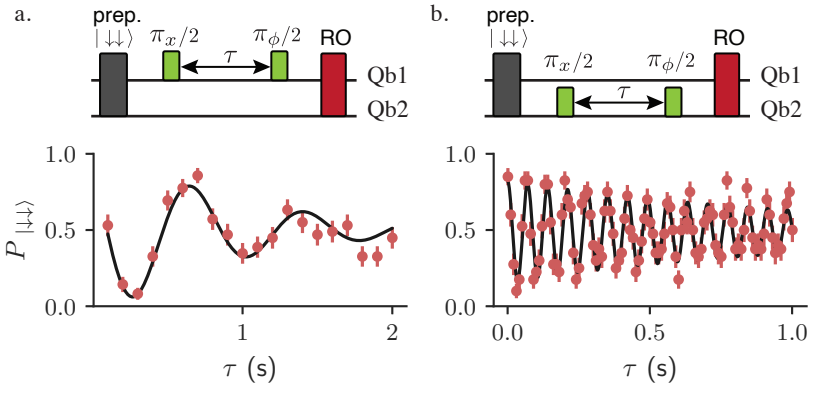

Figure 8.13.: Ramsey measurement of Qb1 and Qb2 (subplots a and b, respectively). The fit (solid line) returns $T_2^* = 0.8(2)$ s for Qb1 and $T_2^* = 1.2(3)$ s for Qb2. Error bars indicate standard error of the mean. Raman drive pulses are applied in the unconditional regime, $\Delta \approx \Delta_u$. The phase of the last pulse is $\phi = \omega_{1,2}^{\text{art}} \cdot \tau$, where $\omega_{1,2}^{\text{art}}$ is an artificial detuning. The difference between the nuclear spin frequency and the artificial detuning gives rise to the oscillations in the measured data.

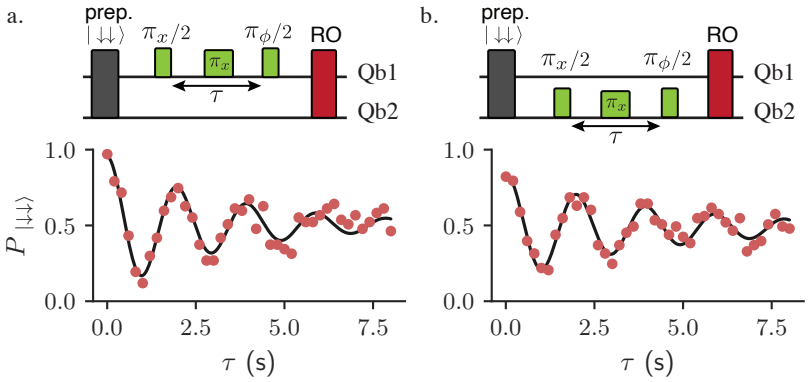

Figure 8.14.: Hahn echo measurement of Qb1 and Qb2 (subplots a and b, respectively). The fit (solid line) returns $T_2 = 3.4(4)$ s for Qb1 and $T_2 = 4.4(6)$ s for Qb2. Error bars indicate standard error of the mean. Raman drive pulses are applied in the unconditional regime, $\Delta \approx \Delta_u$. The phase of the last pulse is $\phi = 2\pi \cdot 0.5\ \text{Hz} \cdot \tau$, creating artificial oscillations.

is due to residual excitations of the Er^{3+} ion, which occur at a rate $\bar{n}\Gamma_R$, $\bar{n} \approx 10^{-4}$ being the mean thermal occupation of the resonator mode, a value roughly consistent with the measured SMPD dark count rate. Energy relaxation of the two nuclear spin qubits likely occurs at a much lower rate, as indicated by ensemble measurements, which yield an upper bound of $\sim 10^{-6}$ s^{-1} for the relaxation rate of ^{183}W proximal to Er^{3+}:$CaWO_4$ [70], and was not directly measured. Dynamically detuning the resonator from the Er^{3+} spin during pulse sequences while employing dynamical decoupling may offer a path to further extend these coherence times.

[70]: Wang et al. (2024), *Month-Long-Lifetime Microwave Spectral Holes in an Erbium-Doped Scheelite Crystal at Millikelvin Temperature*

8.6. Entangling the nuclear spins

We now proceed to implement two-qubit gates in our two-nuclear spin register. First we investigate the direct interaction between Qb1 and Qb2, which we find too small to perform entangling gates. We then proceed to demonstrate how to implement a CNOT by driving stimulated Raman transitions in the unconditional regime.

Being in close proximity, the two nuclear spins are coupled by the dipolar interaction. The first order term can be modeled as $C_{zz} I_{z1} I_{z2}$. If strong enough, this interaction could be used to create a native two-qubit entangling gate. Consequently, we proceed by measuring C_{zz} by

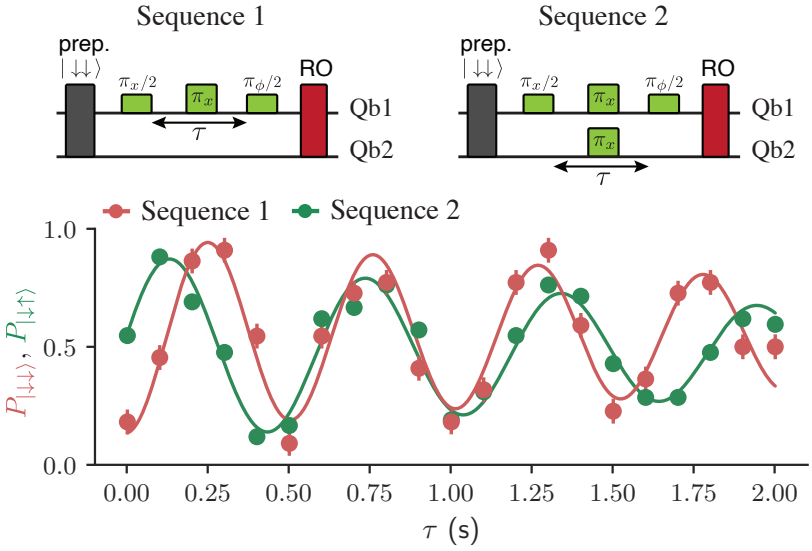

Figure 8.15.: Spin-echo double resonance (SEDOR) measurement (dots) performed on Qb1, in which sequence 1 and sequence 2 (as shown above) yielded the red and green curves, respectively. The fits (solid lines) yield a nuclear–nuclear coupling rate $C_{zz}/2\pi = 0.8$ Hz.

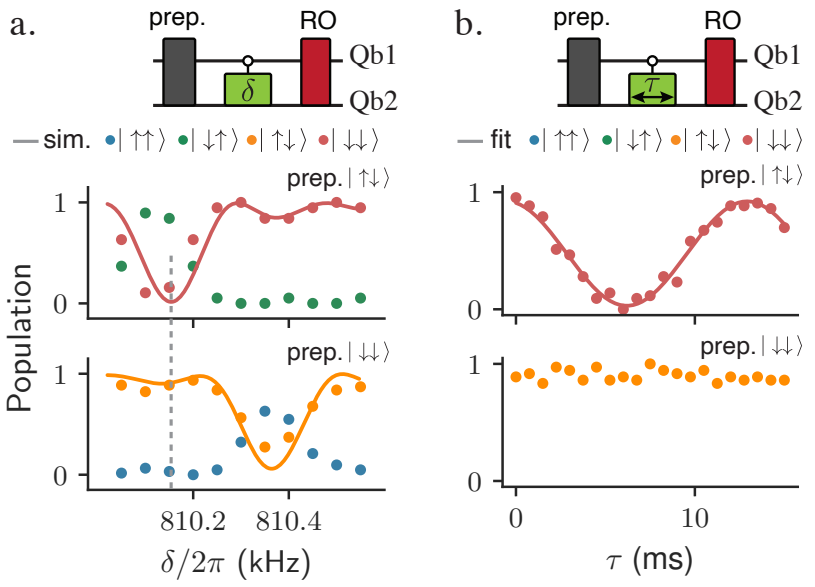

Figure 8.16.: Conditional spectroscopy and CNOT gate on Qb2. The conditional Raman pulses have $\Delta/2\pi = 110$ kHz and $\Omega_B = 5\Omega_A$ and are denoted in the pulse sequence with a green pulse with a connecting line. **(a)** Spectroscopy of Qb2. Qb1 is prepared in state $|\downarrow\rangle$ (top) or $|\uparrow\rangle$ (bottom). Solid line is the result of a simulation using the QuTiP package, based on the measured spin Hamiltonian parameters. Vertical dashed line highlights the frequency used for the CNOT gate. **(b)** Rabi oscillations when Raman-driving Qb2 at 810.12 kHz (vertical dashed line in the previous figure). Data are plotted for Qb1 prepared in the $|\downarrow\rangle$ (red) and $|\uparrow\rangle$ (orange) states, note that Qb2 is rotated only if Qb1 is in the $|\downarrow\rangle$ state, enacting a CNOT gate when $\tau = 6.72$ ms. Red solid line is a cosine fit.

performing a spin-echo double resonance (SEDOR) experiment [12], as shown in Figure 8.15. This consists of a Hahn echo experiment performed on one nuclear spin qubit, the probe qubit, where either no pulse (red curve) or an additional π pulse (green curve) is applied to the other qubit in the middle of the echo sequence. This yields a shift in frequency of the probe qubit equal to $C_{zz}/2$. We measure $C_{zz}/2\pi = 0.8$ Hz, on the same order of magnitude as the qubit dephasing rate. Therefore, any gate implemented through direct nuclear–nuclear coupling will have a duration on the order of seconds, and it is desirable to find an alternative mechanism.

We now focus instead on the conditional AC-Zeeman shifts induced by the stimulated Raman drives. We study the spectrum of Qb2 after preparation of Qb1 in either the $|\downarrow\rangle$ or the $|\uparrow\rangle$ state in the conditional regime with the objective of implementing a two-qubit entangling gate. For this purpose, we try to maximize the value of $\delta_{2\mathrm{qb}}$. We set $\Delta/2\pi = 110$ kHz and $\Omega_B = 5\Omega_A$. This asymmetry is introduced to help preserve the Raman regime ($\Omega_A \ll \Delta$ and $\Omega_B \ll \Delta + \delta_0$) when the value of Δ is reduced. Figure 8.16a shows the two spectra of Qb2 depending on the state of Qb1, from which we measure $\delta_{2\mathrm{qb}}/2\pi = 244(8)$ Hz. Both curves are quantitatively reproduced by simulations based on the spin Hamiltonian performed by Z. W. Huang (see Appendix C), using parameters determined by spectroscopic measurements.

After preparing the $|\downarrow\downarrow\rangle$ or $|\uparrow\downarrow\rangle$ states, we drive Qb2 at 810.13 kHz, as shown in Figure 8.16b. For a 6.72 ms drive pulse, the $|\downarrow\downarrow\rangle$ state is driven to the $|\downarrow\uparrow\rangle$ state, while the same pulse has no effect on the $|\uparrow\downarrow\rangle$ state. The truth table for the pulse is shown in Table 8.2. A logic NOT gate is applied on Qb2 if and only if Qb1 is in the $|\downarrow\rangle$. This effectively implements a Controlled-NOT (CNOT) gate, which can be used to deterministically entangle the state of the two qubits.

Input	Output
$\|\uparrow\uparrow\rangle$	$\|\uparrow\uparrow\rangle$
$\|\uparrow\downarrow\rangle$	$\|\uparrow\downarrow\rangle$
$\|\downarrow\uparrow\rangle$	$\|\downarrow\downarrow\rangle$
$\|\downarrow\downarrow\rangle$	$\|\downarrow\uparrow\rangle$

Table 8.2.: Truth table for a CNOT gate.

8.7. Bell state tomography

We use this CNOT gate to generate the Bell states $|\Phi^+\rangle = (|\downarrow\downarrow\rangle + |\uparrow\uparrow\rangle)/\sqrt{2}$ and $|\Psi^+\rangle = (|\downarrow\uparrow\rangle + |\uparrow\downarrow\rangle)/\sqrt{2}$. Figure 8.17 shows the preparation se-

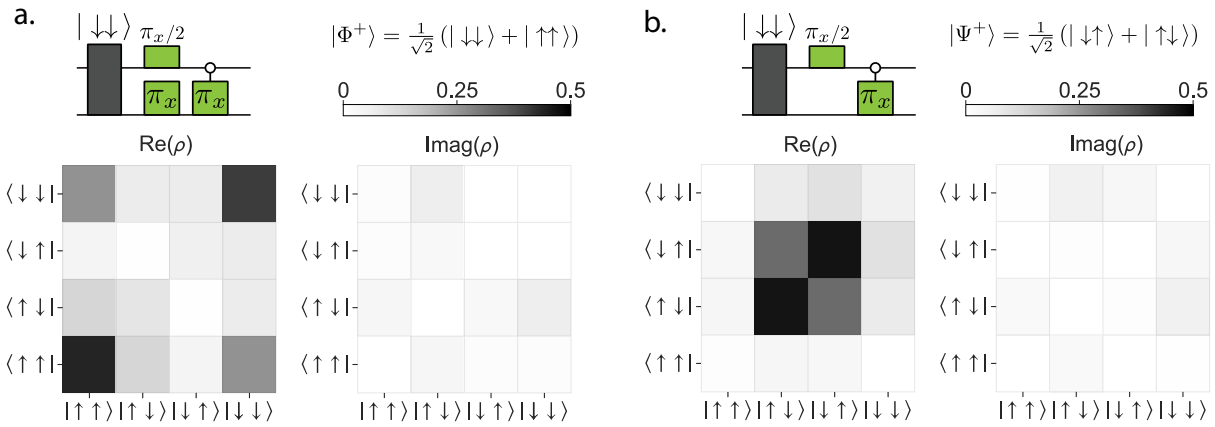

Figure 8.17.: Bell state tomography. Real (left) and imaginary (right) components of tomographically reconstructed density matrices of the Bell states $|\Phi^+\rangle$ and $|\Psi^+\rangle$. State preparation sequences are shown as an inset. Extracted fidelities after SPAM error correction are 0.68 and 0.79, respectively.

quences as well as state tomography of the reconstructed density matrices of the two Bell states. For the purpose of characterization, we define the fidelity of a measured state ρ with respect to a target state ρ_t as [104]

[104]: Nielsen et al. (2010), *Quantum Computation and Quantum Information: 10th Anniversary Edition*

$$\mathcal{F} = \left(\mathrm{Tr}\left\{\sqrt{\sqrt{\rho_t}\cdot\rho\cdot\sqrt{\rho_t}}\right\}\right)^2 \tag{8.6}$$

SPAM error correction was applied during the reconstruction of the state tomography, which yields fidelities of 0.68 and 0.79 for the $|\Phi^+\rangle$ and $|\Psi^+\rangle$ states, respectively.

We studied the contribution of the different coherent and incoherent error sources during Bell state preparation using the numerical simulations described in Appendix C. We simulate the preparation sequence for $|\Psi^+\rangle$ including the required pulses for state tomography to account for the full experimental process. Then, we perform maximum likelihood estimation on the resulting set of measurement results to reconstruct the density matrix and extract the fidelity to the target state.

When including only coherent errors (i.e. removing all decay and dephasing effects) the simulation yields a fidelity of 0.978; when including incoherent errors in addition, we find an expected fidelity of 0.976. The long coherence times of the two qubits (~ s) in comparison to the state preparation time (~ ms) explain the relatively small reduction in fidelity due to incoherent errors. Therefore, the identified coherent and incoherent errors are insufficient to account for the experimentally measured fidelity of 0.79. We attribute the discrepancy to the finite thermal population of the Er^{3+} electron spin under a driving field, an effect that was discussed in Section 8.4. The increase in thermal population may enhance the dephasing rate due to the non-zero population of the Er^{3+} spin excited state. During tomography, the average pulse sequence was on the order of 30 ms. Based on this and $T_{2,\mathrm{drive}}$ as measured in Section 8.4, we expect approximately 15% additional infidelity due to dephasing, which is roughly sufficient to account for the remaining error. Due to time constraints, measurement of $T_{2,\mathrm{drive}}$ under the exact conditions of the Bell state preparation sequence was not performed, and further investigation would be required to verify the origin of the reduced fidelity.

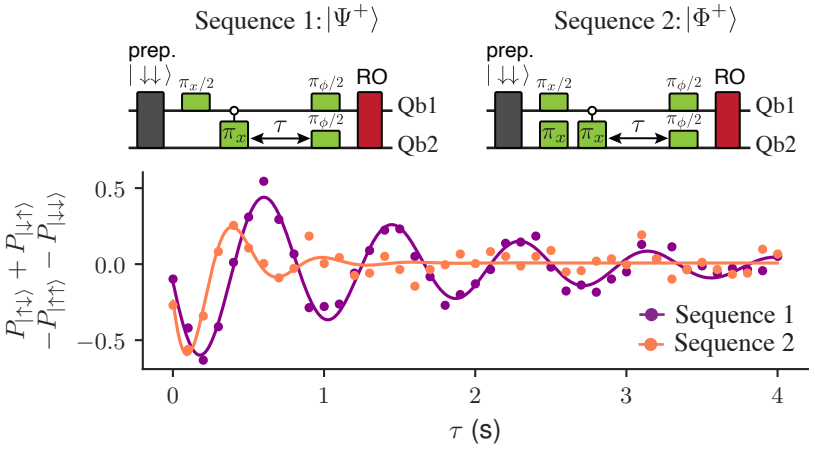

Figure 8.18.: Decoherence-free subspace. Ramsey coherence measurement of the $|\Phi^+\rangle = \frac{1}{\sqrt{2}}(|\downarrow\downarrow\rangle + |\uparrow\uparrow\rangle)$ (coral) state and the $|\Psi^+\rangle = \frac{1}{\sqrt{2}}(|\downarrow\uparrow\rangle + |\uparrow\downarrow\rangle)$ (purple) state, yielding T_2^* values of 0.3(1) and 1.7(2) s, respectively. The final two $\pi/2$-pulses carry a phase ϕ as an artificial detuning, which gives rise to the oscillations. The data (dots) are fit to an exponentially decaying cosine (solid line).

8.8. Decoherence-free subspace

As discussed in Section 8.1, both magnetic field fluctuations and dynamics of the nuclear spin bath are an important source of magnetic noise in solid-state systems. Neighboring nuclear spins experience the same field as well as correlated bath dynamics and a significant suppression of the correlated noise can be expected by preparing the state in specific Bell states [10, 38].

[10]: Bradley et al. (2019), 'A Ten-Qubit Solid-State Spin Register with Quantum Memory up to One Minute'
[38]: Bartling et al. (2022), 'Entanglement of Spin-Pair Qubits with Intrinsic Dephasing Times Exceeding a Minute'

This improvement in coherence time can be traced to the magnetic properties of the prepared states; for example, the Bell state $|\Psi^+\rangle$ corresponds to a triplet state with a total spin of 1, and a magnetic projection of $m_S = 0$. Compared to bare nuclear spin states, the energy difference between the $|\downarrow\uparrow\rangle$ and $|\uparrow\downarrow\rangle$ states is approximately 400 times smaller, which suppresses the effect of spatially correlated sources of magnetic field noise that affect both spins equally. As a result, $|\Psi^+\rangle$ forms an effective decoherence-free subspace, where quantum information can be preserved for a longer period of time.

We proceed to study this effect by measuring the coherence time of these multi-qubit states. We begin by preparing the system in $|\Psi^+\rangle$, followed by an evolution time τ. Then, we project the state back to the single qubit basis with a $\pi/2$-pulse in each qubit, followed by readout of the populations. We define

$$S = \left(P_{\downarrow\uparrow} + P_{\uparrow\downarrow}\right) - \left(P_{\downarrow\downarrow} + P_{\uparrow\uparrow}\right), \tag{8.7}$$

which measures the coherence of the Bell state[4]. Figure 8.18 plots S as a function of τ. We measure a coherence time for $|\Psi^+\rangle$ of 1.7(2) s, which approximately doubles the individual qubit coherence time. In addition, we also measure the coherence of $|\Phi^+\rangle$, also a triplet state but with magnetic projection $m_S = 1$. As expected, the measured coherence time for this state is 0.3(1), as correlated noise sources are enhanced due to the effective increase in gyromagnetic factor.

4: This quantity measures how much of the population remains in the $\{|\downarrow\uparrow\rangle, |\uparrow\downarrow\rangle\}$ manifold compared to the $\{|\downarrow\downarrow\rangle, |\uparrow\uparrow\rangle\}$. As the system decays into a mixed state, $S \to 0$.

If we assume additive contributions of independent dephasing rates, we can consider that the coherence time for the two Bell states is given by

$$\begin{aligned}\frac{1}{T^*_{2,|\Psi^+\rangle}} &= \sqrt{2}\pi\Gamma_u + \frac{1}{T_2},\\ \frac{1}{T^*_{2,|\Phi^+\rangle}} &= \sqrt{2}\pi\Gamma_u + 2\pi\Gamma_c + \frac{1}{T_2}.\end{aligned} \tag{8.8}$$

where Γ_u and Γ_c correspond to the dephasing rate due to spatially uncorrelated and correlated noise. For completely uncorrelated noise, the contribution to the decoherence rate for the two states is identical. However, correlated noise sources from the nuclear spin bath and B_0 fluctuations are suppressed to first order for $|\Psi^+\rangle$, as they couple identically to the two spins, due to their spatial proximity. From the measured coherence times, we extract the contributions of spatially correlated and uncorrelated noise, $\Gamma_u \approx 0.1$ Hz and $\Gamma_c \approx 0.4$ Hz. The amplitude of the correlated noise is in agreement with previous observations of magnetic field noise [70], pointing to this mechanism as the dominant term in correlated noise.

[70]: Wang et al. (2024), *Month-Long-Lifetime Microwave Spectral Holes in an Erbium-Doped Scheelite Crystal at Millikelvin Temperature*

8.9. Conclusion and outlook

In conclusion, we have presented the building blocks for a quantum information processing platform using nuclear spins in the solid state as qubits. Primarily, we have demonstrated how to implement single- and two-qubit gates through stimulated Raman driving. This technique leverages the hyperfine-induced mixing of the electron and nuclear spin energy levels to drive coherent Raman transitions between the nuclear spin levels. We remark that this scheme requires the nuclear spin levels to be resolved and therefore long electron coherence times. In our particular case, the Er^{3+} spin coherence is $T_2^* = 170$ µs, and the Larmor frequency of the nuclear spins is readily resolved. This might not be the case in other systems with shorter electron spin coherence or weakly coupled nuclear spins.

The fidelity of the gates demonstrated here remains significantly lower than the state of the art achieved in other color-center platforms, such as NV centers. A key limitation of the present scheme is that the application of the Raman drives substantially increases the nuclear spin decoherence rate. We attribute this effect to an increased thermal occupation of the excited Er^{3+} state induced by the applied drives. To properly address this problem, an in-depth study would need to be performed, tracking the source of the problem, with the goal of developing strategies to suppress or mitigate their impact.

Readout fidelity is intrinsically limited by cross-relaxation events of the nuclear spin during the readout protocol. Increasing the quality factor of the superconducting resonator is a straightforward path to improve this figure. In addition, achieving a stronger Purcell rate would help address the long readout times of the experiment: readout of the joint 2-qubit state requires ~ 1 s per shot, which is long compared to a previous demonstration of ~ 20 ms for optical QND readout of an Er^{3+} spin [105]. It should be possible to reduce the measurement time by orders of magnitude by increasing the Purcell-enhanced spin decay rate using a resonator with a parallel-plate capacitor design to enhance resonator-spin coupling [18, 106].

[105]: Raha et al. (2020), 'Optical Quantum Nondemolition Measurement of a Single Rare Earth Ion Qubit'

[18]: Bienfait et al. (2016), 'Reaching the Quantum Limit of Sensitivity in Electron Spin Resonance'

[106]: Haikka et al. (2017), 'Proposal for Detecting a Single Electron Spin in a Microwave Resonator'

However, the specific parameter range for which this driving scheme is achievable is not wide: effective driving of the nuclear spin through a stimulated Raman process requires a low-quality resonator to avoid microwave filtering. Indeed, the Larmor frequency of the target nuclear spin must be on the same order of magnitude as the resonator's bandwidth κ. ^{183}W nuclear spins possess a low gyromagnetic moment, which yields a Larmor frequency of $\sim$ 800 kHz at the operating magnetic field. Tuning the electron spin frequency with the resonator results in the two stimulated Raman drives being applied at $\omega_r \pm \omega_I/2$. If the linewidth of the resonator were reduced by an order of magnitude, something desirable as it would enhance the Purcell factor, the necessary microwave amplitude of each drive to achieve the same Rabi rate would be ~ 7 times larger. This could be addressed by adapting the resonator design to have a tunable quality factor, as demonstrated in ref. [95]. One could envision a scheme where κ is dynamically tuned to be wider during the pulse scheme and narrower during the readout sequence.

[95]: Wen et al. (2025), *Addressing Spins at the Clock Transitions with a Frequency- and Bandwidth-Tunable Superconducting Resonator*

If one were able to solve the aforementioned problems, the question of scaling the nuclear spin register becomes relevant. With rf access to the resonator, additional nuclear spin qubits could be interfaced using DDrf control techniques [10, 107]. A possible resonator design would include a Bragg mirror in the form of a mismatched impedance transmission line, which would allow galvanic coupling of the resonator to the microwave lines [108]. However, this scheme would not be ideal, as the Purcell-enhanced relaxation rate of the Er^{3+} spin will ultimately limit its coherence time. This approach would be limited to around 10 qubits due to the weak dipolar coupling of ^{183}W spins to the Er^{3+} which decreases rapidly with distance. Distant Er^{3+} spins could be deterministically entangled using virtual photon exchange via the superconducting resonator [109, 110]. Readout could be frequency multiplexed using multiple SMPDs, allowing multiple clusters of W spins coupled to Er^{3+} ancilla to be controlled via a single resonator. Beyond the Er^{3+}:$CaWO_4$ system, many other crystal hosts and spin species could be investigated. Both the readout and control mechanisms are not limited by system-specific mechanisms, which opens the door to exciting new discoveries and developments in systems that are largely unexplored.

[10]: Bradley et al. (2019), 'A Ten-Qubit Solid-State Spin Register with Quantum Memory up to One Minute'
[107]: Beukers et al. (2025), 'Control of Solid-State Nuclear Spin Qubits Using an Electron Spin-$1/2$'
[108]: Mahashabde et al. (2020), 'Fast Tunable High-Q-Factor Superconducting Microwave Resonators'
[109]: Majer et al. (2007), 'Coupling Superconducting Qubits via a Cavity Bus'
[110]: Landig et al. (2019), 'Virtual-Photon-Mediated Spin-Qubit–Transmon Coupling'

^{93}Nb nuclear spin

Precision spectroscopy of a ^{93}Nb nuclear spin

9.

In this chapter, we investigate an unexpected impurity with nuclear spin $I = 9/2$ found in close proximity to an individual Er^{3+} spin. By analyzing the NMR transitions, excited through stimulated Raman driving, we identify the spin as a ^{93}Nb . We then perform precision spectroscopy by leveraging the long coherence of the ^{93}Nb spin, and we determine the nuclear transition frequencies with hertz precision. By fitting the nuclear spectra to the spin Hamiltonian of the system, we identify a previously unobserved coupling term between the electron spin and the nuclear quadrupole. In addition, we set an upper bound on the hexadecapolar interaction of the ^{93}Nb nuclear spin, one order of magnitude tighter than previous NMR ensemble measurements in the solid state.

The measurements in this chapter were performed by Z. W. Huang, and I performed the data analysis.

9.1 State-of-the-art 106
9.2 Spin system 110
9.3 Readout, preparation and control 113
9.4 Identification and site assignment 117
9.5 Precision NMR spectroscopy 118
9.6 Hamiltonian parameters fit 121
Fitting $\mathscr{H}^{(\Downarrow)}$ and $\mathscr{H}^{(\Uparrow)}$ . . . 121
Fitting $\mathscr{H}$ 125
9.7 Origin of the SDQ interaction 128
Pseudo-quadrupole interaction 128
Electrostatic coupling . . 130
9.8 Octupole and hexadecapolar bounds 131
9.9 Conclusion and outlook . 132

9.1. State-of-the-art

We begin this chapter by highlighting two state-of-the-art experiments in which the spectra of individual quadrupolar nuclei were measured. As in the previous chapters, the systems of interest are NV centers in diamond and donor impurities in silicon.

Quadrupolar spectroscopy of a ^{14}N nuclear spin in diamond

The NV center has C_{3v} point-symmetry. This implies that, in principle, the ^{14}N quadrupole is axial around the NV symmetry axis. As discussed in Section 3.3, the quadrupolar Hamiltonian in this case takes the following form,

$$\hat{\mathscr{H}}_{\mathrm{Q}} = Q_{zz}\left[\hat{I}_z^2 - I(I+1)/3\right]. \tag{9.1}$$

Only one parameter is needed to describe the interaction. Recent work by S. Breitweiser *et al.* tests this hypothesis and shows by precision spectroscopy that C_{3v} symmetry is in fact broken for individual NVs [13]. This is manifested by the appearance of a small but non-zero biaxiality parameter η.

[13]: Breitweiser et al. (2024), 'Quadrupolar Resonance Spectroscopy of Individual Nuclei Using a Room-Temperature Quantum Sensor'

As shown in Figure 9.1a, the sample is located inside a solid immersion lens, which enhances optical photon collection efficiency. The energy level structure of the coupled electron-nuclear system is shown in Figure 9.1b. The spectrum is progressively split by the different interaction terms. Since the magnetic field is applied along the quadrupole axis, the quadrupole interaction is diagonal and splits the levels proportional to m_I^2.

They measure, with high precision, the hyperfine spectrum of the quadrupolar nucleus using a DD pulse sequence. This sequence follows the same principle of electron decoupling as the DDrf sequences

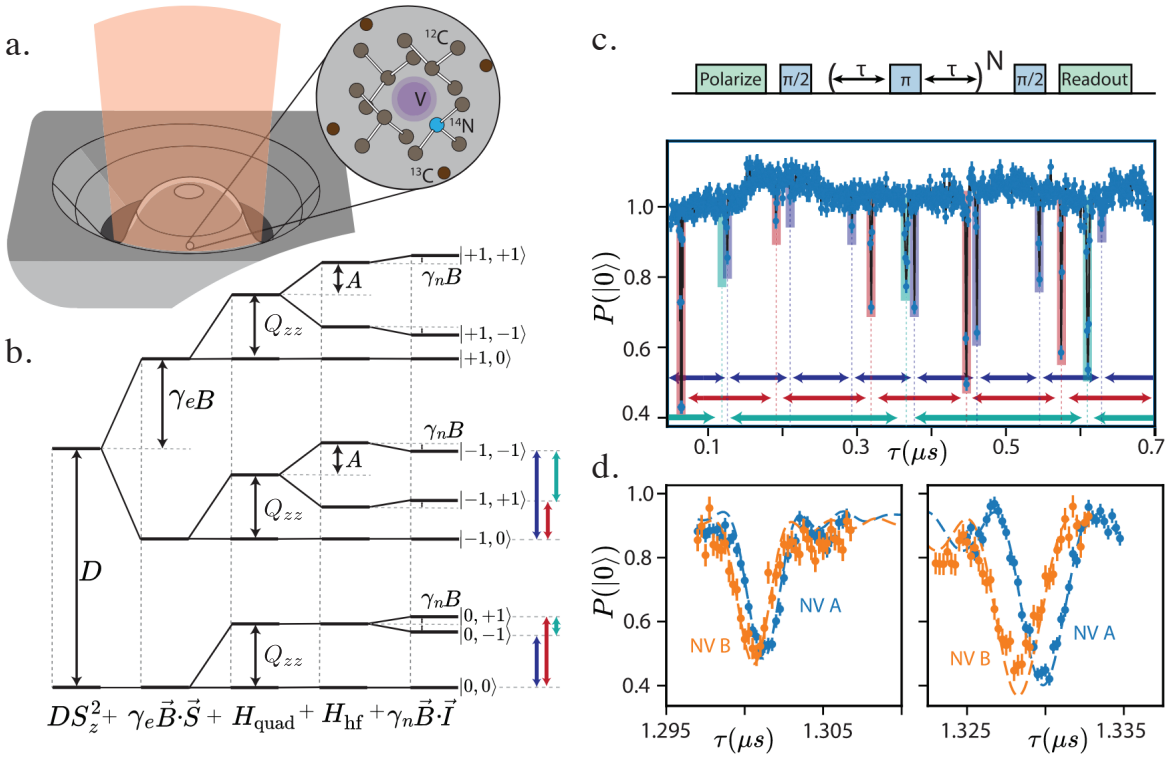

Figure 9.1.: a. Model of a diamond NV center located within a solid immersion lens, composed of an electronic spin (purple) coupled to a ^{14}N nuclear spin (blue). **b.** Energy level diagram of the system. The terms correspond to the zero-field-splitting, the electron Zeeman, the nuclear quadrupole, the hyperfine and the nuclear Zeeman interactions respectively. **c.** DD spectra of the NV center. Peaks corresponding to $\Delta m_I = \pm 1$ transitions (purple and red) appear in the presence of an off-axis magnetic field (B = 193 G). Peaks corresponding to $\Delta m_I = \pm 2$ transitions (green) appear due to the quadrupolar asymmetry parameter, even without an off-axis magnetic field. Arrows mark the different types of transitions highlighted in subplot b. Top shows a schematic of a DD pulse sequence. **d.** DD spectra for two different NV centers (blue and orange), here with $N = 32$ pulse repetitions, reflect significant differences in the ^{14}N quadrupolar Hamiltonian. Data are shown with markers, along with best-fit simulation results as dashed lines.

discussed in Section 8.1. However, instead of using rf pulses, they leverage the hyperfine coupling to create a constructive rotation of the nuclear spin state [96]. Figure 9.1c shows both the pulse sequence and the measured spectra as a function of the interpulse delay. The transitions highlighted in purple and red correspond to $\Delta m_I = \pm 1$. These transitions are enabled by $S_z I_x$ terms in the Hamiltonian, engineered by introducing a small off-axis component of the magnetic field.

In contrast, the green transitions correspond to $\Delta m_I = \pm 2$, which are enabled by quadrupolar terms perpendicular to the magnetic field axis, namely I_x^2 and I_y^2. The observation of these transitions indicates a non-axial component in the Hamiltonian. Using the DD spectroscopy, the authors can extract the small biaxiality parameter with four-digit precision.

They extend this study by measuring the DD spectra of NV centers that are not embedded in a solid immersion lens. Notably, the $\Delta m_I = \pm 2$ transitions are no longer observed, suggesting that strain induced by the fabricated microstructure is responsible for the anomalous biaxiality parameter.

Figure 9.1d shows two $\Delta m_I = \pm 1$ transitions for different NV centers, which do not overlap. This reflects significant variations in the ^{14}N quadrupolar Hamiltonian, attributed to different local strain environments. By measuring the hyperfine spectra of multiple NV centers and fitting the results to a Hamiltonian model, the authors extract the relevant parameters of the system. Figure 9.2 plots the quadrupolar interaction

[96]: Taminiau et al. (2012), 'Detection and Control of Individual Nuclear Spins Using a Weakly Coupled Electron Spin'

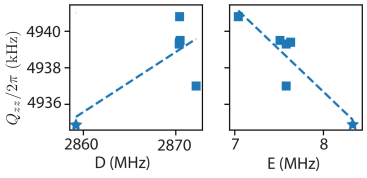

Figure 9.2.: Measured quadrupole strength along the field axis Q_z for a ^{14}N, derived from DD spectroscopy, plotted against the electron zero-field-splitting parameters D and E measured by EPR spectroscopy.

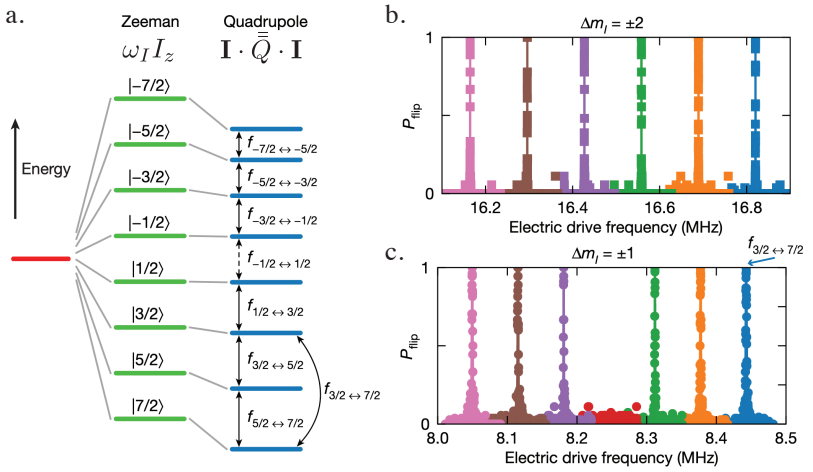

Figure 9.3.: a. Energy level structure of the spin-7/2 nucleus of an ionized ^{123}Sb donor. The Zeeman effect (green) linearly splits the energy levels and the quadrupole interaction causes a further energy split (blue). The transition between $7/2 \leftrightarrow 3/2$ has been highlighted with an arrow. **b.** & **c.** Nuclear electric resonance spectrum of the $\Delta m_I = \pm1$ & $\Delta m_I = \pm2$ transitions as a function of the AC voltage of the driving gate.

strength along the z-axis versus the zero-field splitting parameters, revealing clear correlations. These correlations are attributed to local strain modifying the crystal field experienced by each impurity. These results demonstrate how single-spin quadrupole measurements can be used to probe local strain and microscopic structural variations.

Quadrupole spectroscopy of a ^{123}Sb high-nuclear spin in silicon

Building upon the *state-of-the-art* in Chapters 7 and 8, we now highlight the work by S. Asaad, V. Mourik *et al.*, in which they measure the spectrum of a single ^{123}Sb nuclear spin, using the electron spin of the neutral donor as a probe [111].

[111]: Asaad et al. (2020), 'Coherent Electrical Control of a Single High-Spin Nucleus in Silicon'

Like phosphorus, antimony is a group-V donor. When implanted in silicon, it forms a defect state that binds a single electron in its neutral configuration at low temperatures. Consequently, the methods described in Section 8.1 to read out the donor spin by spin-to-charge conversion apply here as well. A notable difference is that ^{123}Sb has nuclear spin $I = 7/2$, rendering its spectrum sensitive to quadrupolar interactions.

The donor is measured in its ionized state, where the electron is removed from the system and reintroduced only for nuclear spin readout. The energy level structure of the ^{123}Sb nuclear spin is shown in Figure 9.3a. The quadrupole interaction is observed to be much weaker than the Zeeman interaction. Under these conditions, the magnetic quantum numbers m_I remain good quantum numbers, and the Zeeman levels acquire shifts proportional to $Q_{zz}m_I^2$.

Electric fields can modulate the quadrupole interaction of nuclear spins at non-centrosymmetric sites. This mechanism was first proposed by Bloembergen in 1961, who noted that strong electric fields can induce slight lattice distortions, thereby modifying the electric field gradient at the nuclear site [39]. The resulting linear electric Stark shift has since been observed in bulk NMR experiments across various systems [112–114]. This effect will also play an important role in the analysis of the results in this chapter.

[39]: Bloembergen (1961), 'Linear Stark Effect in Magnetic Resonance Spectra'

[112]: Dixon et al. (1964), 'Electrically Induced Perturbations of Halogen Nuclear Quadrupole Interactions in Polycrystalline Compounds. II. Microscopic Theory'

[113]: Ono et al. (2013), 'Coherent Manipulation of Nuclear Spins in Semiconductors with an Electric Field'

[114]: Macfarlane et al. (2014), 'Optical Measurement of the Effect of Electric Fields on the Nuclear Spin Coherence of Rare-Earth Ions in Solids'

By applying an AC electric field, the authors modulate the off-diagonal quadrupole tensor elements and drive the $m_I = \pm1$ and ±2 transitions. Figures Figure 9.3b and c show the corresponding nuclear electric resonance spectra. Notably, the $-1/2 \leftrightarrow 1/2$ transition is absent, as it is first-order

insensitive to quadrupolar effects. From the spectral separations, they estimate $Q_{zz}/2\pi \approx 66$ kHz.

An important aspect emphasized by the authors is that silicon sites are, in fact, centrosymmetric, which should suppress both quadrupole interactions and linear electric Stark shifts. However, aluminum gates induce significant lattice strain at low temperatures due to the mismatch in thermal contraction between the aluminum and the silicon [115, 116]. For impurities located near the surface, this strain can break the site symmetry, thereby generating a finite quadrupole interaction. They calculate the strain map around the donor position (see Figure 9.4), which shows significant values of shear strain. From the strain simulations and the Hamiltonian parameters, they are able to locate the approximate position of the impurity by correlating the strain-induced EFG with the measured data.

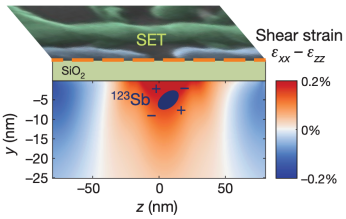

Figure 9.4.: Shear strain in the silicon substrate, calculated on a vertical cross-section under the orange dashed line

[115]: Dehollain et al. (2012), 'Nanoscale Broadband Transmission Lines for Spin Qubit Control'
[116]: Pla et al. (2018), 'Strain-Induced Spin-Resonance Shifts in Silicon Devices'

Precision spectroscopy

A driving motivation of high-resolution spectroscopy is to measure interaction terms beyond the magnetic dipole and electric quadrupole coupling. These are the octupole and hexadecapole interactions, which, at first order, take the following form [117]

$$\begin{aligned} \hat{\mathcal{H}}_{\text{octupole}} &= \frac{C_3}{I(2I-1)(I-1)} I_z^3, \\ \hat{\mathcal{H}}_{\text{hexadecapole}} &= \frac{C_4}{I(2I-1)(I-1)(2I-3)} I_z^4, \end{aligned} \tag{9.2}$$

[117]: Schwartz (1955), 'Theory of Hyperfine Structure'

where C_3 and C_4 are the octupole and hexadecapole coupling strengths. These interactions correspond to the third and fourth order terms of the multipole expansion (see Section 3.3) and appear due to the non-sphericity of the nuclear spin wavefunctions. The octupole is a magnetic interaction that couples spins $I > 1$ to the magnetic field second derivatives. The hexadecapole is an electric interaction that couples spins $I > 3/2$ with the electric field third derivative.

These higher-order interactions are $> 10^5$ times weaker than the leading-order terms, and precision measurements of the NMR spectrum are required to resolve their contribution. The octupole moment has been measured using molecular beam spectroscopy and single-ion experiments [118, 119]. A statistically-significant non-zero hexadecapole moment was claimed using molecular beam measurements [120], but it was three orders of magnitude larger than predicted by theory [121]. This implies that the interaction likely originates from higher-order magnetic interactions (pseudo-hexadecapole).

These measurements are able to achieve exceptional precision by isolating the target from the environment. In contrast, ensemble magnetic resonance measurements of coupled electron-nuclear spin systems in the solid state generally offer a lower spectral resolution (kilohertz at best [122]). The broadening originates from spectral drift and inhomogeneous broadening. In addition, high-nuclear spins are subject to further broadening, as local electric field differences will induce shifts in the quadrupolar interaction. This has so far precluded the observation of higher-order terms in the coupled spin Hamiltonian by magnetic resonance techniques, despite active research [123, 124].

[118]: Gerginov et al. (2003), 'Observation of the Nuclear Magnetic Octupole Moment of 133Cs'
[119]: Lewty et al. (2012), 'Spectroscopy on a Single Trapped $^{137}Ba^+$ Ion for Nuclear Magnetic Octupole Moment Determination'
[120]: Cederberg et al. (1999), 'Evidence for a Nuclear Hexadecapole Interaction in the Hyperfine Spectrum of LiI'
[121]: Thyssen et al. (2001), 'Quadrupole and Hexadecapole Couplings for 127I in Li127I'
[122]: Sielaff et al. (2025), 'Pulsed Dipolar Hyperfine Spectroscopy for Molecular Distance Measurements in the Angstrom to Nanometer Scale'
[123]: Segel (1978), 'Nuclear Electric Hexadecapole Interactions in Solids'
[124]: Doering et al. (1986), 'Search for Hexadecapole Interaction in KTaO3 by 181Ta-NMR'

The tighter bound on the hexadecapole interaction is reported in ref. [41], where they measured a hexadecapolar coupling constant of $C_4 = 60 \pm 140$ Hz.

[41]: Liao et al. (1994), 'The Nuclear Hexadecapole Interaction of Iodine-127 in Cadmium Iodide Measured Using Zero-field Two Dimensional Nuclear Magnetic Resonance'

Discussion

The works on NV centers and donors in silicon illustrate how measurements of quadrupolar interactions at the single-spin level provide access to local structural information and strain-induced lattice distortions. In both cases, high-resolution spectroscopy is used to identify deviations from the expected Hamiltonians; these deviations are then used to understand the interactions in the system. The next step would be to reconstruct the full quadrupole tensor of an individual nuclear spin based on the measured spectroscopic information.

Single nuclear spins in the solid state also provide a platform to investigate higher-order interactions. Compared to ensemble measurements that are limited by inhomogeneous and quadrupolar broadening, individual nuclear spins demonstrate long coherence times, as discussed in the *state-of-the-art* section of Chapter 8. This resolution can be used to test assumptions about the Hamiltonian.

One such example is the dependence of the nuclear quadrupole on the state of neighbouring spins. The nuclear quadrupolar interaction stems from the EFG at the nuclear spin position and should, in principle, not depend on the electron spin state. Such dependence is indeed not described in the standard spin Hamiltonian (see Chapter 3). This is tested and confirmed for the case of a ^{14}N nuclear spin coupled to the NV electron spin in ref. [100], where they measure the Hamiltonian parameters with hertz-level precision in both states of the NV center.

[100]: Bartling et al. (2025), 'Universal High-Fidelity Quantum Gates for Spin Qubits in Diamond'

Given the long coherence times of ^{183}W nuclear spins demonstrated in the previous chapter, $CaWO_4$ is a promising substrate for precision spectroscopy of individual nuclear spins. In this chapter, we identify an impurity in the crystal and use precision spectroscopy to determine its nature and interactions with the Er^{3+} spin.

9.2. Spin system

As discussed in previous chapters, the sample hosts many addressable single Er^{3+} spins, each with its unique nuclear spin environment. The coupled ^{93}Nb – Er^{3+} spin system was discovered fortuitously in the same $CaWO_4$ sample described in Chapter 6 and used throughout Chapters 7 & 8. Figure 9.5a shows a large-range electron spin 2D spectroscopy, where both the amplitude and the in-plane angle of the external magnetic field B_0 are swept. The spin of interest in this chapter is marked with a black arrow.

To characterize the Er^{3+} spin, we first set B_0 to match the resonance condition. Unless otherwise specified, the measurements of this chapter were taken at $B_0 = 446.27$ mT and $\theta = -0.37°$, marked in Figure 9.5a as a red star. The results of the basic electron spin characterization are detailed in Table 9.1.

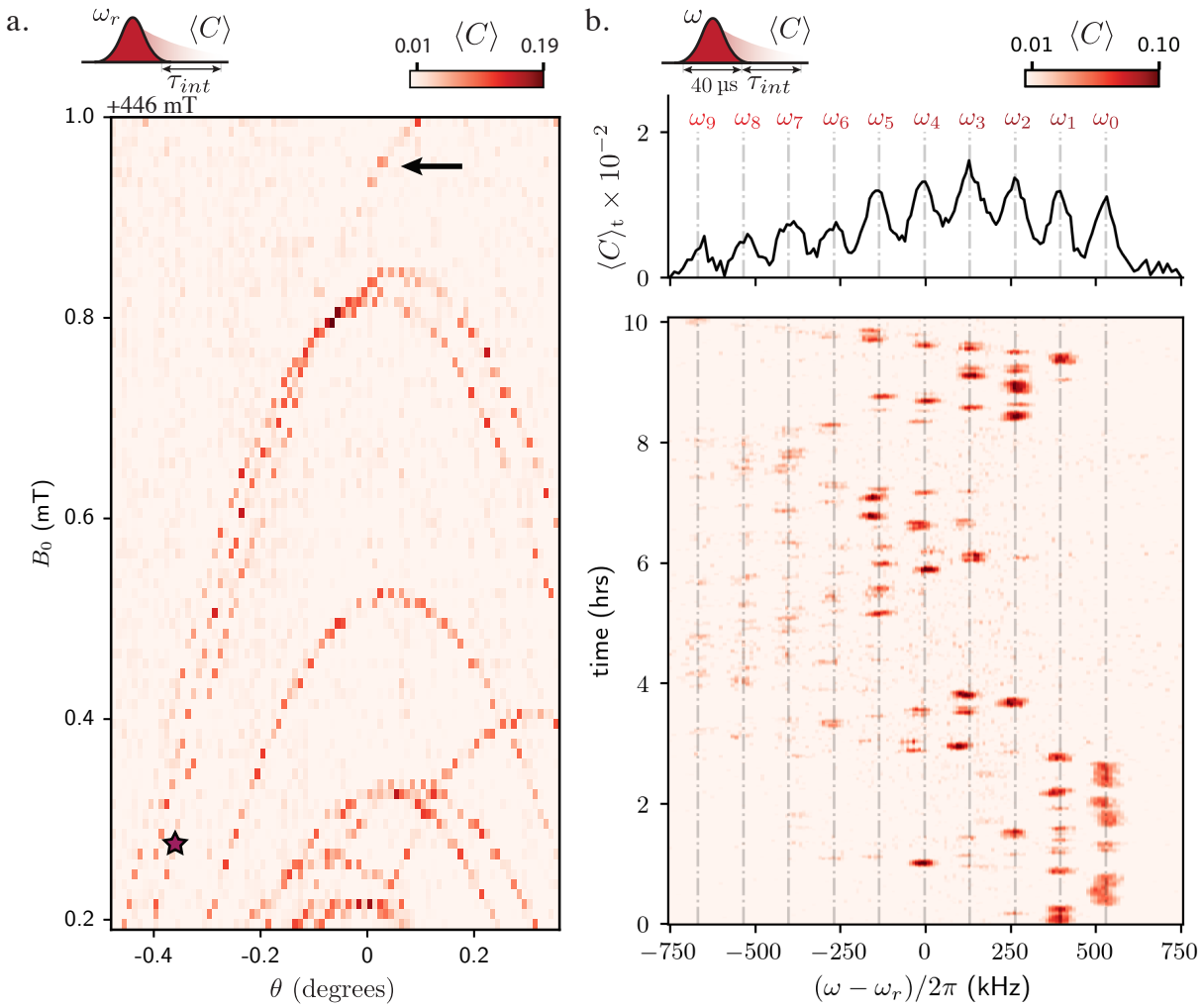

Figure 9.5.: Rotation pattern and time trace of ^{93}Nb – Er^{3+} system. **a.** Rotation pattern. The ensemble-averaged counts $\langle C \rangle$ are plotted as a function of the magnetic field amplitude and the angle θ. The black arrow marks the Er^{3+} spin that is strongly coupled to the ^{93}Nb nuclear spin. The red star at $B_0 = 446.27$ mT and $\theta = -0.37°$ marks the magnetic field amplitude and θ used for this work. **b.** Spectroscopy of the ^{93}Nb–Er^{3+} coupled system as a function of time. A Gaussian pulse with duration 40 µs and frequency $\omega/2\pi$ is first applied to the sample. After a waiting time $\tau_w = 120$ µs, photon counts from the SMPD are integrated over a window of length $\tau_{int} = 2$ ms. The same pulse-and-readout sequence is then repeated at the next pulse frequency. The ensemble-averaged signal $\langle C \rangle$ is obtained by averaging 1000 integrated count values. The top plot shows the total averaged signal $\langle C \rangle_t$ as a function of pulse frequency. Gray dashed lines have been plotted as a guide to the eye for each EPR transition with frequencies ω_n.

As discussed in Section 6.6, the top of the curve for this spin does not match with $\theta = 0$. This implies that the direction of minimal effective gyromagnetic tensor is not aligned with the bulk's c-axis. By fitting the curve to a parabola, we measure a difference of 0.20°. In practice, we define the angle with respect to this spin's c-axis as $\theta_S \equiv \theta - 0.20°$, which we use during the magnetic dipole coupling calculations described in Section 9.4.

Parameter	Value
T_1	0.47(2) ms
$g_0/2\pi$	9.3(0.1) kHz
T_2^*	0.10(2) ms
T_2	0.35(1) ms

Table 9.1.: Er^{3+} characterization.

We then measure a spectroscopic time trace, similar to the ones presented in Section 7.3. We repeatedly measure the Er^{3+} spectrum by sweeping the excitation pulse frequency and monitoring the fluorescence after the pulse. Note that the span of the scan is much larger than the operating bandwidth of the SMPD of ~ 300 kHz. To measure this trace, we actively tune the frequency of the detector to stay in resonance with the excitation frequency ω.

As shown in Chapter 7, strongly coupled nuclear spins are revealed by

sudden jumps of the Er^{3+} EPR-allowed transition frequency. In Figure 9.5b, ten evenly-spaced resonances are observed. They are separated by ~130 kHz and have vastly different cross-relaxation lifetimes, indicating the coupling to a spin-9/2 nuclear spin impurity.

As discussed in Section 3.7, the pseudosecular Hamiltonian of this system is

$$\hat{\mathcal{H}}/\hbar = \omega_S \hat{S}_z + \omega_I \hat{I}_z + A_\parallel \hat{S}_z \hat{I}_z + A_\perp \hat{S}_z \hat{I}_x + \hat{\mathbf{I}} \cdot \bar{\bar{Q}} \cdot \hat{\mathbf{I}}. \tag{9.3}$$

where the terms correspond, in order, to the Er^{3+} spin Zeeman energy, the high-nuclear spin Zeeman energy, the parallel and perpendicular hyperfine interactions, and the quadrupolar term (see Section 3.4 and Section 3.3 respectively).

The Hamiltonian can be separated in two manifolds, depending on the state of the electron spin. Therefore, it can be rewritten as

$$\begin{aligned} \hat{\mathcal{H}} &= |\Downarrow\rangle\langle\Downarrow| \otimes \hat{\mathcal{H}}^{(\Downarrow)} + |\Uparrow\rangle\langle\Uparrow| \otimes \hat{\mathcal{H}}^{(\Uparrow)} \\ \hat{\mathcal{H}}^{(\Downarrow)}/\hbar &= -\omega_S/2 + \omega_I^{(\Downarrow)} \hat{I}_z^{(\Downarrow)} + \hat{\mathbf{I}} \cdot \bar{\bar{Q}}^{(\Downarrow)} \cdot \hat{\mathbf{I}} \\ \hat{\mathcal{H}}^{(\Uparrow)}/\hbar &= +\omega_S/2 + \omega_I^{(\Uparrow)} \hat{I}_z^{(\Uparrow)} + \hat{\mathbf{I}} \cdot \bar{\bar{Q}}^{(\Uparrow)} \cdot \hat{\mathbf{I}}. \end{aligned} \tag{9.4}$$

$\hat{\mathcal{H}}^{(m_S)}$ is the nuclear spin Hamiltonian when the Er^{3+} spin is in $m_S = \Downarrow$ or $m_S = \Uparrow$. As a result of the hyperfine interaction, the nuclear spin quantization axis $z^{(m_S)}$ and Larmor frequency $\omega_I^{(m_S)} \simeq \omega_I + m_S A_\parallel/2$ depend on the Er^{3+} spin state. In the usual coupled spin description, the quadrupolar tensor should not depend on m_S, as confirmed with NV centers in diamond (see Section 9.1). In this chapter we focus on testing this property by separately measuring the tensors $\bar{\bar{Q}}^{(\Downarrow)}$ and $\bar{\bar{Q}}^{(\Uparrow)}$ for each Er^{3+} spin orientation.

We now recall the energy level system defined by this Hamiltonian, which was already described in Section Section 3.7. Figure 9.6 shows the 20 energy levels of the coupled spins, grouped in the two $m_S = \Downarrow$ or $m_S = \Uparrow$ manifolds. The nuclear spin eigenstates are mixed by the quadrupolar interaction and are therefore labeled as $|n\rangle$ in increasing order of energy, with n varying between 0 and 9. Ten transitions between $|\Downarrow, n\rangle$ and $|\Uparrow, n\rangle$ at ω_n are EPR-allowed. Transitions between $|m_S, n\rangle$ and $|m_S, n+1\rangle$ at frequencies $\omega_{n,n+1}^{m_S}$ are NMR-allowed. As described in Section 5.2, double- or zero-quantum transitions between $|\Downarrow, n\rangle$ and $|\Uparrow, n \pm 1\rangle$ are weakly allowed because of the slight hyperfine-induced mixing between the nuclear spin states.

Figures 9.7b & c show the calculated matrix elements and corresponding cross-relaxation probabilities for the parameters of this system using the analytical formulae derived in Section 5.2. Although these parameters will be determined quantitatively in Section 9.6, we use their anticipated values here to provide physical intuition for the observed behavior in Figure 9.5b.

The calculations reveal that both the matrix elements and the associated cross-relaxation probabilities increase with the energy level index n. In particular, the cross-relaxation probability of the state $|\Uparrow, 9\rangle$ is several orders of magnitude larger than that of $|\Uparrow, 0\rangle$.

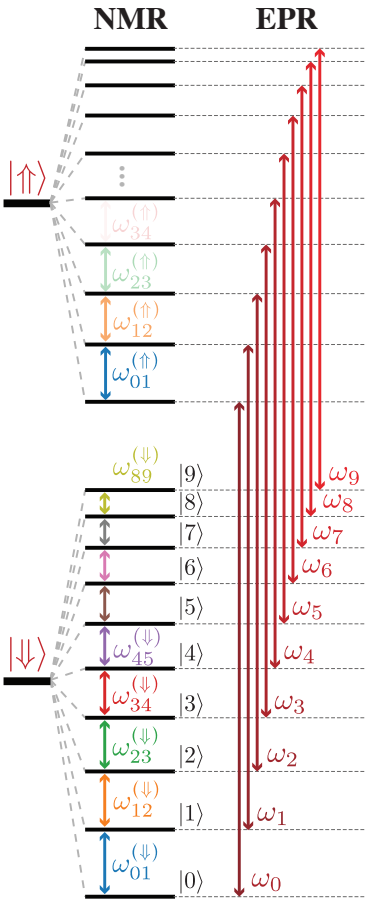

Figure 9.6.: Energy level diagram of an Er^{3+} coupled to a ^{93}Nb nuclear spin-9/2. The twenty energy levels are separated in two manifolds, depending on the state of the electron spin. NMR-allowed and EPR-allowed transitions are represented as multicolored and red arrows respectively.

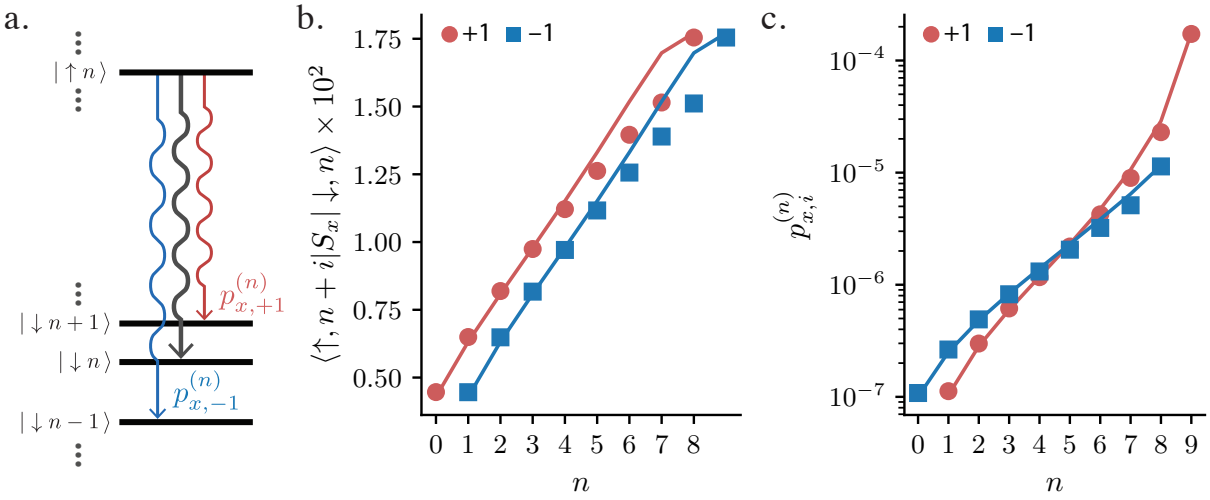

Figure 9.7.: Mixing terms and cross-relaxation probabilities. Throughout this figure, markers are obtained through Eq. 5.20 & 5.24, derived in Section 5.2. Lines are calculated through Hamiltonian diagonalization using the experimental parameters measured in Section 9.6. **a.** Energy level diagram (black horizontal lines) showcasing all possible relaxation paths and their respective probability $p^{(n)}_{x,i}$. Red and blue colors are used for the DQ and ZQ transition, while black is the EPR-allowed transition. **b.** Matrix elements $\langle\uparrow, n+i|S_x|\downarrow, n\rangle$ as a function of n for $i = +1, -1$ (red and blue respectively). **c.** Cross-relaxation probability as a function of n for $i = +1, -1$ (red and blue respectively).

This trend is directly reflected in the time trace shown in Figure 9.5b. The effective lifetime of the $|0\rangle$ state is on the order of tens of minutes, indicating strongly suppressed cross-relaxation. In contrast, the $|9\rangle$ state exhibits a substantially shorter effective lifetime and is barely visible in the spectrum, consistent with its much larger calculated cross-relaxation probability.

9.3. Readout, preparation and control

We proceed to extend the nuclear spin single-shot readout, DNP and coherent control techniques developed in the previous chapters for the characterization and control of ^{183}W nuclear spins.

Single-shot readout

During the experiments performed in Chapters 7 and 8 with ^{183}W , the frequency separation between the EPR-allowed transitions was on the order of ~ 50 kHz, well within the SMPD and the resonator bandwidth. This allowed us to monitor the population of each of the nuclear spin states independently by exciting the appropriate EPR-allowed transition and measuring the subsequent fluorescence (see Section 7.4). However, the ten distinct electron spin frequencies of this system are each separated by ~ 130 kHz, spanning more than 1 MHz, considerably larger than the SMPD and the resonator bandwidth. Additionally, the cross-relaxation probability of the different nuclear states is vastly different, as discussed in the previous section. In fact, the cross-relaxation of the large-n states is too large to achieve high enough SNR for high-fidelity readout using the previous scheme. Consequently, we perform readout on state $|0\rangle$, as it has the lowest cross-relaxation probability (see Figure 9.7c). Later, when we achieve nuclear spin coherent control, the population of any arbitrary state can be coherently transferred to $|0\rangle$ and subsequently read out. We

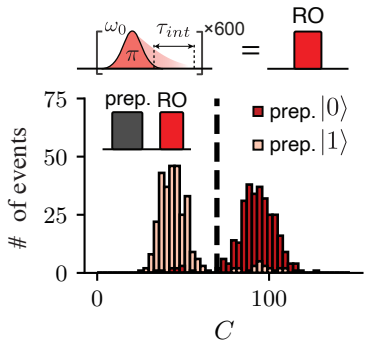

Figure 9.8.: Single-shot readout of the ^{93}Nb spin state. *(top)* Readout is defined as the application of 600 π-pulses with frequency ω_0 and averaging the number of counts during an integration time τ_{int} = 1 ms after each pulse. *(bottom)* Readout histograms after preparing the ^{93}Nb spin in $|0\rangle$ and $|1\rangle$, red and pink respectively. Inset shows the pulse sequence. A vertical dashed line marks the threshold used for state assignment.

also maximize the Purcell effect in the relevant transition by tuning the magnetic field such that $\omega_r = \omega_0$.

Readout on state $|0\rangle$ is achieved by applying ~ 200 successive π-pulses at ω_0 and counting the number of clicks, C. Figure 9.8 plots the count histograms after preparing in $|0\rangle$ or $|1\rangle$, which show two well-resolved histograms. By defining a threshold at $C = 75$, we can discriminate whether the nuclear spin is in state $|0\rangle$ or not.

We note that the value of $A_\parallel$ of this spin is considerably larger than those in Chapters 7 and 8. As a result, we use shorter readout pulses, 40 ms compared to 80 ms used before. Consequently, the readout outcome is not as sensitive to spectral diffusion and frequency tracking is not needed in this experiment.

Solid-effect polarization

In the previous chapters we demonstrated how to perform solid-effect DNP to deterministically prepare the state of strongly coupled ^{183}W nuclear spins. The generalization to a high-nuclear spin $I = 9/2$ is straightforward, as it only requires pumping all the 9 DQ transitions to prepare $|0\rangle$. A crude approach would be to send a chirped pulse that covers a large frequency band of 10 MHz under the EPR-allowed transitions. This pulse would eventually excite one of the DQ transitions, bringing the nuclear spin state closer to $|0\rangle$. However, this technique is not time-efficient. As it chirps, the pulse is mostly off resonance with any transition, and direct driving of the ZQ transitions is preferable. Therefore, we begin by characterizing all ZQ and DQ transitions through EDNMR spectroscopy.

We begin by preparing the nuclear spin into $|0\rangle$[1]. We scan the frequency of the driving microwave pulse and monitor the population of state $|0\rangle$. As shown in Figure 9.9, we measure a depletion of the population in $|0\rangle$ centered around $\omega_0 + 7.418$ MHz, which indicates successful excitation of the ZQ transition.

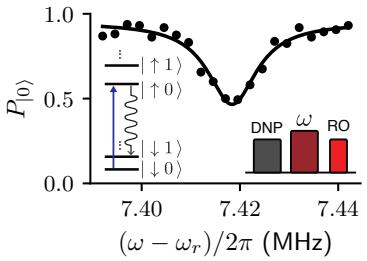

Figure 9.9.: Zero-quantum transition spectroscopy. $|0\rangle$ state population as a function of ω fitted to a Lorentzian curve (solid line). The inset presents the energy diagram, where the straight arrow is the pumping pulse and the wavy line shows the most likely decay path.

1: Naturally, the first characterization was performed using the "crude" method described in the previous paragraph. Subsequent measurements (as shown here) use the known frequencies of the ZQ and DQ transitions to gather well-averaged data more efficiently.

We measure all nine ZQ transitions by extending the protocol to the rest of the nuclear energy levels. As before, the first step is the preparation of $|0\rangle$, then the population is transferred to state $|n\rangle$ by concatenating π-pulses between pairs of adjacent nuclear spin states (see next section). After the excitation pulse, the population is transferred back to $|0\rangle$ by a reverse train of π-pulses and readout. The resulting spectra for the ZQ transitions are displayed in Figure 9.10a.

We can drive Rabi oscillations of the ZQ transitions by modifying the duration of the pulse, as shown in Figure 9.10b. We note two things. First, the contrast of the signal is limited by the coherence of the electron spin, as in the previous chapters. Second, the Rabi frequency for the same pulse amplitude increases with n. This is due to the combined effect of reduced resonator filtering as the resonant ZQ transition frequency gets closer to the center of the resonator, and increased matrix elements, as shown in Figure 9.7.

As discussed in Section 5.2, the ZQ Rabi frequency is proportional to the perpendicular hyperfine coupling term $A_\perp$. We use Eq. 5.21 to estimate the value of the perpendicular hyperfine coupling independently for each transition, which is shown as a function of n in Figure 9.11. The values average to $A_\perp/2\pi = 46(9)$ kHz and are compatible with each other. We note that the uncertainty of the measurement is mainly dominated by the uncertainty on the resonator bandwidth κ. Fitting the quality

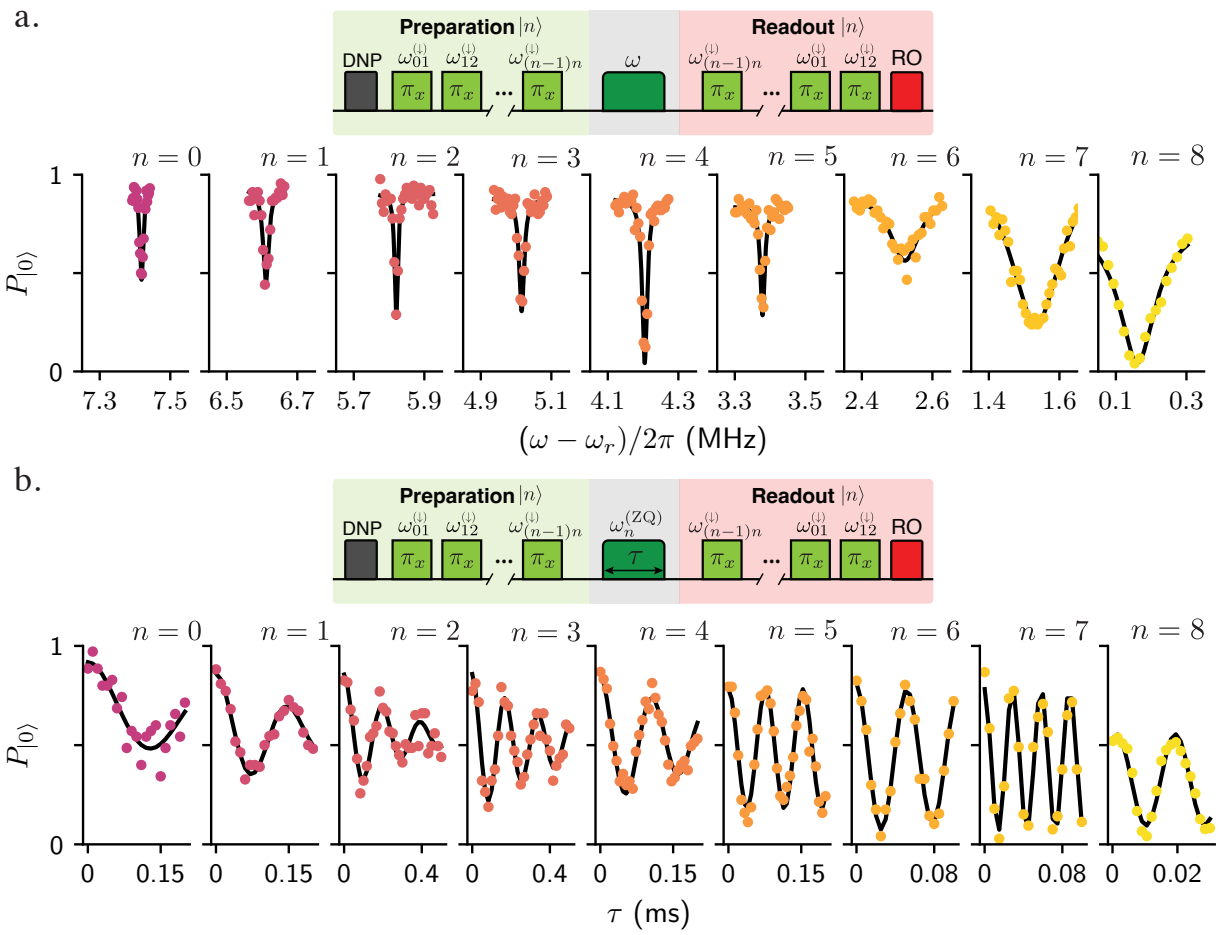

Figure 9.10.: Zero-quantum transitions and Rabi oscillations. **a.** *(top)* Pulse sequence. The nuclear spin state is prepared in $|n\rangle$. A single π-pulse with frequency ω is applied to the sample, and the $|n\rangle$ population is subsequently read out. *(bottom)* Magnified view of each individual zero-quantum transition. **b.** *(top)* Pulse sequence. The pulse duration τ is swept at fixed frequency. *(bottom)* Rabi oscillations for the zero-quantum transitions fitted to a decaying cosine oscillation (black line) for $n \in \{0, ..., 8\}$.

factor of a resonator to a high degree of accuracy is not straightforward as it depends on the probing power due to saturable losses caused by two-level-systems.

We now define the pulse sequence used to polarize to state $|0\rangle$ in all measurements reported below. It is shown in Figure 9.12. We sequentially drive all double-quantum transitions, starting from $n = 8$ down to $n = 0$, using 1 ms microwave pulses. Each pulse is followed by a 1 µs delay to allow the electron spin to relax to its ground state. Because of their small matrix elements and large detuning relative to the allowed transitions, the zero- and double-quantum transitions experience large AC-Zeeman shifts, causing their resonance frequencies to be sensitive to the applied microwave amplitude. To compensate for microwave-power fluctuations and spectral drift, all pulses are chirped by 100 kHz around each transition frequency. Due to the low Rabi frequencies of most sideband transitions, a single pulse is insufficient to achieve full population transfer. We compensate by applying 15 repetitions of the pumping sequence to ensure reliable preparation of the ^{93}Nb nuclear spin. An additional 15 pulses are applied to the $n = 0$ transition, which has the smallest matrix element (see Figure 9.7b) and was experimentally found to be particularly difficult to polarize. Polarization into $|0\rangle$ is achieved with a probability close to 1 at the beginning of each sequence. In addition, the ^{183}W environment is also polarized at the beginning

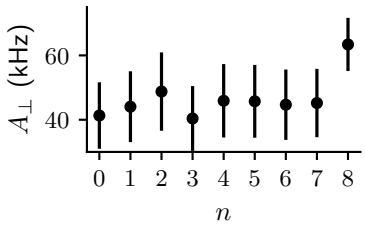

Figure 9.11.: Estimated value of $A_\perp$ using the independent Rabi frequencies of the measurements in Figure 9.10b.

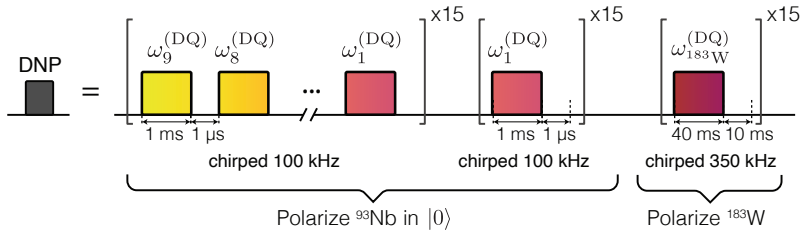

Figure 9.12.: DNP pulse sequence. The sequence is separated in two distinct parts: the preparation of the ^{93}Nb spin in $|0\rangle$ and the polarization of the ^{183}W nuclear spin bath via solid effect. Pulse durations are noted as black arrows and the chirp is explicitly stated under every pulse.

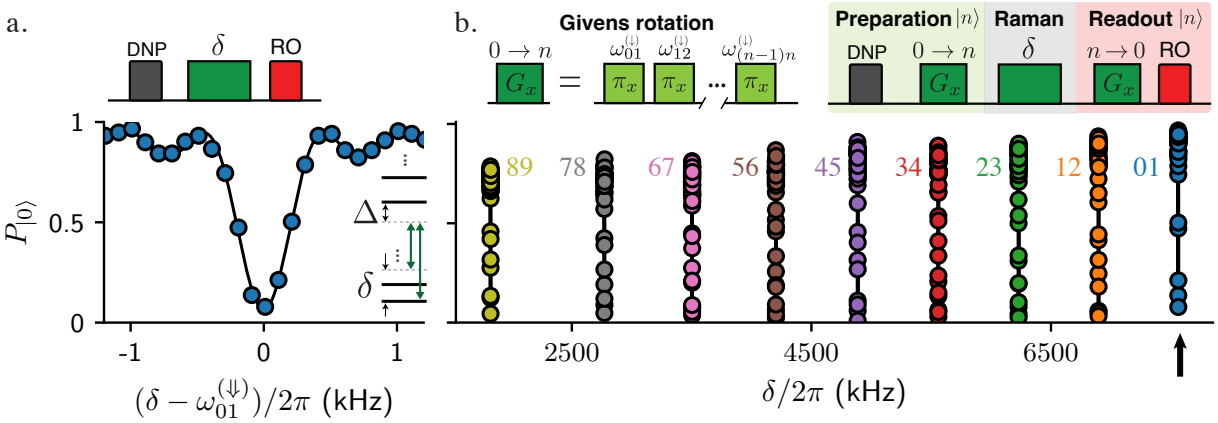

Figure 9.13.: NMR spectroscopy of a ^{93}Nb nuclear spin. **a.** Raman spectroscopy for $n = 0$. Population of $|0\rangle$ as a function of δ. The solid black line corresponds to a cardinal sine fit to the measurement data. The inset presents a diagram of the Raman driving scheme on the four levels of interest. Δ is the detuning of one of the pulses from the EPR transition, and δ is the frequency difference between the two drives. The detuning is set to $\Delta = -\omega_{01}/2$. **b.** *(top)* Pulse sequence of spectroscopy between states $|\Downarrow n\rangle$ and $|\Downarrow n+1\rangle$. A Givens rotation is defined as the accumulation of π-pulses that coherently transfer the population from $|0\rangle$ to $|n\rangle$. The nuclear spin is first unconditionally polarized into $|0\rangle$ followed by a Givens rotation that prepares the ^{93}Nb spin into $|n\rangle$. A Raman pulse of frequency δ is then applied. The Givens rotation is then inverted. Finally, the state of the ^{93}Nb spin is read out. *(bottom)* Raman spectroscopy of all NMR transitions. Black arrow marks the transition corresponding to the previous plot. For each transition $\Delta = \omega_{n,\,n+1}/2$.

of every sequence to reduce the magnetic noise from the neighboring ^{183}W nuclear spins (as discussed in Section 9.5).

Stimulated Raman driving

We coherently drive the ^{93}Nb NMR transitions using microwave stimulated Raman pulses, as discussed in Section 5.2. The first transition we characterize is $|\Downarrow, 0\rangle \leftrightarrow |\Downarrow, 1\rangle$. Spectroscopy of the transition is shown in Figure 9.13a. The choice to begin with this transition is natural, as both the preparation and readout have been defined with respect to $|0\rangle$.

Once the transition frequency and the duration of a π-pulse have been measured, we can reliably transfer the population between this pair of states. As such, we can define a preparation and readout protocol in $|1\rangle$. This is achieved by including a π-pulse between $|\Downarrow, 0\rangle \leftrightarrow |\Downarrow, 1\rangle$ after the original DNP protocol and before the original readout pulse sequence. We can then use the preparation and readout in $|1\rangle$ to measure the next NMR transition between $|\Downarrow, 1\rangle \leftrightarrow |\Downarrow, 2\rangle$, and so on.

This train of π-pulses used to transfer the population from state $|\Downarrow, 0\rangle$ to $|\Downarrow, n\rangle$ is also known as a Givens rotation [125] and has been successfully used previously to control the state of an individual ^{123}Sb nuclear spin in silicon [126].

The spectrum of all ground state NMR-allowed transitions is shown in Figure 9.13b. Their frequencies span a large range, from 1.5 MHz

[125]: Cybenko (2001), 'Reducing Quantum Computations to Elementary Unitary Operations'

[126]: Yu et al. (2024), *Creation and Manipulation of Schrödinger Cat States of a Nuclear Spin Qudit in Silicon*

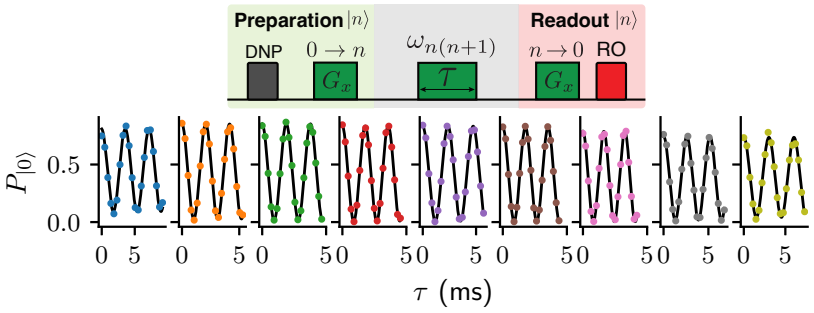

Figure 9.14.: Rabi oscillations for all NMR transitions. *(top)* Pulse sequence. We prepare the state $|\Downarrow n\rangle$ followed by a resonant Raman pulse with duration τ. The population of $|n\rangle$ is subsequently read out. *(bottom)* Measured Rabi oscillations (colored dots) and cosine fit (solid dark line) as a function of τ. The amplitude of the drives Ω_A and Ω_B was calibrated to give similar Raman Rabi frequencies.

to 8 MHz, indicating that the quadrupolar interaction has comparable magnitude to the Zeeman energy.

We confirm the previous measurement of $A_\perp$ by estimating the value of this parameter using the stimulated Raman Rabi frequency. Figure 9.14 shows the ^{93}Nb Rabi oscillations between all 9 NMR-allowed transitions fitted to a cosine curve. As demonstrated in Chapter 5, the Rabi frequency is proportional to $A_\perp$, and we can use Eq. 5.26 to estimate its value. Figure 9.15 plots the measured $A_\perp$ for each of the transitions, which average to $A_\perp/2\pi = 50(11)$ kHz. The value matches quantitatively with the one measured through the sideband driving.

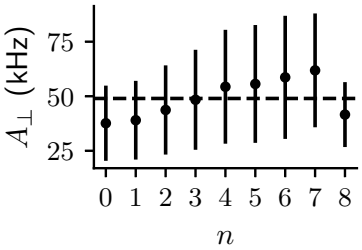

Figure 9.15.: The value of $A_\perp$ measured for each transition is plotted as a function of the transition index n. A dashed horizontal line is plotted at the mean value. The error bars show the uncertainty of the measurement obtained by error propagation, considering an uncertainty of the resonator bandwidth κ of 50 kHz.

9.4. Identification and site assignment

The $|\Downarrow, 4\rangle \leftrightarrow |\Downarrow, 5\rangle$ transition is of particular interest, as it approximately corresponds to the $|\Downarrow, 1/2\rangle \leftrightarrow |\Downarrow, -1/2\rangle$ transition. To first order, the quadrupolar interaction shifts the nuclear energy levels proportionally to $Q\, m_I^2$. Therefore, the states with $m_I = \pm\frac{1}{2}$ are equally shifted. As a result, the transition frequency between $|\Downarrow, 4\rangle$ and $|\Downarrow, 5\rangle$ is first-order insensitive to quadrupolar shifts. Therefore,

$$\begin{aligned} \omega_{45}^{(\Downarrow)} &\approx \omega_I + \frac{A_\parallel}{2} + \mathcal{O}(Q^2), \\ \gamma = \frac{\omega_I}{B_0} &\approx \frac{\omega_{45}^{(\Downarrow)} - A_\parallel/2}{B_0} \simeq 10.80\ \text{MHz/T}. \end{aligned} \tag{9.5}$$

By comparison of γ with the tabulated values of the gyromagnetic ratio of stable nuclei with spin-9/2 (see Table 9.2) we determine that the impurity is a ^{93}Nb atom. The remaining difference with the tabulated value is likely due to a combination of second-order quadrupole effects (see Section 9.6), pseudo-nuclear-Zeeman shift caused by the Er^{3+}, and/or chemical shifts.

This impurity may originate from the crystal growth or from niobium film sputtering during resonator fabrication. We hypothesize that the niobium atom substitutes for a W^{6+} atom in a pentavalent state, thus compensating for the extra positive charge of Er^{3+} compared to Ca^{2+}.

The value of the hyperfine couplings can be used to determine the insertion site of the ^{93}Nb, as already described in Chapter 7. Here, we measure $A_\parallel$ and $A_\perp$ for several values of θ_S, and we compare to the values computed for the ten tungsten sites in the first unit cell using the method described in Section 3.5. As shown in Figure 9.17a & b, the agreement is quantitative for a type 3 site which we plot in red.

Isotope	$\gamma/2\pi$ (MHz/T)
^{73}Ge	−1.489
^{83}Kr	−1.644
^{87}Sr	−1.851
^{93}Nb	+10.452
^{113}In	+9.365
^{115}In	+9.386
^{209}Bi	+6.962

Table 9.2.: Gyromagnetic ratios of stable nuclei with spin $I = 9/2$.

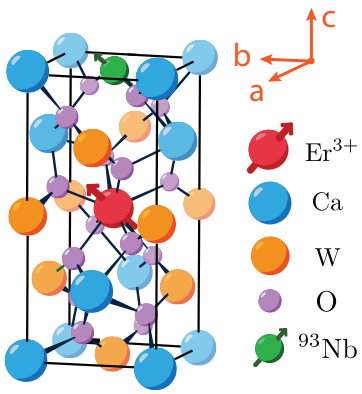

Figure 9.16.: $CaWO_4$ crystal structure with the Er^{3+} and ^{93}Nb impurities in their assigned sites.

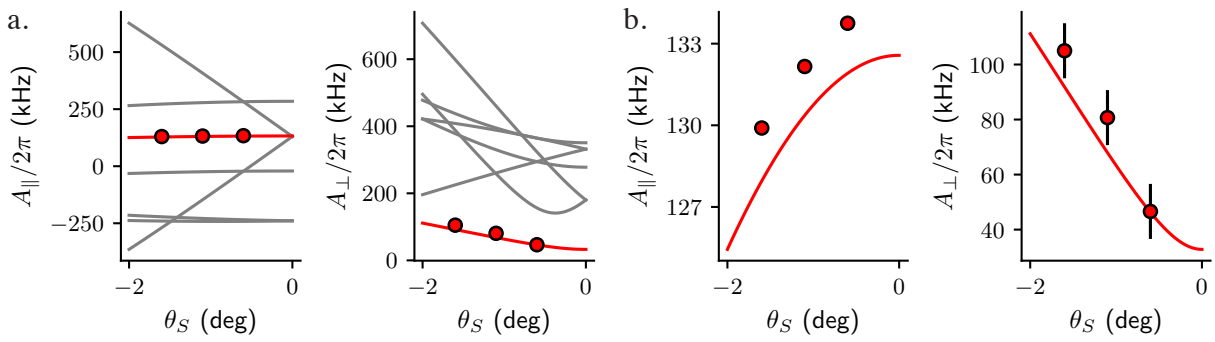

Figure 9.17.: Measured and calculated hyperfine coupling as a function of θ_S. **a.** Calculated hyperfine couplings $A_{\parallel}$ and $A_{\perp}$ (left and right panels, respectively) as a function of the in-plane angle θ_S between Er^{3+} and ^{93}Nb for all ten neighboring W sites in the first unit cell (lines), together with the experimentally measured values (points). The curve for the assigned site has been plotted in red. Note that some sites have the same hyperfine coupling, which results in overlapping curves. **b.** Magnified view of the relevant region only showing the coupling for the assigned site. Error bars for the $A_{\parallel}$ measurement are plotted, but hidden by the marker.

The first unit cell with the Er^{3+} and ^{93}Nb spins is shown in Figure 9.16. Due to this degeneracy in hyperfine coupling between the two sites we are unable to distinguish whether the ^{93}Nb atom is above or below the Er^{3+} ion. Figure 9.17b shows a magnified version of the plot. We note a systematic difference for the values of $A_{\parallel}$ of less than 1% with respect to the measured values, which may be due to a breakdown of the point-dipole approximation or to a slight displacement of the ^{93}Nb position with respect to the ^{183}W site, possibly also impacted by strain caused by differential thermal contraction of the ^{93}Nb thin-film and the $CaWO_4$ substrate [48, 116].

[48]: Billaud et al. (2025), 'Electron Paramagnetic Resonance Spectroscopy of a Scheelite Crystal Using Microwave-Photon Counting'
[116]: Pla et al. (2018), 'Strain-Induced Spin-Resonance Shifts in Silicon Devices'

9.5. Precision NMR spectroscopy

The accuracy of the NMR spectra shown in Figure 9.13 is reduced due to the differential AC-Zeeman shifts that renormalize the energy levels. To access the non-shifted value of ω_n, we use a Ramsey pulse sequence.

Ramsey measurements

We first measure the ground-state-manifold frequencies $\omega^{(\Downarrow)}_{n,n+1}$. We prepare the system in $|\Downarrow, n\rangle$, apply two Raman $\pi/2$-pulses on the $|\Downarrow, n\rangle \leftrightarrow |\Downarrow, n+1\rangle$ transition separated by a time τ, and measure the resulting probability to find the ^{93}Nb in $|n\rangle$. The phase of the second π-pulse has an artificial detuning to compensate for the rapid natural oscillations on the order of MHz. The data for all transitions are shown in Figure 9.18a, together with an exponential cosine fit.

To increase the accuracy of the measurement, we choose to interleave the measurements of all transitions to avoid relative shifts induced by magnetic field drift over time. As discussed in Section 4.3, this comes at the cost of precision in the measured transition frequencies, since longer measurement time increases the decoherence rate during the Ramsey sequence.

The excited-state manifold frequencies $\omega^{(\Uparrow)}_{n,n+1}$ are then measured by including two Er^{3+} π-pulses separated by τ, applied between two Raman $\pi/2$ pulses kept at a constant time delay of 1 ms. The data are shown in Figure 9.18b. By keeping the time separation between the two ^{93}Nb pulses

constant, any phase the state accumulates is proportional to the difference in frequency between the NMR transitions in the ground and excited state of the Er^{3+} spin. Consequently, the oscillation frequency of the measured data directly yields $\omega^{(\Downarrow)}_{n,n+1} - \omega^{(\Uparrow)}_{n,n+1}$.

Figure 9.18c plots the fitted NMR frequencies as a function of the transition index n, both for the ground and excited state of the Er^{3+} spin (green and orange resp.). The ground state transitions are consistently larger than their excited state counterparts, which indicates a positive value of $A_\parallel/2\pi \approx 130$ kHz.

From the fitted coherence (Figure 9.18d & e) we estimate that the uncertainty of the measured frequencies is about 1 Hz for the ground state and about 20 Hz for the excited state. We confirm this by monitoring the frequency drift of the $|\Downarrow 0\rangle \leftrightarrow |\Downarrow 1\rangle$ transition during a prolonged period of 60 hours. Figure 9.19 plots the frequency drift $\delta\omega$ as a function of time, which remains confined within ±1 Hz.

The fitted coherence times for the ground- and excited-state Ramsey measurements are plotted in Figure 9.18d & e, respectively. On the one hand, ground-state transitions display approximately constant behavior[2] with $T_2^* \approx 150$ ms. This indicates that magnetic noise is the dominant contribution to the Ramsey dephasing, since electric noise would more strongly impact transitions with extremal values of n, as was observed in

2: We note that for $n = 5$ the coherence time is slightly lower for unknown reasons.

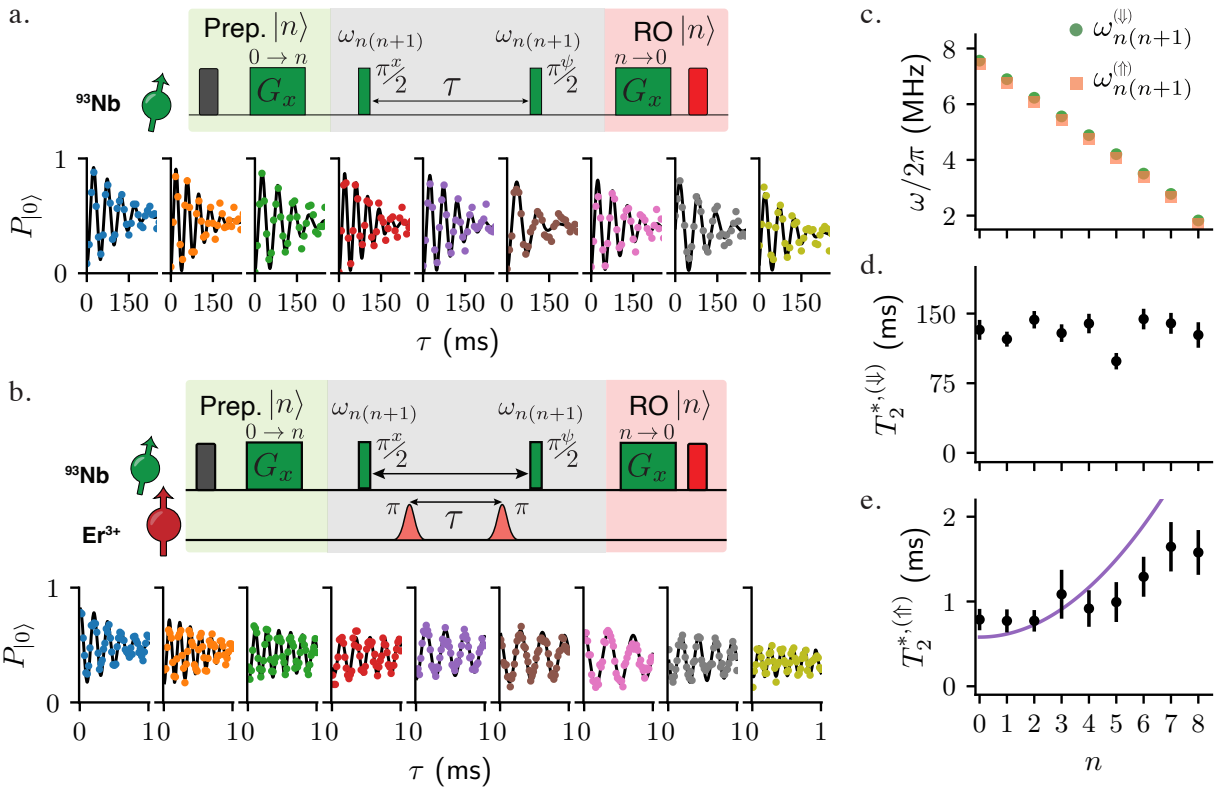

Figure 9.18.: Ramsey measurements of the ^{93}Nb transitions. **a.** *(top)* Ramsey pulse sequence between states $|\Downarrow n-1\rangle$ and $|\Downarrow n\rangle$. The second π-pulse has an artificial phase ψ to compensate for the rapid oscillations of the measurement. *(bottom)* Dots correspond to the measured population from the Ramsey sequence, and the solid black line is an exponentially decaying cosine fit. **b.** *(top)* Excited Ramsey pulse sequence. The second ^{93}Nb π-pulse has an artificial phase ψ to compensate for the rapid oscillations of the measurement. *(left)* Dots correspond to the measured population from the excited Ramsey sequence, and the solid black line is an exponentially decaying cosine fit. **c.** ^{93}Nb nuclear spin transition frequencies $\omega^{(\Downarrow)}_{n,\,n+1}$ and $\omega^{(\Uparrow)}_{n,\,n+1}$ (green and orange markers resp.) as a function of n. **d.** Coherence $T_2^{*,(\Downarrow)}$ for each transition $|\Downarrow n\rangle \leftrightarrow |\Downarrow, n+1\rangle$. **e.** Coherence $T_2^{*,(\Uparrow)}$ for each transition $|\Uparrow n\rangle \leftrightarrow |\Uparrow, n+1\rangle$. Solid line gives an upper bound to the coherence from the relaxation rate through the Purcell effect. Error bars in the figures correspond to the 1-σ fit uncertainty.

an individual ^{123}Sb nuclear spin in silicon [127]. On the other hand, the coherence time of the excited-state Ramsey measurements is limited by the Er^{3+} relaxation time. We observe that $T_2^{*(\Uparrow)}$ slightly increases with n due to the increased detuning of the $|\Downarrow, n\rangle \leftrightarrow |\Uparrow, n\rangle$ transition from the resonator. However, the increase is less than expected from the Purcell effect, shown as a purple line in the plot, suggesting that this Er^{3+} has a relatively short non-radiative lifetime, on the order of ~ 3 ms, possibly linked to the proximal ^{93}Nb impurity.

In conclusion, the value and uncertainty of the transition frequencies in the Er^{3+} ground state are the following

$$\begin{aligned}\omega^{(\Downarrow)}_{n,n+1}/2\pi = [&7563655.5,\ 6897827.7,\ 6230527.8,\ \ldots\\ &5560809.0,\ 4886882.6,\ 4205110.3,\ \ldots\\ &3507057.2,\ 2777446.4,\ 1824936.4]\ \pm 1\ \text{Hz}\end{aligned}$$

given here in increasing order of n. Respectively, the NMR transitions for the Er^{3+} excited state are given by

$$\begin{aligned}\omega^{(\Uparrow)}_{n,n+1}/2\pi = [&7426916\ ,6761742,\ 6095227,\ \ldots\\ &5426468,\ 4753828,\ 4073918,\ \ldots\\ &3378381,\ 2654903,\ 1693679]\ \pm 20\ \text{Hz}\end{aligned}$$

[127]: Fernández de Fuentes et al. (2024), 'Navigating the 16-Dimensional Hilbert Space of a High-Spin Donor Qudit with Electric and Magnetic Fields'

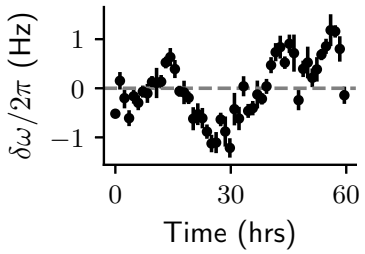

Figure 9.19.: Frequency drift of the $|\Downarrow 0\rangle \leftrightarrow |\Downarrow 1\rangle$ transition as a function of time. Dashed line highlights $\delta\omega = 0$. Error bars correspond to the 1-σ uncertainty of the fitted Ramsey measurement.

The effect of the ^{183}W bath

The nuclear spin bath, primarily consisting of neighboring ^{183}W nuclear spins, significantly contributes to the spectral drift of the ^{93}Nb transition frequencies. To mitigate this effect, we polarize the spin bath using solid-effect DNP by applying microwave pulses resonant with the double-quantum transitions of the coupled ^{183}W spins (see Figure 9.12). To be able to effectively drive weakly coupled ^{183}W nuclear spins, we employ 40 ms pulses separated by 10 ms, and repeat this sequence 15 times. The strong pulse amplitudes induce a substantial AC-Zeeman shift, and we account for this by chirping the pulse 350 kHz around $\omega^{(DQ)}_{^{183}\text{W}}/2\pi = \omega_r - 725$ kHz. Note that it is crucial that the ^{183}W polarization sequence is applied *after* the ^{93}Nb preparation, since the electron-spin allowed transition depends on the ^{93}Nb state, and the ^{183}W double-quantum transition is correspondingly detuned relative to this transition.

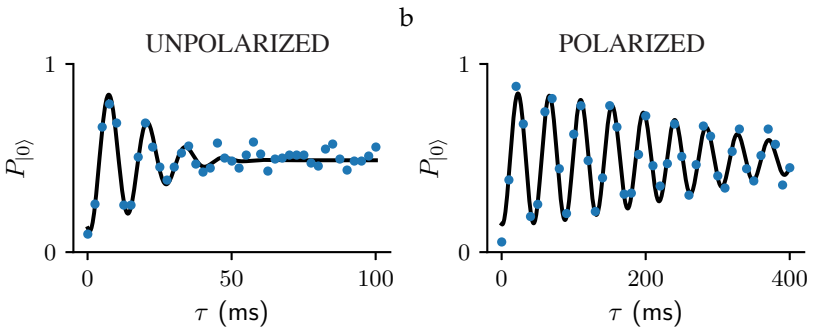

Figure 9.20.: Ramsey sequence with and without ^{183}W polarization pulses. Measurement data (dots) are fitted to an exponentially decaying curve (line), which yields $T_2^* = 22$ ms and $T_2^* = 331$ ms for the unpolarized and the polarized case, respectively.

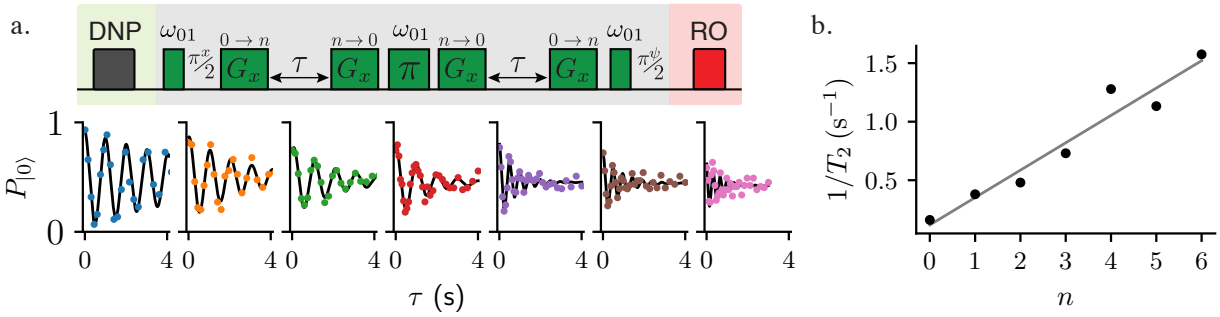

Figure 9.21.: Hahn echo for all $|\Downarrow 0\rangle$ and $|\Downarrow n\rangle$ pairs. **a.** Pulse sequence. **b.** Measurement data (dots) are plotted alongside an exponentially decaying fit (black solid lines). **c.** Decoherence rate $1/T_2$ for all $|\Downarrow 0\rangle$ and $|\Downarrow n\rangle$ pairs. Measurements (dots) are fitted to a linear trend (black line).

To demonstrate the impact of the ^{183}W polarization, Figure 9.20 shows a ^{93}Nb Ramsey measurement with and without ^{183}W polarization. The ^{93}Nb coherence time T_2^* without ^{183}W polarization is 26 ms, and it increases up to 331 ms upon polarizing the ^{183}W bath. Since the measurement time of the curve in Figure 9.20 is much shorter than those in Figure 9.18a, (~3 hours compared to ~32 hours), the T_2^* is considerably larger for this measurement.

Hahn echo measurements

In addition, the large nuclear spin of ^{93}Nb offers interesting perspectives for quantum sensing. Indeed, the magnetic moment of states 0 and n differ by $\sim n\,\mu_{^{93}\mathrm{Nb}}$, implying that the state $|0\rangle + |n\rangle$ is $\sim n$ times more sensitive to a small magnetic signal than $|0\rangle + |1\rangle$. Such "Schrödinger spin-cat" states have been studied in a Sb donor in silicon [126], and used in magnetometry with Rydberg atoms sensing [128]. We perform a preliminary characterization of the magnetic sensitivity of these states by measuring the echo coherence of the state $|\Downarrow 0\rangle + |\Downarrow n+1\rangle$. Figure 9.21a & b show a schematic of the pulse sequence along with the signal, fitted to an exponentially decaying cosine which yields the coherence time T_2. The decoherence rate $1/T_2$ is seen to increase linearly with n (see Figure 9.21c), indicating that decoherence occurs mainly because of magnetic noise. Due to the accumulation of coherent errors on the pulses, we only measure these states until $n = 6$. These measurements were taken in a different magnetic field configuration with an in-plane angle $\theta_S = -0.3°$.

[126]: Yu et al. (2024), *Creation and Manipulation of Schrödinger Cat States of a Nuclear Spin Qudit in Silicon*

[128]: Dietsche et al. (2019), 'High-Sensitivity Magnetometry with a Single Atom in a Superposition of Two Circular Rydberg States'

9.6. Hamiltonian parameters fit

Fitting $\mathcal{H}^{(\Downarrow)}$ and $\mathcal{H}^{(\Uparrow)}$

We now analyze the frequencies shown in Figure 9.18c to extract the nuclear spin parameters. As discussed in Section 9.2, the objectives of this fit are to reconstruct the quadrupolar tensor and to test the assumption that the quadrupole interaction does not depend on the Er^{3+} spin state. In order to do so, we separate the Hamiltonian in two manifolds, as shown in Eq. 9.4. In this picture, we have two independent nuclear spin systems which experience slightly different magnetic fields, both magnitude and orientation. The origin of this difference lies in the parallel

and perpendicular components of the hyperfine interaction which take opposite signs depending on the state of the Er^{3+} spin.

Each of the manifolds can be independently fit to obtain an effective magnetic field and the ^{93}Nb quadrupole tensor. However, they correspond to a "single-axis measurement" as the magnetic field is only applied along one direction. Before proceeding to the fit, we note an intrinsic degeneracy of the quadrupole spectrum under these conditions.

Rotational invariance of the quadrupolar energy spectrum

The quadrupolar interaction is mathematically modeled with a rank-2 tensor that is real, traceless and symmetric. Therefore, 5 variables are needed to fully describe it. As discussed in Section 3.3, a possible set of variables are the quadrupolar interaction strength, C_q, the biaxiality parameter, η, and the three Euler angles that define the rotation from the laboratory frame to the quadrupole principal axes frame. Likewise, the quadrupole can be described in Cartesian coordinates for an arbitrary basis:

$$Q = \begin{pmatrix} Q_{xx} & Q_{xy} & Q_{xz} \\ Q_{xy} & Q_{yy} & Q_{yz} \\ Q_{xz} & Q_{yz} & Q_{zz} \end{pmatrix}, \qquad \mathrm{Tr}\, Q = 0, \tag{9.6}$$

However, when fitting the nuclear transition frequencies in this work, we consider the measurements with a single orientation of the magnetic field. Under these conditions, the measured NMR frequencies are not sufficient to describe the full quadrupole tensor. It is intuitively clear that the measured spectrum should be invariant under a rotation around the applied field direction z, and that only 4 out of the 5 parameters that describe a quadrupole tensor can be determined at best. This is mathematically evidenced when expressing the quadrupole tensor as a function of rank-2 spherical tensors $T_m^{(2)}$. These operators, up to a normalization factor, are related to the spin operator basis by

$$\begin{aligned} T_0^{(2)} &= 3I_z^2 - I(I+1), \\ T_{\pm1}^{(2)} &= \mp\left(I_z I_\pm + I_\pm I_z\right), \\ T_{\pm2}^{(2)} &= I_\pm^2. \end{aligned} \tag{9.7}$$

and by algebraic manipulation we can rewrite the quadrupolar interaction as

$$\hat{\mathcal{H}}_\mathrm{Q}/\hbar = \mathbf{I} \cdot \bar{\bar{Q}} \cdot \mathbf{I} = \sum_{m=-2}^{2} S_m T_m^{(2)}(\hat{\mathbf{I}}) \tag{9.8}$$

with

$$\begin{aligned} S_0 &= Q_{zz}, \\ S_{\pm1} &= Q_{zx} \pm i Q_{zy}, \\ S_{\pm2} &= \tfrac{1}{2}(Q_{xx} - Q_{yy}) \pm i Q_{xy}. \end{aligned} \tag{9.9}$$

One can show (Appendix A) that the coefficients transform as

$$S_m \;\mapsto\; e^{-im\zeta}\, S_m, \tag{9.10}$$

under a physical rotation of angle ζ about the z-axis. Since the energy levels of the Hamiltonian are insensitive to these phase factors and depend only on invariants such as S_0, $|S_{\pm1}|$, and $|S_{\pm2}|$, the energy spectrum is invariant under such rotations. The matrix form of the quadrupole tensor in terms of these invariants is

$$\bar{\bar{Q}}(\zeta) = \begin{pmatrix} -|S_2|\cos(2\zeta+2\Delta) - \frac{S_0}{2} & |S_2|\sin(2\zeta+2\Delta) & |S_1|\cos(\zeta) \\ |S_2|\sin(2\zeta+2\Delta) & |S_2|\cos(2\zeta+2\Delta) - \frac{S_0}{2} & |S_1|\sin(\zeta) \\ |S_1|\cos(\zeta) & |S_1|\sin(\zeta) & S_0 \end{pmatrix} \tag{9.11}$$

where Δ is defined as

$$\Delta = \arctan\left(\frac{2Q_{xy}}{Q_{xx}-Q_{yy}}\right) - \arctan\left(\frac{Q_{yz}}{Q_{xz}}\right) \tag{9.12}$$

For single axis measurements, this leaves S_0, $|S_1|$, $|S_2|$, and Δ to be determined, whereas ζ can be fixed to an arbitrary value. This is a subtle point with an important consequence: any two tensors related by a rotation along the quantization axis produce identical NMR spectra for a fixed field orientation[3]. Equivalently, no matter how precise the measurement of the nuclear transition frequencies, one can only reconstruct the quadrupole tensor up to a rotation about the field axis. Consequently, the only way to lift this degeneracy is by measuring the spectra at different orientations of the magnetic field[4].

Finally, we note that another degeneracy inherent to the one-axis nature of the measurement: $\Delta^{(\Downarrow)}$ is $\pi/2$ periodic. For the purposes of the fit, we fix that $0 < \Delta^{(\Downarrow)} < \pi/2$.

3: It is straightforward to see that the Zeeman term is also degenerate under rotations along the axis of B_0.

4: At zero magnetic field, no orientation information can be extracted, only the magnitudes of the principal components of the quadrupole

Monte Carlo Markov Chains

We now focus on fitting the parameters of the ground state Hamiltonian $\mathscr{H}^{(\Downarrow)}$ to the measured data, but the procedure is identical for $\mathscr{H}^{(\Uparrow)}$. We recall that

$$\mathscr{H}^{(\Downarrow)}/\hbar = -\omega_S/2 + \omega_I^{(\Downarrow)} I_z^{(\Downarrow)} + \mathbf{I}^{(\Downarrow)} \cdot \bar{\bar{Q}}^{(\Downarrow)} \cdot \mathbf{I}^{(\Downarrow)}. \tag{9.13}$$

The parameters to fit are $\bar{\bar{Q}}^{(\Downarrow)}$ and $B_0^{(\Downarrow)} = -\omega_I^{(\Downarrow)}/\gamma_{^{93}\mathrm{Nb}}$, where $B_0^{(\Downarrow)}$ is the effective magnetic field experienced by the ^{93}Nb spin when the Er^{3+} is in the ground state, which combines the external field B_0 and the effective field generated by the Er^{3+} spin. When parameterizing the quadrupole in terms of the rank-2 spherical tensors, the total set of variables to fit is defined as $\mathscr{V}^{(\Downarrow)} \equiv \{B_0^{(\Downarrow)}, S_0^{(\Downarrow)}, |S_1^{(\Downarrow)}|, |S_2^{(\Downarrow)}|, \Delta^{(\Downarrow)}\}$. Following the discussion of the previous section, we fix $\zeta^{(\Downarrow)} = 0$.

The ground state NMR transitions $\omega^{\mathrm{fit}}_{n,\,n+1}(\mathscr{V}^{(\Downarrow)})$ are calculated by numerically diagonalizing $H^{(\Downarrow)}(\mathscr{V}^{(\Downarrow)})$ and calculating the energy differences

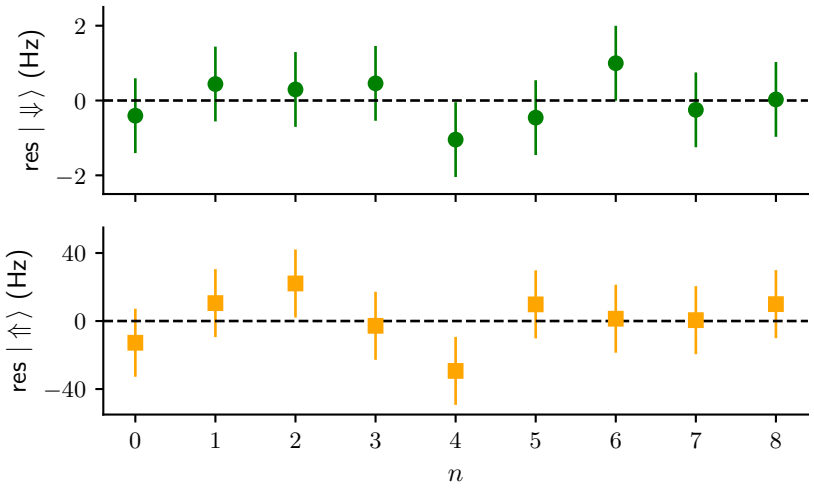

Figure 9.22.: Residuals for the $\mathcal{H}^{(\Downarrow)}$ and $\mathcal{H}^{(\Uparrow)}$ fit, top and bottom respectively. Error bars correspond to the uncertainty of the measured values. Dashed line corresponds to zero deviation.

between the relevant energy levels. We define the logarithmic-likelihood as

$$\mathcal{L}^{(\Downarrow)}(\mathcal{V}^{(\Downarrow)}) = -\frac{1}{2}\sum_{n=0}^{9}\left(\frac{\omega^{(\Downarrow)}_{n,\,n+1} - \omega^{\text{fit}}_{n,\,n+1}(\mathcal{V}^{(\Downarrow)})}{\sigma^{(\Downarrow)}_{n,\,n+1}}\right)^2, \tag{9.14}$$

where $\sigma^{(\Downarrow)}_n = 1$ Hz is the measurement uncertainty. The Hamiltonian fit was performed via a Monte Carlo Markov chain simulation [129]. In brief, the algorithm initializes an arbitrary number of walkers, or particles, in the parameter space. After an evaluation of the $\mathcal{L}^{(\Downarrow)}$ function, the positions of the walkers are updated through the "stretch move" [130] with the objective of maximizing the evaluation for the next iteration. We run the algorithm with 64 walkers and 60000 iterations, from which we obtain the following median values for the ground and excited state parameters

[129]: Foreman-Mackey et al. (2013), *Emcee*

[130]: Goodman et al. (2010), 'Ensemble Samplers with Affine Invariance'

$$\begin{gathered} B_0^{(\Downarrow)} = 460.8320(4)\ \text{mT} \mid S_0^{(\Downarrow)}/2\pi = -237.3609(6)\ \text{kHz} \\ |S_1^{(\Downarrow)}|/2\pi = 2.08(5)\ \text{kHz} \mid |S_2^{(\Downarrow)}|/2\pi = 149.456(6)\ \text{kHz} \mid \Delta^{(\Downarrow)} = 0.2(1) \\ \\ B_0^{(\Uparrow)} = 447.994(6)\ \text{mT} \mid S_0^{(\Uparrow)}/2\pi = -237.256(9)\ \text{kHz} \\ |S_1^{(\Uparrow)}|/2\pi = 5.0(3)\ \text{kHz} \mid |S_2^{(\Uparrow)}|/2\pi = 149.48(8)\ \text{kHz} \mid \Delta^{(\Uparrow)} = 0.2(1) \end{gathered} \tag{9.15}$$

The residuals of the two fits are shown in Figure 9.22. The results agree up to statistical uncertainty (1 Hz for the ⇓ data, 20 Hz for the ⇑ data), and show no discernible trend. We calculate the reduced chi-squared for the ground and excited state and obtain $\chi^{2,(\Downarrow)}_\nu = 0.75$ and $\chi^{2,(\Uparrow)}_\nu = 1.14$, respectively. The proximity of these values to 1 indicates that the model correctly describes the data while avoiding over-fitting. We note that the uncertainty of $S_1^{(\Downarrow)}$ and $\Delta^{(\Downarrow)}$ is much larger than the other parameters. This is readily explained by the effect of these quantities on the energy levels of the Hamiltonian. On the one hand, S_1, Δ are closely related to the values of the quadrupole perpendicular to B_0, and are only observable as second and third order effects respectively. On the other hand, B_0, S_0 and

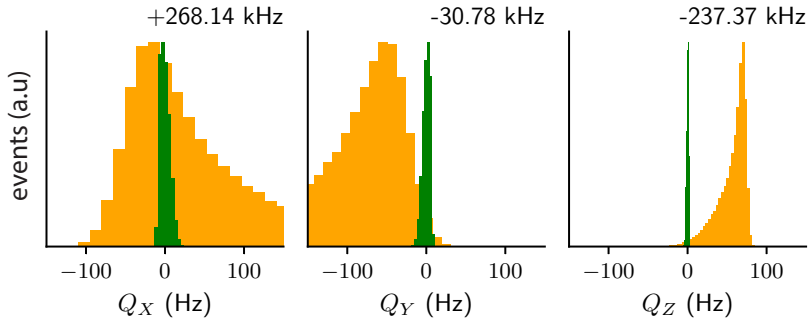

Figure 9.23.: Posterior distribution of the quadrupole tensor principal components for $\mathscr{H}^{(\Downarrow)}$ and $\mathscr{H}^{(\Uparrow)}$ (green and orange resp.). The distributions are normalized to the same height for visual clarity.

S_2 are responsible for zero and first order effects and their estimation is more precise. Appendix D dives into the resulting posterior distributions and explicit details of the fit procedure.

The fit yields the quadrupolar tensors $\bar{\bar{Q}}^{(\Downarrow)}$ and $\bar{\bar{Q}}^{(\Uparrow)}$, up to an arbitrary rotation around the $z^{(\Downarrow)}$ and $z^{(\Uparrow)}$ axes, respectively. Given this degeneracy and the fact that the quantization axes are not parallel in the two cases, component-wise comparison of the tensors is inappropriate. Therefore, we compare the principal values of the tensors obtained by diagonalizing $\bar{\bar{Q}}^{(\Downarrow)}$ and $\bar{\bar{Q}}^{(\Uparrow)}$. This analysis reveals that the principal axis associated with the largest eigenvalue (denoted X) lies approximately within the crystal (a, b)-plane, up to an undetermined in-plane angle. The second-strongest principal axis (denoted as Z) is approximately parallel to the crystal c-axis and therefore to B_0.

The posterior distribution of the quadrupole principal values are shown in Figure 9.23 for both Er^{3+} spin states. The main result is the existence of a statistically-significant (3σ) difference between the values of $Q_Z^{(\Uparrow)}$ and $Q_Z^{(\Downarrow)}$. Due to the larger uncertainty on Q_X and Q_Y, this observation is not reproduced on X or Y. Consequently, our results indicate the existence of a new term in the spin Hamiltonian Eq. 9.3, which modifies the nuclear quadrupolar interaction depending on the electron spin state, or Spin Dependent Quadrupole (SDQ) interaction.

Fitting $\mathscr{H}$

To further test our model, we take a step back in the approximations and simultaneously fit all frequencies. To account for the SDQ coupling, we introduce a new term in the system Hamiltonian,

$$\mathscr{H}_{\text{sdq}} = Q_{\text{sdq}}\, S_z \tfrac{1}{2} \left(3I_z^2 - I(I+1)\right). \tag{9.16}$$

where Q_{sdq} is the interaction coupling strength. Moreover, to account for the high spectral resolution of our data, we include additional terms that we had so far neglected: the non-secular hyperfine and the frequency shifts that arise from coupling to the resonator.

Non-secular hyperfine

Up to this point, we have treated the hyperfine interaction within the pseudosecular approximation, retaining only terms proportional to S_z. This approximation is well justified by the large mismatch between the electronic and nuclear Zeeman energies, which differ by approximately

three orders of magnitude. However, given the smallness of the spin-dependent interaction, it becomes necessary to include non-secular hyperfine contributions.

Given that non-secular hyperfine terms will induce second- and third-order corrections to the energy spectrum and exhibit strong correlation with each other, we choose not to directly fit these terms. Instead, we calculate their values using magnetic dipole simulations (see Section 3.4). This approximation is justified by the robustness of the site assignment, where the discrepancy between the measured and calculated hyperfine is smaller than 10%.

Furthermore, we fix the perpendicular hyperfine term to the independently measured value reported in Section 9.3, $A_\perp/2\pi = 46(9)$ kHz. As shown in Section 9.4, this value quantitatively agrees with the dipole-dipole simulations. However, in the fit we will include the uncertainty of the measured parameter.

Consequently, the hyperfine tensor is given by

$$\bar{\bar{A}}/2\pi = \begin{pmatrix} -438, & 0, & -19.5 \\ 0 & -440.4 & 0 \\ 46(9) & 0 & A_\parallel/2\pi \end{pmatrix} \text{kHz} \tag{9.17}$$

and the only free parameter of the hyperfine interaction is $A_\parallel$.

Lamb shift

First, we consider the Lamb shift of the EPR-allowed transitions, which renormalize the ^{93}Nb transitions in the excited state of the Er^{3+} spin. As discussed in Section 4.2, the Lamb shift of the excited state of a spin-1/2 coupled to a resonator in its (vacuum) ground state, with coupling strength g_0 and detuning Δ is given by

$$\Delta\omega = \Delta \frac{g_0^2}{\Delta^2 + \kappa^2/4}. \tag{9.18}$$

In the case of the coupled ^{93}Nb–Er^{3+} system, the Er^{3+} excited state levels $|\Uparrow, n\rangle$ are shifted by $\Delta\omega_n = g_0^2 \frac{\Delta_n}{\Delta_n^2+\kappa^2/4}$, where $\Delta_n = \omega_0 - \omega_n$ is the detuning of the EPR-allowed transition from the resonator frequency. The order of magnitude is $\Delta\omega/2\pi \sim g_0^2/(2\pi\kappa) \sim 100$ Hz and the dependence on n causes shifts $\Delta_{n+1} - \Delta_n$ of the NMR transition frequencies $\omega^{\Uparrow}_{n,n+1}$, which therefore must be taken into account in our analysis. We achieve this by including the following term in the Hamiltonian

$$\mathcal{H}_L = \Delta\omega_n \, |\Uparrow, n\rangle \langle\Uparrow, n| \tag{9.19}$$

Final Hamiltonian

Combining all the terms, the full Hamiltonian of an Er^{3+}:$CaWO_4$ spin coupled to a ^{93}Nb nuclear spin (and to its detection resonator) is

$$\begin{aligned}\mathcal{H}/\hbar = \omega_S \cdot S_z + B_0\gamma_{^{93}\mathrm{Nb}} \cdot I_z + \mathbf{S}\cdot\bar{\bar{A}}\cdot\mathbf{I} + \mathbf{I}\cdot\bar{\bar{Q}}\cdot\mathbf{I} + \\ + Q_{\mathrm{sdq}}\, S_z \tfrac{1}{2}[3I_z^2 - I(I+1)] + \Delta\omega_n\, |\Uparrow, n\rangle\langle\Uparrow, n|\end{aligned} \tag{9.20}$$

Note that this Hamiltonian is not invariant under rotation around the z axis; therefore, the full quadrupolar tensor can now be obtained. Following the parameterization presented in Section 9.6, the set of eight variables to fit is defined as $\mathcal{V} \equiv \{\gamma_{^{93}\mathrm{Nb}}, A_\parallel, S_0, S_1, S_2, \Delta, \zeta, Q_{zzz}^{(\mathrm{SDQ})}\}$. Naturally, we define the total likelihood as

$$\mathcal{L}(\mathcal{V}) = \mathcal{L}^{(\Downarrow)}(\mathcal{V}) + \mathcal{L}^{(\Uparrow)}(\mathcal{V}). \tag{9.21}$$

The fit is performed using the MCMC algorithm described in the previous section. To account for the 9 kHz uncertainty in the measurement of $A_\perp$, we repeat the fit 400 times while sampling the value of $A_\perp$ from a Gaussian distribution with a standard deviation of 9 kHz. The median values for the parameters, obtained from the resulting ensemble of fits, are given by

$$\begin{aligned}\gamma_{^{93}\mathrm{Nb}} &= 10.6113(1)\ \mathrm{MHz/T} \mid A_\parallel/2\pi = 133.751(5)\ \mathrm{kHz} \\ S_0/2\pi &= -237.314(3)\ \mathrm{kHz} \mid S_1/2\pi = -3.44(1)\ \mathrm{kHz} \\ S_2/2\pi &= -149.457(5)\ \mathrm{kHz} \mid Q_{\mathrm{sdq}}/2\pi = 76(4)\ \mathrm{kHz} \\ \Delta &= 1.62(2) \mid \zeta = 0.9(1),\end{aligned} \tag{9.22}$$

with a reduced chi-squared of $\chi_\nu^2 = 1.2$ and residuals similar to those reported in Figure 9.22. Compared to the estimate of the gyromagnetic tensor in Section 9.4, this value is considerably closer to the literature. We assign the remaining difference to the pseudo-nuclear-Zeeman effect and/or the chemical shift.

From these values, we reconstruct the nuclear quadrupole tensor $\bar{\bar{Q}}$ and diagonalize it to obtain its principal axes X, Y, and Z. We find that the Z axis is tilted by 0.06(3)° with respect to the crystal c axis, while the X axis is rotated by −10(6)° relative to the crystal a axis. The corresponding principal values are $Q_X/2\pi = 268.138(9)$ kHz, $Q_Y/2\pi = -30.799(7)$ kHz, and $Q_Z/2\pi = -237.338(3)$ kHz. These values correspond to a quadrupolar interaction strength of $C_q/2\pi = 19.3059(7)$ MHz and a biaxiality parameter $\eta = 0.77026(7)$.

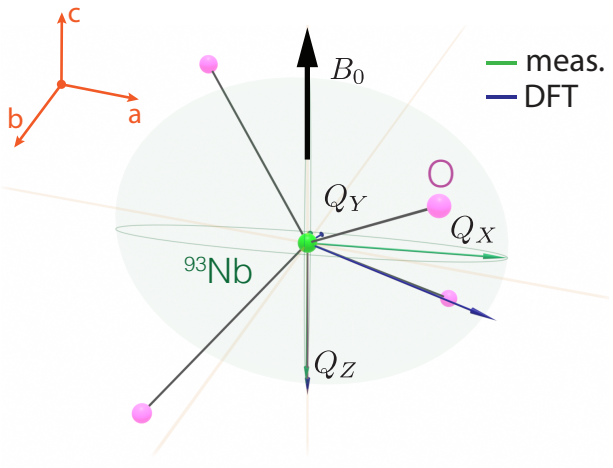

Figure 9.24.: Three-dimensional representation of the quadrupole tensor. The ^{93}Nb nuclear spin (green) lies in the center surrounded by the neighboring oxygen atoms (pink). The crystalline axes a, b, c are shown as orange lines. The measured quadrupole principal axes X, Y, and Z are represented as green arrows, which define the semi-axes of an ellipsoid, represented in green. The principal vectors obtained via DFT simulations have been plotted in dark blue.

The quadrupolar tensor $\bar{\bar{Q}}$ is graphically represented in the crystal frame in Figure 9.24. We compare the fitted quadrupole tensor with DFT calculations performed by our theory collaborator Thibault Charpentier. Due to software limitations in treating systems with unpaired $4f$ electrons, the calculations were carried out for a Y^{3+} ion instead of Er^{3+}.

Despite this substitution, the comparison remains meaningful. The quadrupole tensor is primarily determined by the local crystalline environment and the associated electric field gradient at the nuclear site. Since Y^{3+} and Er^{3+} have similar sizes, the lattice distortions induced by the substitution are expected to be comparable. Consequently, the DFT results provide a reasonable approximation for assessing the experimentally extracted quadrupole tensor.

The simulations yield $C_{q,\mathrm{DFT}} = 22.7$ MHz, $\eta_{\mathrm{DFT}} = 0.76$, and similar orientation of the principal axes, in close agreement with the fitted values. This confirms that Nb^{5+} replaces W^{6+}. Finally, the SDQ term $Q_{\mathrm{sdq}}/2\pi = 76(4)$ kHz is fitted to a non-zero value with a high degree of confidence. We check the consistency and reproducibility of our analysis by repeating these measurements for a small range of in-plane angles θ_S (see Figure 9.25). Despite the vastly different values of the Hamiltonian parameters (in particular, ω_I and $\bar{\bar{A}}$), the values extracted for Q_{sdq} remain approximately unchanged.

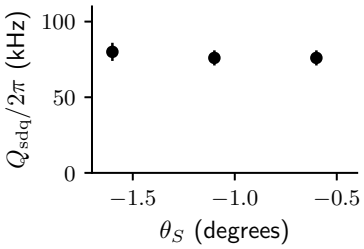

Figure 9.25.: Spin-dependent quadrupole term Q_{sdq} obtained by fitting the ^{93}Nb nuclear spin transitions as a function of the in-plane angle θ_S

9.7. Origin of the SDQ interaction

We identify two possible mechanisms that could account for the SDQ term: the pseudo-quadrupole coupling and a magnetically-induced electrostatic interaction. The origin and strength of these interactions for Er^{3+}:$CaWO_4$ was discussed in Section 3.2. In the following we numerically investigate the strength of these two effects.

Pseudo-quadrupole interaction

In this section we attempt to explain the observed SDQ effect through the action of higher energy Kramers doublets $Z_2, \ldots, Z_8$ on the nuclear transition energies of the ^{93}Nb spin. As explained in Section 3.5, the spin-1/2 model (Eq. 3.29) is a restriction of the more complete Hamiltonian (Eq. 3.27) to the lowest two Er^{3+} energy levels. In particular, the hyperfine

Hamiltonian coupling the effective spin S and the nuclear spin is a two-level restriction of the hyperfine Hamiltonian $\hat{\mathcal{H}}_{\mathrm{hf},J}$ (Eq.3.26). The latter couples the nuclear spin not only to the Z_1 doublet, but also to the other higher-energy Z_{2-8} states. These couplings renormalize the nuclear energy levels in a manner that may mimic an effective quadrupolar interaction. This pseudo-quadrupolar interaction is of purely magnetic origin, contrary to the real quadrupolar interaction [44, 131], and can be of similar order of magnitude as the electric quadrupole when the nuclear spin is located on the nucleus of the paramagnetic ion [64].

[44]: Abragam et al. (2012), *Electron Paramagnetic Resonance of Transition Ions*
[131]: Foley (1947), 'Second-Order Magnetic Perturbations in Nuclear Quadrupole Spectra and the "Pseudo-Quadrupole" Effect in Diatomic Molecules'
[64]: Schweiger et al. (2001), *Principles of Pulse Electron Paramagnetic Resonance*

The effective Hamiltonian of the pseudo-quadrupolar interaction depends on the point-symmetry of the site where the ion is located. It has been predicted that this interaction can be described by a term of the form $S_z I_z^2$ for D_{3h} symmetry [132], which would imply that the pseudo-quadrupolar part may depend on the spin state, as observed in our experiment. However, no prediction was made for the S_4 symmetry. We therefore rely on numerical simulations to estimate the relevance of this effect.

To quantitatively characterize the effect of the pseudo-quadrupole for this specific configuration, we proceed by performing the following numerical analysis. First, we generate a series of the NMR transitions for the ^{93}Nb – Er^{3+} system by diagonalizing the $J = 15/2$ Hamiltonian

$$\mathcal{H} = \mu_B\, g_J \mathbf{B_0}\cdot\mathbf{J} + \mathcal{H}_{\mathrm{cf}} + \omega_I I_z + \mathbf{I}\cdot\bar{\bar{Q}}\cdot\mathbf{I} + \mathbf{J}\cdot\lambda\bar{\bar{A}}_J\cdot\mathbf{I} + \mathcal{H}_{\mathrm{L}}. \qquad (9.23)$$

As for the Hamiltonian fit in the previous section, the hyperfine coupling tensor $\bar{\bar{A}}_J$ is calculated from a dipole-dipole interaction between the Er^{3+} spin and the ^{93}Nb at the expected position. We use the S_4-symmetric crystal-field Hamiltonian $\mathcal{H}_{\mathrm{cf}}$ determined in [53], whose validity is questionable here due to the S_4 symmetry breaking due to the ^{93}Nb presence. Given that the pseudo-quadrupole effect is a second order interaction of the hyperfine coupling, we use a dimensionless scaling parameter λ for the hyperfine interaction strength. Otherwise, the Hamiltonian parameters are set to the measured values.

The NMR transition frequencies computed in the lowest two Er^{3+} manifolds are then fitted with the effective spin-1/2 model, using the same procedure as the one used for the experimental data (described in the previous section), yielding the effective quadrupolar interaction in each Er^{3+} state. The difference between the principal values along the c axis between the $\uparrow$ and $\downarrow$ values, $Q_{\mathrm{sdq,pq}}$, is shown in Figure 9.26a as a function of the scaling parameter λ.

We first note that the computed $Q_{\mathrm{sdq,pq}}$ is 0 when $\lambda = 0$, as expected. For non-zero values of λ, a non-zero spin-dependent pseudo-quadrupole is computed. Its value scales quadratically with the hyperfine scaling factor, as expected for an effect that can be described in second-order perturbation theory. The magnitude of the interaction is of similar order as the experimentally measured value, although the $\lambda = 1$ value $Q_{\mathrm{sdq,pq}}/2\pi = -8$ Hz is a factor 10 smaller than the measurement and has an opposite sign. We also compute $Q_{\mathrm{sdq,pq}}$ at $\lambda = 1$ as a function of θ (see Figure 9.26b). In a window of ±5 degrees, $Q_{\mathrm{sdq,pq}}$ remains consistently smaller than 10 Hz in absolute value.

We conclude that pseudo-quadrupole interactions arising from second-order paramagnetic coupling between the electron J-multiplet and the nuclear spin need to be considered in a complete analysis. However, it has opposite sign and is one order of magnitude smaller than the

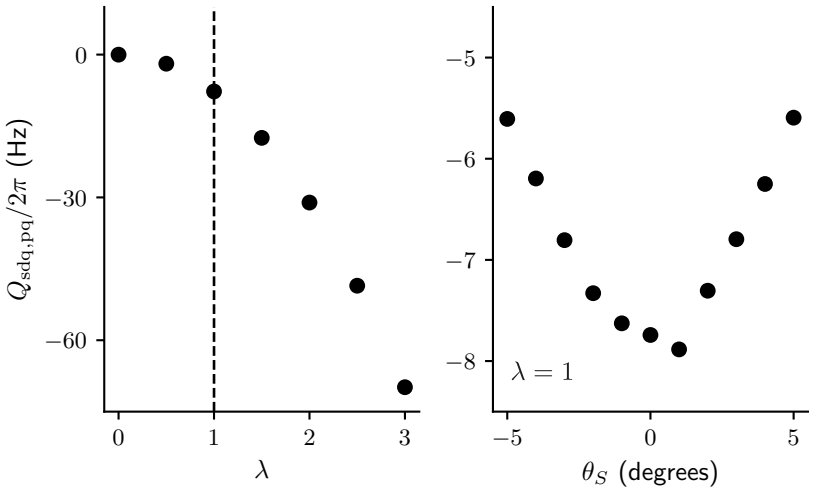

Figure 9.26.: Pseudo-quadrupole shift simulation. *(left)* Effective SDQ interaction from the pseudo-quadrupole, $Q_{\mathrm{sdq,pq}}$, is plotted as a function of the hyperfine scaling parameter λ. The vertical line marks $\lambda = 0$. The simulation was performed for $\theta_S = -0.57°$ and $\beta_0 = -0.57°$. *(right)* $Q_{\mathrm{sdq,pq}}$ as a function of the in-plane angle θ_S with $\lambda = 1$ and $\beta_0 = -0.57°$.

measurements, implying that the effect is likely not the only one at play.

Electrostatic coupling

The second one is the electrostatic interaction between the Er^{3+} and the ^{93}Nb spins. Bloembergen predicted [39] that paramagnetic centers located at sites without inversion symmetry carry an electric dipole whose magnitude is proportional to B_0 and whose orientation changes with the spin state. This leads to linear electric-field shifts of the EPR transition frequency that have been observed in numerous paramagnetic systems [133], including in Er^{3+}:$CaWO_4$ [40, 58]. This effect was discussed in Section 3.2, but we briefly summarize the results here.

[39]: Bloembergen (1961), 'Linear Stark Effect in Magnetic Resonance Spectra'

[133]: Ludwig et al. (1961), 'Splitting of Electron Spin Resonance Lines by an Applied Electric Field'

[40]: Mims (1964), 'Electric Field Effects in Spin Echoes'

[58]: Mims (1965), 'Electric Field Shift in Paramagnetic Resonance for Four Ions in a Calcium Tungstate Lattice'

Ions in non-centrosymmetric sites will experience admixing of wavefunctions with different parity due to the odd terms of the crystal field Hamiltonian [51]. In turn, this results in a magnetoelectric effect which couples static electric and magnetic fields and can be effectively described as a magnetically induced electric dipole. As described in Section 3.2, the Hamiltonian used to describe this effect is

[51]: Kiel (1966), 'Theory of Electric Shifts of the Optical and Magnetic Resonance Properties of Paramagnetic Ions in Crystals'

$$\begin{aligned} \hat{\mathcal{H}}_{\text{m-e}}/\hbar &= \sum_k -d_k E_k = -\mathbf{d}\cdot\mathbf{E}, \\ d_k &= -\sum_{i,j} T_{k,i,j}\langle \hat{S}_i\rangle B_j. \end{aligned} \tag{9.24}$$

where $\mathbf{d_k}$ acts as an effective electric dipole which is proportional to the static magnetic field. The numerical values of the $T_{k,i,j}$ were determined by Mims [58] and are provided in Section 3.2. We note that, in the high-field regime, the spin orientation in the ground state and excited state are opposite and the associated electric dipole moments of each state also point in opposite directions. Consequently, the electric field and electric field gradient generated by the dipole will be different depending on the electron spin state. Bloembergen [39] also predicted that an externally applied electric field modifies linearly the quadrupolar interaction of a nuclear spin if the latter is located at a site lacking inversion symmetry [134]. In our system, both the Er^{3+} and the ^{93}Nb sites lack inversion symmetry, and we hypothesize that the electric field generated by the

[58]: Mims (1965), 'Electric Field Shift in Paramagnetic Resonance for Four Ions in a Calcium Tungstate Lattice'

[39]: Bloembergen (1961), 'Linear Stark Effect in Magnetic Resonance Spectra'

[134]: Armstrong et al. (1961), 'Linear Effect of Applied Electric Field on Nuclear Quadrupole Resonance'

spin-dependent Er^{3+} dipole couples linearly to the ^{93}Nb quadrupole, leading to the SDQ effect. Although the electric quadrupole sensitivity of ^{93}Nb :$CaWO_4$ is not known, values ranging between 0.1 and 1 Hz/(V/cm) were reported for a variety of nuclei [114].

[114]: Macfarlane et al. (2014), 'Optical Measurement of the Effect of Electric Fields on the Nuclear Spin Coherence of Rare-Earth Ions in Solids'

It is relevant to note that for Er^{3+} :$CaWO_4$ the dipole moment is zero when the magnetic field is parallel to the c-axis ($\theta_S = 0, \beta = 0$). However, in the experiment, $\theta_S = -0.57°$ and $\beta = -0.57°$, so the electric dipole is non-zero. Additionally, the symmetry of the system is broken by the presence of the ^{93}Nb impurity, as discussed in the previous section. This will likely result in a different sensitivity to electric fields, and we note that the values for this estimation only work as a reasonable order of magnitude calculation.

We estimate the strength of the dipole by evaluating Eq. 9.24 and obtain $\mathbf{d} = \pm$(-0.26, 0.25, 0.02) mD. The dipole is confined in the (a, b)-plane of the crystal and generates both an electric field and electric field gradient at the position of the ^{93}Nb , with values

$$\begin{aligned} \mathbf{E} &= (34,\ -33.6,\ 7)\ \mathrm{V/cm} \\ \partial E_z/\partial z &= V_{zz}^{(\mathrm{d})} = 0.02\ \mu\mathrm{V/\AA}^2 \end{aligned} \tag{9.25}$$

The electric field gradient induces a spin-dependent quadrupole of $C_{\mathrm{sdq,dipole}} \approx 0.2$ mHz, far smaller than the observed interaction (76 Hz). The electric field at the Nb site is ~48 V/cm, giving a differential field of ~96 V/cm between the two spin states. If we assume a similar sensitivity for ^{93}Nb :$CaWO_4$ as for the previously studied nuclear spins [114] we obtain an interaction strength of ~10 – 100 Hz, consistent with the measured value. Our data therefore bring some evidence for a new type of coupling between a paramagnetic center and a nuclear spin, of electrostatic nature.

[114]: Macfarlane et al. (2014), 'Optical Measurement of the Effect of Electric Fields on the Nuclear Spin Coherence of Rare-Earth Ions in Solids'

9.8. Octupole and hexadecapolar bounds

Given the spectral resolution of the ground-state data, we can test the presence of higher-order terms in the nuclear spin Hamiltonian, beyond the magnetic dipolar and electric quadrupolar interactions. In our system, a magnetic octupole term in the ^{93}Nb Hamiltonian may arise due to the magnetic field gradients caused by the proximal Er^{3+} magnetic dipole, while a hexadecapolar term may be caused by the crystal field. We test the presence of an octupolar and hexadecapolar term by independently adding the following terms to $\mathscr{H}^{(\Downarrow)}$ and fitting the ground state data,

$$\begin{aligned} \hat{\mathscr{H}}_{\mathrm{octupole}} &= \frac{C_3}{I(2I-1)(I-1)}\, I_z^3, \\ \hat{\mathscr{H}}_{\mathrm{hexadecapole}} &= \frac{C_4}{I(2I-1)(I-1)(2I-3)}\, I_z^4. \end{aligned} \tag{9.26}$$

Figure 9.27 shows the posterior distribution of C_3 and C_4 for each of the two fits. We find $C_3 = 8(14)$ Hz and $C_4 = 12(10)$ Hz, compatible with zero in both cases.

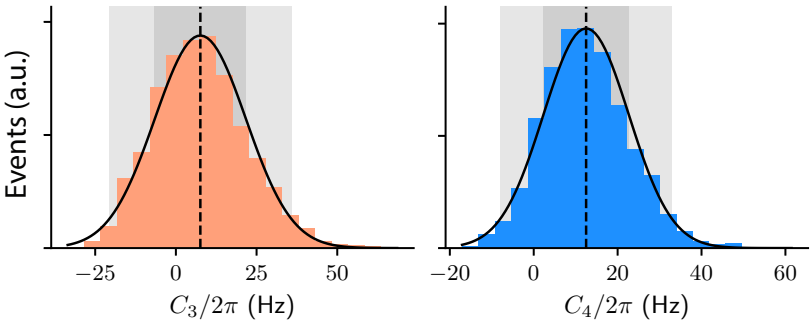

Figure 9.27.: Posterior distributions for the octupole and hexadecapole coupling constant (C_3 and C_4 respectively) from the MCMC fits. The fit was performed by including the term $\hat{\mathcal{H}}_{\text{octupole}}$ ($\hat{\mathcal{H}}_{\text{hexadecapole}}$) to $\mathcal{H}^{(\Downarrow)}$ and following the procedure described in Section 9.6.

The vanishingly low octupolar interaction C_3 is not surprising given the relatively large (0.57 nm) distance between the Er^{3+} magnetic moment and the ^{93}Nb atom. Much larger octupolar interactions may be expected in spin systems combining a high-spin nucleus and a paramagnetic center with large orbital moment on the same atom, such as $^{167}Er^{3+}$. The upper bound on the hexadecapolar interaction C_4 is one order of magnitude tighter than the most precise ensemble NMR measurement reported of $C_4 = 58 \pm 140$ Hz [41]. Indeed, the spectral resolution of ensemble measurements is limited by the dipolar coupling between the constituent nuclear spins. Instead, we achieve one order of magnitude narrower linewidth by measuring an individual impurity in an otherwise nuclear-spin-silent crystal and by polarizing the surrounding heteronuclear spin environment to further reduce the linewidth. With longer coherence times, and applied to nuclei for which larger hexadecapolar interaction is predicted such as ^{175}Lu, ^{179}Hf, or ^{181}Ta, our method may provide a viable route towards hexadecapolar interaction measurements in the solid-state.

[41]: Liao et al. (1994), 'The Nuclear Hexadecapole Interaction of Iodine-127 in Cadmium Iodide Measured Using Zero-field Two Dimensional Nuclear Magnetic Resonance'

9.9. Conclusion and outlook

We now discuss the generality of our findings. The spin-dependent pseudo-quadrupole mechanism should be sizable in paramagnetic centers with low-lying excited states, such as metallic centers and particularly lanthanides. The direct electrical coupling mechanism requires paramagnetic centers with spin-orbit coupling and non-inversion symmetry, also found in metallic centers. Overall, measurable SDQ terms should therefore be found mainly in systems involving metallic paramagnetic centers (molecules or impurities in solids), but not in organic radicals. Larger SDQ values than the one reported here should be observable on the nuclear spin belonging to the metallic center itself, for instance in $^{167}Er^{3+}$.

The detection of single paramagnetic centers by microwave photon counting only requires sufficiently long spin-lattice relaxation times at 10 mK, and should therefore be applicable to a large variety of systems and samples [14]. Our demonstrated ability to chemically and structurally characterize an unknown nuclear-spin-carrying atomic impurity next to a paramagnetic center therefore opens interesting perspectives, such as the ability to characterize the constituent atoms of individual molecules, for instance. The high spectral resolution reached in spectroscopy of the ^{93}Nb levels should be achievable more generally in arbitrary nuclear spin systems, as long as they can be coupled to a paramagnetic center measurable by photon counting. This would be particularly relevant for quadrupolar nuclei in disordered systems (molecules in frozen solutions,

[14]: Wang et al. (2023), 'Single-Electron Spin Resonance Detection by Microwave Photon Counting'

for instance), where high spectral resolution is difficult to achieve by conventional ensemble methods. Regarding the new spin-dependent-quadrupole interaction term evidenced here, future work could measure its magnitude in other coupled paramagnetic-nuclear spin systems, and possibly confirm its electrostatic origin. Finally, our results suggest that precision hyperfine spectroscopy by single-spin measurement using microwave photon counting has the potential to observe and study magnetic octupole and electric hexadecapolar interactions in the solid-state.

10. Conclusion and future directions

Summary

The objective of this thesis has been to demonstrate an all-microwave platform for the detection of nuclear spins in the solid state using an electronic spin as an ancilla, and to show how this system can be used for quantum information and precision spectroscopy.

In Chapter 7, we establish the basis for nuclear spin detection by monitoring the fluorescence of a coupled electronic spin. This demonstration relies on several key technologies. First, the Single Microwave Photon Detector provides the sensitivity required to count individual photons in the microwave regime. Second, Purcell enhancement of radiative spin transitions of Er^{3+} ions in $CaWO_4$ boosts the microwave emission beyond the phonon relaxation rate. By combining these two technologies, the group had previously detected single Er^{3+} spins. Using high-resolution EPR spectroscopy, we resolve the hyperfine splitting of the Er^{3+} spin coupled to a neighboring ^{183}W . We exploit the frequency differences of the EPR transitions, which depend on the ^{183}W nuclear spin state, to define a nuclear spin readout protocol. In addition, we demonstrate solid-effect dynamical nuclear polarization of the nuclear spin environment surrounding the Er^{3+} .

Chapter 8 builds on these techniques to construct a two-qubit register composed of two ^{183}W nuclear spins in close proximity to an Er^{3+} . We demonstrate coherent control using a microwave-stimulated Raman scheme and define single- and two-qubit gates by exploiting microwave-induced energy level shifts. We show that, owing to the low magnetic noise environment of $CaWO_4$, nuclear spins achieve coherence times on the order of seconds. These coherence times can be further extended by preparing a near-zero magnetic dipole Bell state that is inherently protected from correlated magnetic noise.

Finally, in Chapter 9, we chemically and structurally identify a ^{93}Nb impurity neighboring an Er^{3+} spin using the techniques developed in the previous chapters. Leveraging the long nuclear spin coherence, we measure the NMR transitions with hertz-level precision and fit them to a Hamiltonian model. We observe a significant shift in the nuclear quadrupole interaction depending on the electronic spin state, which we attribute to a previously unobserved coupling term between the electron spin and the nuclear quadrupole in the solid state. This interaction originates from the magnetically induced electric dipole of the Er^{3+} spin and is mediated by the crystal lattice. Finally, we use high-resolution data to place an upper bound on the hexadecapole interaction of the ^{93}Nb that is four orders of magnitude more stringent than previous solid-state NMR results.

Perspectives

The procedures and techniques demonstrated in this thesis are a proof-of-concept that can be greatly expanded in many directions.

Improving SNR with new designs

The experiments presented in this manuscript rely on a single-shot readout protocol for the nuclear spins. However, achieving sufficiently high readout fidelity requires approximately 200 electron excitation pulses. Given that each electron spin readout takes approximately 1 ms, the total readout sequence becomes relatively long, on the order of 200 ms. Increasing the SNR of the photon counting measurement is therefore a primary requirement for reducing the overall duration of each experiment, which opens the door to faster data acquisition and the implementation of more complex quantum control and feedback protocols.

As discussed in Chapter 4, the design of the superconducting spin resonator aims to maximize the coupling to the Er^{3+} spins in the $CaWO_4$ substrate. This is done by minimizing its impedance using large interdigitated capacitors, shunted by a small nanowire. For convenience, the resonator is capacitively coupled to the driving lines, but this design choice prevents radiofrequency pulses from reaching the spins, and direct nuclear

spin driving is therefore unachievable. There are two straightforward, although technically challenging, improvements to the design.

By reducing the impedance of the resonator, the coupling to the spins is proportionally increased. Since the relaxation rate of the electron spins is proportional to the square of the coupling, a significant increase in the Purcell effect is expected. This can be achieved by fabricating parallel-plate capacitors separated by a thin dielectric membrane, a design that maximizes capacitance and therefore minimizes impedance for the same frequency range. Finite element simulations predict an increase of an order of magnitude in the coupling, yielding a Purcell factor of 10^{16}.

Directly connecting the resonator to the driving lines through a metallic bond would allow one to send RF pulses to the resonator and therefore resonantly drive the nuclear spins. Additionally, DC pulses can be used to dynamically tune the resonance frequency by leveraging the response of the nanowire's kinetic inductance to a DC current. To avoid direct losses to the line, the resonator would be protected by a transmission line with mismatched impedance sections, which plays the role of a microwave Bragg mirror.

Connecting nuclear spin registers

One key limitation of the quantum computing platform presented in Chapter 8 is scalability: the number of nuclear spins strongly coupled to a single Er^{3+} impurity is very limited. Within the first unit cell, there are only ten ^{183}W atoms, of which only approximately 14% possess nuclear spins. One possible route to overcome this limitation is to use the resonator as a mediator between different Er^{3+} impurities. By implementing the design improvements described previously, reaching the strong-coupling regime between Er^{3+} spins and the resonator should be feasible. In this regime, spatially separated Er^{3+} spins could be entangled via virtual-photon exchange mediated by the resonator.

Moreover, rare-earth ions are promising candidates for the implementation of quantum communication protocols due to their intrinsic spin-photon interface and optical transitions, which lie close to or within the telecom C-band, where fiber losses are minimal. By leveraging this spin-photon interface, distant Er^{3+} impurities could communicate with one another, enabling long-distance entanglement between distinct nuclear-spin clusters.

Probing new substrates

So far, the only substrate and paramagnetic impurity combination that has been studied using single microwave photon counting at the single ion level is $Er^{3+}:CaWO_4$. The choice to focus on this combination is motivated by the excellent properties of the system: the substrate has low microwave losses and low nuclear spin density. Additionally, the Er^{3+} in $CaWO_4$ has a strong gyromagnetic factor, which yields a large coupling strength to the resonator. However, microwave photon counting is a technique that could, in principle, be applied to many electron spin systems, in a wide variety of samples, ranging from organic radicals to transition-metal ions in metallo-enzymes. One can also envision a setup in which the samples are deposited on top of the resonator, instead of being present in the substrate, in the form of nanoparticles or a frozen solution.

Currently, the group is working with erbium-doped Y_2O_3 nanoparticles that have been deposited on top of the nanowire using a micromanipulator tweezer. The complex spin signals observed in the sample promise a rich and interesting system and pave the way for state-of-the-art analysis of new samples.

Appendix

Rotation of the quadrupole tensor around the z-axis

A.

We start from the Cartesian, symmetric traceless tensor

$$Q = \begin{pmatrix} Q_{xx} & Q_{xy} & Q_{xz} \\ Q_{xy} & Q_{yy} & Q_{yz} \\ Q_{xz} & Q_{yz} & Q_{zz} \end{pmatrix}, \qquad \mathrm{Tr}\, Q = 0, \tag{A.1}$$

and rotate the axes by an angle ϕ about z with

$$R_z(\phi) = \begin{pmatrix} \cos\phi & \sin\phi & 0 \\ -\sin\phi & \cos\phi & 0 \\ 0 & 0 & 1 \end{pmatrix}. \tag{A.2}$$

Under this passive rotation,

$$Q' \;=\; R_z(\phi)\, Q\, R_z^{\top}(\phi). \tag{A.3}$$

Carrying out the multiplication gives

$$\begin{aligned} Q'_{xx} &= \cos^2\phi\, Q_{xx} + \sin^2\phi\, Q_{yy} + 2\sin\phi\cos\phi\, Q_{xy}, \\ Q'_{yy} &= \sin^2\phi\, Q_{xx} + \cos^2\phi\, Q_{yy} - 2\sin\phi\cos\phi\, Q_{xy}, \\ Q'_{xy} &= (\cos^2\phi - \sin^2\phi)\, Q_{xy} + \sin\phi\cos\phi\, (Q_{yy} - Q_{xx}), \\ Q'_{xz} &= \cos\phi\, Q_{xz} + \sin\phi\, Q_{yz}, \\ Q'_{yz} &= -\sin\phi\, Q_{xz} + \cos\phi\, Q_{yz}, \\ Q'_{zz} &= Q_{zz}. \end{aligned} \tag{A.4}$$

We define the spherical components (rank-2 irreducible combinations) as

$$\begin{aligned} S_0 &= Q_{zz}, \\ S_{\pm 1} &= Q_{xz} \pm i Q_{yz}, \\ S_{\pm 2} &= \tfrac{1}{2}\,(Q_{xx} - Q_{yy}) \pm i\, Q_{xy}. \end{aligned} \tag{A.5}$$

Using A.4 in the definition of $S'_{\pm 1}$,

$$\begin{aligned} S'_{+1} &= Q'_{xz} + i\, Q'_{yz} \\ &= \big(\cos\phi\, Q_{xz} + \sin\phi\, Q_{yz}\big) \;+\; i\big(-\sin\phi\, Q_{xz} + \cos\phi\, Q_{yz}\big) \\ &= (\cos\phi - i\sin\phi)\, Q_{xz} \;+\; (\sin\phi + i\cos\phi)\, Q_{yz} \;=\; e^{-i\phi}\, S_{+1}. \end{aligned} \tag{A.6}$$

Similarly,

$$\begin{aligned} S'_{-1} &= Q'_{xz} - i\, Q'_{yz} \\ &= \big(\cos\phi\, Q_{xz} + \sin\phi\, Q_{yz}\big) \;-\; i\big(-\sin\phi\, Q_{xz} + \cos\phi\, Q_{yz}\big) \\ &= (\cos\phi + i\sin\phi)\, Q_{xz} \;+\; (\sin\phi - i\cos\phi)\, Q_{yz} \\ &= e^{+i\phi}\,\big(Q_{xz} - iQ_{yz}\big) \;=\; e^{+i\phi}\, S_{-1}. \end{aligned} \tag{A.7}$$

Let $\Delta Q \equiv Q_{xx} - Q_{yy}$. From (A.4),

$$\begin{aligned} S'_{+2} &= \tfrac{1}{2}\,(Q'_{xx} - Q'_{yy}) + i\,Q'_{xy} \\ &= \tfrac{1}{2}\Big[\big(\cos^2\phi - \sin^2\phi\big)\Delta Q + 4\sin\phi\cos\phi\,Q_{xy}\Big] \\ &+ i\Big[\big(\cos^2\phi - \sin^2\phi\big)Q_{xy} - \sin\phi\cos\phi\,\Delta Q\Big]. \end{aligned} \tag{A.8}$$

Use the double-angle identities $\cos 2\phi = \cos^2\phi - \sin^2\phi$ and $\sin 2\phi = 2\sin\phi\cos\phi$ to rewrite

$$\begin{aligned} S'_{+2} &= \tfrac{1}{2}\Big[\cos 2\phi\,\Delta Q + 2\sin 2\phi\,Q_{xy}\Big] + i\Big[\cos 2\phi\,Q_{xy} - \tfrac{1}{2}\sin 2\phi\,\Delta Q\Big] \\ &= \big(\tfrac{1}{2}\Delta Q + iQ_{xy}\big)\,\big(\cos 2\phi - i\sin 2\phi\big) \\ &= \big(\tfrac{1}{2}\Delta Q + iQ_{xy}\big)\,e^{-i2\phi} \;=\; e^{-i2\phi}\,S_{+2}. \end{aligned} \tag{A.9}$$

By complex conjugation or repeating the steps with $-i$,

$$S'_{-2} \;=\; e^{+i2\phi}\,S_{-2}. \tag{A.10}$$

Since $Q'_{zz} = Q_{zz}$,

$$S'_0 \;=\; S_0. \tag{A.11}$$

Collecting the results,

$$S'_m \;=\; e^{-im\phi}\,S_m, \qquad m = 0, \pm 1, \pm 2. \tag{A.12}$$

B. Single Microwave Photon Detector

The detection of single optical photons is performed routinely via photomultipliers and superconducting nanowire photon detectors. However, microwaves are five orders of magnitude less energetic than optical photons, and single-photon detection is not trivial. Our group proposed and developed a detector based on a superconducting circuit with a transmon qubit at its center [21]. In the following, we describe the SMPD architecture, its operating principle, and the key performance metrics (efficiency, dark-count rate, and temporal resolution) relevant for detecting microwave fluorescence from individual Er^{3+} ions. For an in-depth description and characterization of the SMPD, one should refer to previous theses from the group, which focus on the development and fabrication of this device, particularly [20, 24, 25].

[21]: Lescanne et al. (2020), 'Irreversible Qubit-Photon Coupling for the Detection of Itinerant Microwave Photons'

B.1. Working principle

The operating principle of the SMPD can be summarized as follows: an incoming photon is detected by performing an irreversible frequency conversion into a qubit excitation. After the detection window, the qubit is read out dispersively, revealing the arrival of the photon. The architecture is based on the irreversibility of the process, enabled by an engineered dissipation mechanism.

At the center of the SMPD lies a superconducting transmon qubit[135]. This element behaves as a nonlinear oscillator and can be treated as an effective two-level system with frequency ω_q and levels $|g\rangle$ and $|e\rangle$. The qubit is simultaneously coupled to two independent resonators: the *buffer* resonator with frequency ω_b and the *waste* resonator with frequency ω_w. The process that enables the frequency conversion is a parametric four-wave mixing (4WM), in which a buffer photon is mixed with a coherent pump tone to produce an excitation on the qubit and a waste photon. The detection process is divided into two distinct phases: the capture phase, when the qubit excitation via 4WM takes place, and the readout phase, when the state of the qubit is measured.

The capturing process can be summarized in three independent steps which are schematized in Figure B.1.

1. A photon traveling in the microwave lines with frequency ω_b arrives at the input of the detector, populating the buffer resonator. Meanwhile, the SMPD is illuminated with a coherent pump tone at frequency ω_p.
2. With the input resonator populated, the 4WM process transforms the buffer photon and a pump photon into a qubit excitation and a waste photon.
3. To avoid the inverse process, a dissipation channel on the waste resonator is engineered by strongly coupling it to the microwave lines. Consequently, the waste photon is rapidly lost (hence the name), blocking the reverse parametric process from ever taking place.

It is important to note that, for the 4WM process to take place, energy conservation must be satisfied:

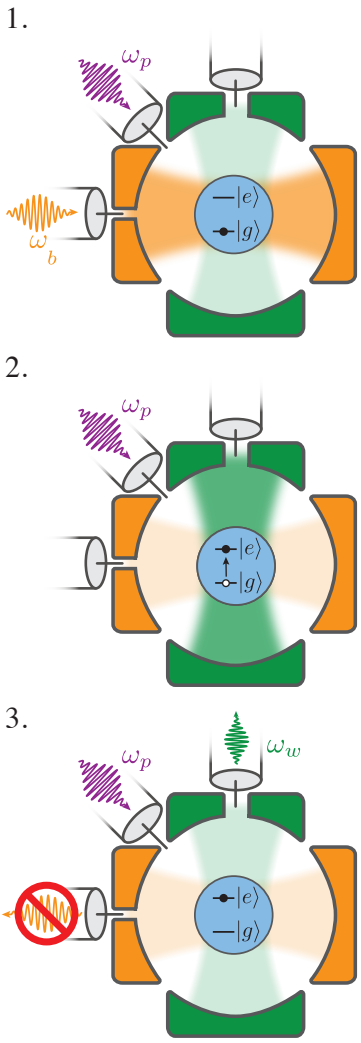

Figure B.1.: Working principle of the SMPD. At the heart of the SMPD lies a qubit with states $|g\rangle$ and $|e\rangle$. There are two resonators coupled to the qubit, the buffer and the waste in orange and green respectively, as well as a transmission line to drive and pump the qubit. The capturing process is divided in three steps. First, capture of the incoming photon. Second, four-wave mixing, where the buffer photon is transformed into a qubit excitation. Third, dissipation of the waste, which inhibits the reverse process.

[135]: Koch et al. (2007), 'Charge-Insensitive Qubit Design Derived from the Cooper Pair Box'

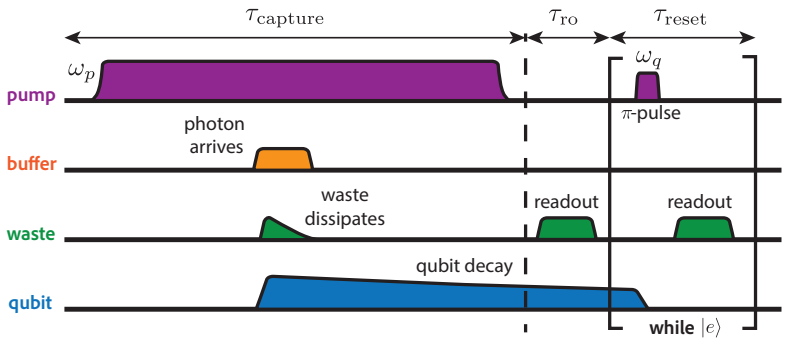

Figure B.2.: The SMPD cycle is divided into two parts, the capture and readout phases, separated by a dashed line. During the detection phase, the pump tone at frequency ω_p illuminates the qubit continuously. An incoming photon triggers 4WM and the qubit is excited while the waste photon is rapidly dissipated. During the readout phase, the qubit is measured using the dispersive shift of the waste resonator. If the qubit is excited, a π-pulse is applied through the pump line at frequency ω_q, then the qubit is read out again until it is found in the ground state.

$$\omega_b + \omega_p = \omega_q + \omega_w, \tag{B.1}$$

This relation can be ensured by adjusting the frequency of the pump tone.

After the capturing process, the state of the qubit is read out dispersively using a coherent tone on the waste resonator [136]. If the qubit is found in the ground state, the detection cycle can restart. However, if the qubit is in the excited state, it first needs to be reset to the ground state before restarting the capturing phase. One could just wait for the qubit to spontaneously relax, but the detector is not operational during this process, effectively reducing the detection efficiency. We implement a conditional reset, in which a π-pulse is applied if the qubit is found in the excited state, followed by another readout step. This repeats until the qubit is in its ground state. Thanks to the high fidelity of the excited-state readout, this procedure also effectively cools down the qubit. The detection process is performed continuously in cycles and can be visualized in Figure B.2. We define the capture, readout, and reset times as τ_{capture}, τ_{ro}, and τ_{reset}, respectively.

[136]: Wallraff et al. (2004), 'Strong Coupling of a Single Photon to a Superconducting Qubit Using Circuit Quantum Electrodynamics'

We note that only photons that arrive during the capturing phase will be detected, as the 4WM process is turned off during the readout phase. In addition, if a second photon arrives at the detector, the 4WM process will not take place, as the qubit is already in the excited state. Consequently, if the input photon rate exceeds the SMPD cycle rate, the detector will saturate and is effectively "blinded".

B.2. SMPD Circuit

We now proceed to describe the individual components of the SMPD. The device is fabricated from a tantalum thin film on a sapphire chip using standard nanofabrication techniques and all Josephson junctions are made from a tri-layer of $Al/AlO_x/Al$ [25]. Figure B.3 shows a schematic representation of the circuit.

- **Qubit.** Transmon design with a Josephson junction and shunted capacitor. It is dispersively coupled to both buffer and waste resonators. For robustness, the frequency of the qubit is non-tunable.
- **Buffer.** The buffer resonator is the capture port for incoming photons. It takes the form of a half-wave coplanar waveguide (CPW) with open ends. One end couples capacitively to the qubit. The resonator has a SQUID embedded in its design [1]. The SQUID

[25]: Pallegoix (2025), 'High Performance Microwave Photon Counter and Application to Single Spin Magnetic Resonance'

1: A Superconducting Quantum Interference Device (SQUID) is a non-linear element with a tunable inductance. It is composed of two Josephson junctions in parallel, forming a loop. The magnetic flux threading the loop modulates periodically the inductance of the element. Experimentally, the flux is controlled by means of a DC current that runs on a nearby grounded line, which generates a local magnetic field.

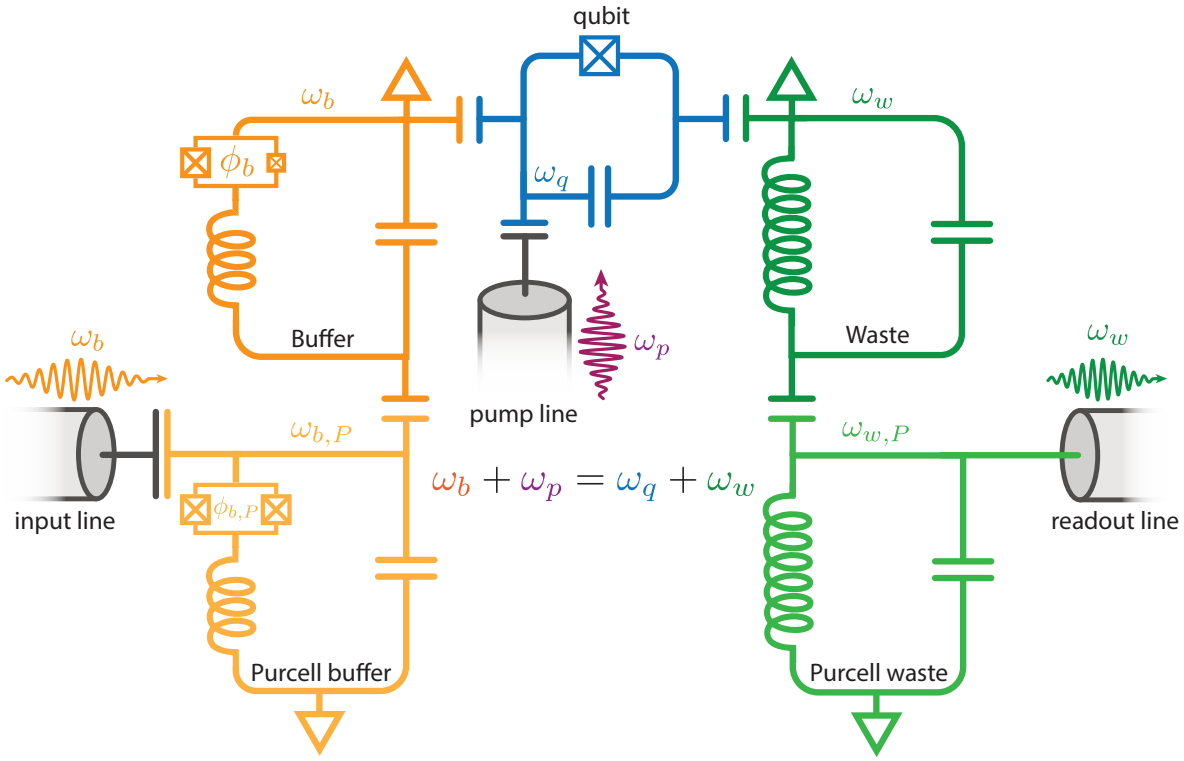

Figure B.3.: SMPD schematic circuit. The qubit (blue) has a fixed frequency and is capacitively coupled to both the waste and the buffer resonators. Both the buffer and its Purcell filter (dark and light orange, respectively) embed a SQUID, used to tune their frequencies. The SQUID of the buffer is strongly asymmetric to reduce spectral diffusion due to magnetic noise. The buffer Purcell filter is capacitively coupled to the input microwave line. The waste and its Purcell filter have a fixed frequency. In contrast to the buffer's, the waste Purcell filter is galvanically coupled to the output microwave line, which ensures a rapid dissipation of any waste photon. The qubit is also capacitively coupled to a CPW line, used to pump the 4WM process and coherently control its state.

is highly asymmetric to reduce spectral diffusion of the buffer resonator.

- **Buffer Purcell filter.** The middle of the buffer resonator is capacitively coupled to the buffer Purcell filter. This second resonator prevents the qubit from rapidly decaying to the microwave lines due to its interaction with the buffer. Additionally, the Purcell filter embeds a SQUID element in the middle of its design. By tuning the frequency of the Purcell filter, the effective detection bandwidth can also be controlled.
- **Waste and its Purcell filter.** The waste resonator receives the converted photon produced by the four-wave mixing process and is also used for dispersive readout. It is galvanically coupled to the microwave lines so that the waste photon is rapidly lost, and the conversion becomes effectively irreversible. The Purcell filter is designed with the same principle as the buffer's.
- **Qubit drive line.** The dedicated pump line delivers the coherent pump tone at ω_p used for 4WM as well as controlling the state of the qubit. The line is designed as a simple CPW element capacitively coupled to the qubit.

All relevant frequencies and linewidths of the elements from the SMPD used in this work are displayed in Table B.1.

Resonator	**Frequency** (GHz)	**Linewidth** (MHz)
Buffer	$\omega_b/2\pi \in [7.70; 7.76]$	$\sim [0; 2.5]$
Buffer Purcell	$\omega_{b,P}/2\pi \in [7.26; 7.78]$	20
Qubit	$\omega_q/2\pi = 6.533$	0.016
Waste	$\omega_w/2\pi = 8.475$	1.75
Waste Purcell	$\omega_{w,P}/2\pi \approx 8.39$	400

Table B.1.: Frequencies and linewidths of different elements of the SMPD. The linewidth of the buffer is controlled by tuning the frequency of the buffer's Purcell filter. The data was taken from [73].

B.3. Performance metrics

To characterize the detector, we define a series of performance metrics, namely the efficiency, the dark-count rate, and the bandwidth of the detector. We now proceed to discuss each of them and how they relate to the performance of the detector.

Efficiency We define the efficiency η_{SMPD} as the probability of successfully detecting a photon arriving at the detector. There are numerous sources of detection infidelity:

- **Conversion efficiency**. The 4WM process is not instantaneous; it is a coherent process with an associated rate. Given the finite losses of the buffer resonator, some photons will inevitably be lost during the conversion process. The efficiency of the process can be estimated as [2]
$$\eta_{\text{b, loss}} = \frac{1}{1 + \frac{\kappa_{\text{b, i}}}{\kappa_{\text{b, c}}}},$$
where we separate the losses of the buffer between internal ($\kappa_{\text{b, i}}$) and coupling ($\kappa_{\text{b, c}}$) contributions.
- **Duty cycle**. During the readout phase of the detector, the parametric conversion is turned off. This interval defines the dead time of the detector. The efficiency associated with the dead time can be estimated by
$$\eta_{\text{dead}} = \frac{\tau_{\text{capture}}}{\tau_{\text{capture}} + \tau_{\text{ro}}},$$
where we have assumed that the reset time is negligible due to the low photon arrival rate. This can be maximized by extending the capture time with respect to the readout time.
- **Qubit lifetime**. Given the finite lifetime of the qubit, $T_{1,q} \approx 80\ \mu\text{s}$, any excitation will eventually be lost. The efficiency associated with this loss channel is given by averaging the loss probability over the detection window,
$$\eta_q = \frac{1}{\tau_{\text{capture}}} \int_0^{\tau_{\text{capture}}} e^{-(\tau_{\text{capture}} - t)/T_1} dt = \frac{T_1}{\tau_{\text{capture}}} \left(1 - e^{-\tau_{\text{capture}}/T_1}\right)$$
Assuming that $\tau_{\text{capture}} \ll T_1$, we arrive at
$$\eta_q \approx 1 - \frac{\tau_{\text{capture}}}{2T_1},$$
From this expression, we conclude that a short detection window compared to the decay time of the qubit minimizes losses in the qubit.
- **Measurement efficiency**. After the conversion, the qubit is read out dispersively. The measurement has a finite fidelity $\eta_{\text{q, meas}}$, which increases with the qubit readout time. In our experiments, the

2: Here we assume that the cooperativity of the parametric process is equal to 1. A more detailed study of the 4WM process is outside the scope of this thesis and can be found in [25]

single-shot threshold is chosen to minimize false positives (dark counts) at the expense of increased false negatives. This choice is made due to the low number of arriving photons; a large false positive rate would disproportionately corrupt the measurement statistics.

The total efficiency of the detector is obtained by combining all sources of infidelity

$$\eta_{\text{SMPD}} = \eta_{b,\text{loss}} \times \eta_{\text{dead}} \times \eta_q \times \eta_{q,\text{meas}} \tag{B.2}$$

We can see that there are conflicting requirements to maximize both η_q and η_{dead}. Extending the detection window increases η_{dead} while reducing η_q, and a compromise must be made. In addition, increasing the readout time to achieve a high readout fidelity effectively increases the dead time of the detector. In the end, we set the detection window and the readout time to $\tau_{\text{capture}} = 17$ µs and $\tau_{\text{ro}} = 1$ µs, from which we estimate $\eta_{\text{dead}} = 0.94$ and $\eta_q = 0.90$. We choose a single-shot threshold that heavily suppresses false positives, with $P(e|g) \approx 2 \times 10^{-3}$, which is close to the optimal condition.

Dark counts The dark count rate of the detector Γ_{DC} is defined as the detection rate when the device is operated without any input signal. As we approach unity efficiency, dark counts become the limiting factor on the detection sensitivity, and a large effort in the group is directed toward minimizing them [137]. The origin of the dark counts can be traced back to two main effects: spurious qubit excitations and thermal photons on the microwave lines.

[137]: May (2025), 'Noise Mitigation in Single Microwave Photon Counting'

Given that the experiments are performed at finite temperature $T \approx 10$ mK, the qubit has a non-zero probability of being in the excited state. Even if no photon has arrived at the end of the detection window, the detector can still measure a count due to the finite probability of excitation. Thanks to the conditional reset, the qubit is effectively cooled down at the end of every cycle, but the population will evolve toward its steady state with the characteristic time T_1. The contribution to the dark count rate is given by

$$\Gamma_q = \frac{p_q}{\tau_{\text{capture}} + \tau_{\text{ro}}}, \tag{B.3}$$

where p_q is the population of the qubit at the end of the detection window.

The second contribution originates from impinging photons due to the finite temperature of the microwave lines, which emit blackbody radiation. In addition, thermal radiation from upper stages of the cryogenic setup can add to this source of noise if the attenuation of the lines is not properly considered. Naturally, the contribution to the dark count rate from impinging thermal photons depends on the detector's bandwidth [3] κ_d. If we take $\bar{n}_b$ as the photon occupation number of the buffer, the total thermal dark count rate is given by

3: For cooperativity equal to 1, this value is double the buffer's bandwidth

$$\kappa_d = 2\kappa_b$$

$$\Gamma_{\text{th}} = \frac{\bar{n}_b \eta_{\text{SMPD}} \kappa_d}{4}, \tag{B.4}$$

where we have considered that the detector has a Lorentzian lineshape and that $\bar{n}_b$ is constant over its bandwidth. The total contribution to the dark count rate is then given by the sum of the two rates, $\Gamma_{\mathrm{DC}} = \Gamma_{\mathrm{th}} + \Gamma_q$, and can be experimentally characterized by simply running the detection cycle without any input signal.

Time-dependent Hamiltonian simulations

C.

The simulations were performed by Zhiyuan W. Huang using `QuTip` [138] and `Dynamiqs` [139] to characterize the coherent and incoherent error sources in our system. The simulations consider an electron spin coupled to two nuclear spins and do not include a cavity or background spin bath. Therefore, the system is described by the Hamiltonian in Eq. 8.1. An additional driving term with frequency ω is modeled by the Hamiltonian

[138]: Johansson et al. (2012), 'QuTiP'

[139]: Guilmin et al. (2025), *Dynamiqs*

$$\hat{\mathcal{H}}_{\mathrm{d}} = \frac{\hbar\Omega_d}{2}(\hat{S}_- e^{i\omega t} + \hat{S}_+ e^{-i\omega t}), \tag{C.1}$$

where Ω_d is the pulse amplitude, and $\hat{S}_-$ and $\hat{S}_+$ are the lowering and raising operators for the Er^{3+} spin, respectively. The pulse amplitude used in the simulation is calibrated using the measured electron spin Rabi frequency, and pulse durations are matched to those used in the experiment.

The simulation results follow from solving the master equation with the total time-dependent Hamiltonian

$$\frac{d\hat{\rho}}{dt} = \frac{1}{i\hbar}\left[\hat{\mathcal{H}}_{\mathrm{tot}}, \hat{\rho}\right] + \sum_k \left(\hat{L}_k \hat{\rho} \hat{L}_k^\dagger - \frac{1}{2}\left\{\hat{L}_k^\dagger \hat{L}_k, \hat{\rho}\right\}\right), \tag{C.2}$$

where $\hat{\mathcal{H}}_{\mathrm{tot}} = \hat{\mathcal{H}} + \hat{\mathcal{H}}_{\mathrm{d}}$. The electron energy relaxation process is modeled by the Lindblad operators $\hat{L}_{s_-} = \sqrt{\Gamma_1(\bar{n}_{\mathrm{th}} + 1)}\,\hat{S}_-$ and $\hat{L}_{s_+} = \sqrt{\Gamma_1(\bar{n}_{\mathrm{th}})}\,\hat{S}_+$, where $\Gamma_1 = \frac{1}{T_1}$ is the electron relaxation rate. Dephasing of the nuclear spins is modeled by $\hat{L}_{n_\varphi,i} = \sqrt{\Gamma_\varphi}\,\hat{I}_{z,i}$ for $i = 1, 2$, where $\Gamma_\varphi = \frac{1}{T_2^*}$ is the nuclear dephasing rate. We also note that this analysis only considers Markovian effects, but a more realistic description should include non-Markovian terms, such as spin-bath dynamics, which could be an additional source of decoherence.

Monte Carlo Markov Chain fitting procedure

D.

In this appendix, we describe in more detail the fit procedure used to obtain the spin Hamiltonian parameters in Chapter 9. We begin with a description of the MCMC algorithm, followed by an analysis of the posterior distributions obtained for each fit.

The algorithm begins by initializing N walkers at random positions in the parameter space of dimension n. The walkers are given by

$$\{x_0, x_1, \dots x_N\} \quad x_i \in \mathbb{R}^n \tag{D.1}$$

The initial positions of the walkers are centered around informed guesses of the parameters and are spread according to a normal distribution with a standard deviation of 1% of the numerical value of the parameter.

To update the position of the walkers, we use the "stretch move" [130]. Each walker x_i is paired with another one x_j. The new position of the walker is given by

[130]: Goodman et al. (2010), 'Ensemble Samplers with Affine Invariance'

$$x_i' = x_j + z(x_i - x_j), \tag{D.2}$$

where z is the stretch factor that is sampled from a bounded distribution. If $z = 1$ the point does not move; if $z > 1$ the walker moves away from its pair, and if $z < 1$ the walker moves toward its pair. Finally, the new position is accepted with probability α, given by

$$\alpha = \min\left(1, z^{d-1}\frac{\mathcal{L}(x_i')}{\mathcal{L}(x_i)}\right), \tag{D.3}$$

where $\mathcal{L}$ is the logarithmic likelihood defined in Section 9.6. This is repeated for all walkers and then iterated for a predefined number of steps. Convergence is not checked during the run and must be evaluated afterwards.

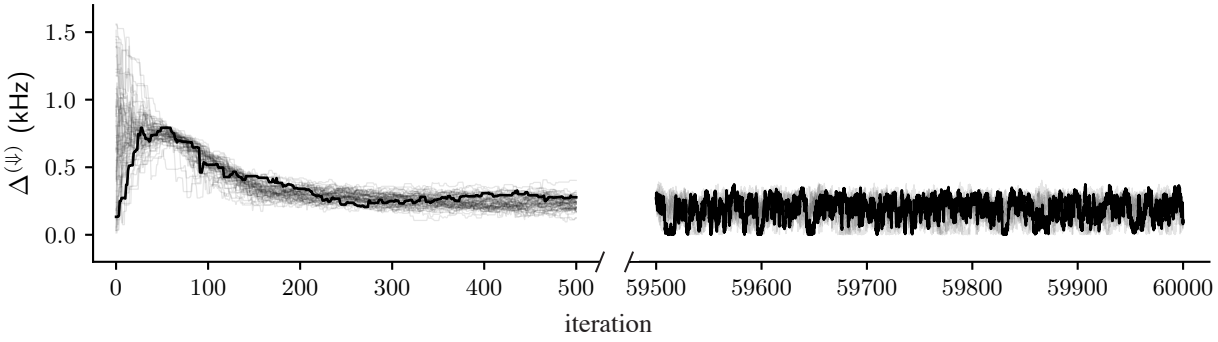

Figure D.1.: Example chain extracted from the ground state fit. The plot shows the evolution of one component of the walker ($\Delta^{(\Downarrow)}$) as a function of the iteration step for the first and last 500 steps. One arbitrary chain has been highlighted.

D.1. Ground and excited fits

Here we discuss the results of the fits performed in Section 9.6. The algorithms were run with 64 walkers and 60000 iterations. An example chain is plotted in Figure D.1 for the first and last 500 iterations. Two different behaviors can be observed. During the first 500 steps the parameter has still not converged and has a freer evolution. During the last 500 steps the chain has converged and the MCMC algorithm is exploring the parameter range where the logarithmic likelihood is maximized. To check for convergence, we perform this visual inspection after every fit.

In addition, we estimate the integrated autocorrelation time for each parameter to ensure that the number of effectively independent samples is sufficient. Since the chain length (60000) is at least 50 times larger than the autocorrelation time for all parameters (approximately 200 iterations), we conclude that we have obtained a large effective sample size.

We use the last 5000 iterations of the algorithm to obtain the final result, which is presented in the form of a corner plot [140] in panels a and b of Figure D.2 for the ground- and excited-state fits. The diagonal panels show the distribution of the individual parameters. The off-diagonal panels show the two-dimensional (2D) distributions as well as iso-probability bars. We take the final result of the fit as the median value of the distribution (shown as a cross) and the uncertainty as the standard deviation.

[140]: Foreman-Mackey (2016), 'Corner.Py'

We note that the parameters show strong correlations, both linear and non-linear. These correlations mostly disappear when performing the fit with the full dataset, as shown in the next section. In addition, the distributions for $\Delta^{(m_S)}$ are cut at $\Delta^{(m_S)} = 0$. This originates from the priors of the fit, where we limit $0 < \Delta^{(m_S)} < \pi/2$ due to the periodic degeneracy of the variable. The large uncertainty of the parameter results

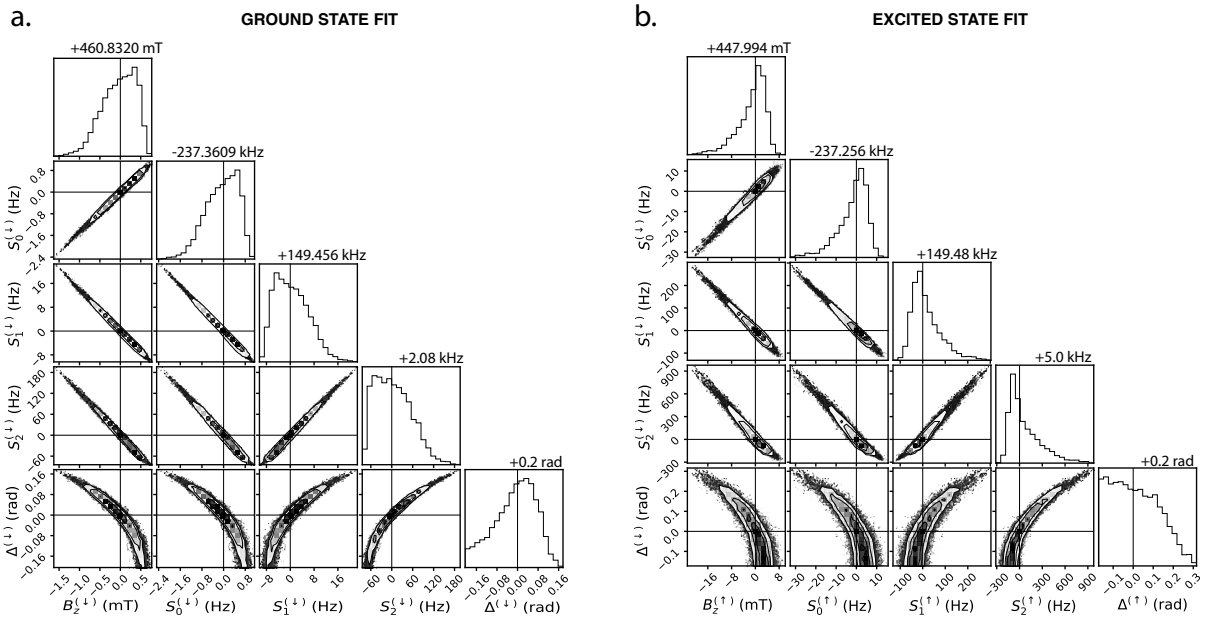

Figure D.2.: Separate Corner plots and chain trace. **a & b.** Corner plot of the posterior distributions of the MCMC fit in the ground and excited state (left and right resp.). Diagonal plots convey the one-dimensional distribution of the samples and off-diagonal plots the two-dimensional projection between two parameters. Vertical lines show the median value of the parameters, which we take as the result of the fit.

in overlapping with the distribution of the next period, which is visualized as a flat region on the posterior distribution.

D.2. Full Hamiltonian fit

The posterior distribution for the full Hamiltonian fit described in Section 9.6 is shown in Figure D.3. Compared to the distributions of the previous figure, the correlations are mostly suppressed.

To account for the 9 kHz uncertainty in the measurement of $A_\perp$, we repeat the fit 400 times while sampling the value of $A_\perp$ from a Gaussian

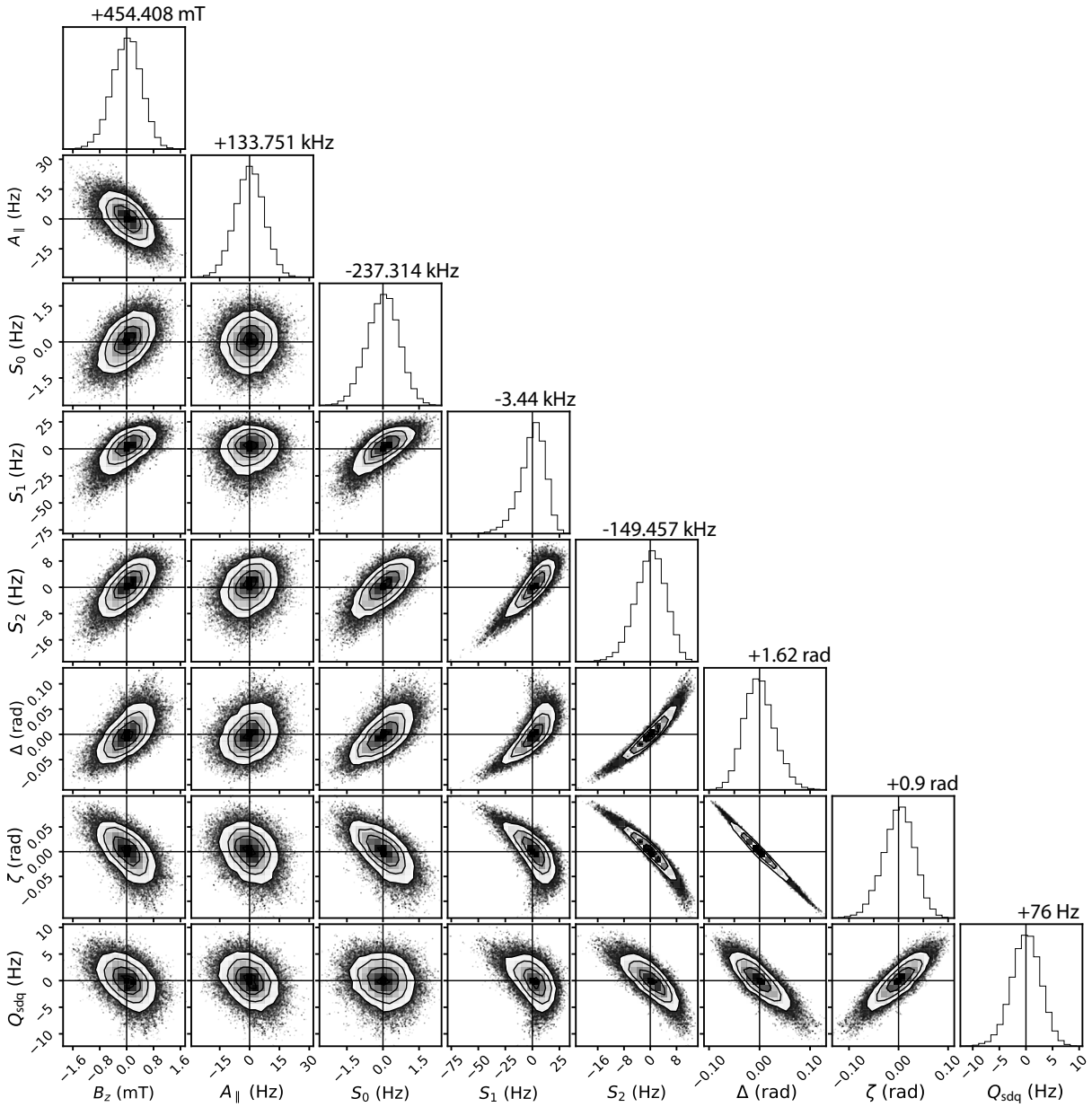

Figure D.3.: Corner plots of the posterior distributions of the full Hamiltonian fit. Diagonal plots convey the one-dimensional distribution of the samples and off-diagonal plots the two-dimensional projection between two parameters. Vertical lines show the median value of the parameters, which we take as the result of the fit.

distribution with a standard deviation of 9 kHz. Each fit yields a median and standard deviation for the parameters. The final value of the parameter is obtained by taking the median of all 400 fit results. The final uncertainty is obtained by adding the standard deviation of all 400 fit results to the mean standard deviation of the posterior distributions.

Bibliography

Here are the references in citation order.

[1] Anatole Abragam. *The Principles of Nuclear Magnetism*. Repr. The International Series of Monographs on Physics. Oxford: Clarendon Pr, 1986. 599 pp. (cited on pages 1, 10).

[2] Charles P. Slichter. *Principles of Magnetic Resonance*. 3., enl. and updated ed., corr. 3. printing. Springer Series in Solid-State Sciences 1. Berlin Heidelberg: Springer, 1996. 655 pp. (cited on pages 1, 10, 28).

[3] P. C. Lauterbur. 'Image Formation by Induced Local Interactions: Examples Employing Nuclear Magnetic Resonance'. In: *Nature* 242.5394 (Mar. 1973), pp. 190–191. DOI: 10.1038/242190a0 (cited on pages 1, 10).

[4] Abby R. Haworth, Chris W. Cook, and John M. Griffin. 'Solid-State NMR Studies of Coatings and Interfaces in Batteries'. In: *Current Opinion in Colloid & Interface Science* 62 (Dec. 1, 2022), p. 101638. DOI: 10.1016/j.cocis.2022.101638 (cited on pages 1, 10).

[5] Kurt Wüthrich. 'Protein Structure Determination in Solution by Nuclear Magnetic Resonance Spectroscopy'. In: *Science* 243.4887 (Jan. 6, 1989), pp. 45–50. DOI: 10.1126/science.2911719 (cited on pages 1, 10).

[6] Ulrike Holzgrabe. 'Quantitative NMR Spectroscopy in Pharmaceutical Applications'. In: *Progress in Nuclear Magnetic Resonance Spectroscopy* 57.2 (Aug. 1, 2010), pp. 229–240. DOI: 10.1016/j.pnmrs.2010.05.001 (cited on pages 1, 10).

[7] V. Ranjan et al. 'Electron Spin Resonance Spectroscopy with Femtoliter Detection Volume'. In: *Applied Physics Letters* 116.18 (May 4, 2020), p. 184002. DOI: 10.1063/5.0004322 (cited on pages 1, 3, 10, 11).

[8] F. Jelezko et al. 'Single Spin States in a Defect Center Resolved by Optical Spectroscopy'. In: *Applied Physics Letters* 81.12 (Sept. 16, 2002), pp. 2160–2162. DOI: 10.1063/1.1507838 (cited on pages 1, 10, 70).

[9] Andrea Morello et al. 'Single-Shot Readout of an Electron Spin in Silicon'. In: *Nature* 467.7316 (2010), pp. 687–691. DOI: doi:10.1038/nature09392 (cited on pages 1, 10, 72).

[10] C. E. Bradley et al. 'A Ten-Qubit Solid-State Spin Register with Quantum Memory up to One Minute'. In: *Physical Review X* 9.3 (Sept. 11, 2019), p. 031045. DOI: 10.1103/PhysRevX.9.031045 (cited on pages 1, 7, 10, 15, 88, 89, 102, 104).

[11] Hermann Edlbauer et al. 'An 11-Qubit Atom Processor in Silicon'. In: *Nature* 648.8094 (Dec. 2025), pp. 569–575. DOI: 10.1038/s41586-025-09827-w (cited on pages 1, 10).

[12] M. H. Abobeih et al. 'Atomic-Scale Imaging of a 27-Nuclear-Spin Cluster Using a Quantum Sensor'. In: *Nature* 576.7787 (Dec. 2019), pp. 411–415. DOI: 10.1038/s41586-019-1834-7 (cited on pages 1, 10, 100).

[13] S. Alex Breitweiser et al. 'Quadrupolar Resonance Spectroscopy of Individual Nuclei Using a Room-Temperature Quantum Sensor'. In: *Nano Letters* 24.51 (Dec. 25, 2024), pp. 16253–16260. DOI: 10.1021/acs.nanolett.4c04112 (cited on pages 1, 10, 106).

[14] Z. Wang et al. 'Single-Electron Spin Resonance Detection by Microwave Photon Counting'. In: *Nature* 619.7969 (July 2023), pp. 276–281. DOI: 10.1038/s41586-023-06097-2 (cited on pages 1, 3, 10, 12, 66, 132).

[15] R. Narkowicz, D. Suter, and I. Niemeyer. 'Scaling of Sensitivity and Efficiency in Planar Microresonators for Electron Spin Resonance'. In: *Review of Scientific Instruments* 79.8 (2008), p. 084702. DOI: 10.1063/1.2964926 (cited on pages 2, 11).

[16] Nir Dayan et al. 'Advanced Surface Resonators for Electron Spin Resonance of Single Microcrystals'. In: *Review of Scientific Instruments* 89.12 (Dec. 26, 2018), p. 124707. DOI: 10.1063/1.5063367 (cited on pages 2, 11).

[17] W. J. Wallace and R. H. Silsbee. 'Microstrip Resonators for Electron-spin Resonance'. In: *Review of Scientific Instruments* 62.7 (July 1, 1991), pp. 1754–1766. DOI: 10.1063/1.1142418 (cited on pages 2, 11).

[18] A. Bienfait et al. 'Reaching the Quantum Limit of Sensitivity in Electron Spin Resonance'. In: *Nat. Nanotechnol.* 11.3 (Mar. 2016), pp. 253–257. DOI: 10.1038/nnano.2015.282 (cited on pages 2, 11, 103).

[19] A. Bienfait et al. 'Magnetic Resonance with Squeezed Microwaves'. In: *Physical Review X* 7.4 (Oct. 17, 2017), p. 041011. DOI: 10.1103/PhysRevX.7.041011 (cited on pages 3, 11).

[20] Emanuele Albertinale et al. 'Detecting Spins by Their Fluorescence with a Microwave Photon Counter'. In: *Nature* 600.7889 (Dec. 2021), pp. 434–438. DOI: 10.1038/s41586-021-04076-z (cited on pages 3, 11, 139).

[21] Raphaël Lescanne et al. 'Irreversible Qubit-Photon Coupling for the Detection of Itinerant Microwave Photons'. In: *Phys. Rev. X* 10.2 (May 2020), p. 021038. DOI: 10.1103/PhysRevX.10.021038 (cited on pages 3, 11, 44, 139).

[22] E. M Purcell. 'Spontaneous Emission Probabilities at Radio Frequencies'. In: *Phys. Rev.* 69 (1946), p. 681 (cited on pages 3, 12).

[23] Zhiren Wang. 'Addressing Individual Electronic Spins with a Microwave Superconducting Resonator'. PhD thesis. Université Paris-Saclay ; Université de Sherbrooke (Québec, Canada), May 9, 2023. (Visited on 10/15/2025) (cited on pages 3, 12, 44, 58, 59, 65–67).

[24] Léo Balembois. 'Magnetic Resonance of a Single Electron Spin and Its Magnetic Environment by Photon Counting'. Theses. Université Paris-Saclay, June 2023. (Visited on 10/27/2025) (cited on pages 3, 12, 139).

[25] Louis Pallegoix. 'High Performance Microwave Photon Counter and Application to Single Spin Magnetic Resonance'. Theses. Université Paris-Saclay, Apr. 2025. (Visited on 10/27/2025) (cited on pages 3, 12, 45, 139, 140, 142).

[26] Marianne Le Dantec et al. 'Twenty-Three–Millisecond Electron Spin Coherence of Erbium Ions in a Natural-Abundance Crystal'. In: *Science Advances* 7.51 (Dec. 15, 2021), eabj9786. DOI: 10.1126/sciadv.abj9786 (cited on pages 4, 7, 12, 15, 22, 25, 43, 67, 73, 91, 98).

[27] P. Schosseler, Th. Wacker, and A. Schweiger. 'Pulsed ELDOR Detected NMR'. In: *Chemical Physics Letters* 224.3 (July 15, 1994), pp. 319–324. DOI: 10.1016/0009-2614(94)00548-6 (cited on pages 5, 14, 33, 83).

[28] Abragam, A., Procto, W. 'Une Nouvelle Méthode de Polarisation Des Noyaux Atomiques Dans Les Solides'. In: *C.R. Acad. Sci. Paris* (1958), p. 2253 (cited on pages 6, 15).

[29] Kamyar Saeedi et al. 'Room-Temperature Quantum Bit Storage Exceeding 39 Minutes Using Ionized Donors in Silicon-28'. In: *Science* 342.6160 (Nov. 15, 2013), pp. 830–833. DOI: 10.1126/science.1239584 (cited on pages 7, 15).

[30] Juha T. Muhonen et al. 'Storing Quantum Information for 30 Seconds in a Nanoelectronic Device'. In: *Nature Nanotechnology* 9.12 (Oct. 12, 2014), pp. 986–991. DOI: 10.1038/nnano.2014.211 (cited on pages 7, 15, 98).

[31] Manjin Zhong et al. 'Optically Addressable Nuclear Spins in a Solid with a Six-Hour Coherence Time'. In: *Nature* 517.7533 (Jan. 2015), pp. 177–180. DOI: 10.1038/nature14025 (cited on pages 7, 15).

[32] M. V. Gurudev Dutt et al. 'Quantum Register Based on Individual Electronic and Nuclear Spin Qubits in Diamond'. In: *Science* 316.5829 (June 2007), pp. 1312–1316. DOI: 10.1126/science.1139831 (cited on pages 7, 15).

[33] David D. Awschalom et al. 'Quantum Technologies with Optically Interfaced Solid-State Spins'. In: *Nature Photonics* 12.9 (Sept. 2018), pp. 516–527. DOI: 10.1038/s41566-018-0232-2 (cited on pages 7, 15).

[34] Floris A. Zwanenburg et al. 'Silicon Quantum Electronics'. In: *Reviews of Modern Physics* 85.3 (July 10, 2013), pp. 961–1019. DOI: 10.1103/RevModPhys.85.961 (cited on pages 7, 15).

[35] Jarryd J. Pla et al. 'High-Fidelity Readout and Control of a Nuclear Spin Qubit in Silicon'. In: *Nature* 496.7445 (Apr. 2013), pp. 334–338. DOI: 10.1038/nature12011 (cited on pages 7, 15, 72).

[36] Hanbin Song et al. 'Entanglement of a Nuclear Spin Qubit Register in Silicon Photonics'. In: *Nature Nanotechnology* 21.1 (Jan. 2026), pp. 53–57. DOI: 10.1038/s41565-025-02066-0 (cited on pages 7, 15).

[37] T. van der Sar et al. 'Decoherence-Protected Quantum Gates for a Hybrid Solid-State Spin Register'. In: *Nature* 484.7392 (Apr. 2012), pp. 82–86. DOI: 10.1038/nature10900 (cited on pages 7, 15, 88).

[38] H. P. Bartling et al. 'Entanglement of Spin-Pair Qubits with Intrinsic Dephasing Times Exceeding a Minute'. In: *Physical Review X* 12.1 (Mar. 14, 2022), p. 011048. DOI: 10.1103/PhysRevX.12.011048 (cited on pages 7, 15, 102).

[39] Nicolaas Bloembergen. 'Linear Stark Effect in Magnetic Resonance Spectra'. In: *Science* 133.3461 (Apr. 28, 1961), pp. 1363–1370. DOI: 10.1126/science.133.3461.1363 (cited on pages 9, 17, 108, 130).

[40] W. B. Mims. 'Electric Field Effects in Spin Echoes'. In: *Physical Review* 133 (3A Feb. 3, 1964), A835–A840. DOI: 10.1103/PhysRev.133.A835 (cited on pages 9, 17, 130).

[41] Ming-Yuan Liao and Gerard S. Harbison. 'The Nuclear Hexadecapole Interaction of Iodine-127 in Cadmium Iodide Measured Using Zero-field Two Dimensional Nuclear Magnetic Resonance'. In: *The Journal of Chemical Physics* 100.3 (Feb. 1, 1994), pp. 1895–1901. DOI: 10.1063/1.466542 (cited on pages 9, 17, 110, 132).

[42] Guokui Liu and Bernard Jacquier, eds. *Spectroscopic Properties of Rare Earths in Optical Materials*. 1st ed. 2005. Berlin, Heidelberg: Springer Berlin Heidelberg : Imprint : Springer, 2005 (cited on page 20).

[43] Mitchel Weissbluth. *Atoms and Molecules*. Elsevier, Dec. 2, 2012. 730 pp. (cited on pages 20, 21).

[44] A. Abragam and B. Bleaney. *Electron Paramagnetic Resonance of Transition Ions*. Oxford Classic Texts in the Physical Sciences. Oxford: Oxford University Press, 2012. 911 pp. (cited on pages 20, 22, 29, 129).

[45] A. Senyshyn et al. 'Lattice Dynamics and Thermal Properties of CaWO4'. In: *Physical Review B* 70.21 (Dec. 23, 2004), p. 214306. DOI: 10.1103/PhysRevB.70.214306 (cited on page 22).

[46] Francesco Cornacchia et al. 'Growth and Spectroscopic Characterization of Er3+:CaWO4'. In: *Journal of Applied Physics* 101.12 (June 15, 2007), p. 123113. DOI: 10.1063/1.2749403 (cited on page 22).

[47] A. Antipin et al. 'Paramagnetic Resonance and Spin-Lattice Relaxation of Er3+ and Tb3+ Ions in CaWO4 Crystal Lattice'. In: *Sov. Phys. Solid State* 10 (1968), p. 468 (cited on page 22).

[48] E. Billaud et al. 'Electron Paramagnetic Resonance Spectroscopy of a Scheelite Crystal Using Microwave-Photon Counting'. In: *Physical Review Research* 7.1 (Jan. 6, 2025), p. 013011. DOI: 10.1103/PhysRevResearch.7.013011 (cited on pages 22, 62, 65, 118).

[49] K. W. H. Stevens. 'Matrix Elements and Operator Equivalents Connected with the Magnetic Properties of Rare Earth Ions'. In: *Proceedings of the Physical Society. Section A* 65.3 (Mar. 1952), p. 209. DOI: 10.1088/0370-1298/65/3/308 (cited on page 22).

[50] S. A. Al'tshuler and Boris Michajlovič Kozyrev. *Electron Paramagnetic Resonance*. Burlington: Elsevier Science, 1964. 383 pp. (cited on page 22).

[51] A. Kiel. 'Theory of Electric Shifts of the Optical and Magnetic Resonance Properties of Paramagnetic Ions in Crystals'. In: *Physical Review* 148.1 (Aug. 5, 1966), pp. 247–256. DOI: 10.1103/PhysRev.148.247 (cited on pages 23, 130).

[52] B. R. Judd. 'Optical Absorption Intensities of Rare-Earth Ions'. In: *Physical Review* 127.3 (Aug. 1, 1962), pp. 750–761. DOI: 10.1103/PhysRev.127.750 (cited on page 23).

[53] Bernal G. Enrique. 'Optical Spectrum and Magnetic Properties of Er3+ in CaWO4'. In: *The Journal of Chemical Physics* 55.5 (Sept. 1971), pp. 2538–2549. DOI: 10.1063/1.1676445 (cited on pages 23, 129).

[54] Edward H. Erath. 'Crystal Field Parameters for Erbium in Er (C2H5SO4)3·9H2O'. In: *The Journal of Chemical Physics* 34.6 (June 1, 1961), pp. 1985–1989. DOI: 10.1063/1.1731805 (cited on page 23).

[55] HA Kramers. 'General Theory of Paramagnetic Rotation in Crystals'. In: *Proc. Acad. Sci. Amsterdam* 33 (1930), p. 959 (cited on page 23).

[56] Antipin, A.A. et al. 'Anisotropy of Er3+ Spin-Lattice Relaxation in LiYF4 Crystals'. In: *Soviet Journal of Experimental and Theoretical Physics* 23 (1981), pp. 2700–2707 (cited on page 25).

[57] Frank S. Ham. 'Linear Effect of Applied Electric Field in Electron Spin Resonance'. In: *Physical Review Letters* 7.6 (Sept. 15, 1961), pp. 242–243. DOI: 10.1103/PhysRevLett.7.242 (cited on page 25).

[58] W. B. Mims. 'Electric Field Shift in Paramagnetic Resonance for Four Ions in a Calcium Tungstate Lattice'. In: *Physical Review* 140 (2A Oct. 1965), A531–A535. DOI: 10.1103/PhysRev.140.A531 (cited on pages 25, 26, 130).

[59] A. Kiel and W. B. Mims. 'Electric-Field-Induced g Shifts for Loose Yb Ions in Three Scheelite Lattices'. In: *Physical Review B* 1.7 (Apr. 1, 1970), pp. 2935–2944. DOI: 10.1103/PhysRevB.1.2935 (cited on page 25).

[60] J. M. Baker and Brebis Bleaney. 'Paramagnetic Resonance in Some Lanthanon Ethyl Sulphates'. In: *Proceedings of the Royal Society of London. A. Mathematical and Physical Sciences* 245.1241 (June 3, 1958), pp. 156–174. DOI: 10.1098/rspa.1958.0074 (cited on page 26).

[61] Silvia Sottini and Edgar J. J. Groenen. 'A Comment on the Pseudo-Nuclear Zeeman Effect'. In: *Journal of Magnetic Resonance* 218 (May 1, 2012), pp. 11–15. DOI: 10.1016/j.jmr.2012.03.009 (cited on page 26).

[62] Ilya Kuprov. *Spin: From Basic Symmetries to Quantum Optimal Control*. Cham: Springer International Publishing, 2023 (cited on page 27).

[63] C. T. G. Knight et al. 'Solid-State Tungsten-183 Nuclear Magnetic Resonance Spectroscopy'. In: *Journal of the American Chemical Society* 108.23 (Nov. 1986), pp. 7426–7427. DOI: 10.1021/ja00283a057 (cited on pages 27, 84).

[64] A. Schweiger and G. Jeschke. *Principles of Pulse Electron Paramagnetic Resonance*. Oxford University Press, 2001 (cited on pages 32, 129).

[65] Daniella Goldfarb. 'ELDOR-Detected NMR'. In: *eMagRes*. Ed. by Robin K. Harris and Roderick L. Wasylishen. Chichester, UK: John Wiley & Sons, Ltd, Mar. 19, 2017, pp. 101–114. DOI: 10.1002/9780470034590.emrstm1516 (cited on pages 33, 83).

[66] Alexandre Blais et al. 'Circuit Quantum Electrodynamics'. May 26, 2020. (Visited on 05/11/2021) (cited on pages 37, 40).

[67] Serge Haroche and J.-M. Raimond. *Exploring the Quantum: Atoms, Cavities, and Photons*. OUP Oxford, Aug. 10, 2006. 616 pp. (cited on pages 38, 42, 49).

[68] E.T. Jaynes and F.W. Cummings. 'Comparison of Quantum and Semiclassical Radiation Theories with Application to the Beam Maser'. In: *Proceedings of the IEEE* 51.1 (Jan. 1963), pp. 89–109. DOI: 10.1109/PROC.1963.1664 (cited on page 39).

[69] Marianne Le Dantec. 'Electron Spin Dynamics of Erbium Ions in Scheelite Crystals, Probed with Superconducting Resonators at Millikelvin Temperatures'. PhD thesis. Univ. Paris-Saclay, Jan. 24, 2022. (Visited on 10/27/2022) (cited on pages 42, 57, 58, 62).

[70] Zhiren Wang et al. *Month-Long-Lifetime Microwave Spectral Holes in an Erbium-Doped Scheelite Crystal at Millikelvin Temperature*. Aug. 22, 2024. DOI: 10.48550/arXiv.2408.12758. Pre-published (cited on pages 42, 75, 99, 103).

[71] E. M Purcell, H. C Torrey, and R. V Pound. 'Resonance Absorption by Nuclear Magnetic Moments in a Solid'. In: *Physical Review* 69.1–2 (Jan. 1946), p. 37. DOI: 10.1103/PhysRev.69.37 (cited on page 42).

[72] L. Balembois et al. 'Cyclically Operated Microwave Single-Photon Counter with Sensitivity of 10^(-22) W / √Hz'. In: *Physical Review Applied* 21.1 (Jan. 23, 2024), p. 014043. DOI: 10.1103/PhysRevApplied.21.014043 (cited on pages 44, 45).

[73] Louis Pallegoix et al. *Enhancing the Sensitivity of Single Microwave Photon Detection with Bandwidth Tunability*. Jan. 13, 2025. DOI: 10.48550/arXiv.2501.07354. Pre-published (cited on pages 45, 66, 142).

[74] J. Wrachtrup et al. 'Optical Detection of Magnetic Resonance in a Single Molecule'. In: *Nature* 363.6426 (May 1993), pp. 244–245. DOI: 10.1038/363244a0 (cited on page 45).

[75] J. M. Elzerman et al. 'Single-Shot Read-out of an Individual Electron Spin in a Quantum Dot'. In: *Nature* 430.6998 (July 2004), pp. 431–435. DOI: 10.1038/nature02693 (cited on page 45).

[76] D. Rugar et al. 'Single Spin Detection by Magnetic Resonance Force Microscopy'. In: *Nature* 430.6997 (July 2004), pp. 329–332. DOI: 10.1038/nature02658 (cited on page 45).

[77] Claude Cohen-Tannoudji, Jacques Dupont-Roc, and Gilbert Grynberg. *Atom - Photon Interactions: Basic Processes and Applications*. Weinheim: Wiley-VCH Verlag GmbH & Co. KGaA, 2024. 656 pp. (cited on pages 48, 50, 56).

[78] Mark Kasevich and Steven Chu. 'Atomic Interferometry Using Stimulated Raman Transitions'. In: *Physical Review Letters* 67.2 (July 8, 1991), pp. 181–184. DOI: 10.1103/PhysRevLett.67.181 (cited on page 50).

[79] Andreas Erb and Jean-Côme Lanfranchi. 'Growth of High-Purity Scintillating CaWO4 Single Crystals for the Low-Temperature Direct Dark Matter Search Experiments CRESST-II and EURECA'. In: *CrystEngComm* 15.12 (Feb. 27, 2013), pp. 2301–2304. DOI: 10.1039/C2CE26554K (cited on page 57).

[80] C. Eichler et al. 'Electron Spin Resonance at the Level of $1{0}^{4}$ Spins Using Low Impedance Superconducting Resonators'. In: *Physical Review Letters* 118.3 (Jan. 19, 2017), p. 037701. DOI: 10.1103/PhysRevLett.118.037701 (cited on page 58).

[81] Marianne Le Dantec. 'Electron Spin Dynamics of Erbium Ions in Scheelite Crystals, Probed with Superconducting Resonators at Millikelvin Temperatures'. PhD thesis. Université Paris-Saclay, Jan. 24, 2022. (Visited on 10/15/2025) (cited on page 61).

[82] Philipp Neumann et al. 'Single-Shot Readout of a Single Nuclear Spin'. In: *Science* 329.5991 (July 2010), pp. 542–544. DOI: 10.1126/science.1189075 (cited on pages 70, 71).

[83] F. Jelezko et al. 'Observation of Coherent Oscillation of a Single Nuclear Spin and Realization of a Two-Qubit Conditional Quantum Gate'. In: *Physical Review Letters* 93.13 (Sept. 20, 2004), p. 130501. DOI: 10.1103/PhysRevLett.93.130501 (cited on page 70).

[84] N. Imoto, H. A. Haus, and Y. Yamamoto. 'Quantum Nondemolition Measurement of the Photon Number via the Optical Kerr Effect'. In: *Physical Review A* 32.4 (Oct. 1, 1985), pp. 2287–2292. DOI: 10.1103/PhysRevA.32.2287 (cited on page 71).

[85] G. L. van de Stolpe et al. 'Mapping a 50-Spin-Qubit Network through Correlated Sensing'. In: *Nature Communications* 15.1 (Mar. 5, 2024), p. 2006. DOI: 10.1038/s41467-024-46075-4 (cited on page 73).

[86] Warren Nagourney, Jon Sandberg, and Hans Dehmelt. 'Shelved Optical Electron Amplifier: Observation of Quantum Jumps'. In: *Physical Review Letters* 56.26 (June 30, 1986), pp. 2797–2799. DOI: 10.1103/PhysRevLett.56.2797 (cited on page 74).

[87] J. C. Bergquist et al. 'Observation of Quantum Jumps in a Single Atom'. In: *Physical Review Letters* 57.14 (Oct. 6, 1986), pp. 1699–1702. DOI: 10.1103/PhysRevLett.57.1699 (cited on page 74).

[88] Th. Sauter et al. 'Observation of Quantum Jumps'. In: *Physical Review Letters* 57.14 (Oct. 6, 1986), pp. 1696–1698. DOI: 10.1103/PhysRevLett.57.1696 (cited on page 74).

[89] Sebastien Gleyzes et al. 'Quantum Jumps of Light Recording the Birth and Death of a Photon in a Cavity'. In: *Nature* 446.7133 (Mar. 2007), pp. 297–300. DOI: 10.1038/nature05589 (cited on page 74).

[90] Christine Guerlin et al. 'Progressive Field-State Collapse and Quantum Non-Demolition Photon Counting'. In: *Nature* 448.7156 (2007), pp. 889–893. DOI: 10.1038/nature06057 (cited on page 74).

[91] R. Vijay, D. H Slichter, and I. Siddiqi. 'Observation of Quantum Jumps in a Superconducting Artificial Atom'. In: *Physical Review Letters* 106.11 (Mar. 2011), p. 110502. DOI: 10.1103/PhysRevLett.106.110502 (cited on page 74).

[92] A. Abragam and W. G. Proctor. *Une Nouvelle Méthode de Polarisation Dynamique Des Noyaux Atomiques Dans Les Solides*. Centre d'études nucléaires, Service de documentation, 1958 (cited on page 86).

[93] A Abragam and M Goldman. 'Principles of Dynamic Nuclear Polarisation'. In: *Reports on Progress in Physics* 41.3 (Mar. 1978), pp. 395–467. DOI: 10.1088/0034-4885/41/3/002 (cited on page 86).

[94] W. T. Wenckebach. 'The Solid Effect'. In: *Applied Magnetic Resonance* 34.3 (Aug. 1, 2008), pp. 227–235. DOI: 10.1007/s00723-008-0121-9 (cited on page 86).

[95] Yutian Wen et al. *Addressing Spins at the Clock Transitions with a Frequency- and Bandwidth-Tunable Superconducting Resonator*. Oct. 22, 2025. DOI: 10.48550/arXiv.2510.19684. Pre-published (cited on pages 87, 104).

[96] T. H. Taminiau et al. 'Detection and Control of Individual Nuclear Spins Using a Weakly Coupled Electron Spin'. In: *Physical Review Letters* 109.13 (Sept. 25, 2012), p. 137602. DOI: 10.1103/PhysRevLett.109.137602 (cited on pages 88, 107).

[97] D. A. Lidar, I. L. Chuang, and K. B. Whaley. 'Decoherence-Free Subspaces for Quantum Computation'. In: *Physical Review Letters* 81.12 (Sept. 21, 1998), pp. 2594–2597. DOI: 10.1103/PhysRevLett.81.2594 (cited on page 89).

[98] Holly G. Stemp et al. 'Scalable Entanglement of Nuclear Spins Mediated by Electron Exchange'. In: *Science* 389.6766 (Sept. 18, 2025), pp. 1234–1238. DOI: 10.1126/science.ady3799 (cited on pages 90, 91).

[99] D.A. Lidar and T.A. Brun. *Quantum Error Correction*. Cambridge University Press, 2013 (cited on page 94).

[100] H.P. Bartling et al. 'Universal High-Fidelity Quantum Gates for Spin Qubits in Diamond'. In: *Physical Review Applied* 23.3 (Mar. 21, 2025), p. 034052. DOI: 10.1103/PhysRevApplied.23.034052 (cited on pages 98, 110).

[101] T. H. Taminiau et al. 'Universal Control and Error Correction in Multi-Qubit Spin Registers in Diamond'. In: *Nat. Nanotechnol.* 9.3 (Mar. 1, 2014), pp. 171–176. DOI: 10.1038/nnano.2014.2 (cited on page 98).

[102] Mateusz T. Mądzik et al. 'Controllable Freezing of the Nuclear Spin Bath in a Single-Atom Spin Qubit'. In: *Science Advances* 6.27 (July 3, 2020), eaba3442. DOI: 10.1126/sciadv.aba3442 (cited on page 98).

[103] R. Guichard et al. 'Decoherence of Nuclear Spins in the Frozen Core of an Electron Spin'. In: *Physical Review B* 91.21 (June 15, 2015), p. 214303. DOI: 10.1103/PhysRevB.91.214303 (cited on page 98).

[104] Michael A. Nielsen and Isaac L. Chuang. *Quantum Computation and Quantum Information: 10th Anniversary Edition*. Cambridge University Press, 2010 (cited on page 101).

[105] Mouktik Raha et al. 'Optical Quantum Nondemolition Measurement of a Single Rare Earth Ion Qubit'. In: *Nature Communications* 11.1 (Mar. 30, 2020), p. 1605. DOI: 10.1038/s41467-020-15138-7 (cited on page 103).

[106] P. Haikka et al. 'Proposal for Detecting a Single Electron Spin in a Microwave Resonator'. In: *Phys. Rev. A* 95.2 (Feb. 2017), p. 022306. DOI: 10.1103/PhysRevA.95.022306 (cited on page 103).

[107] Hans K. C. Beukers et al. 'Control of Solid-State Nuclear Spin Qubits Using an Electron Spin-$1/2$'. In: *Physical Review X* 15.2 (Apr. 11, 2025), p. 021011. DOI: 10.1103/PhysRevX.15.021011 (cited on page 104).

[108] Sumedh Mahashabde et al. 'Fast Tunable High-Q-Factor Superconducting Microwave Resonators'. In: *Physical Review Applied* 14.4 (Oct. 21, 2020), p. 044040. DOI: 10.1103/PhysRevApplied.14.044040 (cited on page 104).

[109] J. Majer et al. 'Coupling Superconducting Qubits via a Cavity Bus'. In: *Nature* 449.7161 (Sept. 1, 2007), pp. 443–447. DOI: 10.1038/nature06184 (cited on page 104).

[110] A. J. Landig et al. 'Virtual-Photon-Mediated Spin-Qubit–Transmon Coupling'. In: *Nature Communications* 10.1 (Nov. 6, 2019), p. 5037. DOI: 10.1038/s41467-019-13000-z (cited on page 104).

[111] Serwan Asaad et al. 'Coherent Electrical Control of a Single High-Spin Nucleus in Silicon'. In: *Nature* 579.7798 (Mar. 2020), pp. 205–209. DOI: 10.1038/s41586-020-2057-7 (cited on page 108).

[112] R. W. Dixon and N. Bloembergen. 'Electrically Induced Perturbations of Halogen Nuclear Quadrupole Interactions in Polycrystalline Compounds. II. Microscopic Theory'. In: *The Journal of Chemical Physics* 41.6 (Sept. 15, 1964), pp. 1739–1747. DOI: 10.1063/1.1726153 (cited on page 108).

[113] Masaaki Ono et al. 'Coherent Manipulation of Nuclear Spins in Semiconductors with an Electric Field'. In: *Applied Physics Express* 6.3 (Feb. 28, 2013), p. 033002. DOI: 10.7567/APEX.6.033002 (cited on page 108).

[114] R. M. Macfarlane et al. 'Optical Measurement of the Effect of Electric Fields on the Nuclear Spin Coherence of Rare-Earth Ions in Solids'. In: *Physical Review Letters* 113.15 (Oct. 7, 2014), p. 157603. DOI: 10.1103/PhysRevLett.113.157603 (cited on pages 108, 131).

[115] J. P. Dehollain et al. 'Nanoscale Broadband Transmission Lines for Spin Qubit Control'. In: *Nanotechnology* 24.1 (Dec. 2012), p. 015202. DOI: 10.1088/0957-4484/24/1/015202 (cited on page 109).

[116] J. J. Pla et al. 'Strain-Induced Spin-Resonance Shifts in Silicon Devices'. In: *Phys. Rev. Applied* 9.4 (Apr. 2018), p. 044014. DOI: 10.1103/PhysRevApplied.9.044014 (cited on pages 109, 118).

[117] Charles Schwartz. 'Theory of Hyperfine Structure'. In: *Physical Review* 97.2 (Jan. 15, 1955), pp. 380–395. DOI: 10.1103/PhysRev.97.380 (cited on page 109).

[118] Vladislav Gerginov, Andrei Derevianko, and Carol E. Tanner. 'Observation of the Nuclear Magnetic Octupole Moment of 133Cs'. In: *Physical Review Letters* 91.7 (Aug. 13, 2003), p. 072501. DOI: 10.1103/PhysRevLett.91.072501 (cited on page 109).

[119] Nicholas C. Lewty et al. 'Spectroscopy on a Single Trapped $^{137}Ba^{+}$ Ion for Nuclear Magnetic Octupole Moment Determination'. In: *Optics Express* 20.19 (Sept. 10, 2012), pp. 21379–21384. DOI: 10.1364/OE.20.021379 (cited on page 109).

[120] J. Cederberg et al. 'Evidence for a Nuclear Hexadecapole Interaction in the Hyperfine Spectrum of LiI'. In: *The Journal of Chemical Physics* 110.5 (Feb. 1, 1999), pp. 2431–2436. DOI: 10.1063/1.477972 (cited on page 109).

[121] Jørn Thyssen et al. 'Quadrupole and Hexadecapole Couplings for 127I in Li127I'. In: *Physical Review A* 63.2 (Jan. 8, 2001), p. 022505. DOI: 10.1103/PhysRevA.63.022505 (cited on page 109).

[122] Lucca Sielaff et al. 'Pulsed Dipolar Hyperfine Spectroscopy for Molecular Distance Measurements in the Angstrom to Nanometer Scale'. In: *Science Advances* 11.30 (July 25, 2025), eady5665. DOI: 10.1126/sciadv.ady5665 (cited on page 109).

[123] S. L. Segel. 'Nuclear Electric Hexadecapole Interactions in Solids'. In: *The Journal of Chemical Physics* 69.6 (Sept. 15, 1978), pp. 2434–2438. DOI: 10.1063/1.436929 (cited on page 109).

[124] Elana B. Doering and J. S. Waugh. 'Search for Hexadecapole Interaction in KTaO3 by 181Ta-NMR'. In: *The Journal of Chemical Physics* 85.4 (Aug. 15, 1986), pp. 1753–1756. DOI: 10.1063/1.451176 (cited on page 109).

[125] G. Cybenko. 'Reducing Quantum Computations to Elementary Unitary Operations'. In: *Computing in Science & Engineering* 3.2 (Mar. 2001), pp. 27–32. DOI: 10.1109/5992.908999 (cited on page 116).

[126] Xi Yu et al. *Creation and Manipulation of Schrödinger Cat States of a Nuclear Spin Qudit in Silicon*. May 24, 2024. URL: http://arxiv.org/abs/2405.15494 (visited on 10/11/2024). Pre-published (cited on pages 116, 121).

[127] Irene Fernández de Fuentes et al. 'Navigating the 16-Dimensional Hilbert Space of a High-Spin Donor Qudit with Electric and Magnetic Fields'. In: *Nature Communications* 15.1 (Feb. 14, 2024), p. 1380. DOI: 10.1038/s41467-024-45368-y (cited on page 120).

[128] E. K. Dietsche et al. 'High-Sensitivity Magnetometry with a Single Atom in a Superposition of Two Circular Rydberg States'. In: *Nature Physics* 15.4 (Apr. 2019), pp. 326–329. DOI: 10.1038/s41567-018-0405-4 (cited on page 121).

[129] Daniel Foreman-Mackey et al. *Emcee: The MCMC Hammer*. Nov. 25, 2013. DOI: 10.1086/670067. Pre-published (cited on page 124).

[130] Jonathan Goodman and Jonathan Weare. 'Ensemble Samplers with Affine Invariance'. In: *Communications in Applied Mathematics and Computational Science* 5.1 (Jan. 31, 2010), pp. 65–80. DOI: 10.2140/camcos.2010.5.65 (cited on pages 124, 146).

[131] H. M. Foley. 'Second-Order Magnetic Perturbations in Nuclear Quadrupole Spectra and the "Pseudo-Quadrupole" Effect in Diatomic Molecules'. In: *Physical Review* 72.6 (Sept. 15, 1947), pp. 504–505. DOI: 10.1103/PhysRev.72.504 (cited on page 129).

[132] M. N. Ghatikar. 'Zeeman-Field-Dependent Quadrupolar Interaction in Rare-Earth Trichlorides'. In: *Proceedings of the Physical Society* 87.3 (Mar. 1966), p. 727. DOI: 10.1088/0370-1328/87/3/314 (cited on page 129).

[133] G. W. Ludwig and H. H. Woodbury. 'Splitting of Electron Spin Resonance Lines by an Applied Electric Field'. In: *Physical Review Letters* 7.6 (Sept. 15, 1961), pp. 240–241. DOI: 10.1103/PhysRevLett.7.240 (cited on page 130).

[134] J. Armstrong, N. Bloembergen, and D. Gill. 'Linear Effect of Applied Electric Field on Nuclear Quadrupole Resonance'. In: *Physical Review Letters* 7.1 (July 1, 1961), pp. 11–14. DOI: 10.1103/PhysRevLett.7.11 (cited on page 130).

[135] Jens Koch et al. 'Charge-Insensitive Qubit Design Derived from the Cooper Pair Box'. In: *Physical Review A* 76.4 (Oct. 12, 2007), p. 042319. DOI: 10.1103/PhysRevA.76.042319 (cited on page 139).

[136] A. Wallraff et al. 'Strong Coupling of a Single Photon to a Superconducting Qubit Using Circuit Quantum Electrodynamics'. In: *Nature* 431.7005 (7005 Sept. 2004), pp. 162–167. DOI: 10.1038/nature02851 (cited on page 140).

[137] Alexandre May. 'Noise Mitigation in Single Microwave Photon Counting'. Theses. Université Paris-Saclay, July 2025. (Visited on 10/27/2025) (cited on page 143).

[138] J. R. Johansson, P. D. Nation, and Franco Nori. 'QuTiP: An Open-Source Python Framework for the Dynamics of Open Quantum Systems'. In: *Computer Physics Communications* 183.8 (Aug. 1, 2012), pp. 1760–1772. DOI: 10.1016/j.cpc.2012.02.021 (cited on page 145).

[139] Pierre Guilmin et al. *Dynamiqs*. 2025 (cited on page 145).

[140] Daniel Foreman-Mackey. 'Corner.Py: Scatterplot Matrices in Python'. In: *The Journal of Open Source Software* 1.2 (June 8, 2016), p. 24. DOI: 10.21105/joss.00024 (cited on page 147).